REPORT NO.
UCB/EERC-79/14
JUNE 1979

EARTHQUAKE ENGINEERING RESEARCH CENTER

SEISMIC BEHAVIOR OF REINFORCED CONCRETE INTERIOR BEAM-COLUMN SUBASSEMBLAGES

by

SUTHIPOUL VIWATHANATEPA
EGOR P. POPOV
VITELMO V. BERTERO

Report to Sponsor:
National Science Foundation

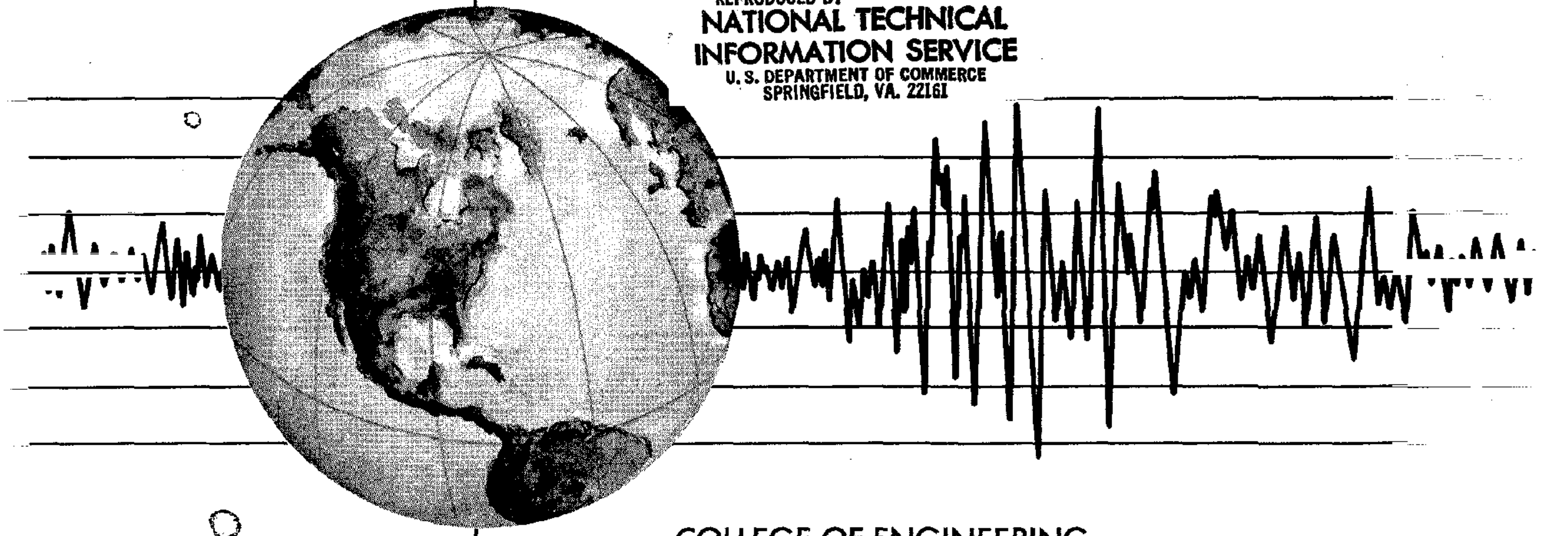

COLLEGE OF ENGINEERING

UNIVERSITY OF CALIFORNIA · Berkeley, California

BIBLIOGRAPHIC DATA SHEET

1. Report No. NSF/RA-790186

2.

3. Recipient's Accession No. PB301326

4. Title and Subtitle
Seismic Behavior of Reinforced Concrete Interior
Beam-Column Subassemblages

5. Report Date June 1979

6.

7. Author(s) S. Viwathanatepa, E.P. Popov, VV. Bertero

8. Performing Organization Rept. No. UCB/EERC-79/14

9. Performing Organization Name and Address
Earthquake Engineering Research Center
University of California
47th. & Hoffman Blvd.
Richmond, CA 94804

10. Project/Task/Work Unit No.

11. Contract/Grant No.
AEN-7307734
ENV-7604263

12. Sponsoring Organization Name and Address
National Science Foundation
1800 G Street, N.W.
Washington, D.C . 20550

13. Type of Report & Period Covered

14.

15. Supplementary Notes

16. Abstracts

This report gives details of experiments to test the seismic behavior of reinforced concrete subassemblages carried out on beam-column subassemblages and evaluates the significance of the analytical and experimental results obtained.

Two virgin concrete subassemblages and one repaired subassemblage were tested. A horizontal force was applied to one subassemblage to generate a large single hysteretic loop, the initial part of which provided information on monotonic loading. Once the loading sequence was completed this specimen was repaired by epoxy injection processes and an incremental cyclic load was applied until failure occurred. The second specimen was tested to failure by applying a similar loading sequence to that applied to the repaired subassemblage.

17b. Identifiers/Open-Ended Terms

17c. COSATI Field/Group

18. Availability Statement
Release Unlimited

19. Security Class (This Report) UNCLASSIFIED

20. Security Class (This Page UNCLASSIFIED

21. No. of Pages 201

22. Price PCA10 / MF-A01

TIS-35 (REV. 10-73) ENDORSED BY ANSI AND UNESCO. THIS FORM MAY BE REPRODUCED USCOMM-DC 8265-P74

la

SEISMIC BEHAVIOR OF R/C INTERIOR BEAM-COLUMN SUBASSEMBLAGES

by

Suthipoul Viwathanatepa
Research Assistant

Egor P. Popov
Professor of Civil Engineering
University of California, Berkeley

Vitelmo V. Bertero
Professor of Civil Engineering
University of California, Berkeley

A report on research sponsored by
the National Science Foundation

Report No. UCB/EERC-79/14
Earthquake Engineering Research Center
College of Engineering
University of California
Berkeley, California

ACKNOWLEDGEMENTS

The authors are grateful for the financial support provided for this investigation by the National Science Foundation under Grants AEN-7307734 and ENV-7604263. The work reported herein is a phase of an ongoing investigation at the University of California, Berkeley, under the supervision of Professors E. P. Popov and V. V. Bertero. Many individuals contributed to the effort described. The original configuration of the subassemblage and experimental setup followed the design by graduate student, David Soleimani. He together with other graduate students and Barry Lotz, assisted with the experiments.

L. Tsai and J. Aldrich assisted with the preparation of the report for publication. L. Hashizume made the technical illustrations.

Joy Kono did the typing of the final manuscript, and Doug Ullman prepared the drawings for publication.

TABLE OF CONTENTS

LIST OF TABLES

LIST OF FIGURES

1. INTRODUCTION

1.1 General

A strong earthquake induces forces and displacements in a typical building structure which could greatly exceed those induced by an earthquake specified in standard building codes; buildings designed for normal code lateral forces could be stressed beyond the elastic limit by a major earthquake. Therefore, in designing a building to withstand severe earthquakes, it is necessary that the large seismic energy input be absorbed and dissipated through large but controllable inelastic deformations of the structure. Therefore, the sources of potential structural brittle failure must be eliminated. Thus, it is necessary to prevent: premature crushing and shearing of concrete; sudden cracking and simultaneous fracturing of steel, sudden loss of bond and anchorage; premature crushing and/or splitting of concrete cover accompanied by local buckling of main reinforcement; and premature dynamic instability resulting from large lateral drifts. Degradation of stiffness and strength under repeated loading must also be minimized or delayed long enough to permit that sufficient energy be dissipated through stable hysteretic behavior.

Although some of these sources of potential brittle failure can be controlled by satisfying present code provisions there are others that continue to pose serious problems. Among the latter bond (anchorage) failure is one of the most undesirable and has been the cause of severe local damage to, and even collapse of, many structures during recent strong earthquakes. Present bond seismic code provisions appear to be inadequate. These provisions are based on results obtained under monotonic loading, which are inadequate for gaging the actual structural behavior during severe seismic shaking. The bond behavior of reinforced concrete under a monotonically increasing load is altogether different from that observed under repeated reversals.

One location in reinforced concrete frame structures where deterioration and loss of bond can create a serious problem is the interior beam-column connection. This region, where the main beam reinforcement is anchored, is usually subjected to the maxima in both moment and shear. The simultaneous occurrence of maximum moment and shear suggests unfavorable interaction: a high moment induces large forces which cause yielding in the main rebars anchored in the joint; a high shear force induces shear cracks in the joint which damage the bond of the embedded rebars. For cyclic loading well in the inelastic range, interface cracks at column faces are often open throughout the beam section, leaving only the steel reinforcement to resist the applied moment. The effective anchorage length of the rebar in such a case is actually reduced to the column width, which is inadequate for bond transfer. As a result the rebars can slip excessively through the connection. In this study an attempt has been made to examine in detail the joint behavior, that is, slippage of the rebar and shear distortion due to the formation of diagonal shear cracks, and to evaluate the significance of joint deformations on the strength and stiffness of a subassemblage modeling a typical lower-story interior beam-column joint of a highrise building.

The poor performances of beam-column connections in severe earthquakes have stimulated several researchers to study their behavior in order to improve the connection details and eliminate the possibility of their premature failure. Hanson, Corley, and Connor of the Portland Cement Association [1 - 3]; Park, Paulay and others of the University of

Canterbury [4-7,12-13]; Townsend [8]; and Japanese investigators [14-17], to name only a few, have already expended considerable effort in this area. The experimental work has recently been summarized by Bertero [18]. Many of these tests have shown that seismic loading can induce yielding of the joint ties followed by loss of integrity of the joint and substantial degradation of strength and stiffness. This has been observed in both interior and exterior joint subassemblages.

During the last few years the epoxy injection technique has been used to repair damage resulting from the Alaska, Santa Rosa, San Fernando, and Managua earthquakes [24]. While this type of structural repair has generally proved to be effective under working loads, little information is available for inelastic loading. Experimental results of repaired beams subjected to cyclic loads of pure bending, bending with low shear, and bending with high shear [10,21] have shown that the repaired beam can attain the same strength as the original, and often has greater strength at first yield. However, the stiffness of the repaired beam was significantly reduced because the bond between the reinforcement and concrete was not completely restored and some of the smaller cracks (under 0.127 mm in width) were not repaired by this method.

Although the epoxy injection method has proven to be very effective for the critical regions of simple elements such as beams and columns, application of this method to repair a damaged beam-column connection is expected to be far less effective. Since substantial bond damage can take place along the bar without clear evidence of surface cracking, it is not possible to inject the epoxy. In the event that there are small cracks, because of the high viscosity of epoxy, the epoxy may not penetrate up to the bar, nor reconstitute the dust surrounding the bar. The efficiency of this method in repairing the connection can be evaluated only by testing. Therefore, the testing of a repaired subassemblage is included in this program.

1.2 Objectives and Scope

This investigation is part of a continuing research program aimed at evaluating experimentally and analytically the seismic behavior of reinforced concrete subassemblages. This research is being carried out in several phases. The work described here is an extension of the study cited in reference 11. The three objectives of this phase of research were as follows:

1. To obtain reliable experimental information regarding the strength, stiffness, ductility, energy absorption, and energy dissipation of reinforced concrete beam-column subassemblages under monotonic and cyclic loading with emphasis on hysteretic behavior.

2. To predict analytically various subassemblage responses using both an elasto-plastic hardening model and a moment-curvature degrading model. Elasto-plastic hardening has been frequently used to analyze the response of reinforced concrete structures. However, the degrading model, which takes into account the deterioration in stiffness on loading, is more appropriate for the reinforced concrete structure.

3. To assess the effectiveness of the epoxy injection method for repairing cracked reinforced concrete members and the connection zone. This is done by comparing the behavior of a repaired subassemblage with the behavior of the virgin specimen with a different loading history and the behavior of another virgin specimen subjected to similar loading history.

To achieve these objectives, two virgin reinforced concrete subassemblages and one repaired subassemblage were tested. A horizontal force was applied to one subassemblage to generate a large single hysteretic loop. The initial part of the loop provided, for all practical purposes. information on monotonic loading. Damage to this specimen was limited to a repairable level. Once the loading sequence was completed, the cracked specimen was repaired by the epoxy injection processes and an incremental cyclic load was applied until failure occurred. To provide a control specimen for cyclic loading, the second subassemblage was tested to failure by applying a loading sequence similar to that applied to the repaired specimen.

This report gives details of the experiments carried out on the beam-column subassemblage and evaluates and discusses the significance of the analytical and experimental results obtained.

2. TEST SPECIMENS

2.1 Selection of Test Specimens

Economic considerations required the simplest beam-column connection test set up which would still retain the mechanical characteristics being studied. In order to derive the simplest possible test set up, qualitative behavior of the frame under gravity and severe lateral load is described. (It should be noted that this phase of the investigation is limited to studying the behavior of beam-column connections at a lower story when lateral load is the dominant excitation.)

A 20-story ductile reinforced concrete frame office building was designed to meet the requirements of the 1970 Uniform Building Code for buildings in seismic zone 3. An elevation of the structure is shown in Fig. 2.1. Member sizes and the amount of longitudinal reinforcement for the structure are given in reference 11.

The free-body diagram of forces acting on a typical four-bay lower story beam-column frame, and the bending moment developed under gravity and the lateral loads are shown in Figs. 2.2a through 2.2c. During a severe earthquake the combination of gravity and lateral loads is likely to produce inelastic deformations at locations B, D, F and H. A further increase in lateral load causes plastic hinges to form at A, C, E, and G. The bending moment diagram at this stage is shown in Fig. 2.2d where M_{y1} and M_{y2} denote the positive and negative yield moment capacities of the beams. The small magnitude of the gravity load in comparison to the lateral load in the lower story eliminates the possibility of the maximum moment occurring at midspan. When the direction of severe lateral load is reversed, the bending moment is as shown in Fig. 2.2e.

The bending moment distribution on the girder shown in Figs. 2.2d and 2.2e, suggests that a set up suitable for studying the behavior of the interior beam-column connection would be as in Fig. 2.2f, where the zero moment locations are assumed to occur at midspan of the beams. To simplify the testing arrangement the points of inflection in the columns are assumed to be at mid-height.

The bending moment diagram for the girder C'D and EE' of the test structure would be as shown by the dotted line curves of Figs. 2.2d and 2.2e.

2.2 Description of Test Specimens

Half-scale models were made of subassemblages from the third floor of the building. Design details of the test specimen are given in Appendix E. The subassemblages consisted of two 9-in. by 16-in. beam girders and a 17-in. by 17-in. square column, as shown in Fig. 2.3. Shear transducers were attached at the beam ends to measure vertical reactions. The column was bolted at top and bottom to steel clevises used for mounting the specimens on the testing frame.

The main longitudinal reinforcement of the beams consisted of 4 #6 reinforcing bars at the top and 3 #5 bars at the bottom so that the area of reinforcement at the bottom was about half that at the top (see Fig. 2.3b). Number 2 tied stirrups were spaced 3.5 in. center-to-center along the beam. In addition to the tied stirrups, #2 hairpin shaped bars were used to furnish a more rigid support for the longitudinal bars inside the rectangular stirrups (Fig. 2.3b).

The columns were reinforced longitudinally by twelve #6 bars, and transversely by #2 cross-shaped ties spaced 1.6 in. apart (Fig. 2.3c).

Seven ties, similar to the ones in the columns, satisfy confinement and resistance to shear requirements in the joint.

2.3 Characteristics of Materials

In the original design, the concrete for the subassemblage was to have 4,000 psi strength at 14 days. However, since the actual experiments were performed between 18 and 30 days, there was a substantial increase in concrete strength, to 4.5 - 4.97 ksi, as shown in Fig. 2.4. The concrete properties on testing dates are summarized in Fig. 2.4 and in Tables 2.1 and 2.2.

The epoxy resin used for the repair is known commercially as Concresive AE 1050-15, manufactured by the Adhesive Engineering Company. The mechnical properties of this resin are listed in Table 2.3, according to information provided by the manufacturers. Note that the tensile strength of the cured epoxy is about twice that of the concrete. The Young's modulus of the epoxy averaged approximately 8% of that for concrete.

Numbers 2, 5, and 6 bars of grade 60 steel were used for reinforcement. Their mechanical properties, characterized by stress-strain curves, are shown in Fig. 2.5. Observe that the yield strength of the #2 bar is 65 ksi, while that of the #5 and #6 bars is about 71.0 ksi.

2.4 Fabrication of Test Specimens

The formwork and reinforcement for the test structure are shown in Fig. 2.6. The reinforcement cage was constructed to close tolerances and was securely tied together with 16-gage wire. Plastic chairs were used to hold the reinforcement cage in position in the oiled wooden form.

The supports of the clip gages used to measure steel strains were silver-soldered to the longitudinal bars of the beams and columns. These supports were covered with modeling clay and plastic tubing to enable them to move without contacting the concrete cover.

Special beam end and column end details are shown in Figs. 2.7 and 2.8. These consisted of #6 threaded rebars welded to the ends of the longitudinal bars and spliced (i.e. two bars overlapped) at the column ends. These end arrangements are essential for mounting the shear transducers on the beam ends and for bolting the column ends to the testing frame.

The specimens were case in-place in plywood forms stiffened with wood battens. The concrete was compacted with a high-frequency vibrator. After seven days, the forms were removed and all subassemblages and control cylinders were cured with wet sacks under a plastic cover for seven more days. Testing was carried out approximately three weeks after casting.

3. EXPERIMENTAL TEST SET UP AND INSTRUMENTATION

3.1 Testing Frame and Specimen Supports

The testing frame used in this experiment (Fig. 3.1) is a modification of one described in reference 23, reduced from 24 feet to 12 feet in length (Fig. 3.2). The gravity load simulation devices and lateral bracing system used in previous subassemblage experiments were removed.

The function of the testing frame was to provide rigid support for the test structure and loading devices. The specimen was supported at the top of the column and at the ends of the beams. The upper column end was connected to the cross piece of the rigid frame by a hinge, so that at this point, rotation, but not translation, could take place. The outer ends of the beams rested on rollers, permitting rotation and horizontal translation, but not vertical movement. See Krawinkler, Bertero, and Popov [23] for more details of the support construction.

3.2 Loading Apparatus

The external loads applied to the beam-column subassemblage consisted of an axial load, P, and a horizontal load, H, at the lower column end (Fig. 3.3). The horizontal load simulated the lateral load induced in the prototype by earthquake ground motions. The load P simulated axial load in the column, and was applied through a 600-kip compression jack mounted on a movable cart. Horizontal load H was applied by means of a two-way hydraulic actuator.

3.3 Instrumentation

Two categories of instrumentation were used in the tests: one for measuring loads and reactions, and the other for measuring strains and deformations.

1. Load and Reaction

Transducers were used to measure the externally applied loads, P and H (Fig. 3.2). The shear reactions at the beam ends, V_W and V_E were measured by specially designed shear transducers bolted to the beam ends. The transducers were guided to move only horizontally by a pair of parallel rails.

2. Strain and Deformation

a) Strains in the reinforcement were measured by six weldable gages, four on the beam longitudinal bars and two on the stirrup ties. These gages were located on the main reinforcement bars (designated REI, REII, RWI and RWII) and on the ties (designated STE and STW) as shown in Fig. 3.4. It should be noted that the gages on the beam longitudinal bars were placed just outside the connection region, so that their presence would not disturb the bond condition of the rebars in the joint, which is the most crucial parameter in this test.

b) Clip gages were used to measure the average curvature in the critical regions of the beams and columns: sixteen gages for the beams and four gages for the columns. For the purposes of identification, the beam curvature gages are classified into four different groups: CE (gages CEI, CEII, CE2 and CE22), CW (gages CWI, CWII, CW2, and CW22), KE (gages KEI, KEII, KE2, and LE22), and KW (gages KWI, KWII, KW2, and KW22), see Figs. 3.5a, 3.6a and 3.6b. The letter

C in CE and CW groups indicates the clip gages mounted on steel pins "silver-soldered" to the main beam rebars; K in KE and KW denotes gages mounted on steel rods embedded horizontally through the beam. The letters E (east) and W (west) identify the locations of the gages (see Fig. 3.5a). With this instrumentation, average curvatures of the beam could be obtained from deformation of either the rebars or the concrete elements, thus permitting detection of slippage of the rebars and also determination of the average strain distribution across the beam section.

The column curvatures were measured by the gages designated EU, EB, WU, and WB in Fig. 3.5c. These gages were mounted on steel pins, silver-soldered to the column rebars.

c) Shear Deformation - Four diagonally mounted clip gages, designated SWI, SWII on the west beam, and SEI and SEII on the east beam, are used to measure shear deformation. (See Figs. 3.5a, 3.6a, and 3.6b).

d) Rebar Slippage in Beam-Column Connections and Crack Openings at Beam-Column Junction - Four precision linear potentiometers designated PE1, PE11, PW1 and PW11, in Fig. 3.5c were used to measure rebar slippage. These potentiometers were rigidly connected to the steel pins soldered to the rebars adjacent to the beam-column faces. The installation details of the potentiometers are illustrated in Fig. 3.7.

The sizes of the cracks formed at the beam-column faces were measured by four additional potentiometers, viz., FE1, FE11, FW1, and FW11, which were attached to steel rods encased in the concrete section at the beam-column intersection (Fig. 3.5c). There are two reasons why measurements of the interface cracks are necessary. First, they are used to compute slippage between the steel bars and concrete at the connecting faces. Secondly, they provide an alternative determination of the fixed-end rotation due to slippage of the rebars in the connection.

e) Displacements of Upper and Lower Column Hinges - One of the most important parameters in this experiment was the horizontal displacement of the lower column hinge, designated δ . It was measured by using a 15 in. range linear potentiometer, D, in Fig. 3.5c, and was recorded continuously through the test on an XY recorder. The lower column hinge displacements were also measured frequently at specific points of the loading history by a precision theodolite. This provided a check of the column deflections.

Even though the testing frame was relatively rigid in the plane of the specimen, it did tend to undergo small vertical and horizontal displacements on application of H and P at the lower column. To correct for the small horizontal deflection, the upper column hinge displacement was measured periodically bu the theodolite. Figure 3.5c shows the targets, T_1 and T_2, hung from the upper and lower column hinges respectively, for theodolite sighting.

3.4 Recording Equipment

All gage readings were recorded and printed out at specific points of the loading history by a low-speed scanner data acquisition system. A few gage measurements were recorded continuously on XY and XYY recorders. These included beam shear forces versus rotations of the critical regions, shear versus rebar slippage at the connections, and horizontal load, H, versus the lower column deflection, δ .

3.5 Test Procedures for Subassemblages BC4 and BC3

The specimen was whitewashed to aid in crack detection and grid lines were carefully drawn on the joint and beams to facilitate location of cracks and to give an idea of the deformed shapes. The specimen was then plumbed and the recording equipment connected. A 470-kip axial load was then applied to the column and maintained at that value throughout the experiment. The shear transducers attached to the ends of the beams were lowered, gradually, until a 3.5-kip downward reaction was produced, simulating the subassembly under dead and working live load conditions.

Loading was controlled throughout the test by the magnitude of the lower column hinge deflection, δ . The loading history for BC3 is shown in Fig. 3.8. This specimen was subjected to an incremental cyclic load sequence until the maximum deflection safely accommodated by the testing frame was reached.

The loading sequence for BC4 is illustrated in Fig. 3.9. Basically, it consisted of a few cyclic loops with small displacement amplitudes to simulate the working load conditions, and a single large loop. The displacement amplitudes of the loop were carefully limited during the experiment so that damage to the specimen would still be repairable by the epoxy injection method. These limit amplitudes were +3.6 in. and -3.57 in. It should be noted that the response under essentially monotonic load was obtained from the loading sequence LP6RB to LP23 (Fig. 3.9a).

3.6 Repairing Process and Testing Procedure for Subassemblage BC4E

a) Repairing Process

BC4E was plumbed prior to beginning repair work by a trial and error procedure of reloading and unloading the lower column hinge. During the repair process, a temporary surface seal was first troweled over the cracks. Small entry ports along the cracks were spaced all about the sides of the member. Then if the cracks extended through the member, back sealing was used to prevent runout. The sealing material was a quick-setting epoxy. The appearance of a member after sealing off the cracks can be seen in Fig. 3.10a.

The two components of the fast-setting epoxy resin were pumped through a mixing head into the entry port on the face of the crack until the injected material began to ooze out at the adjacent port. Paraffin was then used to seal the latter port and injection of the epoxy was continued, either from the same location or from another port, until the cracks were repaired. From observing the injection operation, it appeared that the cracks in the specimen were connected. This was later verified by inspecting shattered specimens.

Under normal conditions, effective injection is limited to cracks wider than 0.005 in.; although with special procedures, cracks one half this width can be sealed.

During the severe cycling of BC4, some concrete outside of the confined core of the beams at the column interface spalled off. Such regions were repaired by casting a slow-setting epoxy mixed with sand and grout against a form (see Fig. 3.10b).

b) Subassemblage BC4E Test Procedure

The epoxy injected into the repaired specimen was allowed to cure for 3 to 4 days before the test was resumed. The specimen was whitewashed again to help the detection of new cracks, and the grid lines were redrawn.

Prior to application of the horizontal load, the column was compressed with a 470-kip axial load which was kept constant throughout the test. The specimen was then loaded according to the loading history shown in Fig. 3.11. As can be seen in that figure, three complete cycles were carried out at each selected value of the deflection. Comparison of the first cycle of the hysteretic loop with following cycles at the same peak deflection provided a measure of degradation in stiffness and energy dissipation. The specimen was loaded by progressively increasing the peak deflection, δ , until maximum deflection, 4 in. was reached.

4. BC4 EXPERIMENTAL RESULTS AND DISCUSSION

4.1 General

The overall behavior of this subassemblage is measured by the H vs δ response, where H is the horizontal force applied at the hinge of the lower column and δ is the total horizontal displacement of the same point. This behavior depends on the interrelated performance of the connected elements, i.e., the two beams, the column, and the joint. When the horizontal and the axial forces are applied at the lower column end, each element resists some portion of the loads and deflects according to its relative stiffness. The total displacement, δ, is composed of several independent components (see Fig. 4.1), namely:

$$\delta = (\delta_{rf} + \delta_{rs}) + (\delta_{colf} + \delta_{cols}) + (\delta_{js} + \delta_{jp}) \tag{4.1}$$

where the first, second, and third sets of parentheses denote the beam, column, and joint contribution to the deformation respectively. The subscripts f and s denote flexural and shear modes of deformation, while the subscript p denotes push-in and pull-out of the rebars in the joint causing fixed-end rotation. The physical interpretation of each term is given in Fig. 4.1.

Equation 4.1 includes all possible sources of deformation. However, as was observed from the BC3, BC4, BC4E, and earlier tests [11] both the column and joint shear deformations are very small in comparison with the other components and can be neglected. Then Eq. 4.1 reduces to:

$$\delta = \delta_{rf} + \delta_{rs} + \delta_{colf} + \delta_{jp} \tag{4.2}$$

The horizontal displacement, δ, is mainly governed by deformations of the critical regions which develop in the beams adjacent to the beam-column connection and in the connection itself. Note that no critical regions were developed on the columns since the subassemblage was designed according to the weak girder - strong column concept. The location of critical regions can be identified from observations made in previous tests (ref. 11). The critical regions are designated BW1 and BW2 for the west beam and BE1 and BE2 for the east beam (Fig. 4.2).

In the following sections, the experimental results obtained for the three specimens are presented. Results for BC4 are presented first, then the results of BC4E are given, and the two are compared. Finally, the results of the BC3 tests are given and are compared with the other two specimens.

The general behavior of BC4 is described first, followed by a presentation of curves showing the mechanical behavior of the total subassemblage and its critical regions. The test results are evaluated whenever possible by comparing them with results obtained either analytically or as recommended by standard codes.

4.2 General Behavior of BC4

At load point (LP) 12 (see Fig. 3.9a), 3.5-kip downward dorces were applied at the far ends of both beams to produce a net 223 K-in. negative moment at the column support to simulate the effect of a gravity load. Because of the initial negative moment on the beams, the first flexural cracks developed on the top surfaces of east and west beams at LP 1 and LP 2, respectively.

Diagonal shear cracks started to form near the load corresponding to LP 9 and LP 10 in the east beam as a continuation of flexural cracks.

The shear force necessary to start the diagonal cracks was 16.6 kips, compared with 17.4 kips predicted by the 1971 ACI Code (see Appendix A). Cracks in regions BW1 and BW2 were less inclined than in BE1 and BE2.

At LP 19 (see Fig. 3.9a) crushing and splitting were observed at the upper corner of BE1 and the lower corner of BW1 adjoining the column. As δ increased from LP 19 to LP 23, the cracks widened and their lengths increased. Figures 4.3 and 4.4 shows the locations and approximate sizes of the major cracks and splits at LP 23. The bulges in the concrete column cover, just above BE1 and below BW1 indicate considerable slippage of the rebars anchored in the joint.

While loading in the opposite direction, new cracks appeared on the top of BW1 and the bottom of BE1 at LP 28. At this load point all of the old major cracks remained open. From LP 33 to LP 36 the new cracks increased in width and propagated deeper into the beams, some of them connecting with the old cracks which had closed. The crack pattern at the end of LP 36 is illustrated in Fig. 4.5. Observe that, at the end of this load point, the largest cracks were the two at the beam-column interfaces, indicating that there was substantial slippage of the rebars of both beams from the joint. The bulging of the concrete column cover confirms this slippage.

The column was returned to its original (vertical) position ready for repair at LP 45. The condition of the beams and the joint before injecting epoxy into the cracks is shown by the photographs in Figs. 4.6a and b. As can be seen from these figures, the cracks at the two beam-column interfaces are larger than the other cracks and run nearly through the beam sections. This indicates that pull-put and push-in of the bars in the joint may play an important part in the overall subassemblage response. Their effects will be examined in more detail from hysteretic curves of the critical regions.

4.3 Total Response (H-δ, H_{eq}-δ)

Figure 4.7 shows the deformed configuration of the subassemblage and its external forces and reactions (H, P, V_W, and V_E), with their positive senses as indicated. Equilibrium of the deformed structure requires:

$$H = (V_W - V_E) - \frac{P\delta}{L} \quad \text{or} \quad H = H_{EQ} - \frac{P\delta}{L} \qquad (4.3)$$

where $$H_{EQ} = V_W - V_E \qquad H_{EQ} = H + \frac{P\delta}{L} \qquad (4.4)$$

The quantity H_{EQ} may be interpreted physically as the result of increasing the measured H by the $P\delta$ effect. Equation 4.4 indicates that the H-δ diagram can be constructed from a known H_{EQ}-δ curve or vice versa.

In the experiment, both H and H_{EQ} were measured and recorded continuously with XY recorders. It should be noted that the H measured by the lateral load transducer shown in Fig. 3.2 included the effects of frictional forces developed at the two rollers on the beam ends and at the upper and lower column hinges. H-δ diagram obtained from the H_{EQ}-δ diagram in Fig. 4.8 using Eq. 4.3 differs from the H-δ diagram obtained from direct measurement because of these frictional forces. This is clearly indicated in Fig. 4.9, where a comparison between the measured H-δ curve and the one derived from the H_{EQ}-δ diagram is made. By observing the overall difference in H at the same deflection, δ, it is estimated that the frictional forces contribute from 3 to 5.5 kips to the horizontal resisting force.

To overcome the uncertainty of the frictional forces, the $H_{EQ}-\delta$ curve and $H-\delta$ curve obtained from it will be used in studying the response of the subassemblage.

Since the $H_{EQ}-\delta$ and $H-\delta$ diagrams differ only in that the latter includes the $P-\delta$ effect, this effect can immediately be deduced from the figures. As can be seen in Fig. 4.8b, the $P-\delta$ effect tends to reduce the subassemblage strength, H_{EQ}, in the first and third quadrants while increasing it in the second and fourth quadrants. For a lateral displacement ductility ratio* of ± 5 (see Fig. 4.8b), the $P-\delta$ effect causes more than a 40% decrease in the story shear capacity, H .

This effect cannot be neglected in either analysis or design as it may lead to premature lateral instability. Comparison of the $H-\delta$ and $H_{EQ}-\delta$ loops also shows that if the hysteretic behavior of the subassemblage consisted only of loops with full reversals of displacement, the $P-\delta$ effect would not affect the energy dissipation capacity of the subassemblage.

By differentiating Eq. 4.4 with respect to δ , another conclusion regarding the $P-\delta$ effect can be reached:

---

*In this report the following definitions are used for ductility:

Subassemblage Lateral Displacement Ductility or Tip Deflection Ductility is defined as the ratio of the lower column hinge displacement to the displacement at first yield of main reinforcement.

Average Curvature Ductility Factor is defined as the ratio of the average curvature to curvature at first yield of main reinforcement.

Pull-out Rotational Ductility is defined as the ratio of the pull-out rotation to the pull-out rotation observed at first yield of main reinforcement.

$$\frac{dH}{d\delta} = \frac{dH_{EQ}}{d\delta} - \frac{P}{L} \qquad (4.5)$$

From Eq. 4.5 it follows that the stiffness in the H-δ diagram is always less than that of the H_{EQ}-δ curve by P/L .

For the small displacement amplitudes, (see Fig. 4.8a), the subassemblage behaved like an elastic system with the average stiffness, measured from the H_{EQ}-δ curve, ranging from 131-137 K-in. As the specimen was loaded to first yield, from LP6RB to LP 17 in Fig. 4.8b, its stiffness decreased monotonically from 132 to 75 K-in. This reduction in stiffness is due to progressive cracking in the critical beam regions and the increase in tensile force in the rebars, which leads to more pull-out. This is confirmed by the decrease in the stiffnesses of the critical beam regions and of the push-in and pull-out at the joint (see Table 4.1).

Yielding was first observed at LP 17 on the H_{EQ}-δ diagram. The specimen exhibited strong strain-hardening characteristics immediately after this yielding. This may be a consequence of the non-simultaneous yielding of the two beams -- when one beam is in the yielding stage, the other remains in the elastic range; when the elastic beam enters the yielding stage, the yielded beam is already in the strain-hardening range. Since the 3.2 K-in. slope of the strain hardening region is smaller than the P/L value of 6.53 K-in., the slope of the experimental H-δ is negative in this region (see Fig. 4.8b).

Because the critical regions of the beams and their connections suffered considerable damage during the first loading to peak displacement, of 3.6 in. at LP 23 as shown by the crack patterns (Figs. 4.3 and 4.4), significant deterioration in subassemblage stiffness was observed when the specimen was loaded in the opposite direction (LP 27 to LP 32 in Fig. 4.8b). In fact, its initial elastic stiffness of 132 K-in. had degraded to 31.4 K-in. at LP 27 and to 7.8 K-in. at LP 32. Furthermore, the abrupt change in stiffness caused by yielding of the beam rebars could not be detected from the $H_{EQ}-\delta$ diagram. In spite of these drastic reductions in stiffness the specimen was able to offer practically the same peak resistance since the values of H_{EQ} at LP 23 and at LP 36, are 49 and 46 kips, respectively.

The severe degradation of stiffness and reduction in strength of the subassemblage that can be observed in the $H_{EQ}-\delta$ plot between LP 39 and LP 42 resulted from failure of the bond between the beam rebars and the concrete in the anchorage zone of the joint. The loss of bond is clearly shown by the push-in and pull-out rotations of the joint illustrated in Figs. 4.10 and 4.11, and by the moment curvature diagrams of the critical beam regions in Figs. 4.12 through 4.15. From LP 39 to LP 42, the beam critical regions underwent little change in deformation while there was a considerable change in the rotation due to slippage of the column rebars. Measurements shown in Fig. 4.16 and 4.17 indicate that most of the slip occurred along the bottom beam reinforcements. This phenomenon will be discussed later.

4.4 External Reaction Curves: $H-V_E$ and $H-V_W$

This test demonstrated that under monotonic loading a beam-column subassemblage designed according to current codes could sustain displacement ductilities of up to six without undergoing a loss in strength. Subsequent reversed loading in the second half of the cycle also failed to diminish the ductility of the subassemblage.

Since the structure is indeterminate to the first-degree, the magnitudes of the reactions V_W and V_E relative to the horizontal load H depend on the relative stiffnesses of the east and west beams. In this experiment the main sources of the subassemblages stiffness degradations were located at the critical beam flexural regions and at the beam-column interface where significant slippage of the rebars occurred. This slippage can be modeled by spring elements as shown in Fig. 4.18.

The $H\text{-}V_E$ and $H\text{-}V_W$ curves (Fig. 4.19) depict the relationship between relative stiffness and the $P\text{-}\delta$ effect. Differentiating Eq. 4.3 with respect to V_W yields

$$\frac{dH}{dV_w} = 1 - \frac{dV_E}{dV_w} - \frac{P}{L}\frac{d\delta}{dV_w} \tag{4.6}$$

where $P = 470$ kips and $L = 72$ in. in this test. From the definition of member stiffness shown in Fig. 4.20

$$dM_w = 63.5\ dV_w = K_w d\theta \tag{4.7a}$$

$$dM_E = 63.5\ dV_E = -K_E d\theta \tag{4.7b}$$

where $d\theta$ is the angle change which results from slippage and beam deformation and is the same for members on either side of the column. Using Eqs. 4.7a and 4.7b, Eq. 4.6 can be transformed into:

$$\frac{dH}{dV_w} = 1 + \frac{K_E}{K_w} - \frac{P}{L}\frac{d\delta}{dV_w} \tag{4.8}$$

and similarly,

$$\frac{dH}{dV_E} = -\left(1 + \frac{K_w}{K_E}\right) - \frac{P}{L}\frac{d\delta}{dV_E} \tag{4.9}$$

Equations 4.8 and 4.9 describe the $H\text{-}V_w$ and $H\text{-}V_E$ curves throughout the loading sequence. In the elastic loading range LP 6RB-12 or the unloading ranges LP 23-29 and LP 36-39 (Fig. 4.11), $d\delta/dV_E$ and $d\delta dV_w$ are small relative to the rest of the terms. Thus the following approximation can be introduced in Eqs. 4.8 and 4.9:

$$\frac{dH}{dV_w} = 1 + \frac{K_E}{K_w} \tag{4.10}$$

$$\frac{dH}{dV_E} = -\left(1 + \frac{K_w}{K_E}\right) \tag{4.11}$$

For the linear portions of the curves in Fig. 4.19, the ratio of the stiffnesses, K_w/K_E, is constant. The value of K_E/K_w can be calculated from Eqs. 4.10 and 4.11, once the values of dH/dV_w and dH/dV_E are determined. From LP 6RB-12, where the average values of dH/dV_w and dH/dV_E are 2.26 and -1.79 respectively, the estimated K_E/K_w is about 1.27. This result is reasonable since K_E in this range applies to the strong reinforced side of the beam while K_w applies to the weak reinforced side.

In the ranges, LP 17 to 23, LP 29 to 36, and LP 39 to 41 in Fig. 4.17, the beam rebars were either in the yielding or the strain-hardening stages. In these ranges, the total subassemblage stiffness was considerably reduced (see Fig. 4.8b), i.e., δ increased significantly without a corresponding increase in the resistance offered by the yielding members. As a result, the P-δ effect overrode the increase in load resistance; that is, H decreased while V_E and V_w continued to increase.

4.5 Moment and Fixed End Rotation Due to Push-In and Pull-Out of Joint Rebars $M_E - \theta_{PE}$ and $M_w - \theta_{PW}$

Analyses of R/C moment-resisting frame structures usually assume joint rigidity, attributing deformations to the flexibility of girder and column members. There is very little information available on which to base accurate estimates of the influence of joint flexibility. In this experiment, the instrumentation was carefully designed to obtain reliable data regarding the behavior of the joint (see section 3.3). Results showing the significance of joint deformation to the total response are discussed.

Figures 4.10 and 4.11 show the moment vs. fixed-end rotation associated with push-in and pull-out of the main rebars at the column faces. From LP 6RB to LP 12, the behavior is generally linear. The elastic stiffnesses measured in this range, together with the moment-curvature stiffnesses of the critical regions obtained from Figs. 4.12 and 4.13 and listed in Table 4.1, were used to calculate the influence of slippage on the total beam stiffnesses (see Appendix B). The total stiffness was calculated for two cases, one including and the other excluding the slippage in the joint. The computed total beam stiffnesses are listed in Table 4.2. It is clear from the table that even in this small deflection range, joint flexibility can reduce the flexural stiffness of the beam (assuming no fixed-end deformation occurs) by 20% to 30%.

An abrupt change in the stiffnesses of the $M_E - \theta_{PE}$ and $M_w - \theta_{PW}$ curves occurred at LP 17 (Figs. 4.10, 4.11). Strains in the beam rebars show they are yielding here. Notice that the yield moments M_w and M_E at this point are in good agreement with those predicted by conventional beam theory and shown in the figures.

On reloading in the opposite direction, from LP 27 to LP 32, the average stiffnesses of $M_W - \theta_{PW}$ and $M_E - \theta_{PE}$ are reduced to about 1/5 of their elastic stiffnesses (between LP 6RB and LP 12). This stiffness degradation can be attributed partly to bond deterioration in the joint and partly to the Bauschinger effect in the rebars, which are consequences of slippage and yielding of the rebars in tension when the specimen was previously loaded to LP 23. An examination of the individual push-in and pull-out curves in Figs. 4.16 and 4.17, indicates that the changes in displacements Δ_{PW1} and Δ_{PE1} were rather small in comparison with Δ_{PW11} and Δ_{PE11} in this range. Thus, θ_{PW} and θ_{PE} were determined mostly by the slip of the bottom rebars.

From LP 39 to LP 42 bond failure occurred in the bottom joint rebars (see section 4.3). Because of the failure, the average stiffnesses of $M_E - \theta_{PE}$ and $M_w - \theta_{PW}$ were reduced to about 1/28 and 1/10 of their initial stiffnesses, respectively. There was also a pronounced reduction in the maximum moments; max. M_E and max. M_W were approximately 0.35 and 0.65 of the moments at LP 23, respectively.

4.6 Causes of Bond Deterioration in the Joint

As has been mentioned earlier, the degradation in overall stiffness and drop in strength of subassemblage BC4 is related to the pull-out and push-in responses of the main beam rebars in the joint. Between LP 39 and LP 42, during which the bottom bars slipped through the column, bond failure in the joint was the primary cause of the reductions (see $H_{eq}-\delta$ in Fig. 4.8b). Understanding the pull-out and push-in mechanism is essential for improving the detailing of the joint so as to avoid such a premature failure.

A series of diagrams illustrating the behavior of the longitudinal beam rebars in the joint in this test is shown in Fig. 4.21. These figures were constructed from the following information.

1. The individual push-in and pull-out curves in Figs. 4.16 and 4.17 provided data on the slippage of the rebars, the beam fixed-end rotation, and the joint bond conditions. The probable length of the regions where bond was severely damaged, shown by shading in the figures, was crudely estimated from these curves. The calculation involved summing the absolute values of each slippage from the beginning of the test to the load point investigated. At LP 36, most of the bond of the bottom rebar in the 17 in. wide column was destroyed. Thus, the accumulated slippage of this rebar was computed by summing slips Δ_{PW11} and Δ_{PE11} from LP 6RB to LP 23 and from LP 23 to LP 36, yielding a sum of 0.598 in. Therefore, the accumulated slippage per inch of bond damage was 0.598/17 = 0.34 in.

2. The average rebar strains (Figs. 4.22 and 4.23) calculated from 9-in. clip gage readings together with the $\sigma_s - \varepsilon_s$ diagram for the #5 and #6 rebars (in Fig. 2.5) are used to determine the pull-out and push-in stresses σ_1 to σ_4 (Fig. 4.21). Although the strains recorded by 1/2-in. weldable gages (REI and RWII) can be used to give more accurate estimates, the strain values after intensive yielding of the rebar, $\varepsilon > 0.015$, are unobtainable because of gage failure. The correlations between the readings from the clip and weldable gages are shown in Figs. 4.22 and 4.23. The values of σ_1 to σ_4 were determined from an empirical reload curve similar to the one suggested by A. Singh, and others [22], except that the constants were adjusted to fit the ultimate strength of the rebar; i.e.:

$$|\sigma_s| = 90 - 52.7\ (0.838)^{1000\varepsilon}$$

with ε in in./in. and steel stress σ_s in ksi.

Figure 4.21a shows the slippage of the rebars at LP 23. Since the stresses σ_2, σ_3, and σ_4 are larger than the yield stress, 70 ksi, the rebars continue to yield for a distance inside the joint. This results in a significant slip in the portions of the bars near the column face and inside the joint and leads to a further reduction in the effectiveness of bond transfer.

From LP 27 to LP 31, the cracks run through the beam-column interface on both sides, leaving only the reinforcing steel to resist the bending (Fig. 4.21b). Since the upper part of the beam contains almost twice as much reinforcement as the lower part, the stresses σ_4 and σ_2 can increase up to and beyond the yield stress, 70 ksi, while σ_1 and σ_3 remain below the elastic limit. Stresses σ_1 and σ_4 at LP 32 are shown in Fig. 4.21c. Again, the bottom rebars suffer additional bond damage because their high stresses cause large deformation, and slips.

As the specimen was loaded to LP 36, the bottom corner crack of beam west closed, allowing the top rebar to develop larger forces. At the end of LP 36 stress σ_1 went into the inelastic range. Meanwhile, the increase in M_E forced σ_4 well into the strain-hardening range, while σ_3 remained in the elastic range. Therefore from LP 33-36, more bond damage was introduced in the top left and bottom right bars of the joint (Fig. 4.21d).

From the above description it is clear that the loading sequence imposed on BC4 caused more bond damage to the bottom bars simply because there was less reinforcement there, resulting in the development of high steel stresses through most of a given loading cycle.

4.7 Moment-Curvature Diagrams

Besides joint slippage, degradation in flexural resistance in the critical beam regions was also a major cause in reducing the total stiffness of the assemblage, particularly before the bottom bars slipped through the column. The bending characteristics of these critical regions can be described by the following average moment-curvature diagrams.

(1) $M_{E1} - \phi_{E1}$ and $M_{W1} - \phi_{W1}$ (Figs. 4.12 and 4.13) show the moment-curvature behavior of the BE1 and BW1 regions defined in Fig. 4.2.

(2) $M_{E2} - \phi_{E2}$ and $M_{W2} - \phi_{W2}$ (Figs. 4.14 and 4.15) show the moment-curvature relations of the BE2 and BW2 regions.

From LP 6RB to LP 12, the flexural responses of critical regions BE1, BE2, BW1, and BW2 were nearly linear-elastic, showing continuous and slightly diminishing bending stiffnesses as loading progressed to LP 12. The average bending stiffnesses measured from Figs. 4.12 through 4.15 at selected load points are shown in Table 4.1. As can be seen from the table, the stiffnesses of the two critical regions of the same beam are quite close. These stiffness values are also close to the theoretically predicted stiffnesses (see Appendix A and Table A.1), namely, 57.8×10^5 K-in^2. in the strong direction and 39.3×10^5 K-in^2. in the weak direction.

Yielding in the first critical regions, BE1 and BW1, was observed at LP 17. Since there were moment gradients along the beams, the second critical regions, BE2 and BW2, showed no sign of yielding until LP 19. Table 4.3 compares the first experimental yield moments with those predicted from standard beam theory and from ACI code recommendations. In general, the agreement between them is good. In particular, the yield moments observed from the $M_{E1} - \phi_{E1}$ and $M_{W1} - \phi_{W1}$ curves are within 10% of the predicted ones.

The yield moments for the first critical regions were, on the average 12% higher than those in the second critical regions (see Table 4.3). This may be attributed to the fact that the cracks in the second regions are more inclined than those of the first (see crack pattern in Fig. 4.4). Figure 4.24 shows how these cracks could make the measured yield moments in $M_{E2} - \phi_{E2}$ lower than those of the $M_{E1} - \phi_{E1}$. Note that M_{E1} and M_{E2} are the moments computed at section A-A and B-B, respectively; M_y is the yield moment capacity of the beam section.

In the first critical regions, the strain-hardening stiffnesses appeared immediately after LP 18 whereas in the second, they are delayed until LP 20. The average strain-hardening stiffnesses, measured from Fig. 4.12 to 4.15, are listed in Table 4.5. There is good agreement among the measured stiffnesses of the critical regions on the same beam.

As the direction of the bendings reversed (LP 27-30), the moment-curvature diagrams for BE1, BE2, BW1, and BW2 again showed a continuous and gradual degradation in stiffness. This degradation comes mainly from the following three causes.

1. Reduction in Concrete Resistance to Compressive Forces

Upon reversal of the direction of loading (LP 27-31), new cracks develop on the opposite sides of the beams and connect with those formed prior to LP 23 (Fig. 4.25a). This results in cracks which run through the entire beam section (Fig. 4.25b). Because of the formation of these cracks, the moment is resisted only by the upper and lower beam reinforcement, without contribution from the concrete; thus, the beam stiffnesses are reduced. In this range the most significant deformations developed in the bottom rebars (see Fig. 4.25b) because the amount of reinforcement provided there was smaller than in the upper layer.

2. Reduction in Elastic Modulus of Bottom Rebar -- The Inherent Bauschinger Effect

This effect is introduced because the bottom rebars experienced some compressive yielding in BE1 and extensive tensile yielding in BW1 when the beam was loaded to LP 23 (Figs. 4.22 and 4.23).

3. Bending of Rebars Between Cracks Due to Dowel Action

With the cracks running through the beam sections (Fig. 4.25b), the transfer of shear force depends primarily on the dowel action of the main rebars. This tends to bend the rebars at the cracks (Fig. 4.25b) and substantially reduces the effectiveness of the bar in transmitting axial compressive forces. Thus the stiffnesses of the regions decrease.

From LP 31 to 33 the cracks in the bottom part of BW1 closed, resulting in an increase in stiffness (Fig. 4.13); whereas, the cracks of the critical regions on the east beam remained open (Fig. 4.14). Actually, in this range, the bottom rebars had already started to yield while the cracks had not yet fully closed.

The reloaded yield moments obtained from the moment diagrams in Figs. 4.12 to 4.15 are listed in Table 4.4. Since there is no definite yield point, the second yield moment in $M_{E1} - \phi_{E1}$ is only approximate. The severe disruption of the concrete and extensive yielding in the rebars from the previous loading, LP 6RB-12, resulted in a yield moment almost 20% less than that predicted theoretically.

The bending curvatures of the critical regions exhibited strain-hardening characteristics after the second yielding (see Figs. 4.12 to 4.15 and Table 4.6). It is interesting to note that the new stiffness values are slightly higher than the ones obtained when the beams were loaded to LP 23 (Table 4.5).

4.8 Shear Force -- Shear Deformation Diagrams ($V_W - \gamma_W$ and $V_E - \gamma_E$)

Shear deformations in the members, although not as significant as flexural deformation or joint slippage, do affect the horizontal displacement, δ , of the subassemblage. Moreover, as previously mentioned, the degradation in flexural stiffness is interrelated with the shear deformation. There are four regions where most of the shear deformation takes place. These are the critical beam regions, BE1 and BW1, close to the column faces, and also at the junctions between the beams and column where large cracks develop due to slippage of the rebar in the joint.

The shear force -- shear distortion developed on both beams is shown in Figs. 4.26 and 4.27. The beam shear deformation, as measured by a pair of crossed clip gages, is due to two types of mechanisms.

1. Closing or Opening of Diagonal Cracks

This action is predominant in the ranges LP 6RB to LP 23 and LP 31 to LP 36 in the curves.

2. Sliding Along Cracks Through Beam Sections

This type of action governs in the ranges LP 27 to LP 31 and LP 39 to LP 42.

Unfortunately, because of difficulties with instrumentation, the shear distortions at the beam-column interfaces were not measured. It is clear from Fig. 4.21b that the shear deformation could be significant since large cracks developed, and at certain periods in the loading history these cracks were open through the beam sections.

4.9 Contributions of Various Components to Horizontal Displacement, δ

As has been mentioned in section 4.1, the total horizontal displacement, δ , depends on several component deformations, e.g., deformation of the beams and of the beam-column connection due to pull-out and push-in of the rebars. Figures 4.28(a) through (3) illustrate the significance of each component of deformation at selected points in the loading history for the east and west beams respectively. Calculations of the component displacements for the left side of the column are given below, where the terms are also explained.

From the curvature distribution in Fig. 4.28, the contributions to the flexural deformations of the west beam, that is, deformations in BW1 and BW2 and the rest of the beam, denoted by δ_{W1}, δ_{W2}, and δ_{EW}, are established as follows

$$\delta_{W1} = (\phi_{W1} \times 9) \times 59 \qquad \text{(in.)}$$

$$\delta_{W2} = (\phi_{W2} \times 9) \times 50.5 \qquad \text{(in.)}$$

$$\delta_{EW} = \frac{V_W(46.5)^3}{3(EI)} \qquad \text{(in.)}$$

where ϕ_{W1}, ϕ_{W2} are taken from Figs. 4.13 and 4.15. The average cracked stiffness tabulated in Table A.1 in Appendix A is used for the value of EI . The reason for selecting this value rather than the average between the cracked and uncracked stiffnesses is that in the post-elastic range the major contribution to δ from the beam other than the first and second critical regions is from the cracked portions. Furthermore, in the second half of the loading sequence, (LP 27 to LP 36, see Fig. 3.9a) there may be a further reduction in the stiffness from loading in the reverse direction.

The shear deformation in the beam is assumed to take place mostly at the critical regions where inelastic deformation occurs. The shear deformation for the rest of the beam is assumed to be small and is neglected. This assumption proves to be valid since the maximum shear deformation of the rest of the beam, estimated by the expression (6/5)VL/GA, yields not more than 15% of the maximum measured shear distortion. This leads to

$$\delta_{sw} = \gamma_w \times 11 \quad \text{(in.)}$$

where γ_w is obtained from Figs. 4.26 and 4.27. It should be emphasized at this point that there is still another important source of shear deformation which is not included in Fig. 4.28, i.e., the shear distortions at the column faces. As mentioned in section 4.8, problems with instrumentation for measuring this source of shear deformation obscured the significance of its contribution to the total horizontal displacement.

The contribution from pull-out and push-in, δ_{PW}, is computed as

$$\delta_{PW} = \theta_{PW} \times 63.5 \quad \text{(in.)}$$

where values for θ are taken from Figs. 4.10 and 4.11.

The column component, δ_{col}, is calculated by assuming linear-elastic behavior along the column (see Fig. 4.29). That is,

$$\delta_{col} = \frac{\phi_u}{3}(28)^3 + \frac{\phi_b}{3}(28)^3$$

where ϕ_u and ϕ_b are computed from the readings of the gages EU, WU, EB, and WB (Fig. 3.5c).

The same procedure is followed for computing the contributions of the components, δ_{EL}, δ_{E2}, δ_{PE}, and δ_{EE} in Figs. 4.28a and 4.28b from the east beam and the joint slippage on the East side of the column.

The following points can be observed from Fig. 4.28.

1. The discrepancy between the measured δ and the one computed by summing the different sources varies, but in general the error is not more than 12% of the horizontal displacement.

2. Deformations of three critical regions contribute more than 80% of the horizontal displacement: the first and second critical regions of the beams, and the push-in pull-out region of the joint. The bending of the first critical region contributes 40-50%; the second critical region, 11-18%; and 20-38% comes from joint slippage.

3. After LP 17 (first yielding), the contributions to δ from shear deformation of the beam and flexural deformation of the column and the elastic portion of the beam are generally quite small.

4. On the east side of the column, slippage of the beam rebars through the joint contributed a larger percentage to δ during reloading (LP 29 to LP 36) than during monotonic loading (LP 6RB to LP 23). The contribution was virtually unchanged on the west side (see Fig. 4.28c and d). From LP 6RB-23, the BE2 region contributes about 18%, the BE1 region about 45%, and the joint slippage about 23%; while on reloading in the opposite direction (LP 33-36) the contributions change to 11%, 33%, and 38%, respectively.

A significant cause of the above phenomenon is that the bond conditions on the rebars between LP 6RB and LP 23 differ from those between LP 33 and LP 36. Notice the bond condition of the bars under tension at LP's 36 and 23 in Fig. 4.21; the major contribution to the push-in and pull-out rotations, θ_{PW} and θ_{PE} , between the two ranges depends on the pull-out of the bars under tension. Note the bond damage in the portion of the bottom bar close to the east side column face at LP 36 is much more severe than that of the top bar at LP 23. Conversely, the bond damage to the top bar close to the west side column at LP 36 is nearly the same as to the bottom bar at LP 23. Therefore, the push-in and pull-out components on the east side, δ_{PE} , between LP 33-36 should be greater than those between LP 6RB-23; on the west side, δ_{PW} components should be approximately the same.

4.10 Conclusions

From the results obtained for BC4, the following observations can be made.

1. Displacement ductilities as high as 6 can be achieved without loss of lateral load resistance during both monotonic loading and also the subsequent reverse loading of the second half of the cycle. The hysteretic loop is spindle-shaped.

2. The P-δ effect may have a pronounced effect on the lateral load deformation response of the lower stories of tall buildings, and should be considered in their design and analysis.

3. The beams are reinforced only 50% as much at the bottom as at the top, giving rise to a more extensive yielding in the bottom rebars.

This introduces considerable bond damage along the entire embedment length in the joint. It is therefore recommended that the longitudinal steel at the bottom of the beam should be more than 50% of the top steel to delay the excessive bond deterioration in the bottom rebars.

4. The pushing-in and pulling-out of the top and bottom reinforcement contribute significantly to the stiffness degradation of the subassemblage.

5. BC4E EXPERIMENTAL RESULTS AND DISCUSSION

5.1 General

A qualitative assessment of this experiment can be made from a direct comparison of the response parameters before and after crack repair. However, a great deal of information regarding the general behavior of repaired reinforced-concrete subassemblages subjected to incremental loading is available, and this will be presented and interpreted whenever possible.

5.2 General Behavior of the Repaired Subassemblage

As the 470-kip axial load was applied to the plumbed columns, downward reactions developed at the beam end supports of $V_W = -4.4$ kips and $V_E = -2.7$ kips. During the small amplitude displacement of the lower column hinge, LP 0 - LP 4 (see loading Fig. 3.11), the initial negative moments in the beams, produced by the downward shear reactions, provided favorable conditions for the formation of small flexural beam cracks and interface cracks on the top surfaces of the beams. The cracks appeared on top of the west beam at LP 2 and on top of east beam at LP 3 whereas no flexural cracks developed in the bottom of the west beam until LP 4E and in the bottom of east beam until LP 5E (Fig. 3.10).

Interface cracks at the bottom surface of the east beam and bulging of the concrete column cover below the west beam which indicate appreciable pulling on the bottom bear rebar, were first observed at LP 4E. Bulging of the concrete column cover below the east beam and interface cracks at the bottom surface of the west beam developed at LP 5E. From LP 6 to the end of the test few additional cracks formed, and some of them remained active. The interface cracks on the column faces alternately opened and closed, the beam splitting cracks along the bottom rebars propagated deeper into the beams, and occasionally the concrete column cover below the beams would spall off. The deformation of the subassemblage and appearance of typical cracks on the beams after LP 6 are shown in Figs. 5.1a and 5.1b. The interface cracks were far larger than other cracks formed in the beams, thereby reflecting the relative importance of beam fixed-end rotations (caused by excessive slippage of the joint rebars) to the overall response of the assemblage.

The effectiveness of the epoxy injection method in repairing cracks is demonstrated in Fig. 5.2. Except for the interface cracks and the cracks in the beam cover along the bottom rebar adjacent to the column, most of the new cracks in the repaired specimen formed at different locations. Thus, good bond between disrupted concrete surfaces and infilled epoxy resin can be achieved with this injection process.

The maximum width of the new cracks appearing on the beam during the test was about 1/64 in. as compared with the 1/8-in. width of the old cracks; i.e., the new cracks are about 1/8 the size of the old ones. This reflects the fact that the repaired critical beam regions underwent much less rotation than the originals. The opposite is true, however, for the new interface cracks, which were more than twice the widths of the old ones.

The above observations on cracking seem to indicate conclusively that damaged bond of the bottom rebar along the joint was not effectively repaired, and therefore the restoration of bond in an interior joint by the present technique of epoxy injection is questionable. However, this repair method works satisfactorily in restoring the stiffness and strength at working load level of the beam critical region.

5.3 Comparison of Experimental Results: BC4E and BC4

As mentioned in section 4.1, the overall response of the subassemblage, is composed of contributions from the beams, the columns, and the joint and described by $H-\delta$ or $H_{EQ}-\delta$ diagrams. The efficiency of the epoxy repair method in restoring a severely cracked subassemblage can be judged by comparing the $H-\delta$ or $H_{EQ}-\delta$ diagrams of the repaired and original specimen. Such a comparison would not give information regarding which of the critical regions accounts for the difference in total response of the two subassemblages, however. To overcome this, the characteristics of the various critical regions of the repaired specimen will be examined in detail and compared with the corresponding critical regions of the original specimen. Since the different critical regions resist the applied force by different mechanisms (e.g., in the joint, the bond between a rebar and the surrounding concrete), the investigation will provide data on which regions, hence mechanisms, can be satisfactorily repaired by the injection process.

The experimental results for the repaired specimen, and a comparison of these with the original specimen will be presented in two phases as functions of the displacement, δ . The small displacement levels, LP I2 - LP 6RB in BC4 and LP 1 - LP 4R in BC4E (see Figs. 3.9b and 3.11), for which the behavior of the two specimens was almost linear (see Figs. 5.3 and 5.4), define the first phase. In this phase, the displacement loading programs for both specimens are similar (Figs. 3.9a and 3.11). The second phase includes the large displacements, LP 6RB to LP 44 for

BC4 and LP 4 to LP 28 for BC4E, where the behavior of both specimens was highly nonlinear. The displacement loading programs in this phase were quite different. Progressively larger displacements were imposed on the repaired specimen, while a single loop of large displacements was applied to the original.

The $H_{EQ}-\delta$ and $H-\delta$ diagrams for BC4E for the small displacement levels are shown in Fig. 5.3. Except for a slight deviation from linearity during unloading, this specimen behaved almost as a linear-elastic system with an average stiffness of 76 kips/in. in the $H_{EQ}-\delta$ curve. Because of the $P-\delta$ effect, the stiffness of the $H-\delta$ diagram is consistently lower than that of the $H_{EQ}-\delta$ diagram.

The $H_{EQ}-\delta$ curves for the repaired and original specimens at small displacements are shown in Fig. 5.4. A marked difference in the two diagrams is the more than 50% reduction in the initial elastic stiffness of BC4E from that of BC4; namely, 137 kips/in. before repair to 72 kips/in. after repair. A possible explanation for this difference lies in the fact that while epoxy injection restored the continuity between the two faces of the crack, it probably did not completely restore the bond between the concrete and the steel rebars, particularly for those bars that suffered bond damage throughout their embedment length in the joint. In addition cracks of size smaller than 0.005 in. in critical beam regions could not be injected, thus remained open. Evidence to support this conjecture is given in Table 5.1 where the average elastic stiffnesses of the moment push-in and pull-out diagrams and the moment-curvature diagrams are listed. As can be seen from the table, the push-in and pull-out elastic stiffnesses of the repaired joint are about half those of the original specimen.

The performance of the repaired specimen subjected to the progressively larger displacement sequence, LP 4 to LP 28, is demonstrated by the $H_{EQ}-\delta$ and $H-\delta$ diagrams in Figs. 5.5 and 5.6, where the yield displacement of BC4 is used to establish the ductility scale. Two distinctive characteristics of the curves are easily observed, namely the degradation in initial stiffness and the greatly reduced energy dissipation in the second and third loops relative to the first loop for a given displacement level.

It can be seen from Fig. 5.5 that the initial stiffness is about 72 kips/in. After loading to LP 5 it drops to 23 kips/in. After loading to LP 7 it drops further to about zero. These low initial stiffnesses are too small to overcome the reduction in stiffness due to the $P-\delta$ effect and thereby result in the negative slope in the $H-\delta$ diagram (see Fig. 5.6). Continued reduction in energy dissipation capacity as a result of cycling at a given displacement level is clearly shown in col. 4 of Table 5.2. From this table, the energy dissipation of the second and third repeating loops is seen to be only 40% to 80% that of the first loop.

Since elasto-plastic models have long been used in seismic analysis as a basis for developing more sophisticated models, it is interesting to compare the ability of the repaired specimen to dissipate energy with an ideal elasto-plastic model subassemblage. (For details of the ideal elasto-plastic subassemblage response, see Appendix F.) As noted in the last column of Table 5.2, for loops with the same displacement level, the energy dissipation of the repaired subassemblage varies between 10 and 50% of that of the idealized elasto-plastic subassemblage -- a considerable reduction. The energy continues to drop as the displacement level increases.

The reduction in story shear capacity due to the P-δ effect is shown in Fig. 5.6. As can be seen from the figure, at a ductility of about 4.5 for the repaired specimen the reduction in story-shear resistance is about 50% and more than 80% for a ductility of 5.3. The reduction in energy absorption is also easily observed from the figure.

Since the loading history of BC4 between LP 6RB and LP 23 is quite different from the loading history of BC4E between LP 4 and LP 26 (see Figs. 3.9b and 3.11), few relevant comparisons of the performance of the repaired and original specimens are possible. Comparisons can be made of the differences in response when the specimens are loaded to the inelastic range for the first time (serviceability condition, Fig. 5.7), of the maximum resistances of the subassemblages (Fig. 5.8), and of the energy dissipations at the same displacement level of 3.6 in. (Fig. 5.9).

The performance of the repaired specimen at the serviceability level as well as up to the first significant inelastic deformation was satisfactory despite its slightly larger deflections (see Fig. 5.7).

The ability of the repaired specimen to maintain the same order of magnitude of maximum resistance as the original is demonstrated in Fig. 5.8. In the second loop cycle, however, there is a considerable reduction (about 20%) in strength from the original specimen.

Although both specimens could be deflected without developing brittle-type failure, there is a great difference in the energy dissipation capacities of the subassemblages. This is clearly indicated in Fig. 5.9 where the area enclosed by the loop, BC4E, is about 1/6 that for BC4 .

Figure 5.10 and 5.11 show $M_W - \theta_{PW}$ and $M_E - \theta_{PE}$, the push-in and pull-out moment rotations on the west and east sides of the column faces of the repaired specimen. A continuous record of joint moment-rotation on the east face of the column is not available because the welded pins which supported the potentiometer for measuring the slip of the bottom rebar broke off early in the test. Therefore, the envelope of the moment-rotation curve (Fig. 5.11) computed from readings of gages FE1 and FE11 in Fig. 3.5c is presented instead. In addition, the $M_w - \theta_{PW}$ and $M_E - \theta_{PE}$ curves for BC4 are also plotted in Figs. 5.9 and 5.10, to provide a direct comparison. It is evident that the main cause of the low initial stiffness and pinching in the $H_{EQ}-\theta$ diagram after LP 9 (see Fig. 5.5) is excessive bar slippage in the joint causing beam end rotation. The rotations θ_{PW} and θ_{PE} of the repaired joint were far greater than those of the BC4 joint, which indicates poor epoxy restoration of the joint bond.

The moment-curvature diagrams for the first critical beam regions for both repaired and original specimens are shown in Figs. 5.12 and 5.13. As can be seen from Fig. 5.12, the initial stiffness of the repaired beam's critical region was as great as the unrepaired beam. Therefore, there was no significant contribution to the degradation in stiffness of the BC4E total response, $H_{EQ}-\delta$, from the critical beam regions. The critical regions of the repaired beam underwent much less rotation than the original beam, reflecting the minor damage to the BC4E beams. This again indicates how well the epoxy injection method restored the cracked beams.

5.4 Joint Behavior and Mechanism of Deterioration in Stiffness of the Repaired Subassemblage

As mentioned before, degradation in subassemblage stiffness is mainly due to deteriorating rebar bond in the joint (see section 5.3). In this section, the push-in and pull-out action of the joint rebars and other causes of reduction in the stiffness will be described in more detail.

The stiffness degradation of the subassemblage can be classified in two phases:

1. Before destruction of joint bond and surrounding concrete, from LP 4B to LP 7R (see Fig. 5.10).

   In this phase, the major source of degradation is the extremely rapid bond deterioration on the bottom rebars under full cyclic loading.

2. After complete destruction of the bottom rebar bond, from LP 9 to the end of the test (see Fig. 5.10).

   The behavior of the joint and the causes of degradation in stiffness will be explained below by studying a typical loop of the $M_W - \theta_{PW}$ plot (Fig. 5.14 taken from Fig. 5.10). Since the bond in the bottom rebars was completely destroyed, θ_{PW} , which is mainly produced by the slip-in and slip-out of the bottom rebars (see the individual slip curve in Fig. 5.15) is also markedly influenced by the moment on the other side of the column, M_E . Therefore, $M_E - \theta_{PW}$ for the loop is also shown in Fig. 5.14 to give a more complete picture of the joint behavior.

As can be seen from Fig. 5.14, $M_W - \theta_{PW}$ and $M_E - \theta_{PW}$ represent two kinds of joint behavior. The first occurs during closure of the interface cracks and corresponds to the portion of the curve having zero slope (labelled AB, A'B', DE and D'E'). The second is apparent after the complete closure of the cracks (labelled BC, B'C', EF, and E'F'). This joint behavior will be described in detail using ranges ABC and A'B'C' as examples.

A sketch of the joint deformation during loading from A to B is shown in Fig. 5.16a. Note that in this range the interface cracks run completely through the beam section, leaving only the top and bottom reinforcement bars to resist the moment; M_W (about 25.6 kips-in.) and M_E (about 153.8 kips-in.) act in the same sense, i.e., they both produce compressive strain in the bottom rebars. The free-body diagram showing how the equilibrium requirement for the joint is satisfied is shown in Fig. 5.16b. Since bond is completely destroyed along the bottom rebar, it is free to slip through the joint with little resistance. Because M_E is larger than M_W, the force in the rebars due to M_E determines the direction of slip and controls both rotations θ_E and θ_W. As the column is displaced from left to right, the joint rotates freely until the column face contacts the bottom part of the east beam. The free rotation is equal to the amount of rotation from A to B and depends upon the interface crack width, ΔC. The progressively increasing displacements imposed on the subassemblage result in more damage at the interface crack, thereby increasing the crack width, ΔC, and the portion of the curve with zero slope becomes larger.

The deflected joint and its corresponding free body diagram, in the range B to C of $M_W - \theta_{PW}$, are illustrated in Fig. 5.16c and d. The concrete surface at the interface crack adjacent to region I, which was open previously, is now in contact with the column surface on the east side. Because of loss of bond in the bottom rebars in the connection, the anchorage zone of the force T, induced by M_W, shifts from the column to the region I. This leads to a force distribution in the east beam at the column face as shown, i.e., the compression concrete block surrounds the tension force, T', of the bottom rebar. Such a force distribution pattern causes a large relative slip between the reinforcement and compressive concrete which leads to formation of the splitting crack along the bottom rebar (see close-ups in Figs. 5.17a and b). This crack formation not only impairs the force transfer in bond but it also decreases the effectiveness of the concrete cover in resisting compression and accelerates the spalling of the cover. The loss of bond in this region increases the flexibility of the bottom rebars in the joint and prevents them from developing large tensile forces. Meanwhile, the loss of concrete cover tends to reduce the length of the internal moment arm. The same action occurred in region II when the column was displaced in the opposite direction; i.e., the joint rotated from E and T in Fig. 5.14. The damage in regions I and II due to the increase in unbonded length of the bottom rebars and the loss of concrete cover is believed to be a primary mode of stiffness degradation in ranges BC and EF of the curve in Fig. 5.14 as the specimen was loaded to increased peak displacements and as the number of cycles increased.

5.5 Conclusions

From a review of the experimental results of the repaired subassemblage the following observations can be made.

1. The influence of the P-δ effect on the lateral deformation response is very pronounced.

2. The stiffness of the repaired subassemblage even at service load conditions is about one half that of the virgin specimen. However, the maximum resistance capacity of the repaired subassemblage in this range is higher than that of the virgin specimen. Therefore the performance of

the repaired specimen under working conditions can be considered to be satisfactory.

3. Beyond a deflection ductility of the subassemblage of 2.3, there is a pronounced degradation in the initial stiffness of the repaired specimen. The repaired hysteretic loops are N-shaped, showing a very large reduction in energy dissipation and energy absorption. Therefore, the epoxy injection repair method proved to be ineffective in restoring the original mechanical properties of the specimen for more severe displacement conditions.

The main cause of the poor performance of the repaired subassemblage was the ineffectiveness of the repair method in restoring bond of the bottom rebar along its embedment length in the column. When the specimen was subjected to a few cycles of large displacements of ductility of 2.3 and higher, the bottom rebars slipped through the column.

4. The repair method is very effective in repairing the cracked beam where flexural behavior is of primary importance.

Conclusions 3 and 4 suggest that if the major cause of failure in the virgin specimen is a loss of bond in the anchorage zone, the effectiveness of the present method of epoxy injection repair in restoring the beam-column subassemblage is highly questionable. On the other hand, if beam failure is due to cracking, the repair method is quite satisfactory.

6. INFLUENCE OF LOADING HISTORY ON THE BEAM-COLUMN SUBASSEMBLAGE RESPONSE

6.1 General

This chapter is devoted to evaluating the effects of different loading sequences on the performance of the beam-column subassemblages. In order to achieve this, the behavior of subassemblage BC4, subjected to monotonic loading (see Fig. 3.9a), is compared with subassemblage BC3, loaded cyclically to progressively increasing peak displacements (Fig. 3.8). It should be noted that the loading history for BC4 can be considered to be monotonic only from LP 6RB to LP 23, and not for the large cycle beyond LP 23. In spite of this fact, this loading sequence will be called "monotonic reloading" for later reference.

The general loading history will be presented first followed by an investigation of the effects of the loading history on the strengths, sttiffnesses, ductilities, and energy dissipation capacities of the subassemblages. The presentation of the general loading history serves to introduce some of the basic responses of BC3 needed for later discussion and to give a direct comparison of the overall responses for BC4 and BC3. More information on the behavior of BC3 is given in ref. [11].

6.2 Comparison of BC4 and BC3

6.2.1 Overall Response

To avoid the complication introduced to the H-δ diagram by the P-δ effect, the influence of the loading sequence on the overall response of BC3 and BC4 is commented on using the H_{EQ}-δ diagrams in Fig. 6.1. Two features are clearly seen in this curve:

1. BC3 experienced a sudden drop in load resistance after LP 28 (at a displacement level of -2.8 in.), while BC4 is able to maintain an increasing resistance of up to -3.5 in. This implies that the capacity of a subassemblage for deforming without loss of strength is adversely affected by cyclic loading.

2. Load-deformation response curves for BC3 before the -2.8 in. displacement are spindle shaped with slight reductions in the peak H_{EQ} and moderate degradation in stiffnesses in the repeated loop. Beyond a -2.8 in. displacement, the loops are unstable showing sharp decreases in strength and stiffness.

6.2.2 Response of the Joint

The moment-rotation relationships, with fixed end rotations θ_{PW} and θ_{PE} caused primarily by the push-in and pull-out of the beam rebars, for the two loading sequences are shown in Figs. 6.2 and 6.3. As shown, the maximum fixed end rotation of BC3 is far greater than that of BC4. For instance, the values of θ_{PE} and θ_{PW} of BC4 at LP 23 are -0.018 and 0.010 rad., respectively, while those of BC3 at LP 29 and at approximately the same displacement level are 0.068 and 0.059. The shapes of the BC3 $M_W - \theta_{PW}$ and $M_E - \theta_{PE}$ curves starting from LP 27 indicate that the sudden decrease in load resistance and in stiffness of the specimen's overall response (Fig. 6.1) is caused by poor bond transfer between the main rebars and the concrete in the joint.

6.2.3 Flexural Response of the Critical Beam Regions

Comparison of the flexural behavior of the critical beam regions of specimens BC3 and BC4 is shown in Figs. 6.4 and 6.5 where the maximum average curvature of ϕ_{E1} and ϕ_{W1} for BC3 is seen to be less than that for BC4. While the values of ϕ_{E1} and ϕ_{W1} of BC3 at Lp 25 are about 0.00185 rad/in., those for BC4 at Lp 23 are about 0.0028 rad/in., about one and one-half times larger. Because the joint rotations, θ_{PW} and θ_{PE} (see Figs. 6.2 and 6.3) developed in BC3 are considerably larger than those in BC4, smaller flexural rotations, θ_{E1} and θ_{W1}, were needed in the critical regions of BC3 for the assemblage to assume the imposed deflection, δ . The sharp decrease in curvature between LP 28 and LP 31 (Figs. 6.4 and 6.5) reflects the bond failure of the main rebars in the joint and the large increase in joint rotations.

6.2.4 Rotation at Column Faces and in Critical Beam Regions

Since the main contributors to the subassemblage deflection, δ , are deformations in the joint, θ_{PW} and θ_{PE}, and bending along the critical beam regions adjacent to the column faces, θ_{W1} and θ_{E1}, it is interesting to see how the loading sequences affect these deformations. Figures 6.6 to 6.9 show the relation between the peak rotations of θ_{PW}, θ_{W1} $(9 \times \phi_{W1})$, θ_{PE}, and θ_{E1} $(9 \times \phi_{E1})$ under different cycles and the corresponding deflections, δ . For BC4 the first quadrants of the graphs represent the rotations for a monotonically increasing load; i.e., the specimen was in its virgin condition before loading, while the third quadrants correspond to monotonic reloading, or the response obtained after damage from an analysis of the curves, the following observations are made:

1. The beam-end rotations, θ_{PW} and θ_{EW}, caused by slippage of the bars from the joint for δ's less than 3 in. are generally larger under cyclic loading than under monotonic loading for bending in the weak

direction. For bending in the strong direction the rotations are not greatly effected by the type of loading sequence (see Figs. 6.6 and 6.8).

2. The rotations of the critical regions, θ_{W1} and θ_{E1} in the weak direction and in the same displacement range are smaller for cyclic than for monotonic loading, while for the strong direction the differences are slight (see Figs. 6.8 and 6.9). Since δ is mainly a function of the beam-end and critical region rotations only, it is expected that, under the two loading conditions, if one beam's end rotation is relatively larger than the other, then its corresponding critical region rotation will be smaller than the other to achieve the same δ in both.

3. No definite conclusions can be reached for the tip deflection in the third quadrant in the 0 to -3-in. range with regard to which of the loading sequences produces greater rotations in the critical regions.

4. At displacements greater than 3 in., bond failure due to the effects of load reversal appears to be the cause of the large increase in beam-end rotations observed between LP 25 and 29 (Figs. 6.6 and 6.8). No such phenomenon is observed for the monotonic curves. This sudden increase in beam-end rotation accounts for the sharp decrease in critical region rotations (see Figs. 6.7 and 6.9).

5. Joint rotations are generally larger for the repeated loop of cyclic load than for the first loop (Figs. 6.6 and 6.8); while rotations of the critical regions are greater for the first than the second loop (Figs. 6.7 and 6.9). This indicates that progressive cyclic loading induces more significant deterioration in the joint than in the beams.

6.2.5 Mode of Failure BC4 vs. BC3

The failure of both specimens was caused by slippage of the main rebars in the joint. However, detailed study of the four slippage curves for BC3 (Figs. 6.10 to 6.13), and those for BC4 (Figs. 4.16 and 4.17), indicates that joint failure was restricted to slippage of the bottom bars in BC4, whereas slippage occurred in both the top and bottom bars of BC3. Appreciable slippage of top bars starts near LP 26 (Figs. 6.10 and 6.11), while in the bottom bar this happens around LP 27 (Figs. 6.12 and 6.13)). Because of the excessive, almost simultaneous, slippage in both layers of the main rebars of BC3, the drop in load resistance and degradation in stiffness became so great that the subassemblage was unable to overcome the $P-\delta$ effect and became unstable, terminating the test. The onset of instability in BC3 is illustrated in Fig. 6.14 where it is shown to occur after LP 26.

6.3 Strength Characteristics of BC3 and BC4

Yielding and maximum strength definitions are employed in the comparison herein. From Fig. 6.3, it is observed that the yield strengths of BC3 are clearly defined in both positive and negative directions of loading, whereas for BC4, only the positive yield load is clearly discernible.

An inspection of the curves in Fig. 6.1 indicates the negligible effect of loading sequences on the yielding and maximum strengths of the beam-columns. The strength is insensitive to the loading sequences because of the following:

1. The strength of the beam-column, which was designed and detailed according to the strong column-weak girder concept, is governed by the

load-resisting capacity of the two beams. The strengths of these beams, in turn, depend primarily on the yield strength of the rebars.

2. The increase in load-carrying capacity of the beam members over their computed ultimate strength according ACI is usually small. This is because any increase in strength due to strain-hardening in the rebar is largely offset by bond deterioration in the joint and damage in the compressive concrete block caused by spalling of the cover or splitting along the compressive rebar.

6.4 Stiffness Deterioration

To facilitate study of the effects of loading sequence on stiffness degradation, the curves shown in Figs. 6.1 to 6.5 are re-plotted in Figs. 6.15 to 6.19. The responses of BC4 are indicated by dashed lines. The curve ending at LP 17 represents monotonic response while that ending at LP 33 represents monotonic reloading.

From these curves, the following observations can be made:

1. In all cases, monotonic loading results in the higher specimen stiffnesses.

2. The initial stiffness degradation of $H_{EQ}-\delta$ is greatly influenced by the peak displacements of the previous cycles. This is clearly seen in Fig. 6.15, which shows the initial stiffnesses of BC3 at different displacement levels.

3. The stiffness deterioration of $H_{EQ}-\delta$ for BC3, subjected to progressive incremental displacements, surpasses that observed for BC4 to which one single loop was applied. The initial stiffness of the loop

in BC3 having a peak displacement of 2.8 in. and ending at LP 29 (Fig. 6.15) is about 1/4 of that corresponding to the monotonic reload curve of BC4 and about 1/4 of that of the monotonic load curve.

4. The degree of pull-out stiffness degradation in the joint for BC3 is considerably larger than that for BC4 (Figs. 6.16 and 6.17). The stiffness of the monotonic reloading curve of BC4 is about 10 times greater than the pull-out stiffness of BC3 (LP 29). Both have the same peak displacement of 3.6 in. Upon loading to LP 31, the joint pull-out stiffness degrades to near zero.

5. For specimen BC3 the beam stiffnesses of the post-elastic curves, labeled 21, 25, and 29 in Figs. 6.18 and 6.19, undergo considerably more degradation than the first-yield curves, labeled 17. After yielding, the post-elastic curves have approximately the same initial stiffnesses.

6. In bending the beams in the weak direction (tensile strain produced at bottom of the beams), the initial bending stiffness of the two specimens is nearly the same; in the strong direction, the bending stiffness of BC4 is slightly lower than that of BC3 .

Thus, it can be concluded that the overall stiffness degradation of a specimen is more severe under full cyclic reversals than under monotonic loading or reloading having the same final displacement. This is clearly shown by comparing the monotonic reloading curves of BC4 with the curves of BC3 after initial yielding (Fig. 6.15). The difference in stiffness deterioration under different loading sequences is mainly caused by the bond deterioration in the joint. As shown in this study, damage to the bond of the main rebars in a joint is more severe under cyclic loading, while the flexural behavior of critical beam regions are not significantly affected by the loading sequence.

6.5 Ductilities of BC3 and BC4

As mentioned earlier, the yield points of BC3 were readily apparent for both positive as well as negative loading sequences (see Figs. 6.1 to 6.5). These first-yield deformations are used as a basis for computing the ductilities. In BC4 the first-yield deformation that was observed during loading is used as a reference since the yield points for the opposite loading direction could not be determined precisely.

Figures 6.20 and 6.21 show rotation ductilities at different values of tip deflection for BC3 and BC4 . The BC3 displacements and rotations at the peak of the first loop of a series are employed in calculating the ductilities. For a comparison of the various ductilities as functions of different loading sequences, the curves shown in Figs. 6.20 and 6.21 are shown again in Figs. 6.22 and 6.23. After studying these curves, the following remarks can be made:

1. The tip deflection ductilities for BC3 and BC4 yield the lowest values of ductility (see Figs. 6.20 and 6.21). There appears to be no fixed relations among the different ductilities developed in the critical regions of BC3 . For monotonic loading of BC4 the bending ductilities, however, are consistently larger than the pull-out ductilities and the tip deflection ductility.

2. No ultimate ductility values can be estimated from BC4 data since the loading sequence was selected to limit the amount of damage to a reasonable degree; BC3, however, was tested to destruction. Since

the major cause of the drop in load resistance of BC3 was the deterioration in bond of the joint, the ultimate subassemblage ductilities and the ultimate pull-out ductilities could be obtained. These values are:

West pull-out, weak side bending ≈ 4.6
strong side bending ≈ 7.5

East pull-out, weak side bending ≈ 5.6
strong side bending ≈ 9.2

3. The effect of the loading sequences on the ultimate tip deflection ductility is indicated in Figs. 6.21 and 6.23. As noted, BC4 can reach tip displacement ductility of 6 in each direction, whereas BC3 can only reach ductility of around 4. In fact, a larger tip deflection ductility could have been attained for BC4 had it been tested to its ultimate failure.

4. Since more damage occurred in the BC3 joint, the bending ductilities in the critical region under monotonic loading in BC4 were consistently and considerably higher than under cyclic loading (see Fig. 6.23).

6.6 Energy Dissipation for BC4 and BC3

For ideal elasto-plastic materials, energy absorption and energy dissipation can be expressed explicitly as a function of strength and ductility. However, the highly irregular hysteretic response curves illustrated in Fig. 6.1 obscure any such relationship, and energy absorption and energy dissipation of such members must be calculated directly from the experimental hysteresis loops.

7. EFFICIENCY OF EPOXY INJECTION REPAIR OF THE BEAM-COLUMN SUBASSEMBLAGE

7.1 General

Although the comparison between the behavior patterns of BC4 and BC4E in Chapter 5 gives some insight into the performance of the repaired subassemblage, conclusive judgment on the degree of effectiveness of the repair method cannot be made. The main drawback of the previous comparison comes from the fact that a different loading history was imposed in the two experiments. As observed in Chapter 6, the characteristic specimen responses under monotonic and incremental cyclic loading are considerably different, especially with regard to degradation in stiffnesses, ductilities, energy absorption, and energy dissipation. In order to assess the effectiveness of the epoxy injection method in more precise terms, it is appropriate to use BC3 as the basis of comparison.

In this chapter the experimental results of BC3 and BC4E will be directly compared, emphasizing the influence of the epoxy injection repair method on the restoration of strength, stiffnesses, ductilities, and energy dissipation. In observing the results that are presented, it must be kept in mind that the loading sequences applied to both specimens are not exactly the same, as shown in Figs. 3.8 and 3.11. These figures show that specimen BC3 was subjected to a few more cycles at low amplitude displacement before being loaded to induce yielding. Therefore, it could be expected that the BC3 specimen would have less stiffness and energy dissipation in the first yielding loop. This is confirmed by Figs. 7.1a where the BC3 average stiffness is slightly less than that of BC4E . On the other hand, specimen BC4E was subjected to more inelastic cycles

In this investigation, the energy to be considered is given by the areas enclosed by the moment-rotation curves for the beam critical regions and for the joint. To make the presentation more complete, the following procedure will be adopted: The total energy dissipation (measured from $H_{EQ}-\delta$ diagrams) is first presented, and then, the energy dissipation in the various critical regions is considered.

Figure 6.24 shows the magnitudes of the energy dissipating components for BC3 and BC4 . The amount of the total energy dissipated per cycle decreased for BC3 between the two displacements levels of $\delta = 2.9$ in. and 4 in. at which it was measured. This is as to be expected, since the large displacement cyclic loading causes a large degradation in stiffness which reduces the area enclosed by a loop. Direct comparison of the total energy dissipated per cycle in BC3 and BC4 is not especially useful, because of the dramatically different types of the loading patterns. The relative magnitudes of the components of energy dissipation are significant, however. The distribution of energy dissipated by different mechanisms in BC3 and BC4 is quite different, and changes with the displacement level (see Fig. 6.24). For BC3, at a displacement level of 2.9 in., the first critical beam regions contributed nearly 50% of the energy dissipated per cycle while the joint pull-out contributed only 25%. At the 4 in. level the energy dissipated by the first critical region decreased to near zero while the contribution from pull-out increased to almost 100%. In BC4, at a displacement level of 3.6 in., only 25% of total energy is dissipated by the joint, with 38% and 18% dissipated by the first and second critical regions respectively. Noteworthy is the good condition of the bond of the bars in the joint of BC4.

(in the displacement range of 1 to 3.6 in.) than BC3 . Thus, it could be expected that the smaller stiffness and energy dissipation values for BC4E (see Figs. 7.1a and b), are partly due to this effect.

7.2 Strength of BC3 and BC4E

The ability of the repaired specimen to attain the same ultimate load as BC3 is apparent from Fig. 7.2. The strength envelope for the repaired specimen for first loop displacements is seen to vary from 90 to 110% of the corresponding BC3 strength. It is also evident that the shapes of the strength envelopes for the two subassemblages are similar. At displacements, δ , over ± 3 in. the strengths of both specimens decrease considerably.

Although the envelope for the repaired specimen is very close to that for specimen BC3, a comparison of similar envelopes for the strength reached during the second cycle at the same peak displacement shows that there is a considerable drop in strength in the case of BC4E with respect to BC3 (see Fig. 7.3). The BC3 maximum load resistance is from 104 to 124% of that of BC4E .

Since the H_{EQ} in Figs. 7.2 and 7.3 is the difference between the shear reactions at the ends of the beams, V_E and V_W , it is rather interesting to see how the beam-end reactions of the repaired specimen compare with those of BC3 . Figure 7.4 shows the envelope of the shear reactions, V_E and V_W, during first loading to a new peak displacement. From the figure it can be seen that the strength of the epoxy-repaired beam in the weak direction of bending is smaller than that of BC3 at all displacement levels. Except at displacements larger than 2.5 in., the repaired beam's strength in the strong direction is greater. The decrease in strength of the repaired specimen in the weak direction of bending is caused by the slip of the bottom bars along the joint (see Fig. 7.5). This prevents the development of the full strength of the bars.

The ineffectiveness of the repairing process in restoring the bond of the bottom rebars within the joint is clearly demonstrated by the considerably larger amount of slip, Δ_{PW11} , (Fig. 7.5) that occurred in BC4E compared with BC3 . At the same time the upper rebars in both specimens, exhibit approximately the same amount of slip, Δ_{PW1} . However, this may be due to the fact that these rebars did not suffer a large amount of bond damage before being repaired.

7.3 Deterioration in Stiffnesses

In this section the effectiveness of the repair on the stiffnesses of the specimen is evaluated. First the overall subassemblage stiffnesses of BC4E and BC3 are compared. Then, the stiffness deterioration characteristics in the various critical regions are discussed, and causes of the differences in total stiffness deterioration determined.

Figures 7.1a and b show the H_{EQ}-δ loops of BC3 and BC4E at specific displacement levels. From these it can be concluded that the degradation in the initial stiffness of BC4E is considerably larger than of BC3 . For instance, as the displacement, δ , increases from 1 to 2 in., the BC4E initial stiffness decreases from 69.3 kips/in. to almost zero (see loops labeled 5 and 21 in Fig. 7.1a). For a similar displacement range, the initial stiffness of BC3 changes from 47.8 kips/in. to 23.3 kips/in. (see loops labelled 17 and 21 in Figs. 7.1a and b, respectively).

Comparisons of the stiffness deterioration in the joint and the critical regions corresponding to the hysteresis loops shown in Figs. 7.1a and b are given in Figs. 7.6 and 7.7.

Considering joint stiffness, except at the 1 in. displacement cycles, the initial pull-out stiffness of the repaired specimen is considerably lower than that of BC3 . The flexural bending stiffness in the strong direction of BC3, except for the curves in Fig. 7.7a is less than that of BC4E; in the weak direction of bending, their initial bending stiffnesses are not much different (Fig. 7.7b). Therefore, the cause of the deterioration of BC4E's total initial stiffness, $H_{EQ}-\delta$, is the poor performance of the repaired joint.

It is interesting to note that increased displacements in subsequent loops have only a small effect on degrading the BC4E elastic bending stiffness of critical beam regions (see Fig. 7.7). This arises from the fact that the repair process effectively restores the flexural capabilities of the member, and that negligible damage occurs in the critical region of the beam since most of the deformation is concentrated in the joint.

7.4 Ductilities of BC3 and BC4E

To define various ductilities, the first-yield deformation of the specimen is necessary. In the case of the repaired beam-column, a definite yield point does not exist, and it is not possible to define precisely the various ductility ratios. To overcome this difficulty, direct comparisons of deflection, δ , beam rotations of the critical regions, and pull-out rotations are made for BC4E and BC3 .

From Fig. 7.2, it is apparent that specimens BC4E and BC3 can sustain approximately the same displacement of 3 in. before the load resistance starts to drop.

The rotations induced in the joint (pull-outs) and beam bending critical regions for first loop cycles are shown in Figs. 7.8 and 7.9. An inspection of Fig. 7.8 shows that the pull-out of the bottom bars in BC4E causes joint rotations that are consistently and considerably larger than in BC3 . This evidence confirms the inefficiency of epoxy injection in restoring bond damage. The rotation induced in the critical bending region of BC4E, Fig. 7.9, is near to that found for BC3 up to displacements of ± 0.7 in., and considerably lower for displacements larger ± 1 in. (due to more joint rotation induced at that stage). The ultimate rotation in the critical beam regions in BC3 and BC4 could not be obtained from these tests since a premature failure occurred in the joint.

7.5 Energy Dissipation Capacities of BC3 and BC4E

As in section 6.5, the total energy dissipation measured from H_{EQ}-δ is presented first, then the relative energy dissipation of various critical regions is discussed.

From the typical hysteretic loops for BC3 and BC4E shown in Figs. 7.1a and b it can be seen that BC3 dissipates more energy that BC4E at similar displacement cycles. The relationship between the total energy dissipated and the corresponding displacement for the two specimens is shown in Fig. 7.10. The total energy per cycle dissipated by BC3 is consistently and considerably larger than that dissipated by BC4E . The percentage of energy dissipation for BC4E relative to that of BC3 for the same displacement ranges from 26 to 74% for first loading and from 25 to 50% for the repeated loop (see Fig. 7.11). Since only a small amount of energy can be dissipated in the repaired specimen compared with BC3, the conclusion is again reached that the epoxy-repair process does not effectively restore the original subassemblage capabilities.

Since most of the energy dissipation occurs in the critical regions where inelastic behavior arises, it is interesting to see both how much energy is dissipated in the different regions and what the effects are on their dissipation capacities. To answer these questions, curves showing the percentage of energy dissipated in the critical regions of BC3 and BC4E were prepared (see Figs. 7.12 and 7.13). It should be noted that in the case of BC3 70 to 100% of the total energy is dissipated through the four critical regions. Up to a displacement of 3 in., the first critical beam regions dissipate about 60% and the joint dissipates about 15 to 20%. It is rather different from the case of BC4E for which the bond between the rebars in the joint and the surrounding concrete is poor. Therefore, more energy is dissipated in the joint pull-out and less in the beam critical regions: for the BC4E, about 30% by the west joint pull-out and 10% by the east beam critical region (see Fig. 7.13) compared with about 9% by the joint and 30% by the beam region for BC3 . (Unfortunately, information regarding the energy dissipation in the east joint pull-out and the west beam critical region is not available to complete Fig. 7.13.)

A comparison of the energy dissipated in the joints of BC4E and BC3 is shown in Figs. 7.14 and 7.15. It can be seen that during first displacement loops, the repaired joint of BC4E can dissipate more energy than the joints in BC3, in spite of the greater total energy dissipated in BC3 . For the repeated loop, however, considerably less energy is dissipated in the BC4E joint in comparison with that of BC3 (see Fig. 7.16).

In BC3, for displacements less than 3 in., the critical beam regions are actively involved in dissipating energy while in BC4E the failure in the joint bond effectively prevents the beam critical regions from participating in the energy dissipation. This behavior is shown in Figs. 7.16 and 7.17.

8. ANALYTICAL PREDICTIONS

8.1 General

Recently, various mathematical models representing the behavior of reinforced concrete members have been used in predicting the response of a structure under earthquake excitation. These include the elasto-plastic hardening model (or bilinear model) used by Anderson and Bertero [25] and the degradation model proposed by Clough [26]. Usually, only the flexural properties of the reinforced concrete members are used in constructing the hysteretic model; the effects of shear distortion and joint flexibility are neglected. In this chapter an attempt is made to assess the accuracy of predicting subassemblage response using the bilinear and degrading models.

8.2 Assumptions and Geometric Considerations

In order to account for the P-δ effect, which is one of the significant parameters in the subassemblage experiments, a second-order analysis which includes the relative displacement of the columns was carried out. The parameters defining the deformed configuration of the subassemblage are given in Fig. 8.1

The following assumptions are made in the analysis:

1. The joint is rigid and therefore the deformation of the subassemblage comes from the flexibility of the beam and columns.

2. Shear deformations in the beams and columns are negligible.

The second assumption is reasonable, as has been shown in Fig. 4.28. The first assumption, although not entirely correct, is usually made in most analyses. With these assumptions,

$$\delta = \theta \times 72 + \delta_{col} \tag{8.1}$$

and

$$\delta_{col} = \delta_o^{\,t} + \delta_o^{\,b} \tag{8.2}$$

where $\delta_o^{\,t}$ and $\delta_o^{\,b}$ are the deflections contributed by the upper and lower columns, respectively (see Fig. 8.1).

From Fig. 8.1, the equilibrium conditions dictate that

$$H = (V_W - V_E) - \frac{P\delta}{L} = H_{eq} - \frac{P\delta}{L} \tag{8.3}$$

$$P' = P + (V_W + V_E) \tag{8.4}$$

where H, V_W, V_E, P and P' are forces acting on the subassemblage.

8.3 Analysis of Column Deflection

Since the predicted cracking moment for the column section (M_{cr} = 2260 k-in., see Appendix D) is approximately the sum of the yield moments in the weak and strong directions of the beam section (see Appendix A), the column will essentially behave as if in its elastic uncracked state. Since it is in the linear elastic range, the closed form solution describing the deflections of the column can be found.

In the analysis, P' in Eq. 8.4 is assumed to be equal to P. This assumption is justified since $P \gg (V_E + V_W)$. (From the experiment, $P = 470$ kips, $V_E + V_W \simeq 20$ kips.) The distance from the center of the joint to the hinge is used as the effective length in the beam-column action (see Fig. 8.2). As a result of these approximations, the deflected shapes of the upper and lower columns are identical and hence,

$$\delta_{col} = 2\delta_o^t = 2\delta_o \tag{8.5}$$

Figure 8.2 illustrates the deformation of the column. The moment induced in the column at distance x can be expressed as

$$M(x) = P(\delta_o + L'\theta - y - x\theta) + H(L' - x) \ , \qquad 0 \le x \le L' \tag{8.6}$$

where y is the deflection due to the flexural deformation of the column section.

Equation 8.6 can reduced to

$$M(x) = -Py + A - Bx \tag{8.7}$$

where

$$A = P(\delta_o + L'\theta) + HL' \tag{8.8}$$

$$B = (P\theta + H) \tag{8.9}$$

and

$$L' = L/2 \tag{8.10}$$

From Eqs. 8.2 and 8.3,

$$H = H_{eq} - (P/L)(L'\theta + 2\delta_o) = H_{eq} - P(\theta/2 + \delta_o/L) \ , \tag{8.11}$$

The moment-curvature relation for elastic structures is

$$\frac{d^2y}{dx^2} = \frac{M(x)}{EI} \tag{8.12}$$

where EI = uncracked stiffness of the column section .

Combining Eqs. 8.7 and 8.12 yields

$$EI \frac{d^2y}{dx^2} + Py = A - Bx \tag{8.13}$$

The general solution of Eq. 8.13 is

$$y(x) = C_1 \cos \alpha s + C_2 \sin \alpha x + \frac{1}{P} (A - Bx)$$

in which

$$\alpha = P/EI \tag{8.14}$$

The boundary conditions, $y(0) = 0$ and $y'(0) = 0$, yield

$$y(x) = -\frac{A}{P}\cos\alpha x + \frac{B}{P\alpha}\sin\alpha x + \frac{1}{P}(A - Bx) \tag{8.15}$$

To determine δ_o, one more condition is needed, i.e.,

$$y(L') = \delta_o = -\frac{A}{P}\cos\alpha L' + \frac{B}{P\alpha}\sin\alpha L' + \frac{1}{P}(A - BL') \tag{8.16}$$

Using the definitions of A and B, Eq. 8.16 is solved for δ_o, and

$$\delta_o = \beta L\left(1 - \frac{\delta L'}{\tan\delta L'}\right) \tag{8.17}$$

where

$$\beta = H_{eq}/P$$

From Eqs. 8.1 and 8.2,

$$\delta_o = \beta L(1 - \alpha L/[2\tan\alpha L/2])\frac{H_{eq}}{P} + L\theta \tag{8.18}$$

Using the experimental values, $P = 470$ kips, $EI = 488.2 \times 10^5$ kips/in. and $L = 72$ in., Eq. 8.17 becomes

$$\delta = 6.376 \times 10^{-4}\,H_{eq} + 72\,\theta \tag{8.19}$$

8.4 Analysis of the Beam Deformation

To determine the relationship of θ, V_E, and V_W for a subassemblage subjected to a well-defined loading history, beam deformations are analyzed using various nonlinear material models. The solutions are obtained from a step-by-step numerical approach.

The structure is represented by Fig. 8.3. The mathematical expressions for describing this incremental procedure are:

$$\Delta M_w^i = \frac{K_w^i \ \Delta M^i}{K_w^i + K_E^i} \tag{8.20a}$$

$$\Delta M_E^i = - \frac{K_E^i \ \Delta M^i}{K_W^i + K_E^i} \tag{8.20b}$$

Where the superscripts correspond to the i-th step; ΔM^i is the incremental moment introduced by the horizontal force, H ; ΔM_W^i and ΔM_E^i are the corresponding changes in beam member moments (see Fig. 8.3) and the beam stiffnesses, K_E^i and K_W^i are as defined in Fig. 4.20.

$$\Delta M_W^i = K_W^i \ \Delta\theta_W^i \tag{8.21a}$$

$$\Delta M_E^i = K_E^i \ \Delta\theta_E^i \tag{8.21b}$$

where $\Delta\theta_W^i$ and $\Delta\theta_E^i$ are the corresponding changes in the angle of rotation of the beams. Details for determining K_W^i and K_E^i are presented in section 8.5.

Once ΔM_W^i and ΔM_E^i are found, the horizontal force acting at the bottom hinge of the column, H, and the corresponding horizontal displacement, δ , are established as follows:

$$M_W^{i+1} = M_W^i + \Delta M_W^i \tag{8.22a}$$

$$M_E^{i+1} = M_E^i + \Delta M_E^i \tag{8.22b}$$

$$H_{EQ}^{i+1} = V_W^{i+1} - V_E^{i+1} = (M_W^{i+1} - M_E^{i+1})/63.5 \tag{8.23}$$

$$\Delta\theta_w^i = \Delta\theta_E^i = \Delta\theta^i = \Delta M/(K_E^i + K_W^i) \tag{8.24}$$

and from Eq. 8.19,

$$\delta^{i+1} = \theta^{i+1} \times 72 + 6.376 \times 10^{-4}\, H_{EQ}^{i+1} \qquad (8.25)$$

From Eq. 8.3,

$$H^{i+1} = H_{EQ}^{i+1} - \frac{P\delta^{i+1}}{72} \qquad (8.26)$$

8.5 Moment-Curvature Relation for the Beam Section

To simplify the subsequent analysis, the moment-curvature relations originally obtained by analyzing the cross section of the beam (Appendix A) are approximated as linear curves (bilinear model) (Fig. 8.4). The stiffness in the linear range is based on the cracked transformed cross-section, i.e., uncracked section behavior is neglected.

8.6 The Elasto-Plastic Hardening Model

The analytical work presented in this section is based on the assumption that the bilinear model of Fig. 8.4 is applicable to the reinforced concrete member at the $M-\phi$ level.

8.6.1 Moment-Curvature Hysteresis of the Beam Section

Figure 8.5 shows the hysteresis rule adopted for this model. The curves OAB and OJK are taken from the modified moment curvature diagram for the weak and strong directions of bending, respectively.

8.6.2 Determination of the Beam Member Stiffness, K_E and K_W

For the elastic loading and unloading, the stiffness, K, of the member with the far end simply supported is

$$K = \frac{3(EI)}{L}$$

where the elastic EI's are given in Fig. 8.5.

For a member loaded beyond yielding, the stiffness is computed from

$$K = \frac{\Delta M}{\Delta \theta}$$

where $\Delta\theta$ is determined from the change in the angle of rotation when the moment changes from M to $M + \Delta M$. Each beam is subdivided into small elements which follow their own moment-curvature hysteretic paths. The moments and curvatures are then evaluated at the centers of the elements.

8.6.3 Comparison of Analytical and Experimental Results (BC4)

For purposes of comparison, the maximum horizontal displacement, δ, in the analysis will be matched to the experimental one. The initial 3.5 kips downward reactions are included in the analysis. Figures 8.6 and 8.7 show the H_{EQ}-δ and H-δ diagrams obtained from both analysis and the experiment. The following observations are made from the curves.

1. There is relatively good agreement between the predictions and the test in the range LP 17 to 23 and fair agreement for LP 32 to 36. Hence, the strength of BC4 can be reasonably accurately predicted.

2. The first yield deflection obtained from the analysis is less than that of the experiment. This is not surprising since the prediction does not include flexibility introduced by the joint.

3. As anticipated, a large discrepancy occurs between the prediction and the experiment from LP 26 to 31. This discrepancy arises because the same elastic stiffness of the beam section used to predict the first yield is employed to calculate the response of this part of the

curve in the model (see Fig. 8.5). During reverse loading when cracks are still open, large forces are transmitted thru the rebars which exhibit a strong Bauschinger effect. This makes the stiffness at the critical regions much lower than the elastic stiffness used in the model. Furthermore, the model used in the analysis does not allow for slippage of bars in the joint.

4. A considerably larger discrepancy between prediction and experiment occurs from LP 38 to 42 (ss Figs. 8.6 and 8.7). As has been mentioned in section 4.5, in this range the controlling mechanism of the subassemblage behavior is the pull-out and push-in of the joint. This is completely ignored in the model.

5. The model considerably overestimates the energy absorption and dissipation of the subassemblage. The energy dissipation for the complete experimental cycle is about 70% of the predicted one.

8.7 Degradation Model

The analytical work presented in this section is based on the assumption that a degradation model which approximates the mechanical properties of a reinforced concrete member is applicable at the $M-\theta$ level. This approach has been used by Otani and Sozen [27] in predicting the response of a three story reinforced concrete building under simulated earthquake excitation.

8.7.1 Hysteresis of the Moment-Rotation $M-\theta$

The moment rotation curves, $M-\theta$, of a beam with the far end supported on a roller are first constructed by using the bilinear $M-\phi$ diagram of Fig. 8.4. These $M-\theta$ relations for both the weak and strong are established as illustrated in Fig. 8.8. The curves are then approximated by the bilinear diagrams, OAK and ODM, as shown by the dashed lines in Fig. 8.8. For the unloading and reloading branches, they are assumed to follow Clough's degradation rules [26].

8.7.2 Comparison of the Predicted and Experimental Results

Figures 8.9 and 8.10 illustrate the total response of the subassemblage, $H-\delta$ and $H_{EQ}-\delta$, obtained from experimental and analytical work. Except for slightly overestimated maximum load resistances, the predicted results are in good agreement with the experimental ones, particularly in terms of the energy dissipation which is represented by the area enclosed by the curves.

Although there is relatively good agreement between prediction and experiment in the $H-\delta$ diagrams, the correlation in the $M-\theta$ diagrams is not that close (see Figs. 8.11 and 8.12). The rotations due to the flexural deformations of the east and west beams, denoted θ_{bE} and θ_{bW}, together with the joint pull-out rotations, θ_{pE} and θ_{pW}, are plotted to show their relative contributions to total joint rotation. It should be emphasized that the fact that the contribution of the joint slippage is quite substantial indicates that a large error may result if the joint slippage is not included in the prediction.

8.8 Conclusions and Summary

The results obtained in this chapter emphasize the following points:

1. For monotonically increasing loads, the prediction based on the elasto-plastic model is fairly accurate. However, for the behavior of the complete hysteretic loop at large displacements, the elasto-plastic

hardening model yields considerably higher energy dissipation than the actual one. This suggests that the elasto-plastic hardening model is unsuitable for predicting behavior of R/C members under seismic excitation when full or partial reversal of lateral displacement is likely to occur.

2. The prediction using Clough's degradation model agrees well with experimental results.

3. Joint pull-out substantially influences subassemblage response during monotonic loading. For cyclic loading, this influence is even greater. Therefore, if an accurate prediction is to be made for a beam-column subassemblage, it must take the joint pull-out into account.

REFERENCES

1. Hanson, N. W., "Seismic Resistance of Concrete Frames with Grade 60 Reinforcement," Journal of the Structural Division, American Society of Engineers, Vol. 97, No. ST6, June 1971, pp. 1685-1700.

2. Hanson, N. W., and Connor, H. W., "Seismic Resistance of Reinforced Concrete Column Joints," Journal of the Structural Division, American Society of Civil Engineers, Vol. 93, No. ST5, October 1967, pp. 533-560.

3. Corley, G., and Hanson, N. W., "Design of Beam-Column Frames," Proceedings Fourth World Conference on Earthquake Engineering, Santiago, 1969, Vol. II, pp. B-3, 69-82.

4. Megget, L. M., and Park, R., "Reinforced Concrete Exterior Beam-Column Joints Under Seismic Loading," New Zealand Engineering, Vol. 26, No. 11, November 1971, pp. 341-353.

5. Smith, B. J., "Exterior Reinforced Concrete Joints with Low Axial Load Under Seismic Loading," M. E. Thesis Presented at University of Canterbury, Christchurch, New Zealand, 1972, 91 pp.

6. Renton, G., "The Behavior of Reinforced Concrete Beam-Column Joints Under Cyclic Loading," M. E. Thesis Presented at University of Canterbury, Christchurch, New Zealand, 1972, 163 pp.

7. Patton, R. N., "Behavior Under Seismic Loading of Reinforced Concrete Beam-Column Joints with Anchor Blocks," M. E. Thesis Presented at University of Canterbury, Christchurch, New Zealand,

8. Townsend, W. H., "The Inelastic Behaviour of Reinforced Concrete Beam-Column Connections," Ph.D. Dissertation Presented at the University of Michigan, 1972.

9. Bulletin of Adhesive Engineering Co., "Managua, Nicaragua: Building Repairs Underway in Earthquake-Struck City," Vol. VIII, No. 3, August 1973.

10. S. A. Mahin and V. V. Bertero, "Rate of Loading Effects on Uncracked and Repaired Reinforced Concrete Members," Report No. EERC 72-9, Dec. 1972.

11. Soleimani, D., "Reinforced Concrete Ductile Frames Under Earthquake Loadings with Stiffness Degradation," Ph.D. Dissertation, University of California, Berkeley, December 1978.

12. Megget, L. M., "Exterior Reinforced Concrete Joints with and without Intersecting Beams Under Seismic Loading," Bulletin of International Institute of Seismology and Earthquake Engineering, Tokyo, Japan, Vol. II, 1973, pp. 115-167.

13. Blakeley, R. W. G., Megget, L. M., Priestley, M. J. N., "Seismic Performance of Two Full Size Reinforced Concrete Beam-Column Joint Units.

14. Umemura, H., and Ikeda, A., "Study on Improvement of Structural Ability of Reinforced Concrete Construction, 1-Tests of the Beam-Column Connections Under Repeated Loading, 2-Tests of the Beam-Column Connections with Special Reinforcement," Trans. of A.I.J., Tokyo, Japan, No. 89, 1963 and No. 103, 1964.

15. Owada, Y., et al, "Study of Reinforced Concrete Beam-Column Connection Subjected to Lateral Loads," Trans. of the A.I.J., Tokyo, Japan, Extra, October 1967, p. 337.

Koreishi, I., "Test of Reinforced Concrete Beam-Column Connection," see Reference 38, pp. 185-194.

16. Inomata, S., "Comparative Study on Behaviour of Prestressed and Reinforced Concrete Beams Subjected to Reversed Loading," Journal of Japan Prestressed Concrete Engineering Association, Vol. 11, No. 1, March 1969.

17. Higashi, Y., and Ohwada, Y., "Failing Behavior of Reinforced Concrete Beam-Column Connection Subjected to Lateral Load," Memoirs of Faculty of Technology, Tokyo Metropolitan University, No. 19, 1969, pp. 91-101.

18. Bertero, V. V., "Experimental Studies Concerning Reinforced, Prestressed and Partially Prestressed Concrete Structures and Their Elements," Introductory Report for Theme IV, Symposium on Resistance and Ultimate Deformability of Structures Acted on by Well Defined Repeated Loads, International Association for Bridge and Structural Engineering, Lisbon, 1973, pp. 67-99.

19. ACI Standard Building Code Requirements for Reinforced Concrete (ACI 318-71), American Concrete Institute, Detroit, Michigan, 1971.

20. International Conference of Building Officials, "Uniform Building Code," 1970 Edition, Vol. 1, Pasadena, California.

21. E. P. Popov and V. V. Bertero, "Repaired R/C Members Under Cyclic Loading," 5th Congress of Yugoslav Association of Structural Engineers and 3rd Congress of the (Yugoslav) Association for Earthquake Engineering.

22. Singh, A., Gerstle, K. H., and Tulin, L. C., "The Behavior of Reinforcing Steel Under Reversed Loading," Materials Research and Standards.

23. Krawinkler, H., Bertero, V. V., and Popov, E. P., "Inelastic Behavior of Steel Beam to Column Subassemblages," Earthquake Engineering Research Center, Report N. EERC 71-7, University of California, Berkeley, Oct. 1971.

24. Bulletin of Adhesive Engineering Co., "Managua Nicaragua: Building Repairs Underway in Earthquake-Struck City," Vol. VIII, No. 3, August 1973.

25. Anderson, J. D., and Bertero, V. V., "Seismic Behavior of Multistory Frames Designed by Different Philosophies," Earthquake Engineering Research Center, Report No. EERC 69-11, University of California, Berkeley, Oct. 1969.

26. Clough, R. W., "Effect of Stiffness Degradation on Earthquake Ductility Requirements," Structures and Materials Research Report No. 66-16, Department of Civil Engineering, University of California, Berkeley, Oct. 1966.

27. Otani, S., Sozen, M. A., "Behavior of Multistory Reinforced Concrete Frames During Earthquakes, Civil Engineering Studies, Structural Research Series No. 392, University of Illinois, Urbana, Nov. 1972.

Table 2.1 Compressive Strength of Concrete

Specimen	Age (Days)	Compressive Strength f'_c psi (MPa)	Initial Modulus of Elasticity E_c		
			E_c psi (MPa)	$\frac{E_c}{w^{1.5}\sqrt{f'_c}}$ *	$\frac{E_c}{w^{1.5}\sqrt{f'_c}}$ **
BC3		4510 (31.11)	4.07×10^6 (2.81×10^4)	33.0	35.0
BC4	18	4570 (31.52)	3.93×10^6 (2.71×10^4)	31.6	33.8
BC4E	30	4970 (34.28)	3.90×10^6 (2.69×10^4)	30.1	33.6

* f'_c from test

** f'_c = 4000 psi (27.6 MPa), original design concrete strength at 14 days

Table 2.2 Tensile Strength of Concrete

Specimen	Age (Days)	Splitting Tensile Test f_t			Modulus of Rupture, f_t		
		psi MPa (kN/cm^2)	$f_t/\sqrt{f'_c}$ *	$f_t/\sqrt{f'_c}$ **	psi MPa (kN/cm^2)	$f_t/\sqrt{f'_c}$	$f_t/\sqrt{f'_c}$
BC3							
BC4	18	450 (3.10)	6.66	7.12	678 (4.68)	10	10.7
BC4E	30	442 (3.05)	6.25	6.99			

* See above definition.

** See above definition.

Table 2.3 Physical Properties of Cured Adhesive

Type of Testing	Cure Time at 77°F (25°C) Days	Ultimate Strength psi (MPa)	Modulus of Elasticity psi (MPa)	Elongation
Tension	7	6900 (47.59)		0.003
Flexure	1	9900 (68.28)	$2.9 \times 10^5 = 0.074\ E_c$ (2.0×10^3)	
"	3	10,700 (73.80)	$4.0 \times 10^5 = 0.10\ E_c$ (2.76×10^3)	
"	7	11,450 (78.97)	$4.1 \times 10^5 = 0.10\ E_c$ (2.83×10^3)	
Compression	1	9850 (67.94)	$2.9 \times 10^5 = 0.074\ E_c$ (2.0×10^3)	

Table 4.1 Elastic and Pull-out Stiffnesses of Beams, Specimen BC4

A. East Beam Properties

L_p	Measured Beam Stiffness k - in^2 (kN - m^2)		Measured*** Pull-out Stiffness k - in (kN - m)
	$M_{EI} - \phi_{EI}$ *	$M_{EZ} - \phi_{EZ}$ **	$M_E - \theta_{PE}$
6RB-9	63.3×10^5 (1.82×10^4)	61.6×10^5 (1.77×10^4)	13.2×10^5 (1.49×10^5)
9-12	52.9×10^5 (1.52×10^4)	51.1×10^5 (1.47×10^4)	5.83×10^5 $(.659 \times 10^5)$

* See Fig. 4.12.

** See Fig. 4.14.

*** See Fig. 4.10.

B. West Beam Properties

L_p	Measured Beam Stiffness k - in^2 (kN - m^2)		Measured*** Pull-out Stiffness k - in (kN - m^2)
	$M_{WI} - \phi_{WI}$ *	$M_{WZ} - \phi_{WZ}$ **	$M_W - \theta_{PW}$
6RB-9	47.3×10^5 (1.36×10^4)	47.3×10^5 (1.36×10^4)	8.85×10^5 (1.00×10^5)
9-12	41.3×10^5 (1.19×10^4)	34.0×10^5 (0.976×10^4)	5.22×10^5 (0.590×10^5)

* See Fig. 4.13.

** See Fig. 4.15.

*** See Fig. 4.11.

Table 4.2 Elastic Member Stiffnesses, Specimen BC4

Member	LP	Member Stiffness k - in (kN - m)		Stiffness Ratio $\frac{b}{a}$
		(pull-out) Joint Flexibility Included (a)	(pull-out) Joint Flexibility Neglected (b)	
East Beam	6RB-9	3.24×10^5 (3.66×10^4)	2.61×10^5 (2.95×10^4)	0.81
	9-12	2.58×10^5 (2.92×10^4)	1.79×10^5 (2.02×10^4)	0.69
West Beam	6RB-9	3.08×10^5 (3.48×10^4)	2.28×10^5 (2.58×10^4)	0.74
	9-12	$1.87 \times 10^5)$ (2.11×10^4)	1.38×10^5 (1.56×10^4)	0.74

Table 4.3 Experimental and Predicted Yield Moment, BC4

Critical Region	Diagram	Experimental** M_y K-in (kN-m)	Predicted* M_y K-in (kN-m)	M_y from ACI K-in (kN-m)	Experimental M_y / Predicted M_y
First	$M_{E1} - \phi_{E1}$	1470 (166.1)	1570 (177.4)	1550 (175.2)	.94
	$M_{W1} - \phi_{W1}$	892 (100.8)	880 (99.5)	910 (102.9)	1.01
Second	$M_{E2} - \phi_{E2}$	1270 (143.5)	1570 (177.4)	1550 (175.2)	.81
	$M_{W2} - \phi_{W2}$	800 (90.4)	880 (99.5)	910 (102.9)	.91

* See detail in Appendix A.
** From Figs. 4.12-4.15.

Table 4.4 Reloaded Yield Moments, BC4

Critical Region	Diagram	Experimental** M_y K-in (kN-m)	Predicted* M_y K-in (kN-m)	Experimental M_y / Predicted M_y
First	$M_{E1} - \phi_{E1}$	755 (85.3)	880 (99.5)	.86
	$M_{W1} - \phi_{W1}$	1320 (149.2)	1570 (177.4)	.84
Second	$M_{E2} - \phi_{E2}$	684 (77.3)	880 (99.5)	.78
	$M_{W2} - \phi_{W2}$	1160 (131.1)	1570 (177.4)	.74

* See detail in Appendix A.
** See Figs. 4.12-4.15.

Table 4.5 Strain Hardening Flexural Stiffnesses After First Yielding Specimen BC4

Diagram*	Average Strain Hardening Stiff $K\text{-}in^2$ $(kN\text{-}m^2)$	% of Average** Elastic Cracked Stiff
$M_{E1} - \phi_{E1}$	1.48×10^5 (4.25×10^2)	2.54
$M_{W1} - \phi_{W1}$	$.662 \times 10^5$ (1.90×10^2)	1.49
$M_{E2} - \phi_{E2}$	1.34×10^5 (3.86×10^2)	2.38
$M_{W2} - \phi_{W2}$	$.614 \times 10^5$ (1.76×10^2)	1.51

* See Figs. 4.12-4.15.

** Average Elastic Cracked Stiffnesses from Tables 4.1a and b.

Table 4.6 Strain Hardening Flexural Stiffnesses After Second Yielding Specimen BC4

Diagram*	Average Strain Hardening Stiff $K\text{-}in^2$ $(kN\text{-}m^2)$	Average Elastic Cracked Stiff $K\text{-}in^2$ $(kN\text{-}m)$	% of Average** Cracked Stiff
$M_{E1} - \phi_{E1}$	$.951 \times 10^5$ (2.73×10^2)	58.1×10^5 (1.67×10^4)	1.64
$M_{W1} - \phi_{W1}$	1.44×10^5 (4.13×10^2)	44.3×10^5 (1.27×10^4)	3.25
$M_{E2} - \phi_{E2}$	$.854 \times 10^5$ (2.45×10^2)	56.3×10^5 (1.62×10^4)	1.52
$M_{W2} - \phi_{W2}$	1.34×10^5 (3.85×10^2)	40.6×10^5 (1.17×10^4)	3.30

* From Table 4.1a.

** From Table 4.1b.

Table 5.1 Comparison of Average Initial Elastic Stiffnesses Before and After Repair

Specimen	Pull-out and Push-in Stiffness of $M_E - \theta_{PE}$ K-in (kN-m)	Pull-out and Push-in Stiffness of $M_W - \theta_{PW}$ K-in (kN-m)	Stiffness of $M_{E1} - \phi_{E1}$ K-in^2 (kN-m^2)	Stiffness of $M_{W1} - \phi_{W1}$ K-in^2 (kN-m^2)
BC4	16.8×10^5 (1.90×10^5)	16.4×10^5 (1.86×10^5)	72.5×10^5 (2.08×10^4)	Not Available
BC4E	9.83×10^5 $(1.11 \times 10^5$	7.91×10^5 (0.894×10^5)	62.2×10^5 (1.79×10^4)	52.2×10^5 (1.50×10^4)

Table 5.2 Energy Dissipation Capacity for BC4E

Displacement in, (cm)	Loop No.	Energy K-in (kN-m)	% of the First Loop	Energy Dissip. of Ideal Loop* K-in, (kN-m)	% of Ideal Loop
± .97 (2.46)	1	30.5 (3.45)	100	60.4 (6.83)	50
	2	12.0 (1.36)	39.2		20
	3	13.4 (1.51)	44.0		22
± 1.32 (3.35)	1	37.5 (4.24)	100	135 (15.3)	28
	2	29.9 (3.38)	79.7		22
	3	22.4 (2.53)	59.7		17
± 1.99 (5.05)	1	59.5 (6.72)	100	238 (26.9)	25
	2	37.9 (4.28)	63.8		16
	3	28.1 (3.17)	47.2		12
± 2.32 (5.89)	1	59.2 (6.69)	100	289 (32.7)	20
	2	37.9 (4.28)	64.1		13
	3	28.1 (3.17)	47.4		10
± 3.00 (7.62)	1	63.3 (7.15)	100	394 (44.5)	16
	2	49.5 (5.59)	78.3		13
	3	46.4 (5.24)	73.4		12

* See Eq. F.3 and F.4.

Table A.1 Flexural Bending Properties of the Beam Section from Theory

Bending Properties	Direction of Bending	Numerical Value
Uncracked Section M-ϕ Stiffness	Weak	15.3×10^6 K-in^2 (4.39×10^4 kN-m^2)
	Strong	15.3×10^6 K-in^2 (4.39×10^4 kN-m^2)
Average Cracked Section M-ϕ Stiffness	Weak	3.92×10^6 K-in^2 (1.12×10^4 kN-m^2)
	Strong	5.78×10^6 K-in^2 (1.66×10^4 kN-m^2)
Cracked Section Moments	Weak	204 K-in (23 kN-m)
	Strong	212 K-in (24 kN-m)
First Yield Moments	Weak	880 K-in (9.9 kN-m)
	Strong	1570 K-in (177.4 kN-m)

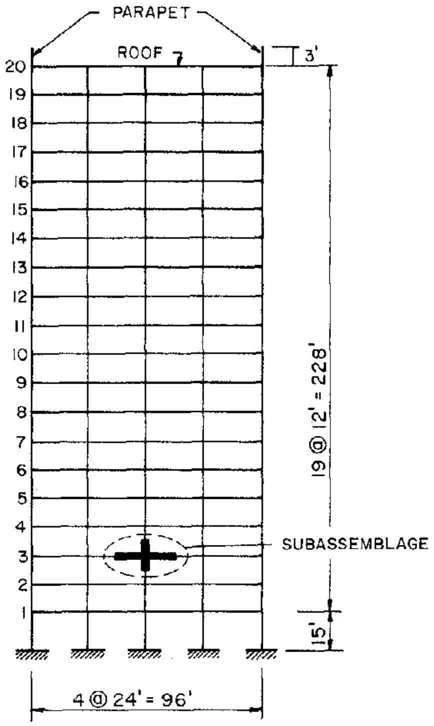

Fig. 2.1 Prototype of 20 Story R/C Frame Building

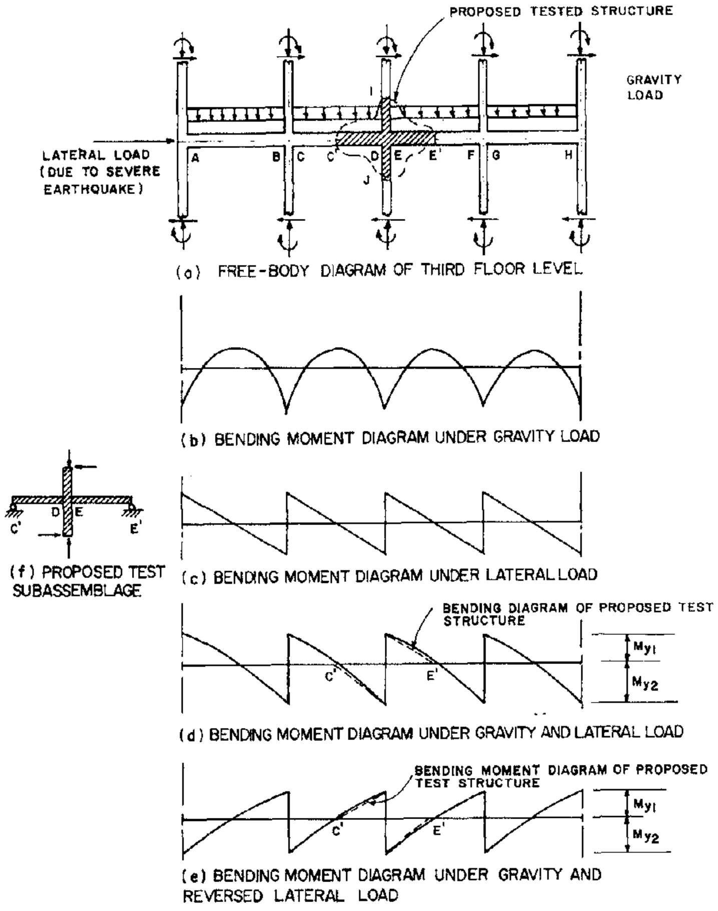

(a) FREE-BODY DIAGRAM OF THIRD FLOOR LEVEL

(b) BENDING MOMENT DIAGRAM UNDER GRAVITY LOAD

(f) PROPOSED TEST SUBASSEMBLAGE

(c) BENDING MOMENT DIAGRAM UNDER LATERAL LOAD

(d) BENDING MOMENT DIAGRAM UNDER GRAVITY AND LATERAL LOAD

(e) BENDING MOMENT DIAGRAM UNDER GRAVITY AND REVERSED LATERAL LOAD

Fig. 2.2 Load Patterns for Test Subassemblage

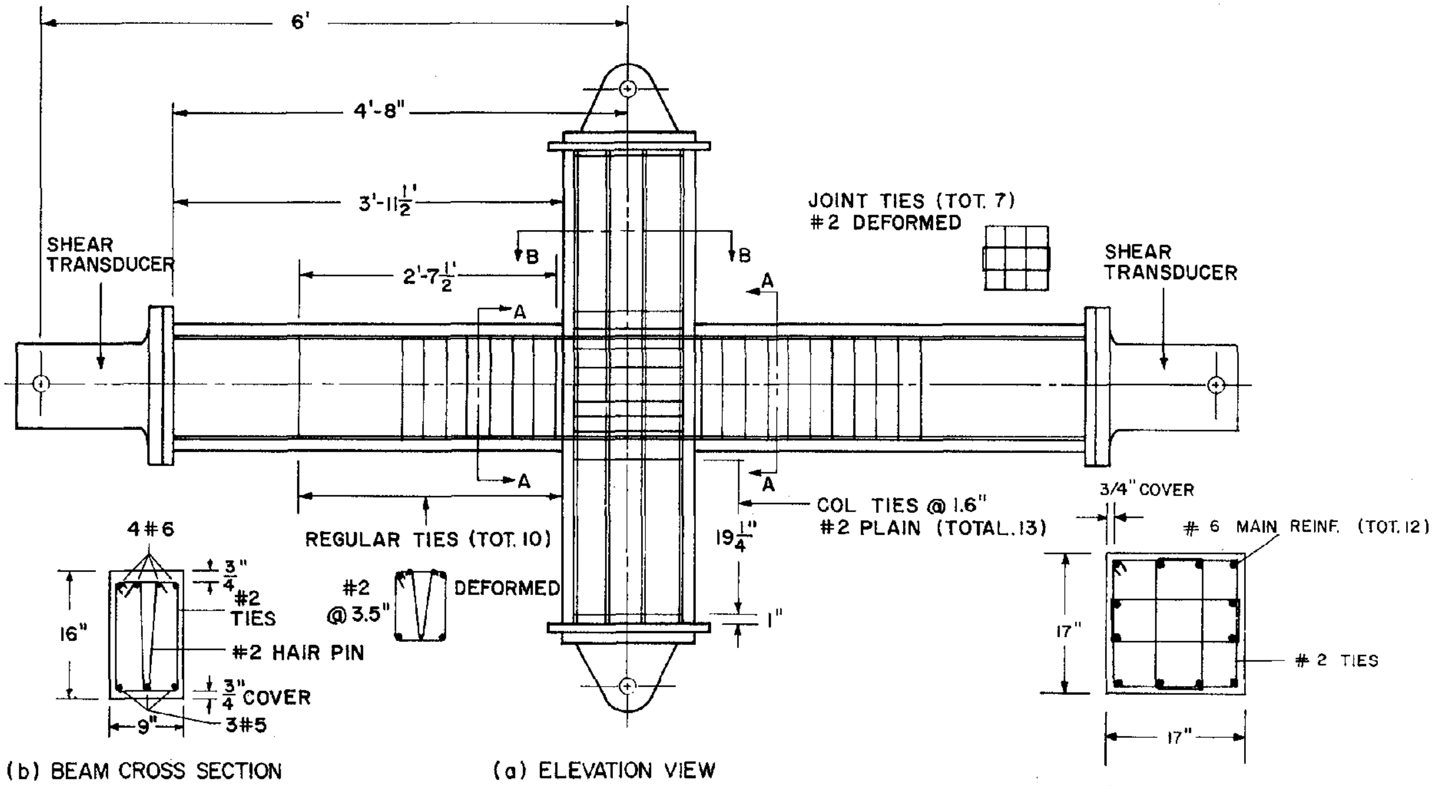

(b) BEAM CROSS SECTION

(a) ELEVATION VIEW

(c) COLUMN CROSS SECTION

Fig. 2.3 Typical Steel Reinforcement in Beam-Column Subassemblage

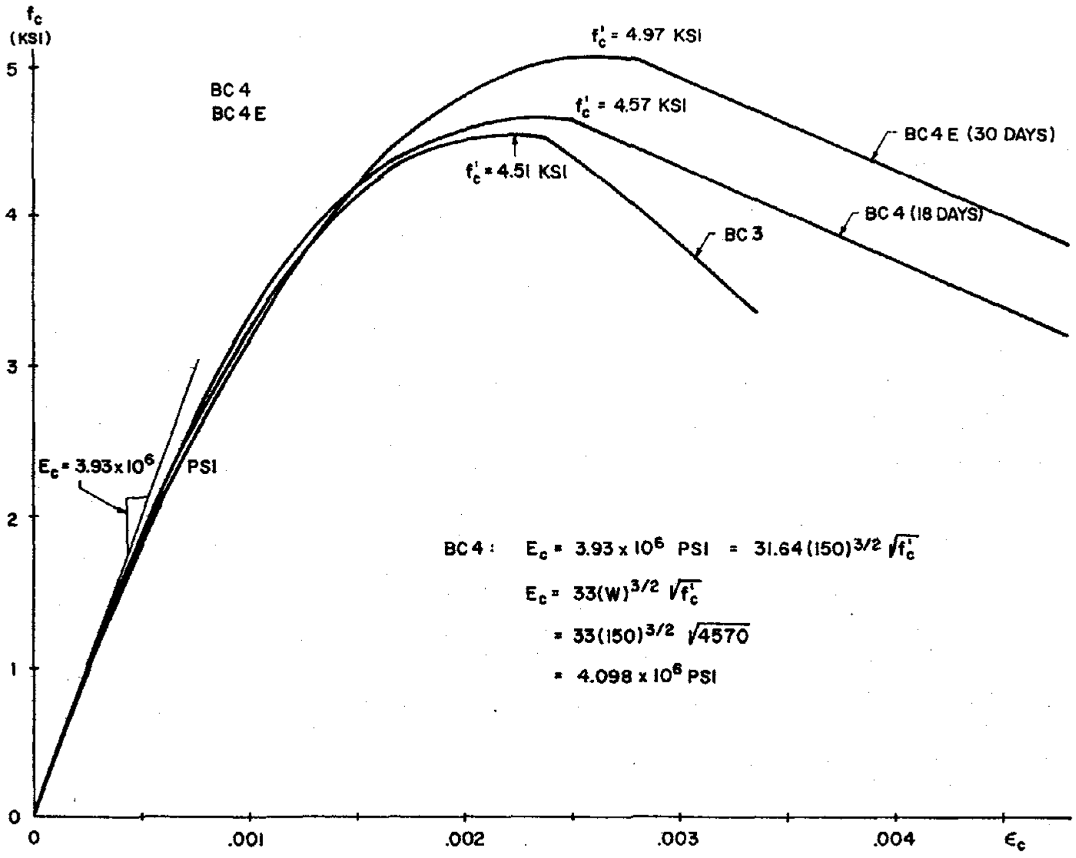

Fig. 2.4 Concrete Stress-Strain Curves

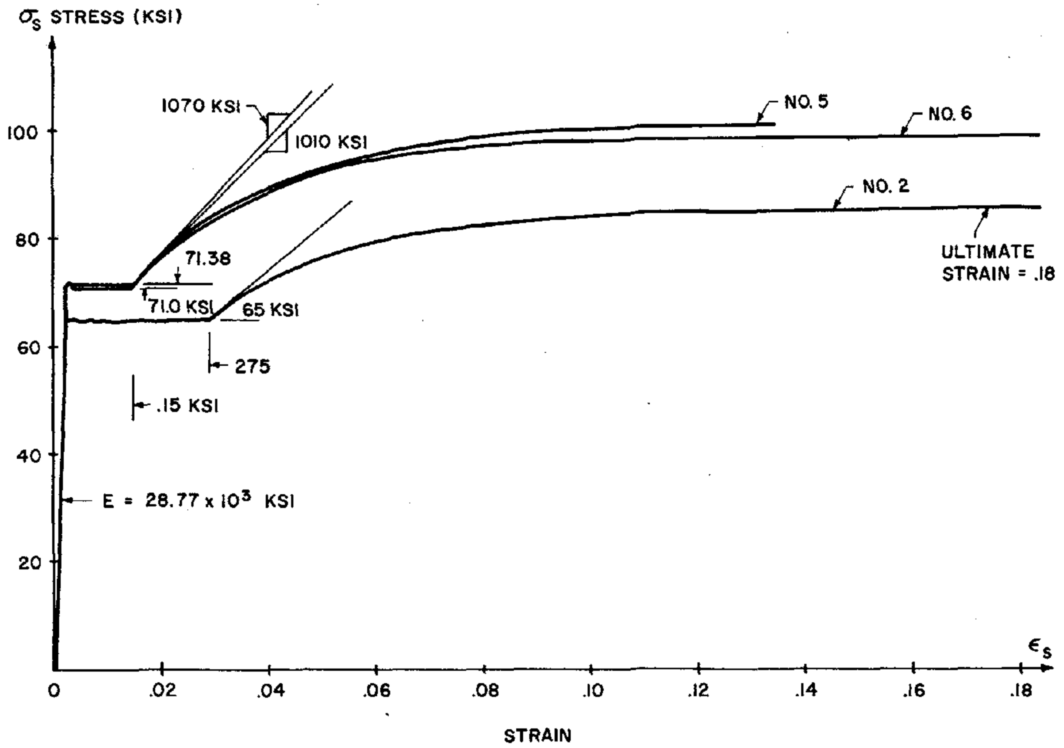

Fig. 2.5 Steel Reinforcing Bars Stress-Strain Curves

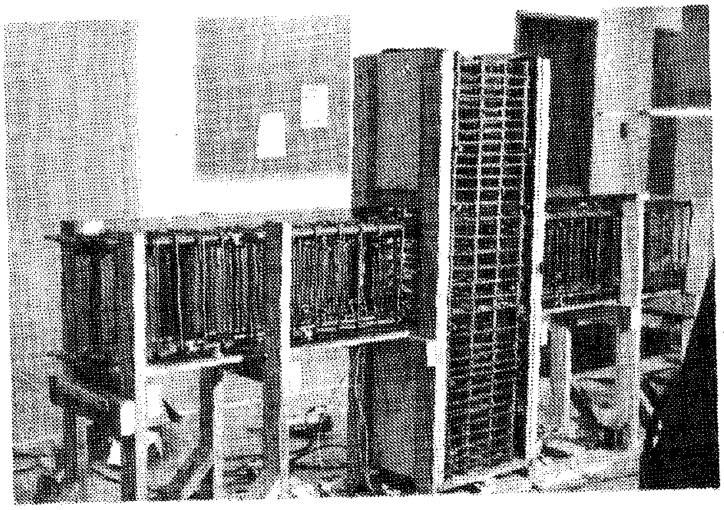

Fig. 2.6 Formwork and Reinforcement

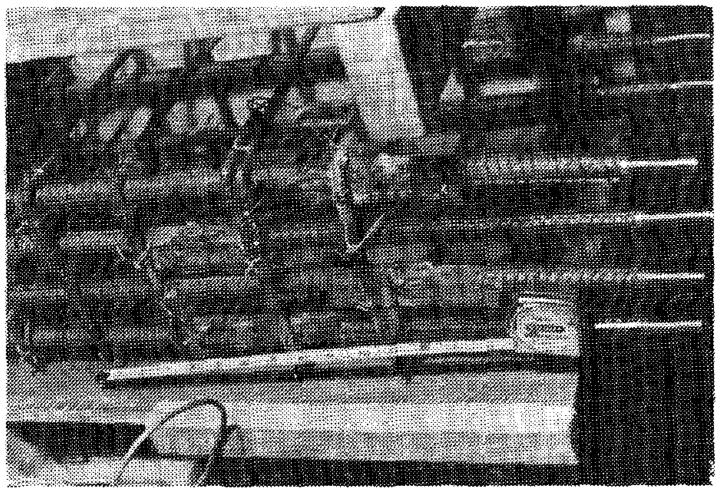

Fig. 2.7 Beam End Detail

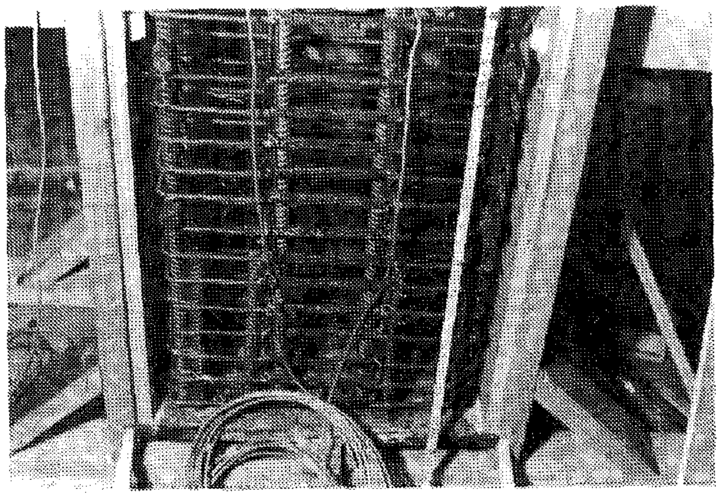

Fig. 2.8 Column End Detail

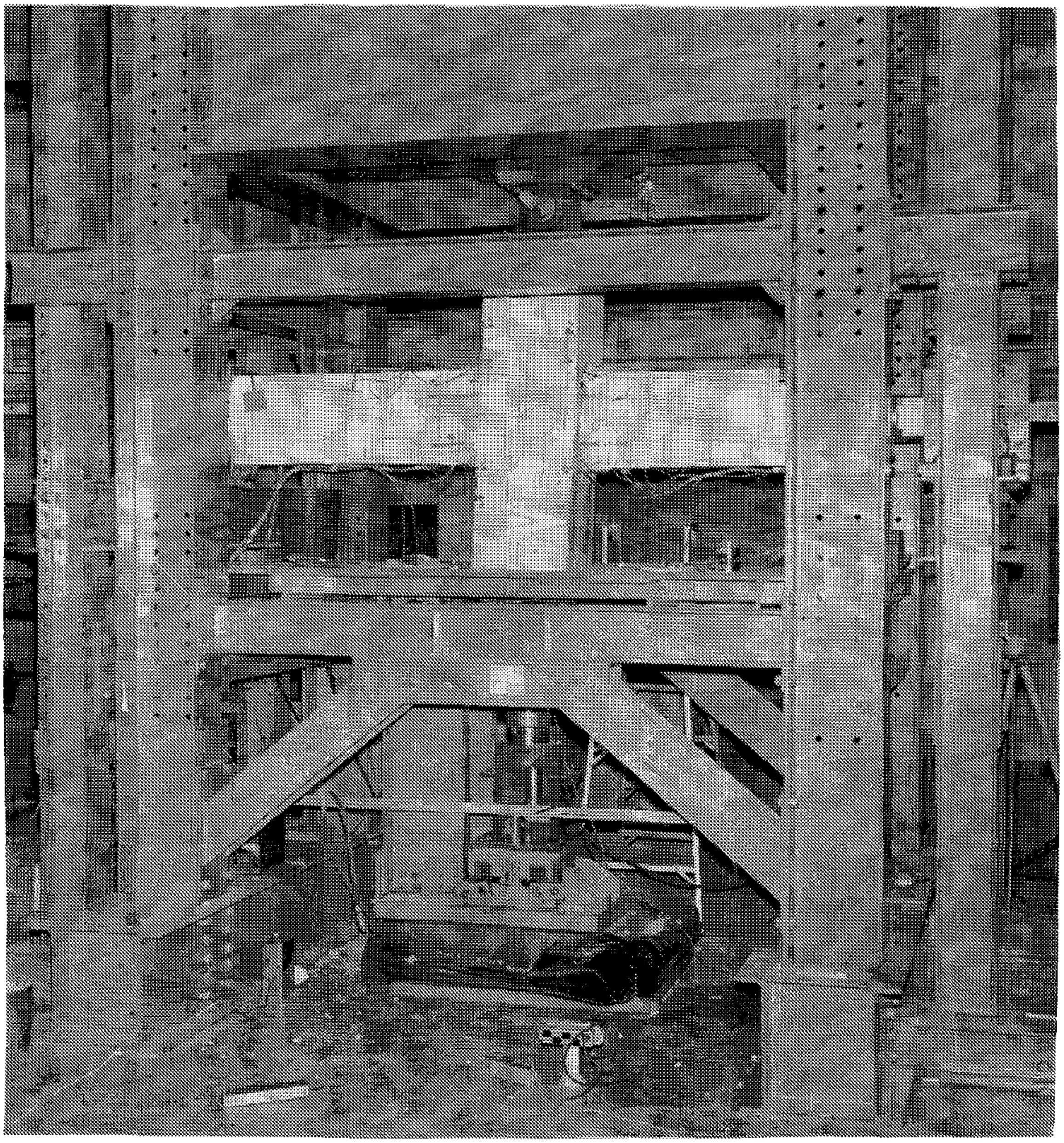

Fig. 3.1 Specimen Mounted in Testing Frame

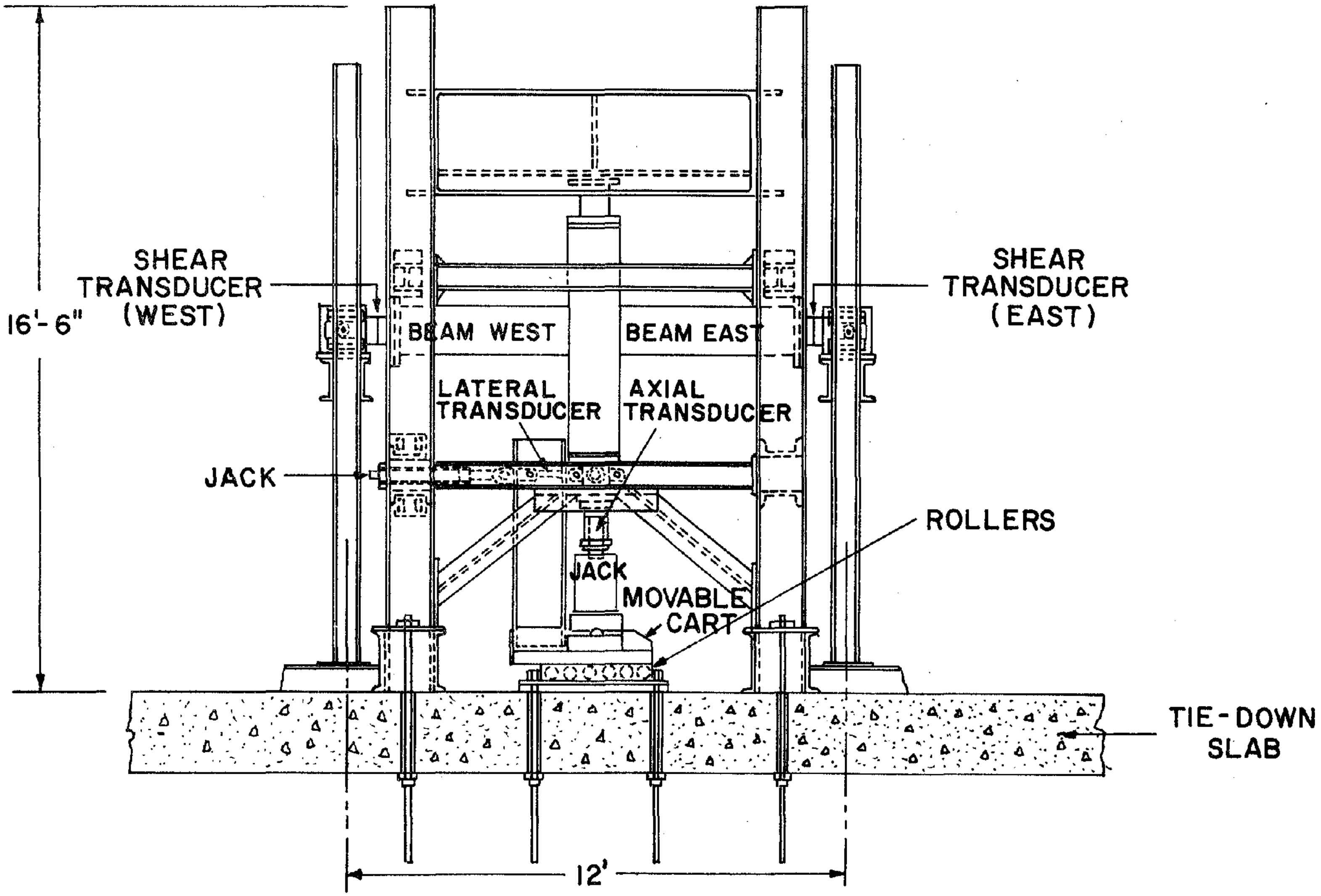

Fig. 3.2 Beam-Column Test Set Up

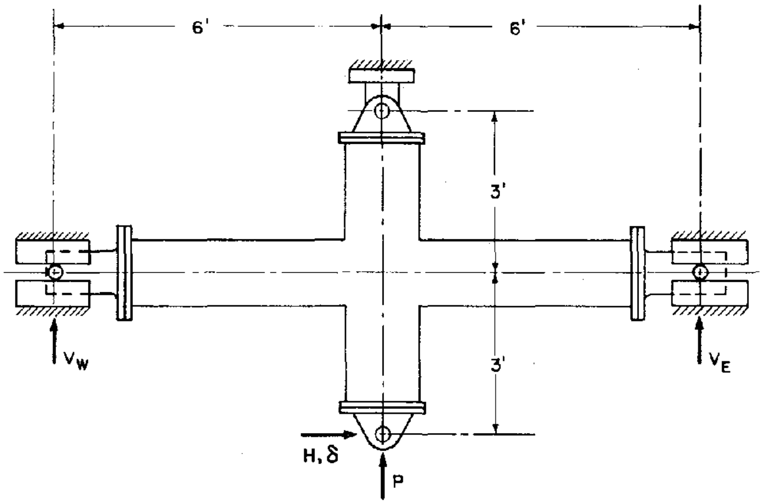

Fig. 3.3 Positive Sense of External Forces Applied to Beam-Column Subassemblage

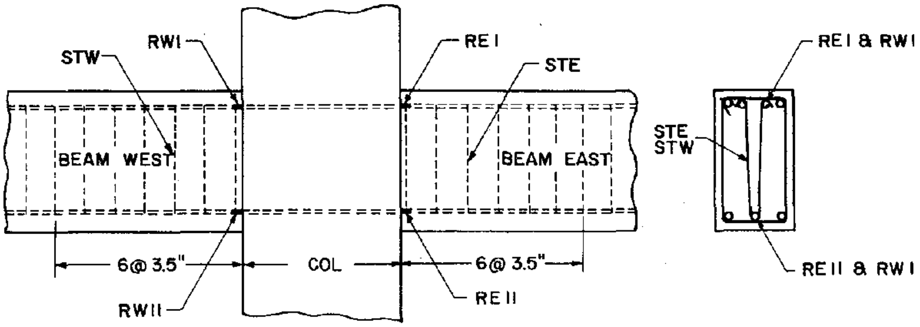

Fig. 3.4 Locations of Weldable Gages on Longitudinal Rebars and Stirrups

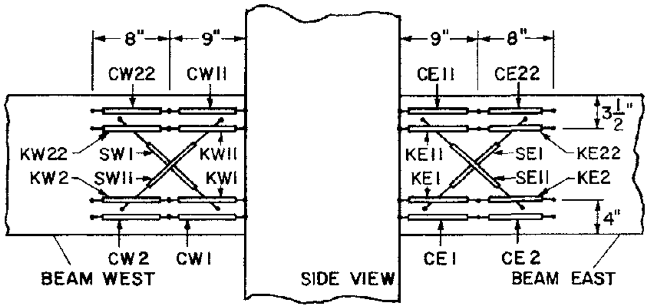

FIG. 3.5a LOCATIONS OF CURVATURE AND SHEAR GAGES

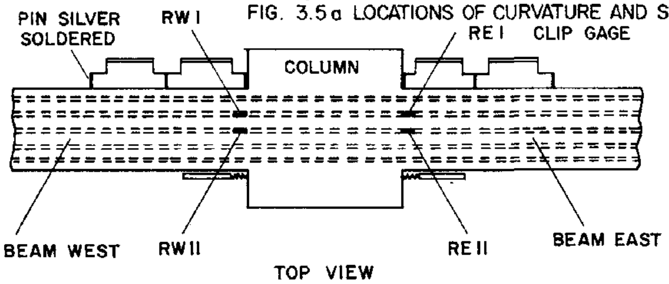

FIG. 3.5b LOCATIONS OF WELDABLE GAGES

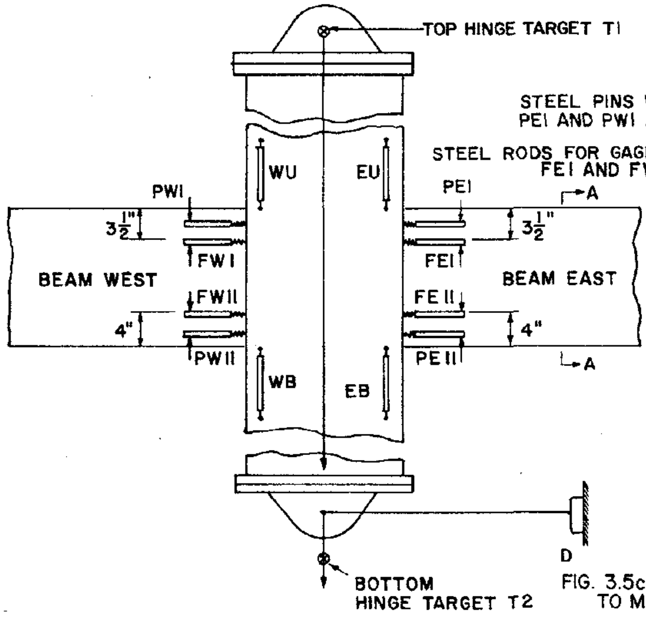

FIG. 3.5c INSTRUMENTATIONS TO MEASURE SLIPPAGES

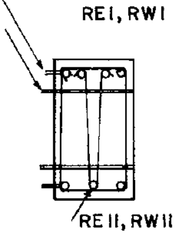

FIG. 3.5d SECTION A-A

Fig. 3.5 Instrumentation for Measuring Deformations

(a) West Beam

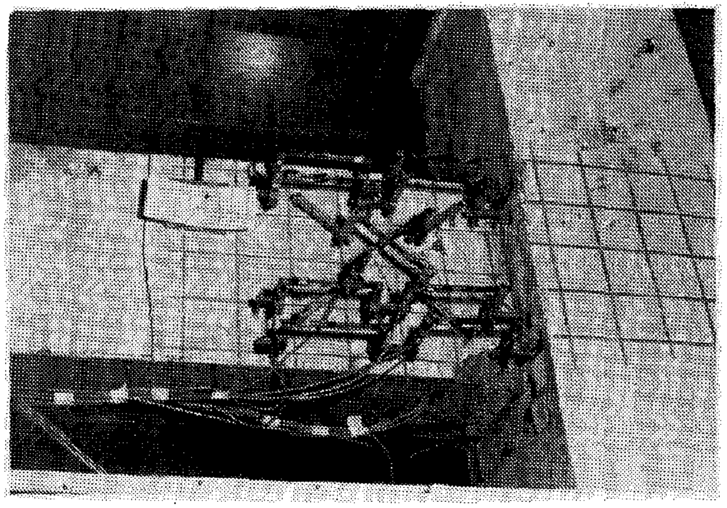

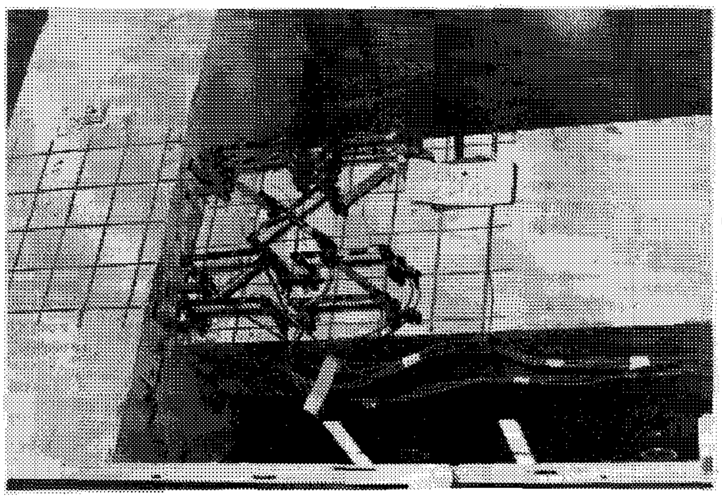

(b) East Beam

Fig. 3.6 Instrumentation Measuring Shear and Flexural Deformations

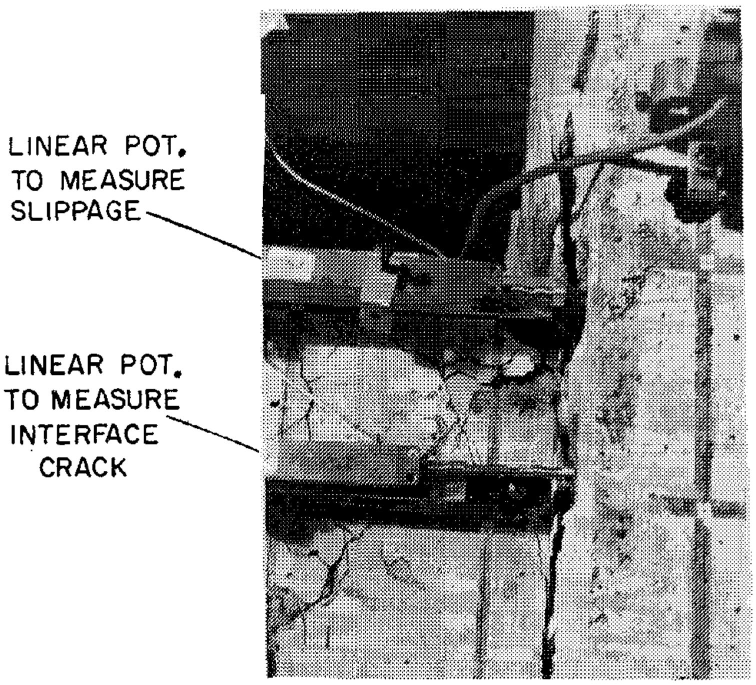

Fig. 3.7 Gages Measuring Rebar Slippage and Interface Crack Width

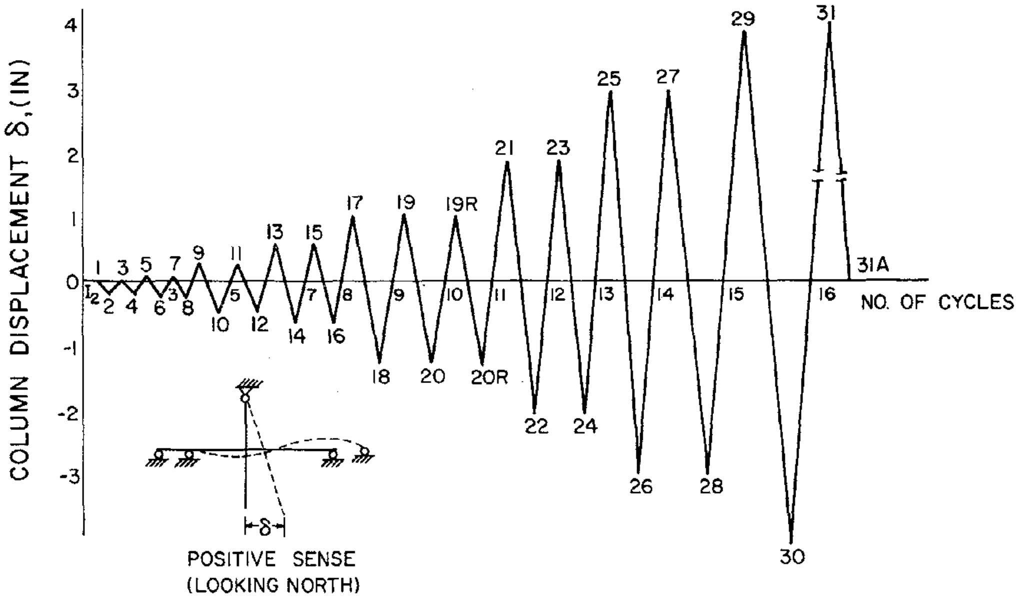

Fig. 3.8 Loading History for Specimen BC3

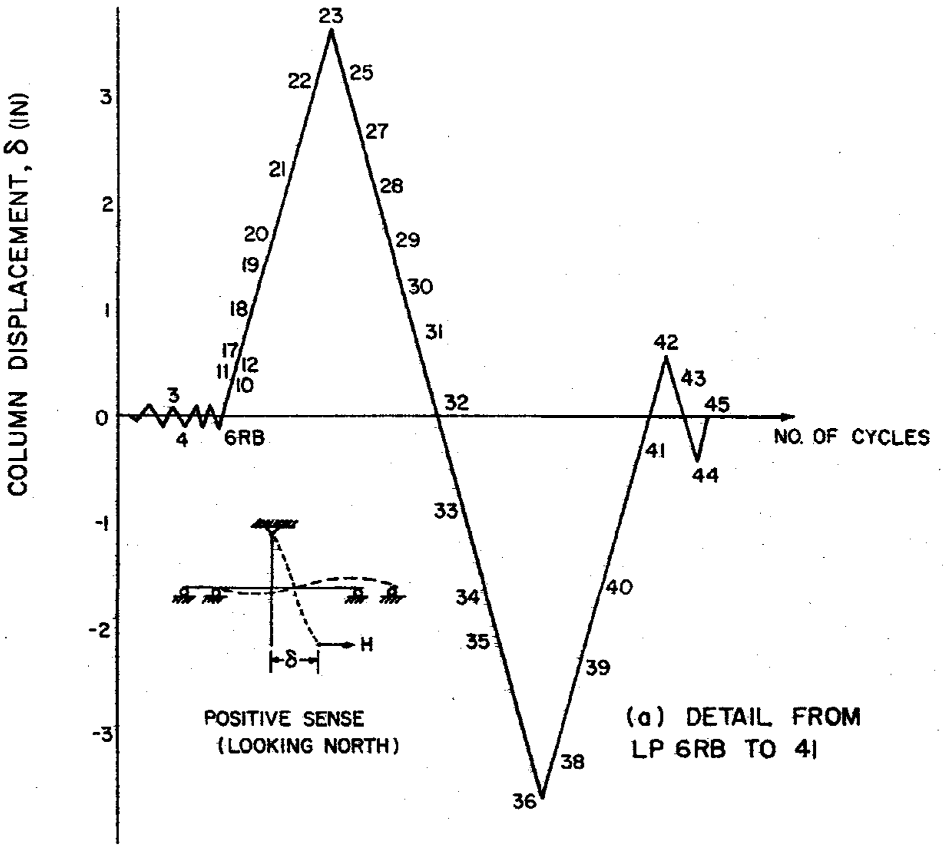

(a) DETAIL FROM LP 6RB TO 41

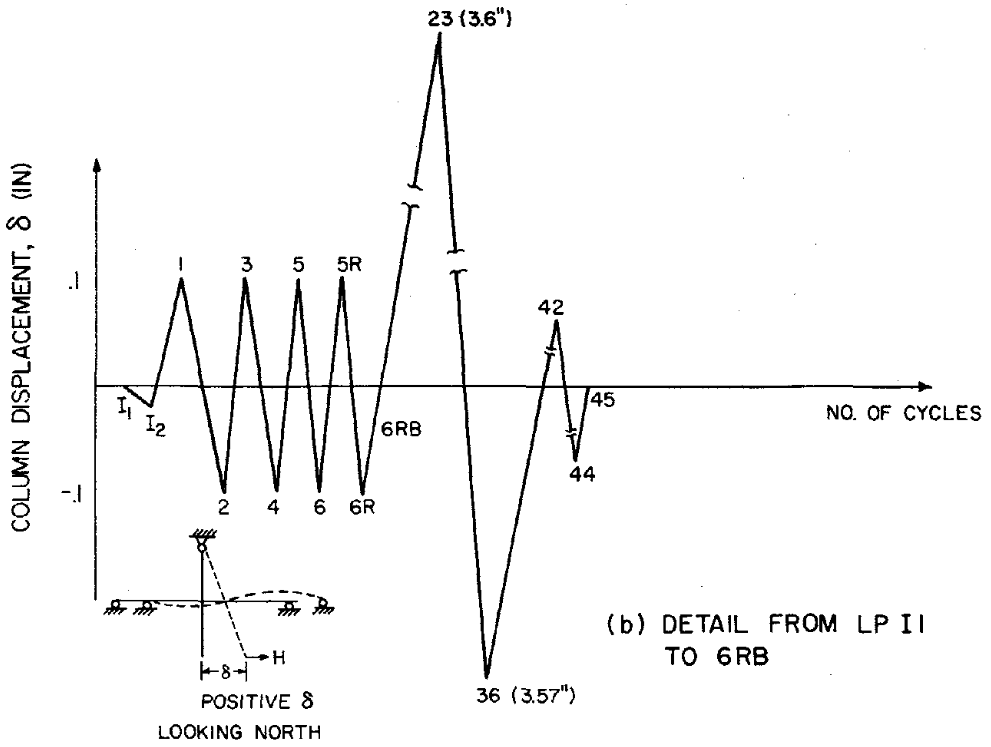

(b) DETAIL FROM LP I1 TO 6RB

Fig. 3.9 Loading History for Specimen BC4

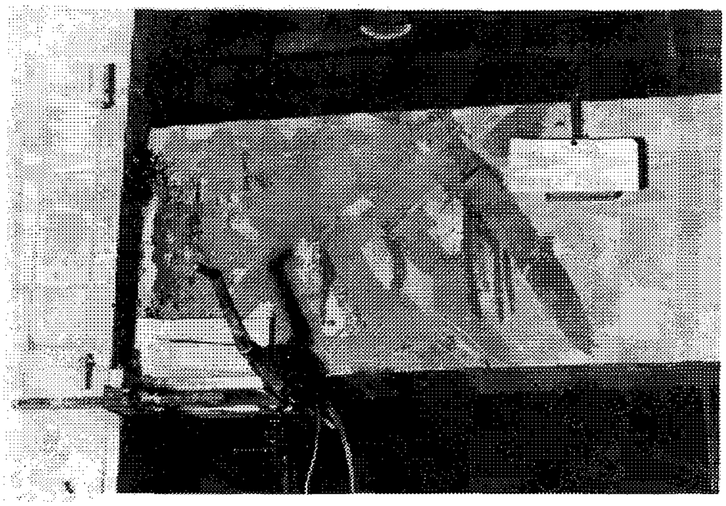

(a) BC4 After Sealing of Cracks

(b) Spalled Concrete Corner After Patching

Fig. 3.10 Epoxy Repair of Specimen BC4

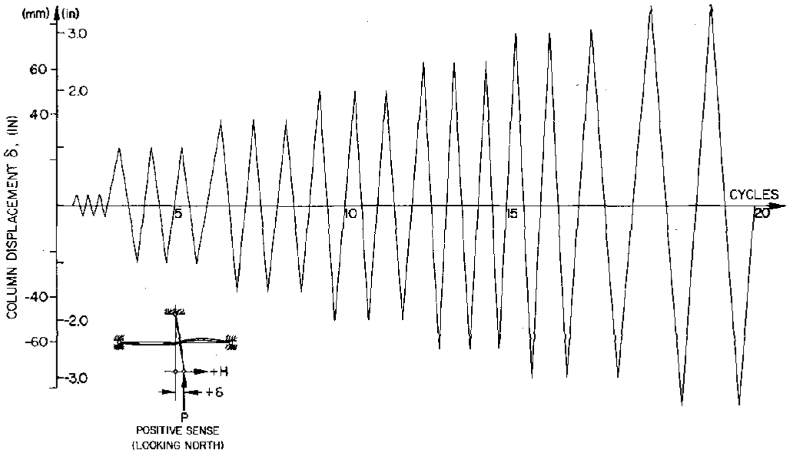

Fig. 3.11 Loading History for Specimen BC4E

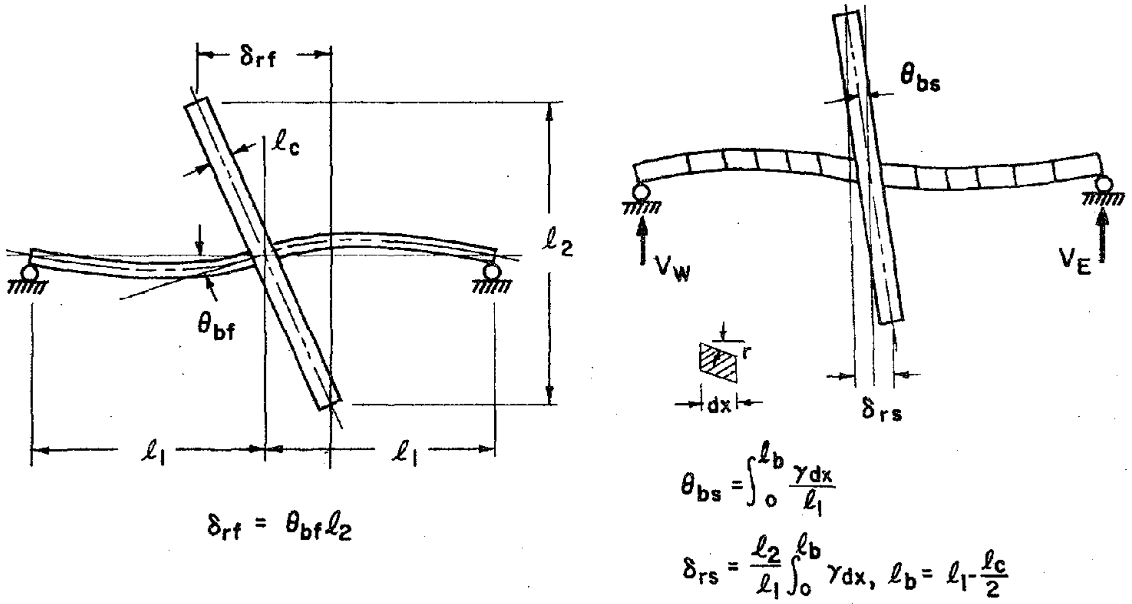

$\delta_{rf} = \theta_{bf}\ell_2$

$\theta_{bs} = \int_0^{\ell_b} \frac{\gamma dx}{\ell_1}$

$\delta_{rs} = \frac{\ell_2}{\ell_1}\int_0^{\ell_b} \gamma dx, \ \ell_b = \ell_1 - \frac{\ell_c}{2}$

(a) FLEXURAL DEFORMATION OF THE BEAMS

(b) SHEAR DEFORMATION OF THE BEAMS

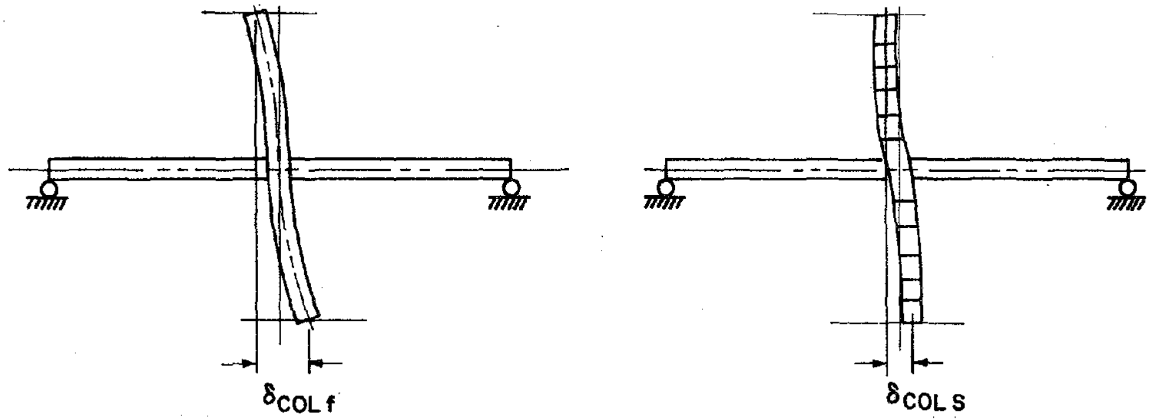

(c) FLEXURAL DEFORMATION OF COLUMNS

(d) SHEAR DEFORMATION OF COLUMNS

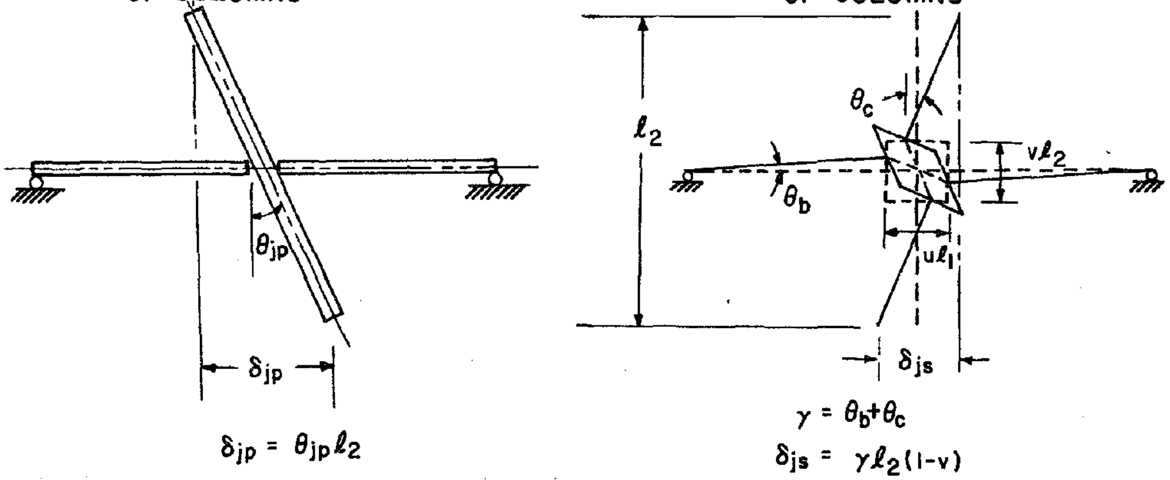

$\delta_{jp} = \theta_{jp}\ell_2$

$\gamma = \theta_b + \theta_c$

$\delta_{js} = \gamma\ell_2(1-v)$

(e) FIXED END DEFORMATION DUE TO PULL-OUT AT JOINT

(f) JOINT SHEAR DEFORMATION (SIZE OF THE JOINT IS EXAGGERATED)

Fig. 4.1 Components of Horizontal Displacement, δ

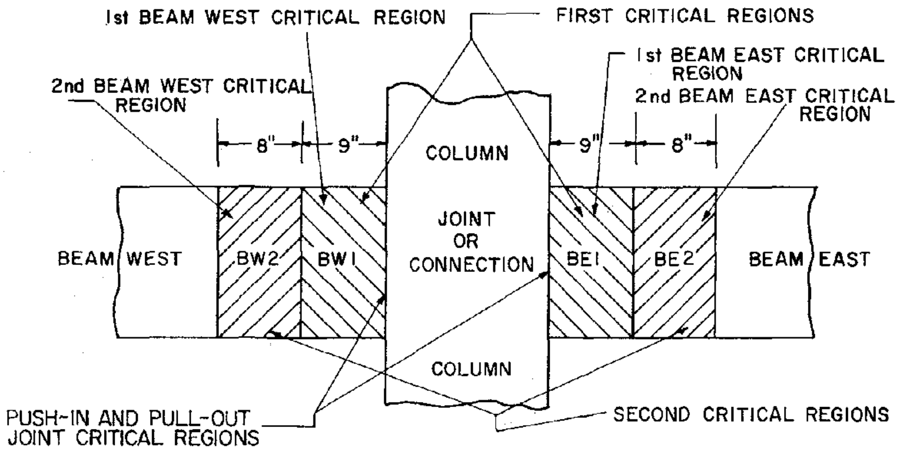

Fig. 4.2 Critical Regions in Beam-Column Connection

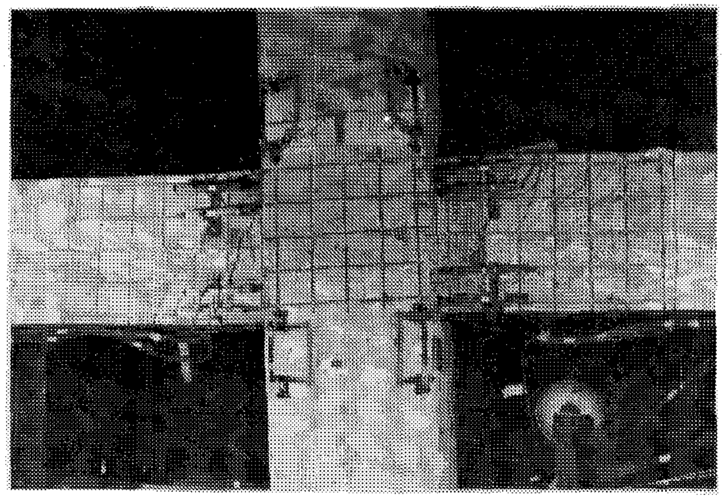

Fig. 4.3 Deformed Shape of Subassemblage BC4 at LP 23

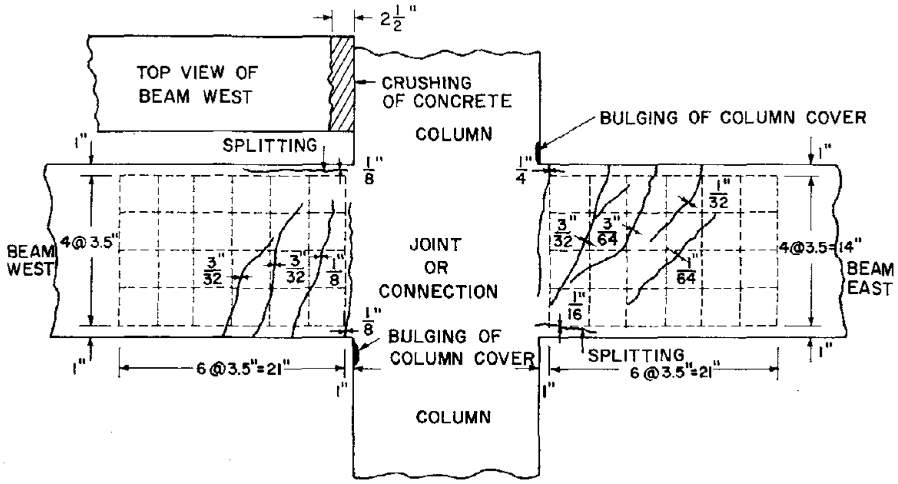

Fig. 4.4 Major Cracks in Subassemblage BC4 at LP 23

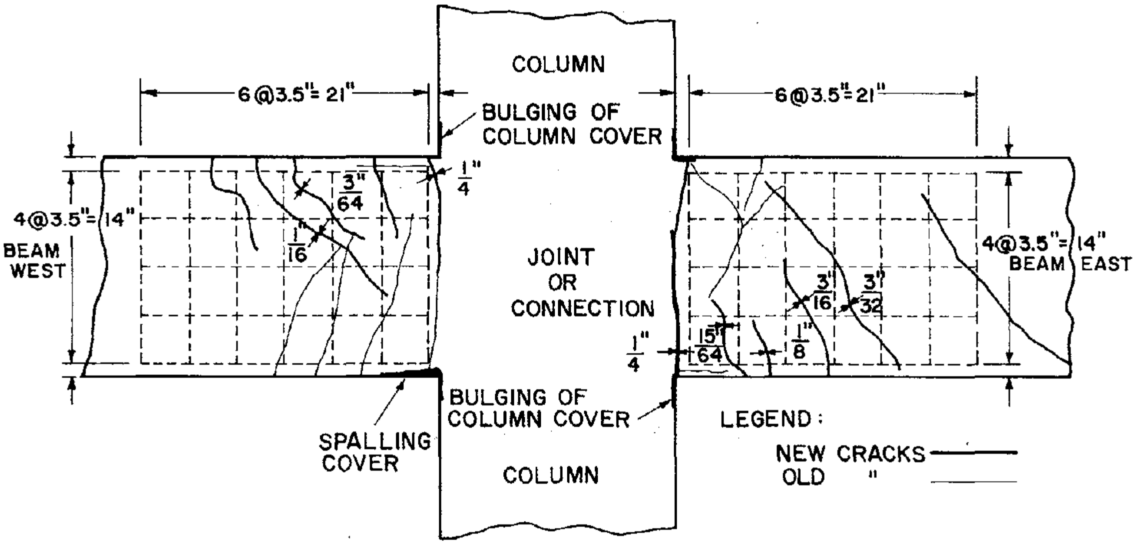

Fig. 4.5 Major Cracks in Subassemblage BC4 at LP 36

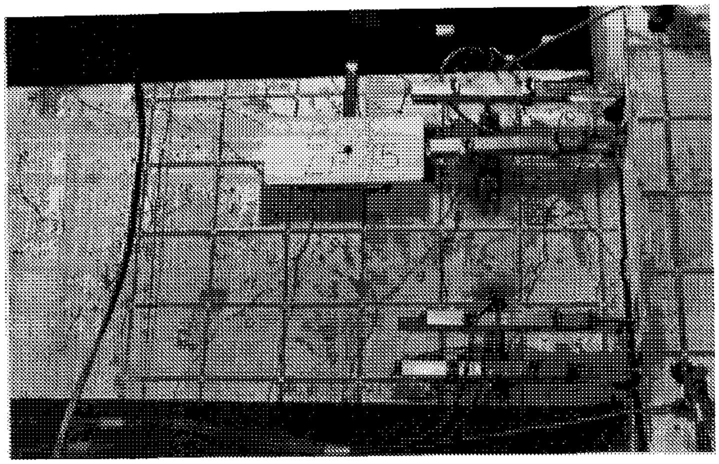

(a) West Beam

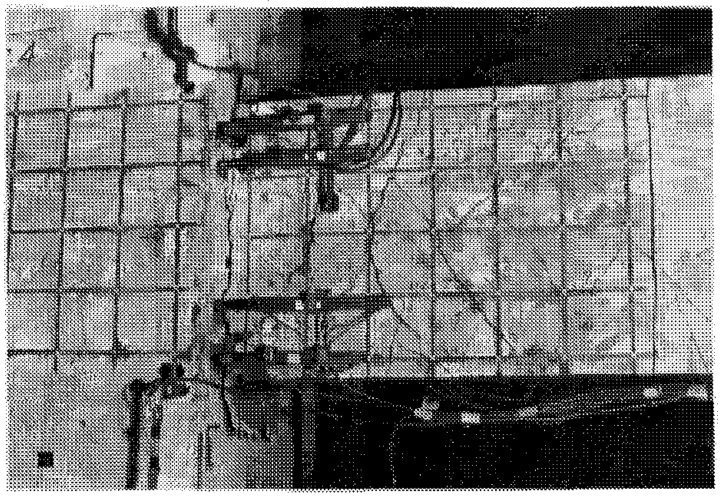

(b) East Beam

Fig. 4.6 Critical Beam Regions at LP 45, Prior to Epoxy Repair

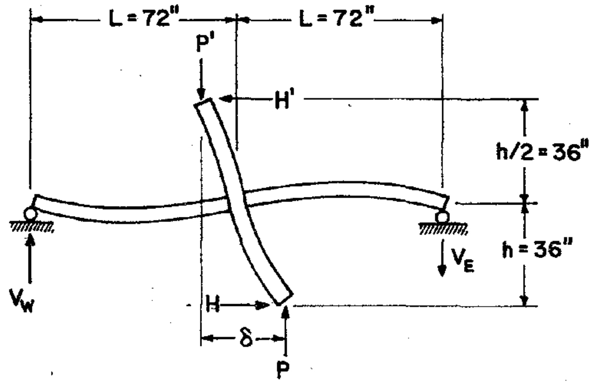

Fig. 4.7 Definition of Positive Forces and Displacements for Subassemblage

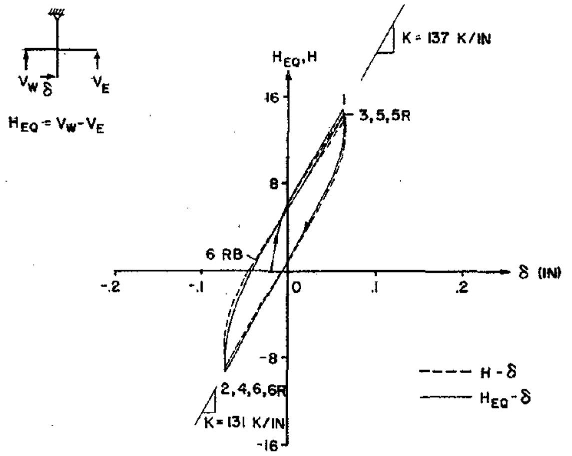

(a) UNDER SERVICE LOAD CONDITIONS

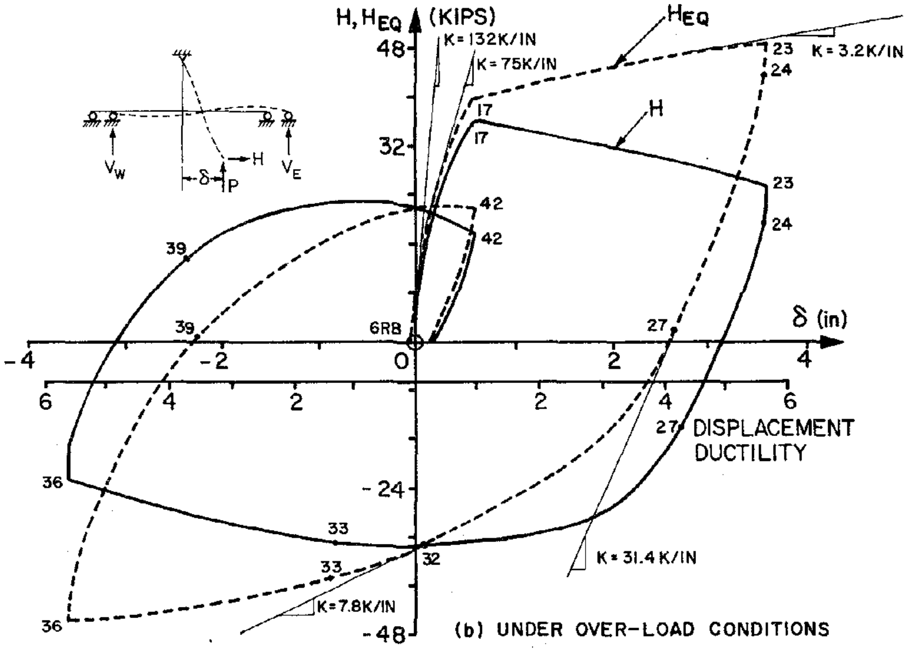

(b) UNDER OVER-LOAD CONDITIONS

Fig. 4.8 $H_{EQ} - \delta$, $H - \delta$ for Specimen BC4

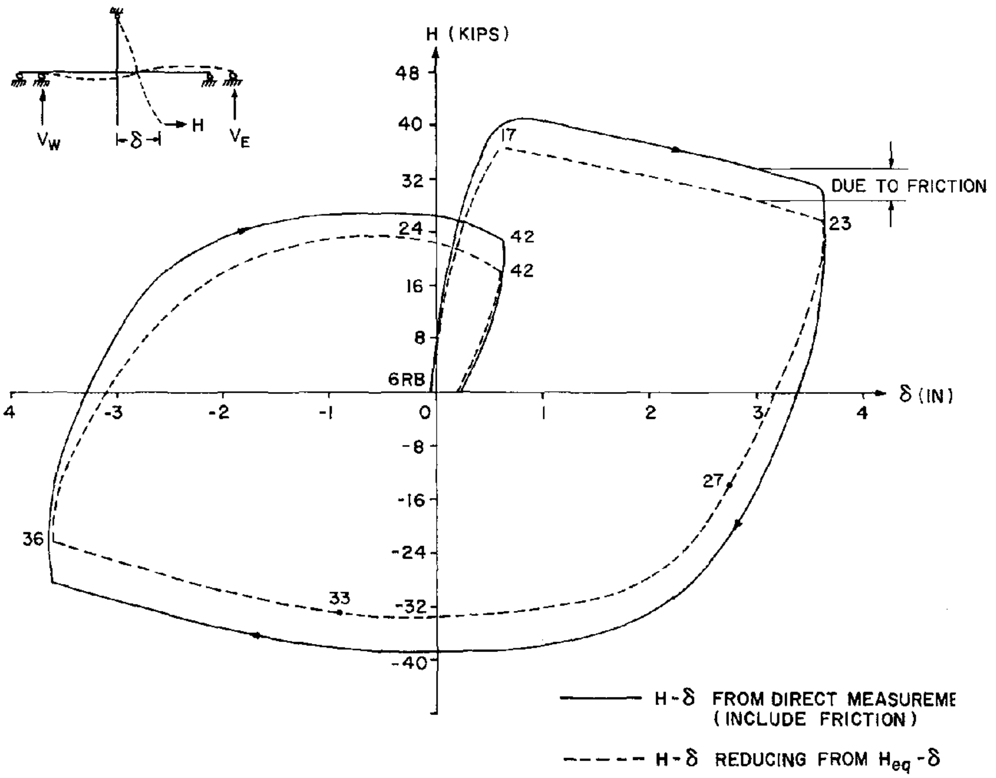

Fig. 4.9 Comparison Between Measured H-δ and H-δ Curve Reduced from H_{EQ}-δ

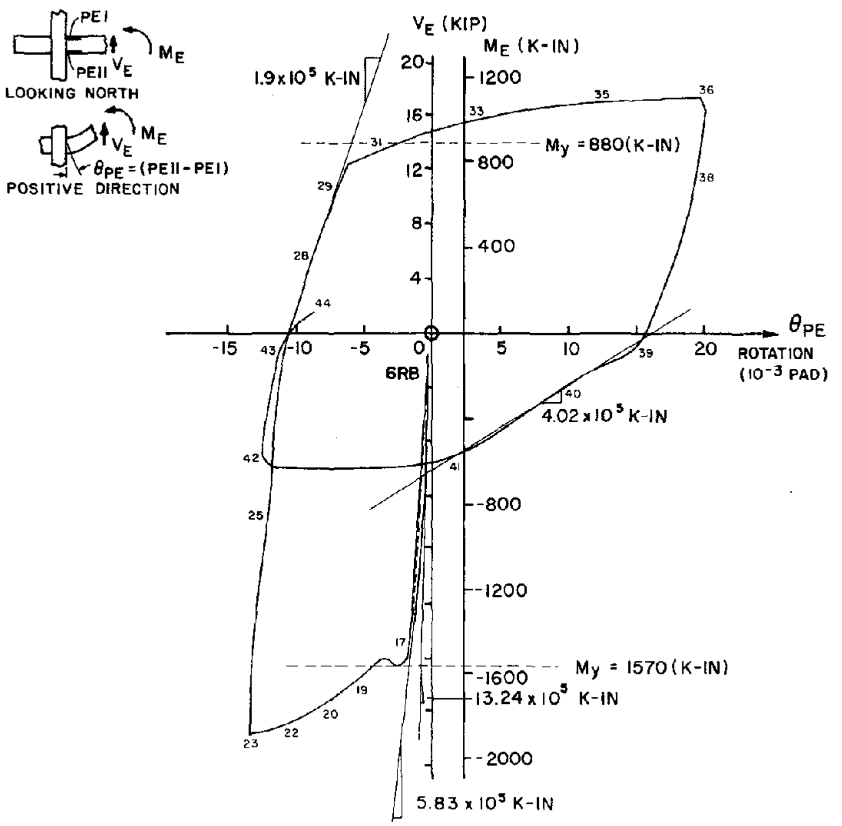

Fig. 4.10 M_E-θ_{PE} Diagram for Specimen BC4

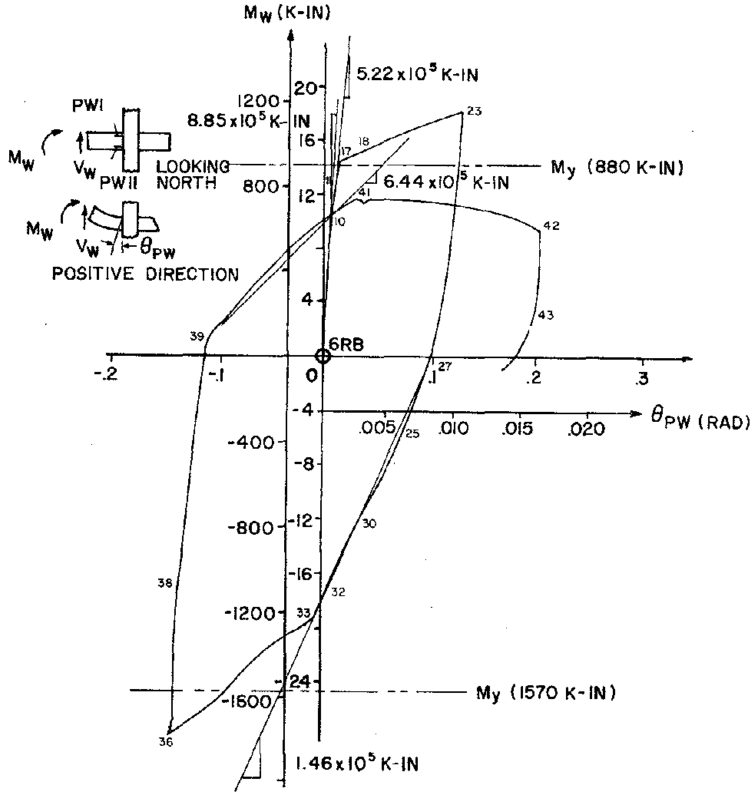

Fig. 4.11 $M_W - \theta_{PW}$ Diagram for Specimen BC4

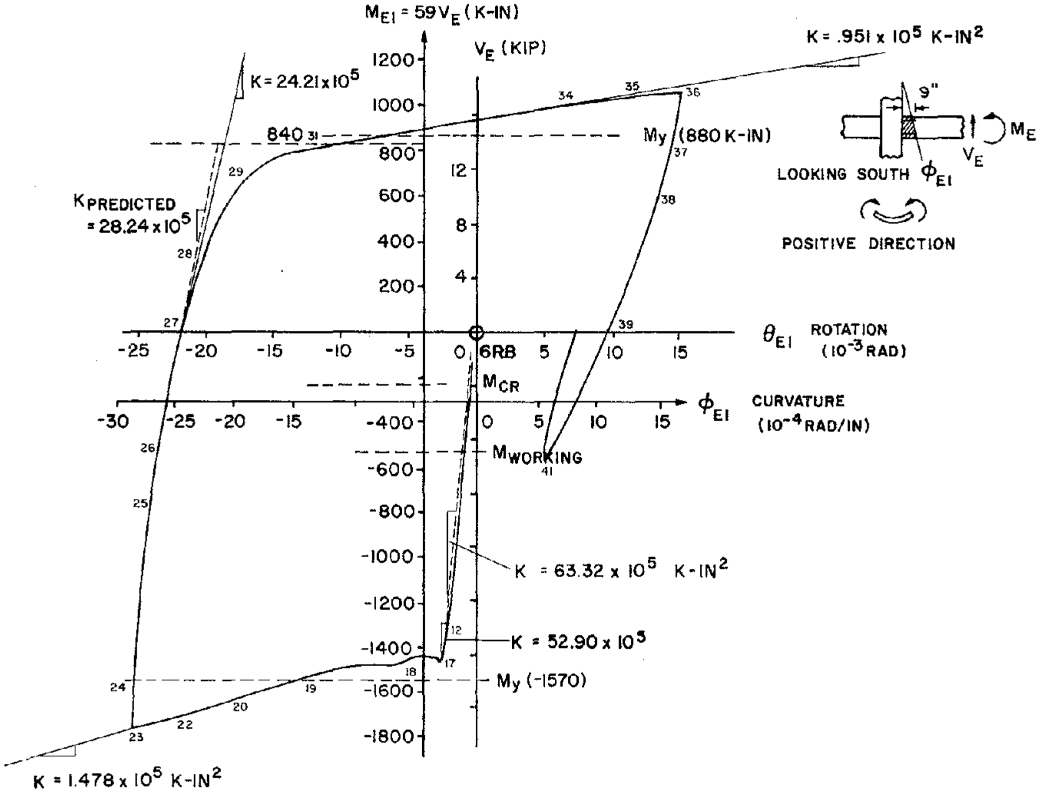

Fig. 4.12 $M_{E1} - \phi_{E1}$ Diagram for Specimen BC4

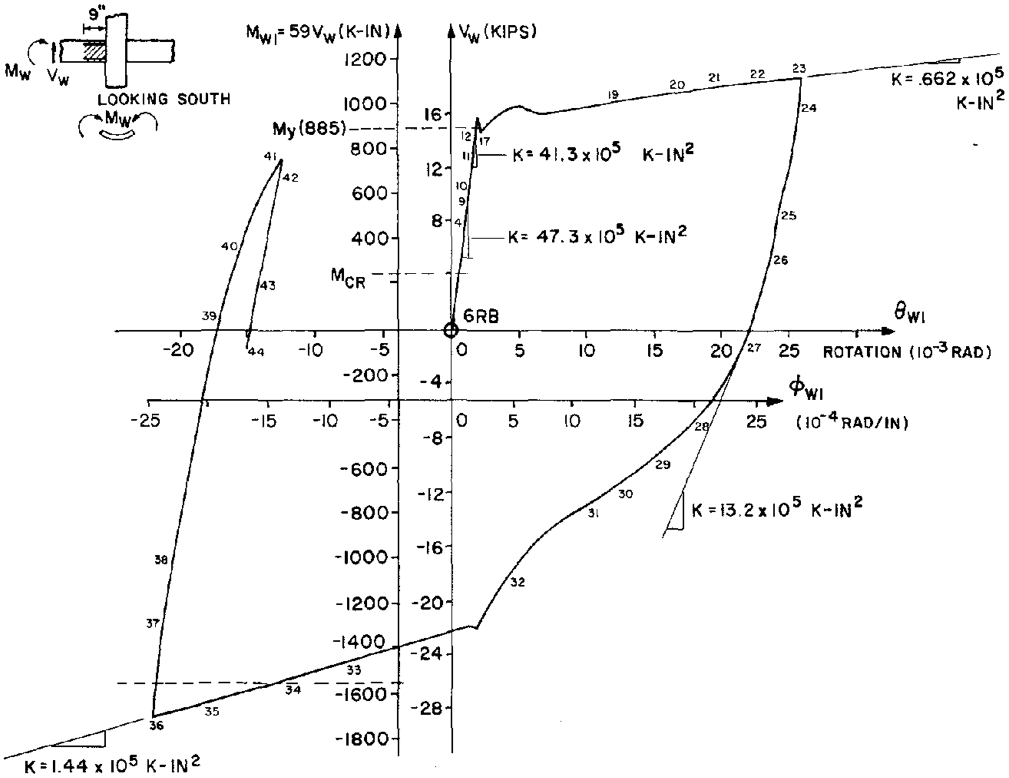

Fig. 4.13 $M_{W1} - \phi_{W1}$ Diagram for Specimen BC4

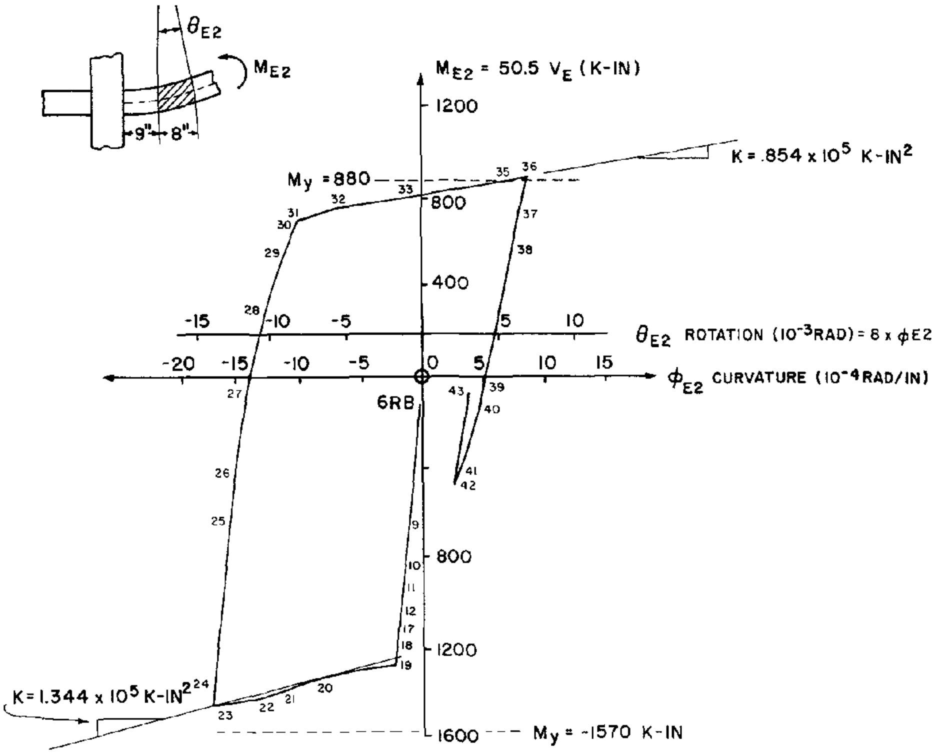

Fig. 4.14 $M_{E2} - \phi_{E2}$ Diagram for Specimen BC4

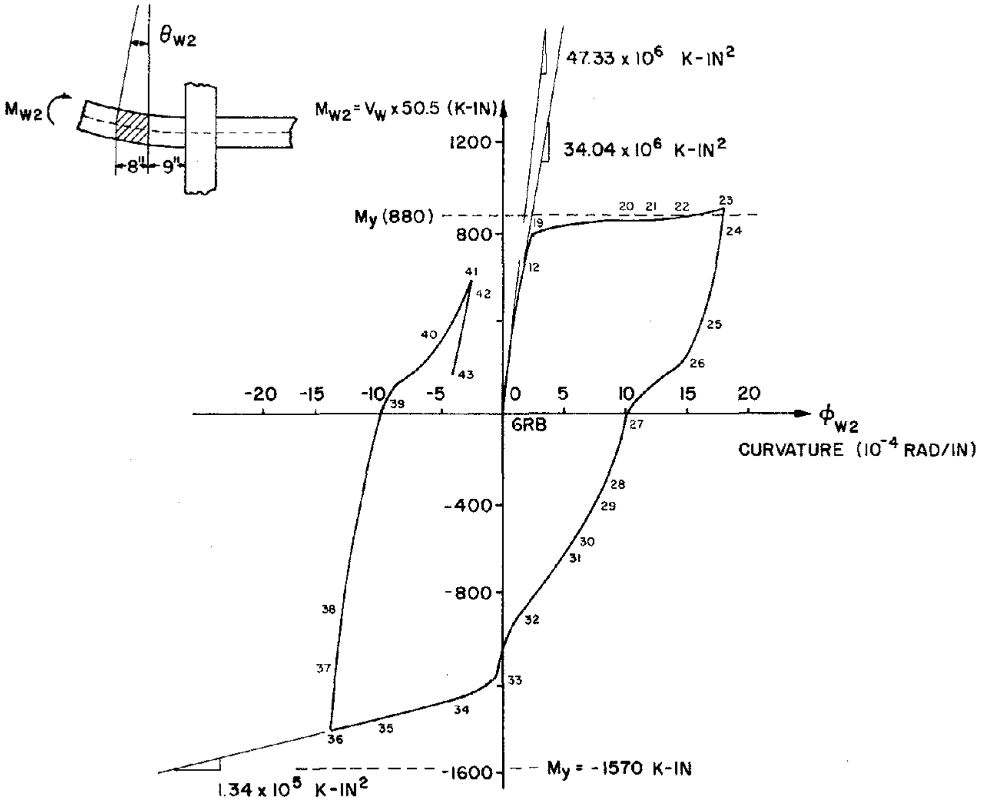

Fig. 4.15 $M_{W2}-\phi_{W2}$ Diagram for Specimen BC4

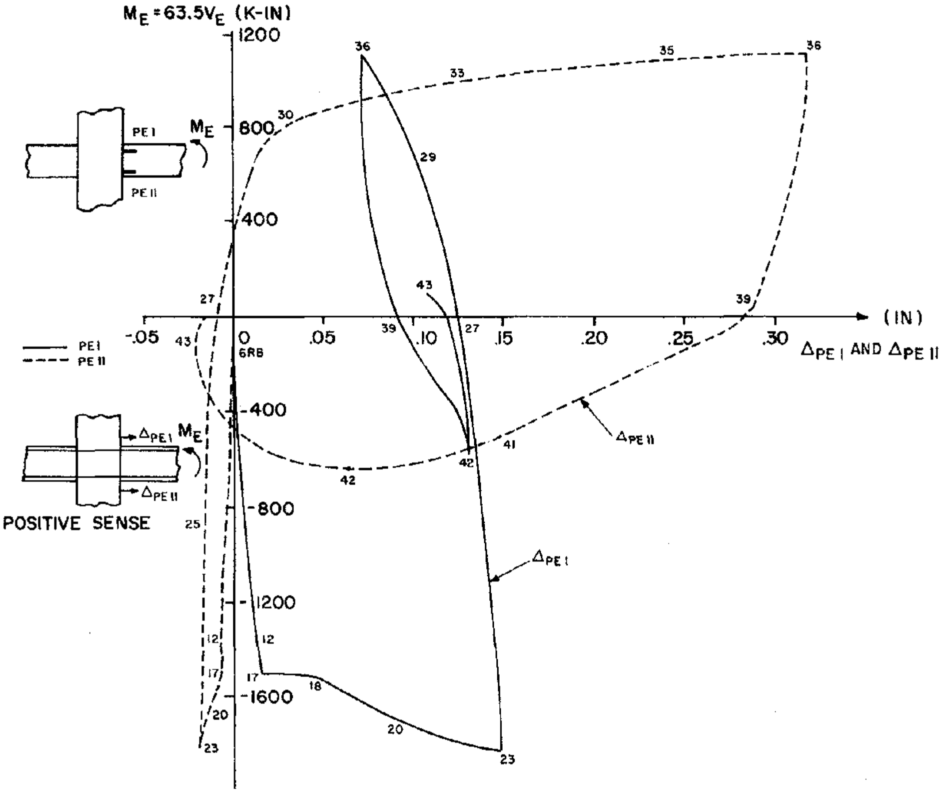

Fig. 4.16 Anchorage Slip of Top and Bottom Rebars, for the East Beam, Specimen BC4

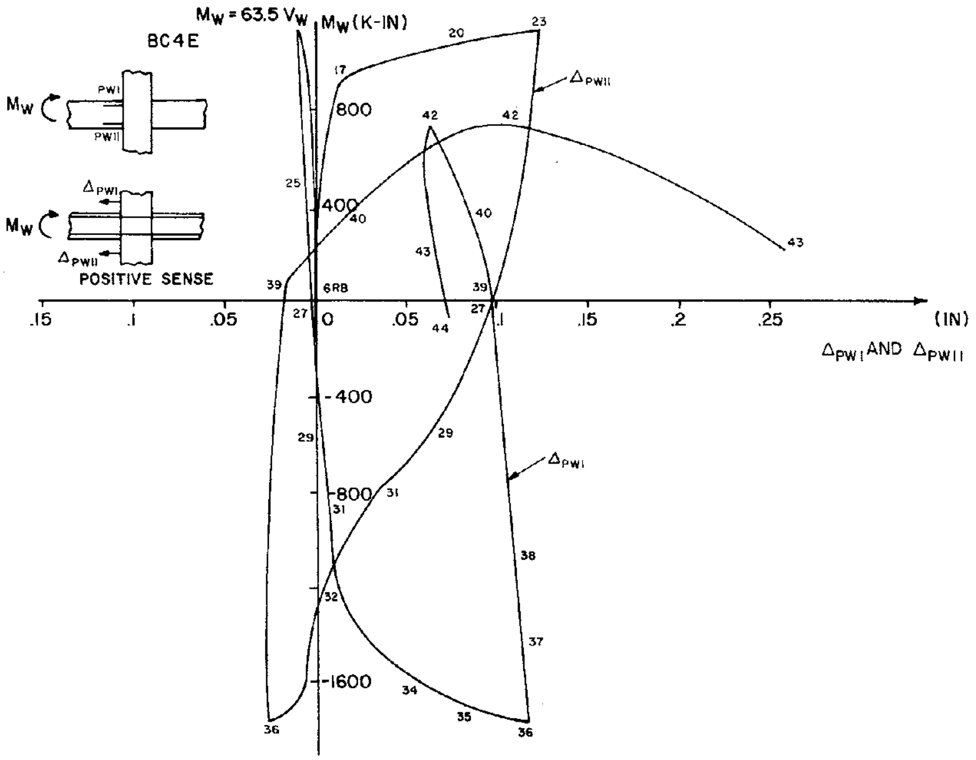

Fig. 4.17 Anchorage Slip of Top and Bottom Rebars, for the West Beam, Specimen BC4

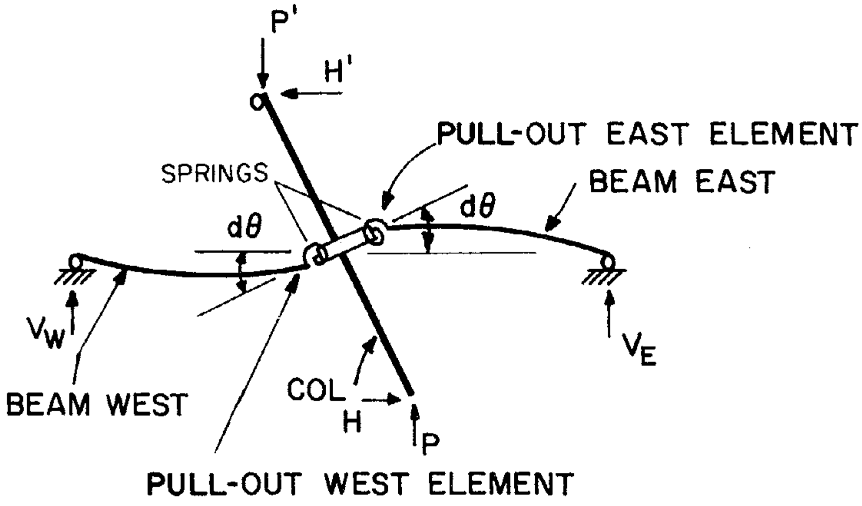

Fig. 4.18 Idealized Mechanical Behavior of Subassemblage

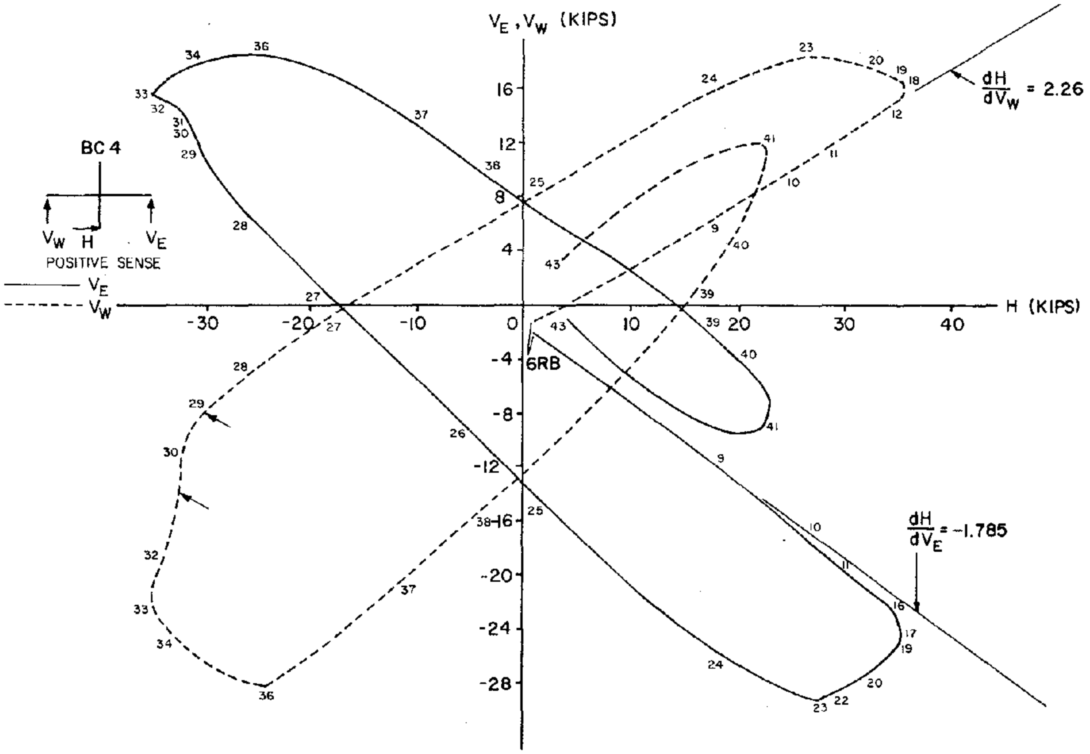

Fig. 4.19 H - V_E and H - V_W Diagrams for Specimen BC4

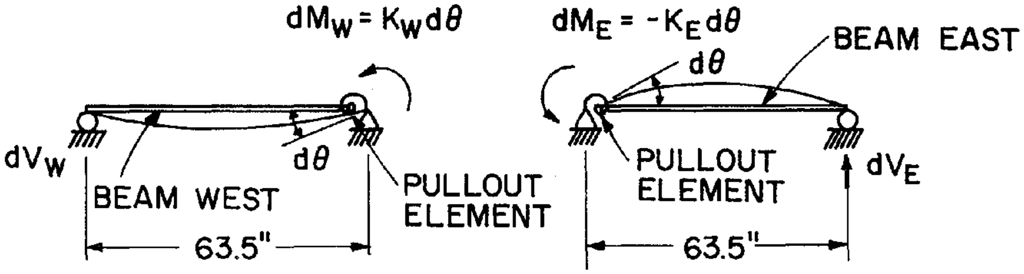

Fig. 4.20 Definition of Beam Stiffness for Incremental Rotation

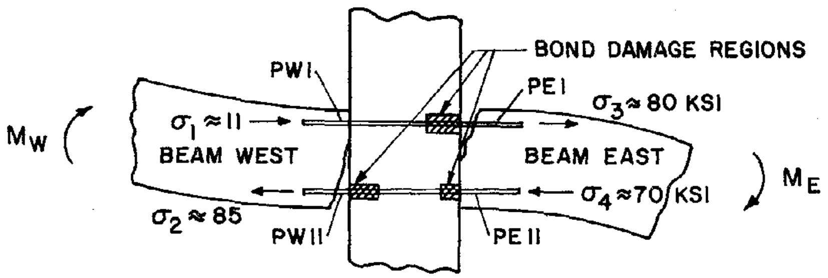

(a) AT LP 23

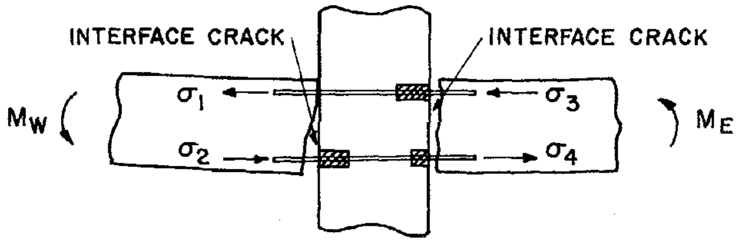

(b) FROM LP 27-31

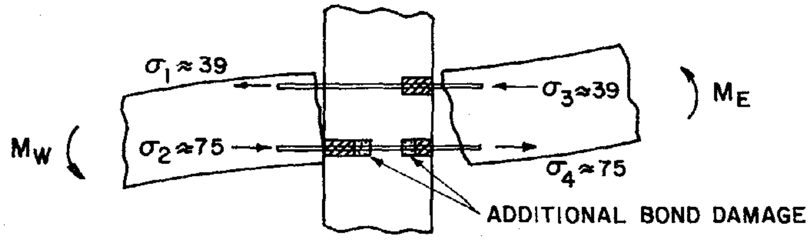

(c) AT LP 32

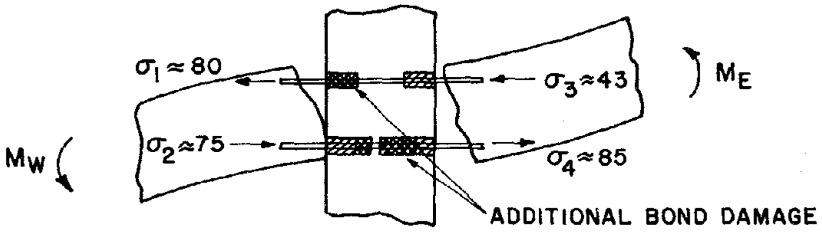

(d) AT LP 36

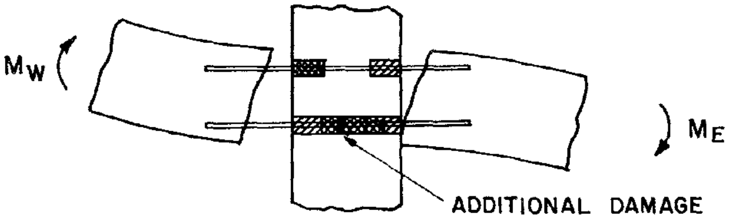

(e) AT LP 42

Fig. 4.21 Illustrations of Hypothetical Bond Deteriorations of Beam Rebars in the Joint

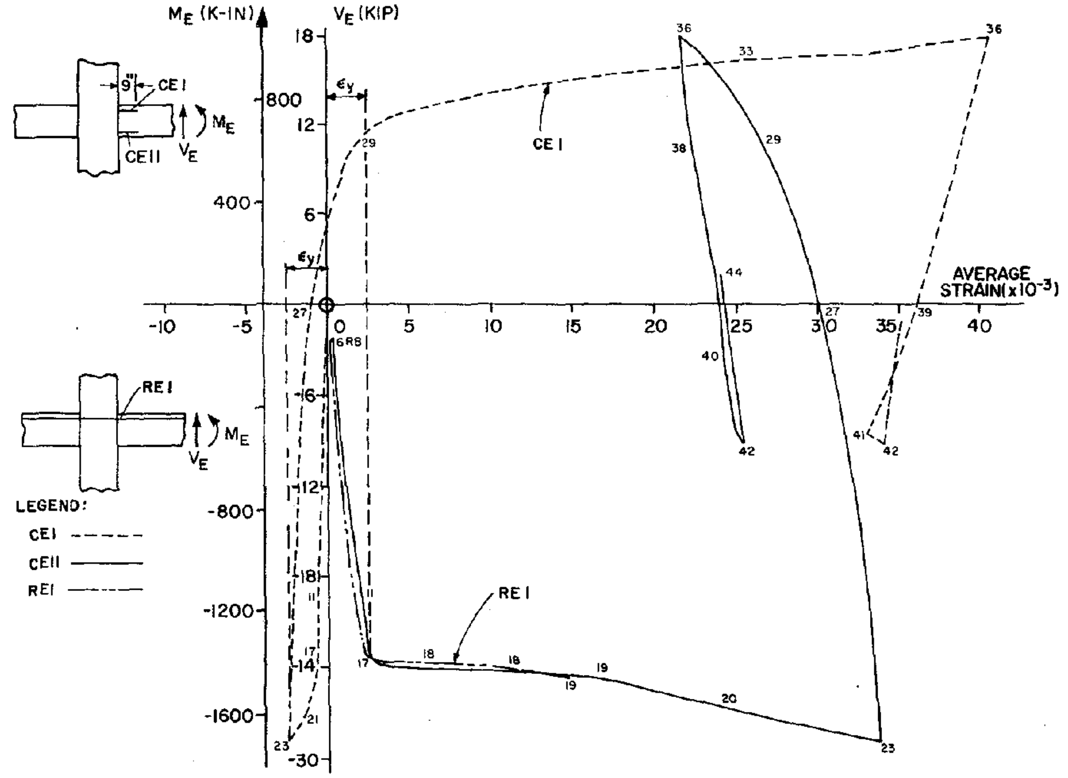

Fig. 4.22 M_E vs. Strains in Rebars of Specimen BC4

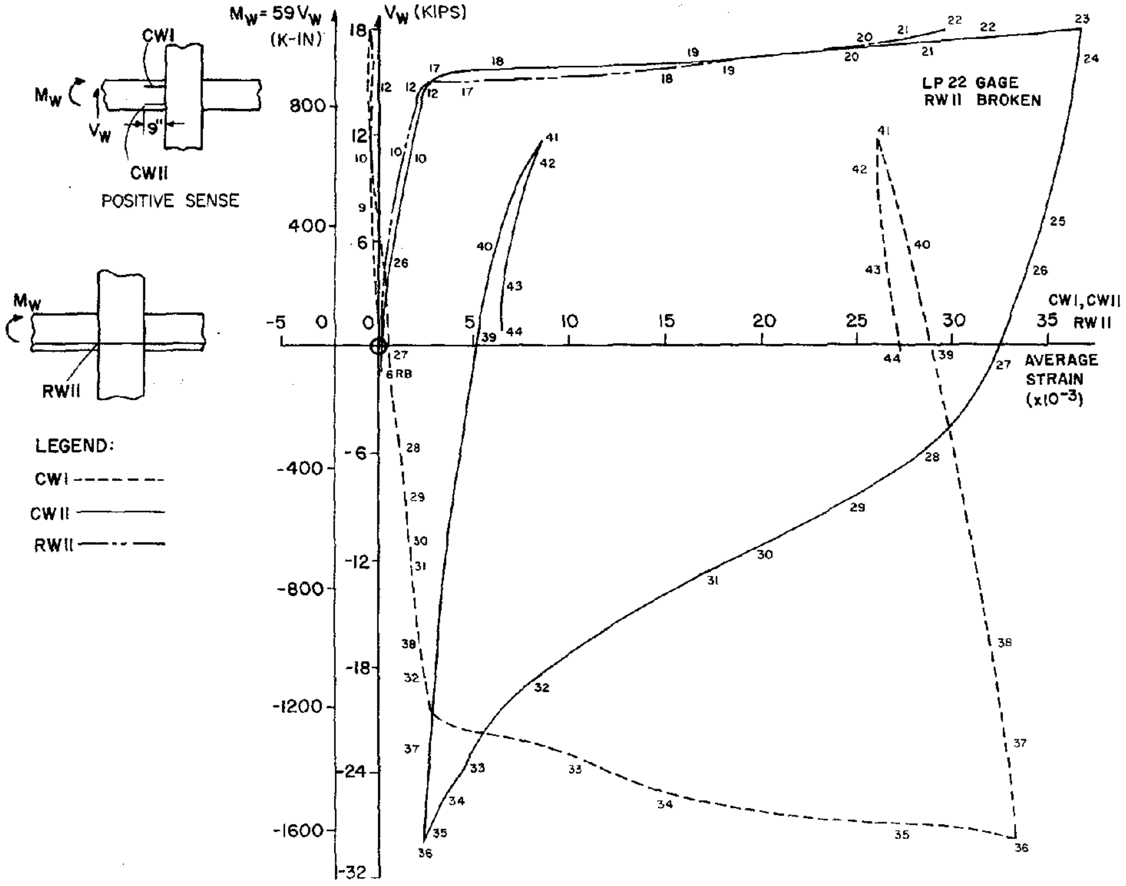

Fig. 4.23 M_W vs. Strains in Rebars of Specimen BC4

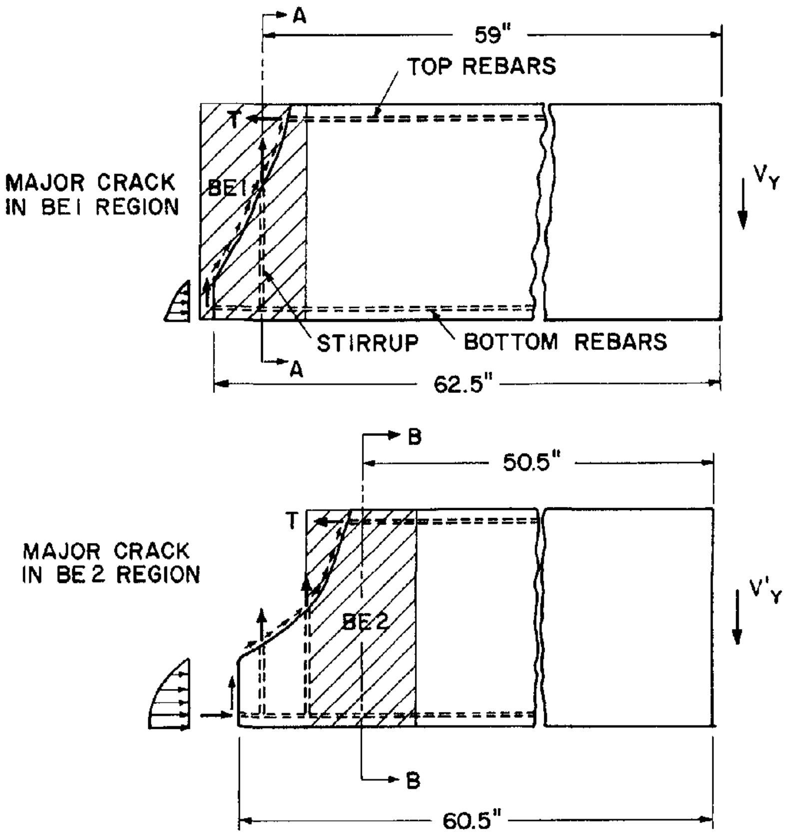

Fig. 4.24 Free-Body Diagram Along Major Cracks at Yield

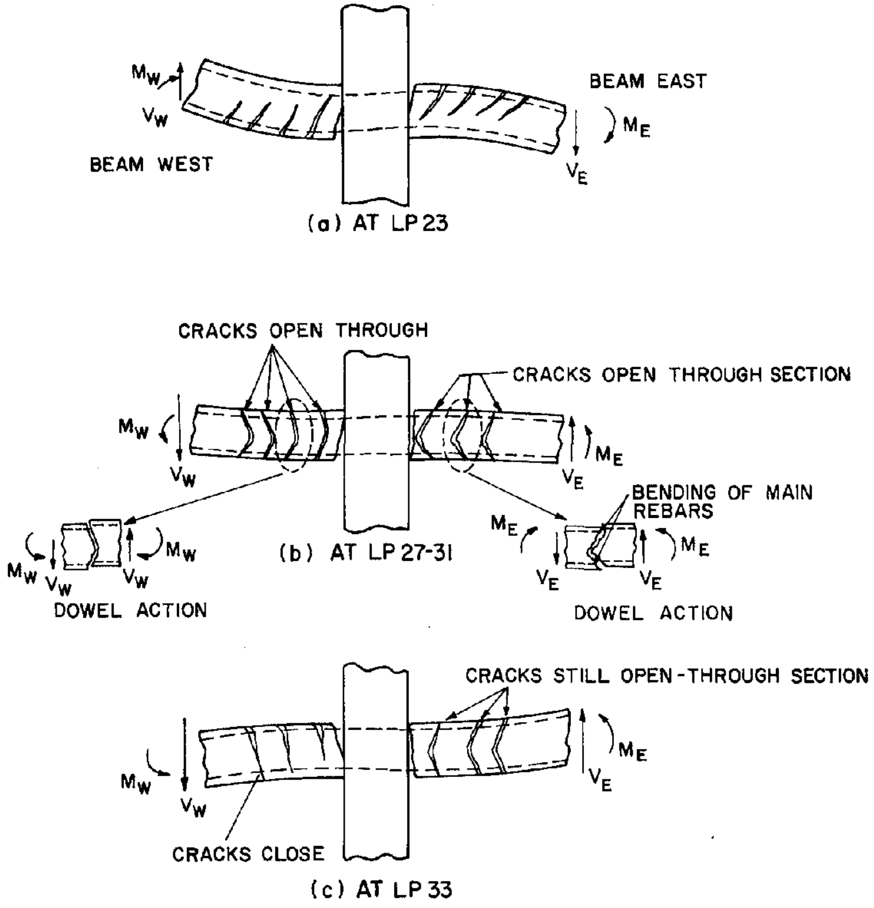

Fig. 4.25 Deformation of Critical Beam Regions at Load Reversal (LP 27-33)

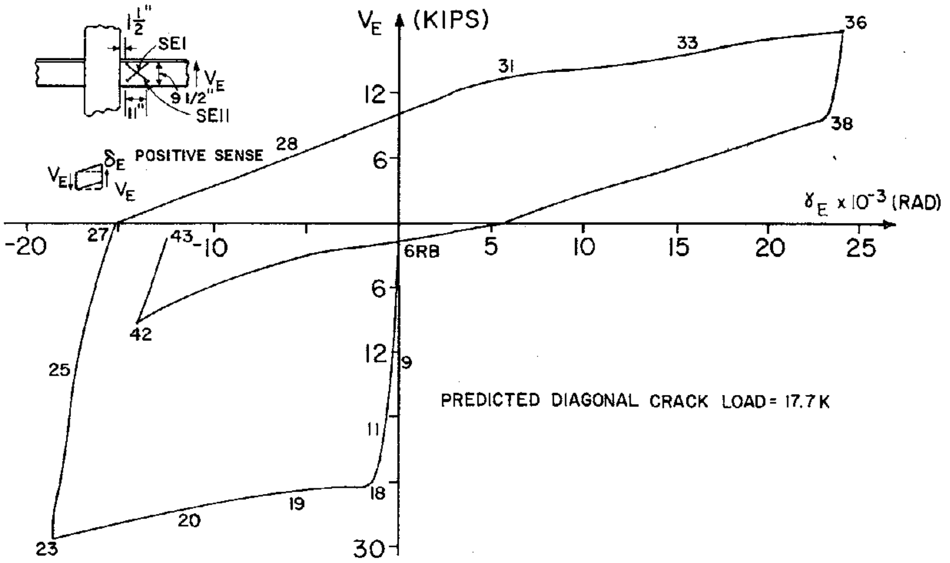

Fig. 4.26 Shear vs. Shear Distortion of the First Critical Region in the East Beam, Specimen BC4

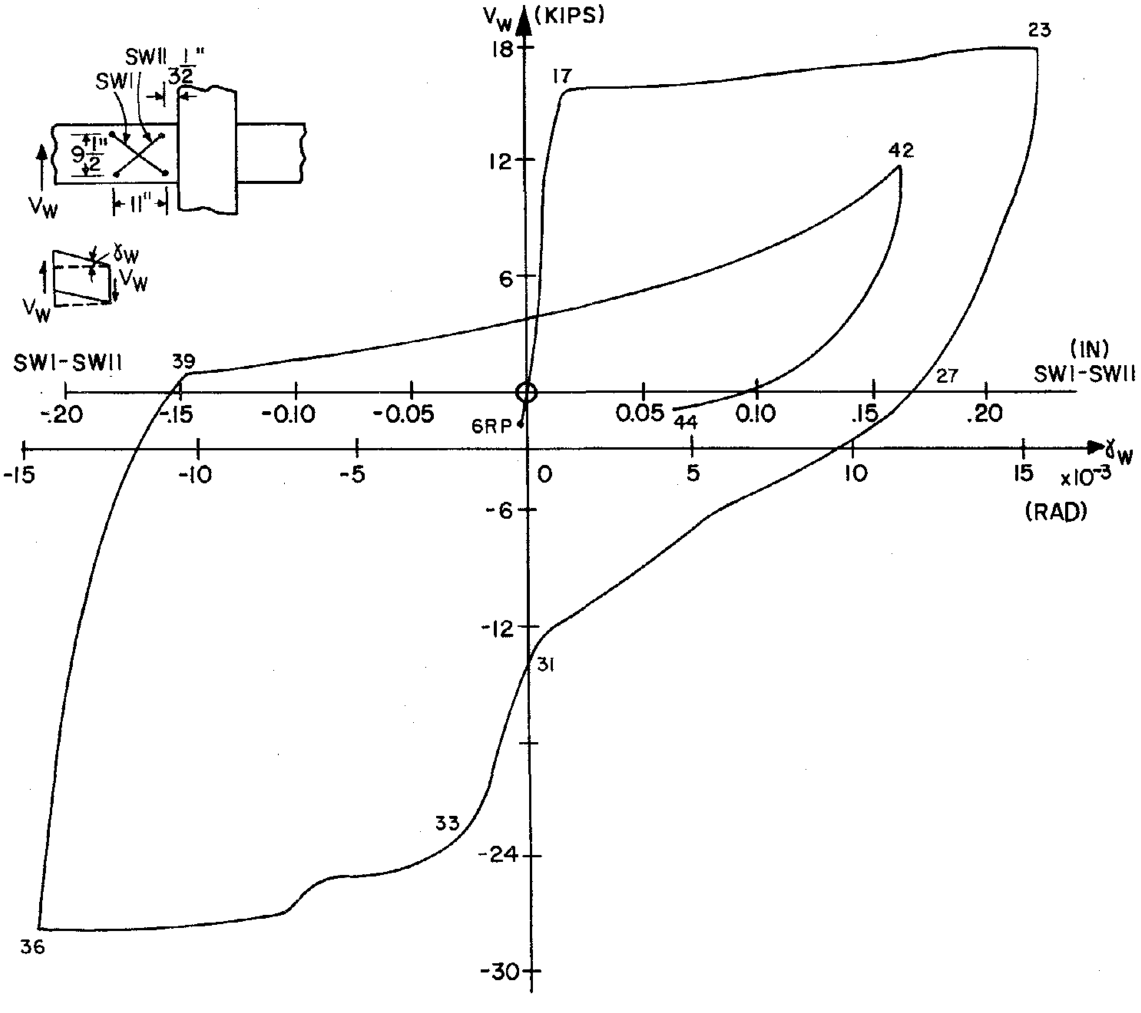

Fig. 4.27 Shear vs. Shear Distortion of the First Critical Region in the West Beam, Specimen BC4

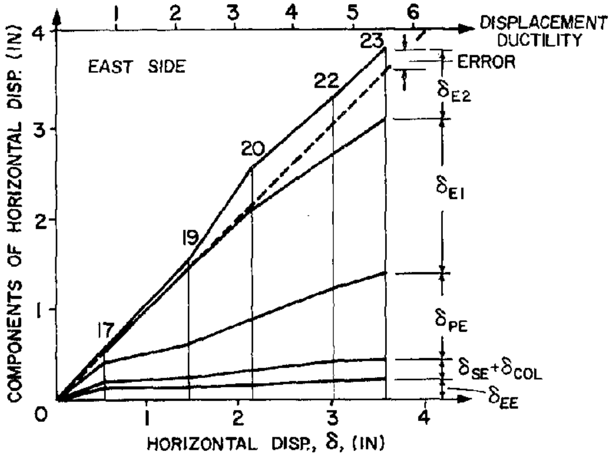

(a) LP 6RB-23

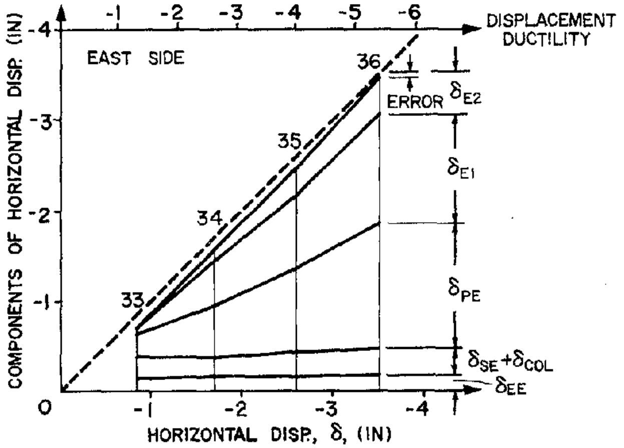

(b) LP 33-36

Fig. 4.28(a,b) Contributions to Horizontal Displacement, δ, from the East Beam

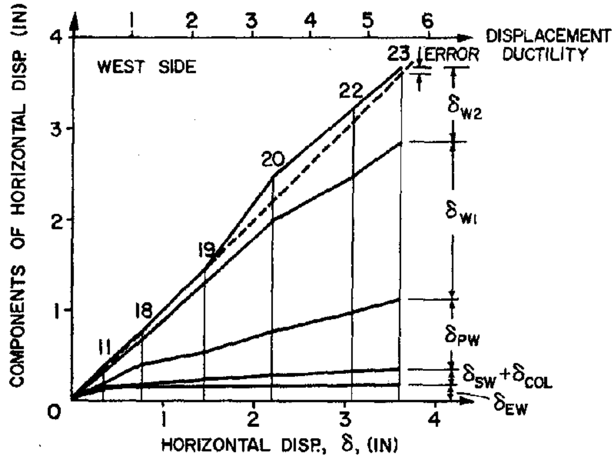

(c) LP 6RB-23

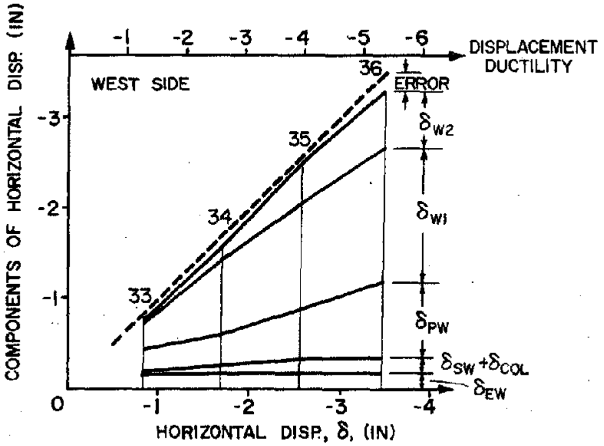

(d) LP 33-36

Fig. 4.28(c,d) Contributions to Horizontal Displacement, δ, from the West Beam

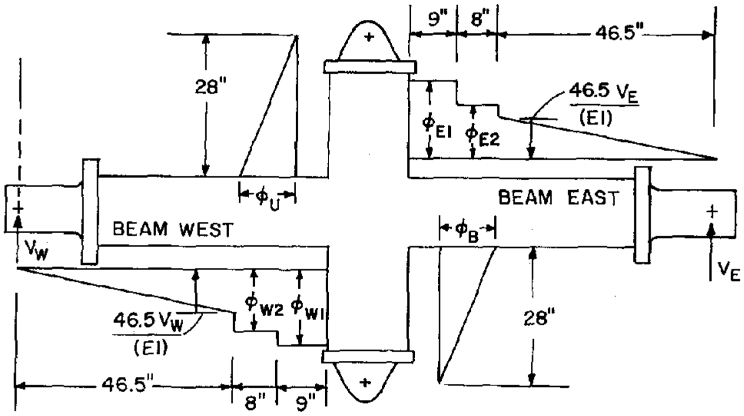

Fig. 4.29 Assumed Curvature Distribution Along the Beams and Columns

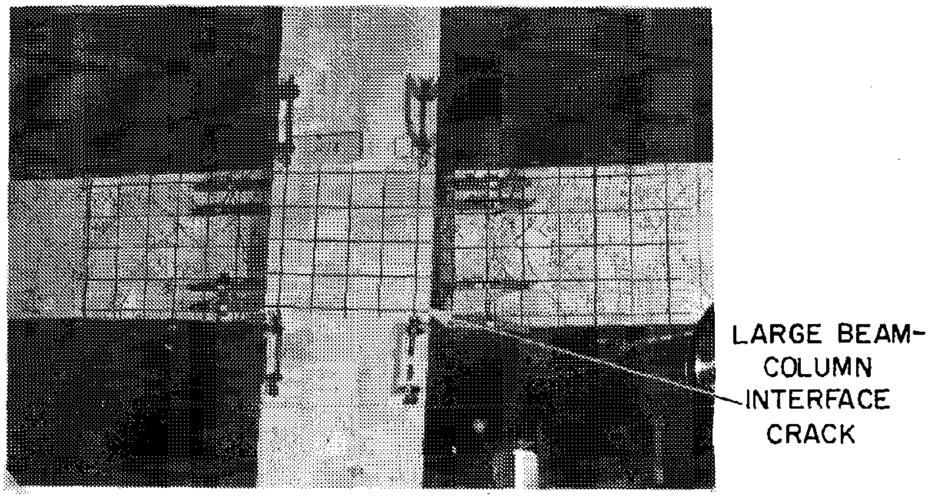

(a) Deformed Subassemblage Shape and Crack Patterns

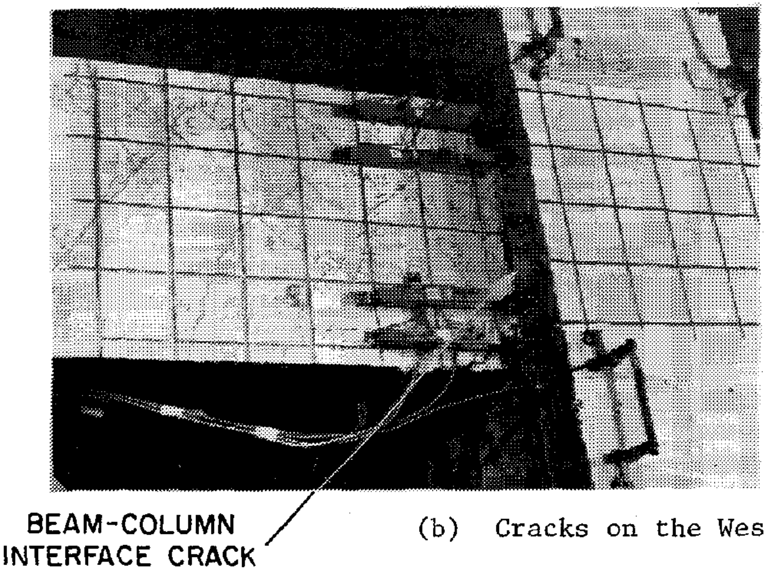

(b) Cracks on the West Beam

Fig. 5.1 Deflected Shape and Crack Patterns, Specimen BC4E

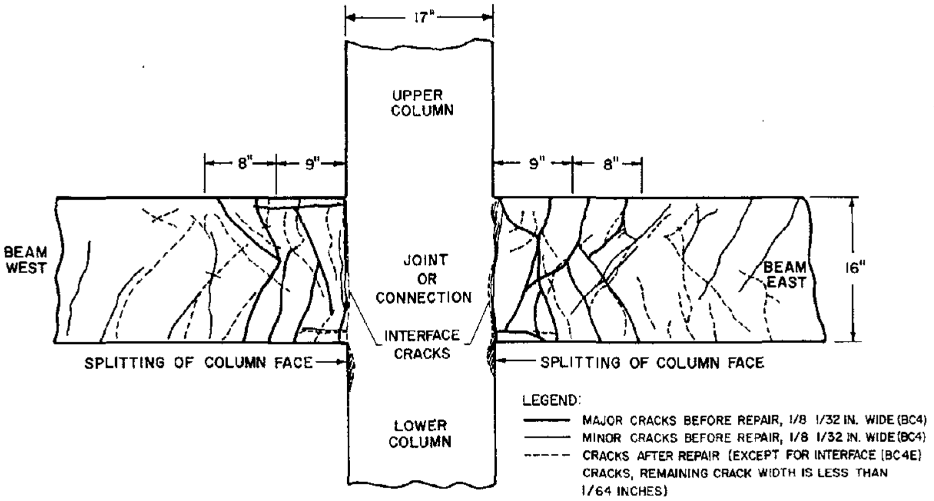

Fig. 5.2 Crack Patterns Before and After Epoxy Repair

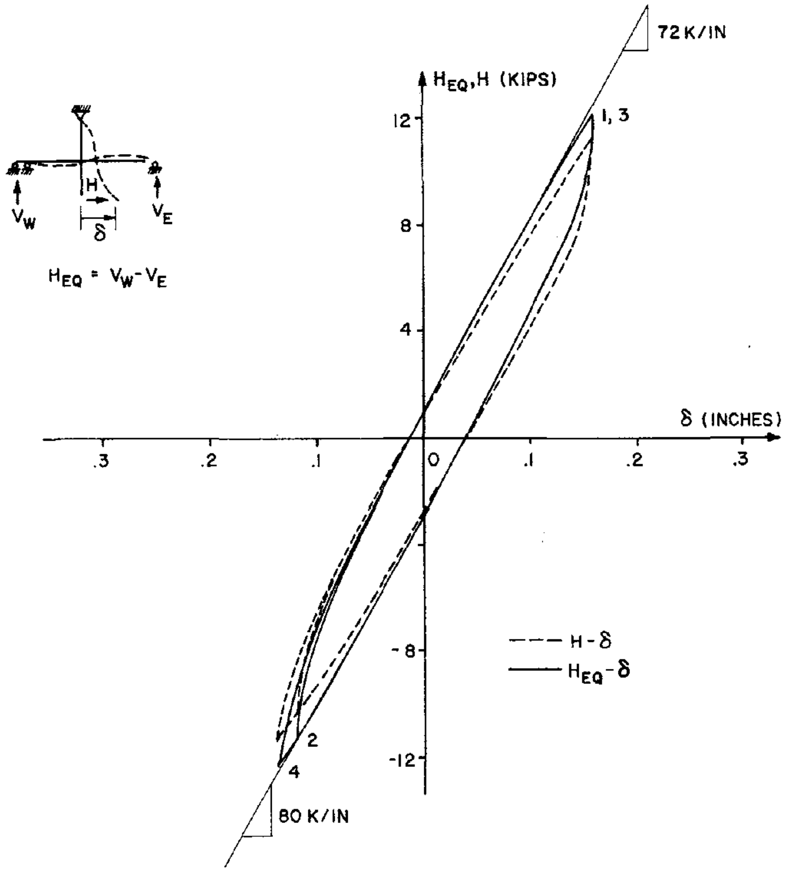

Fig. 5.3 H-δ and H_{EQ}-δ Diagrams for Specimen BC4E at Small Displacements

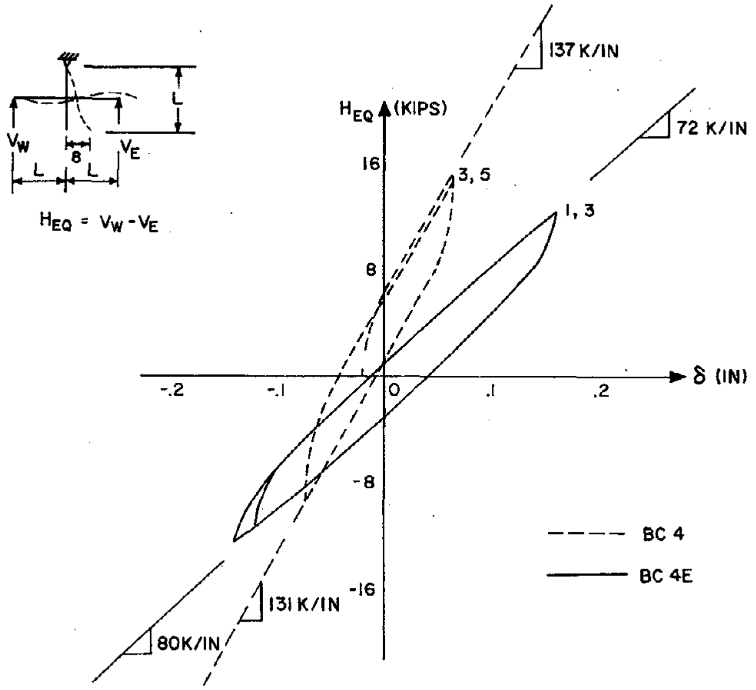

Fig. 5.4 H_{EQ}-δ Diagram Before and After Epoxy Repair at Small Displacement Amplitude

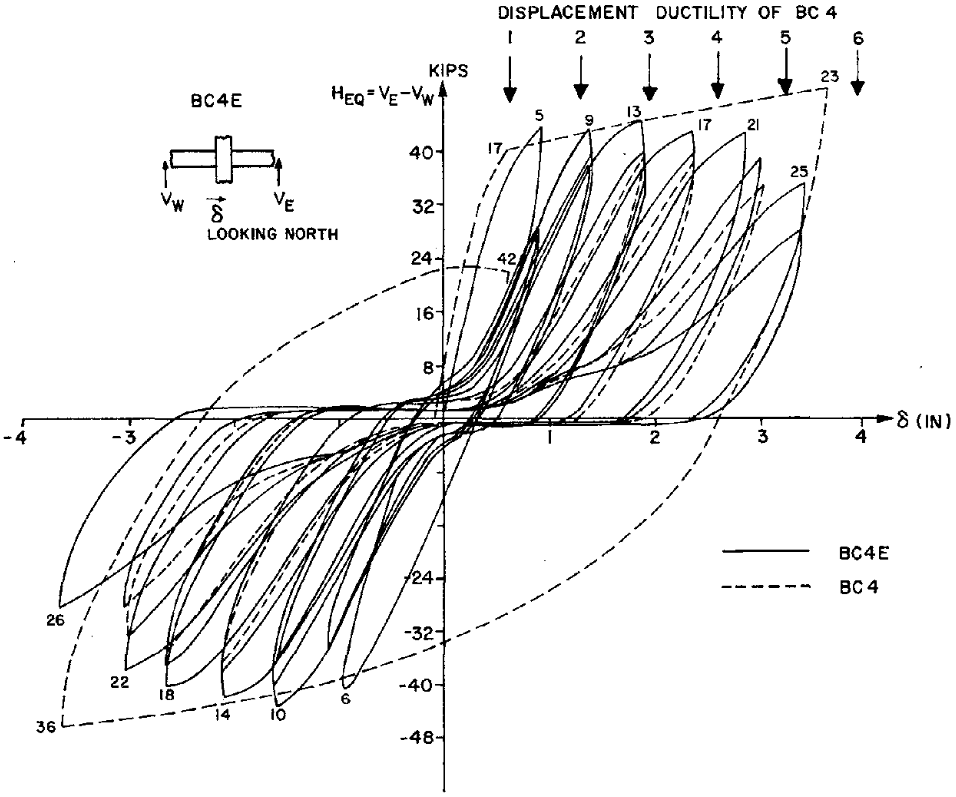

Fig. 5.5 H_{EQ}-δ Diagrams Before and After Epoxy Repair at Large Displacement

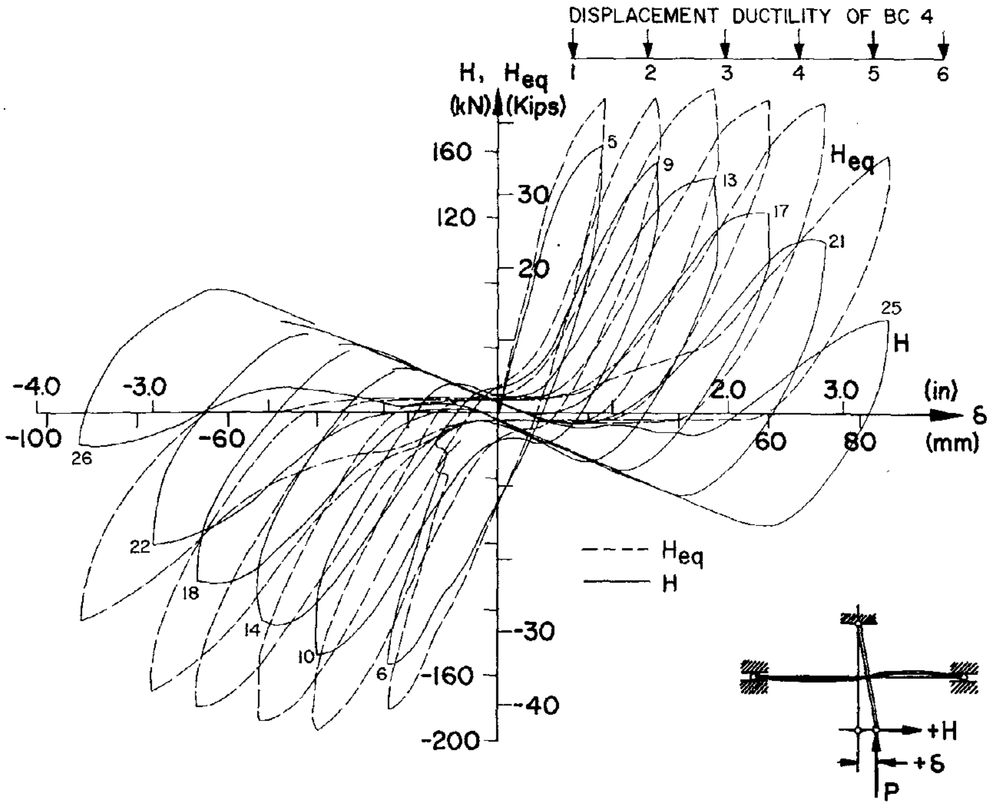

Fig. 5.6 H-δ and H_{EQ}-δ Diagrams for Specimen BC4E

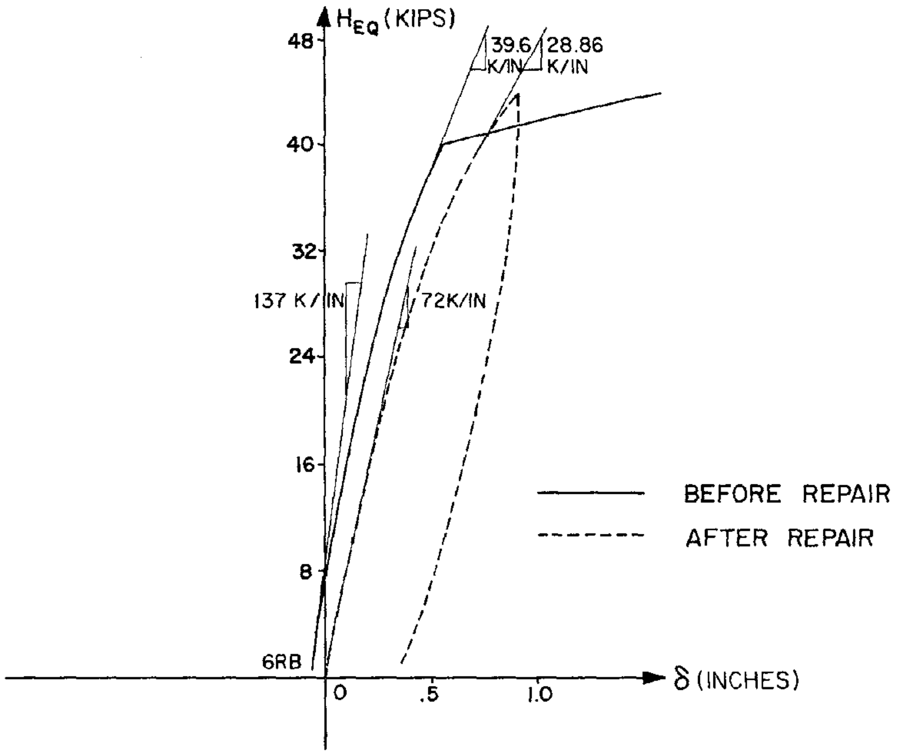

Fig. 5.7 H_{EQ}-δ Diagram Before and After Epoxy Repair, Loading to First Yield

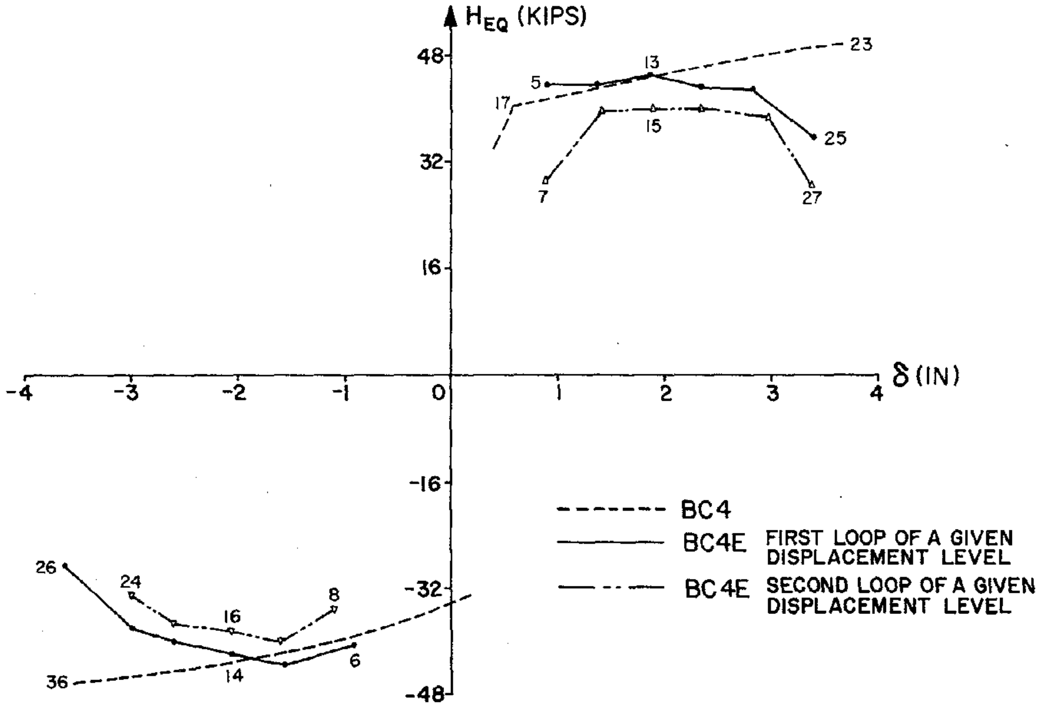

Fig. 5.8 Maximum Resistance Envelope Before and After Epoxy Repair

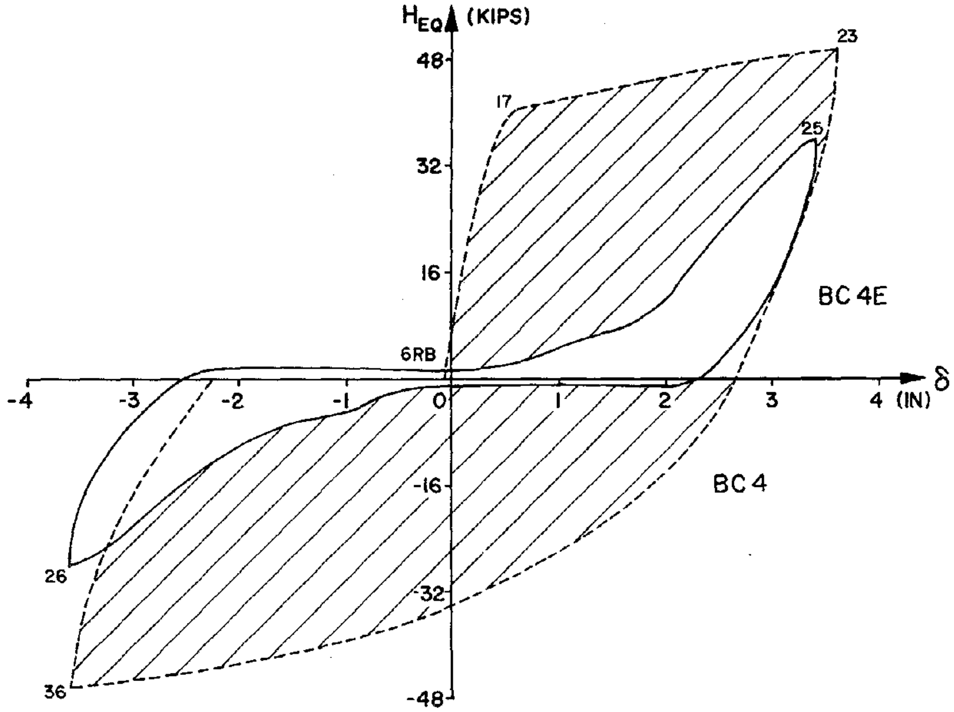

Fig. 5.9 Energy Dissipation Capacities at a Displacement Level of ± 3.6 in., Before and After Epoxy Repair

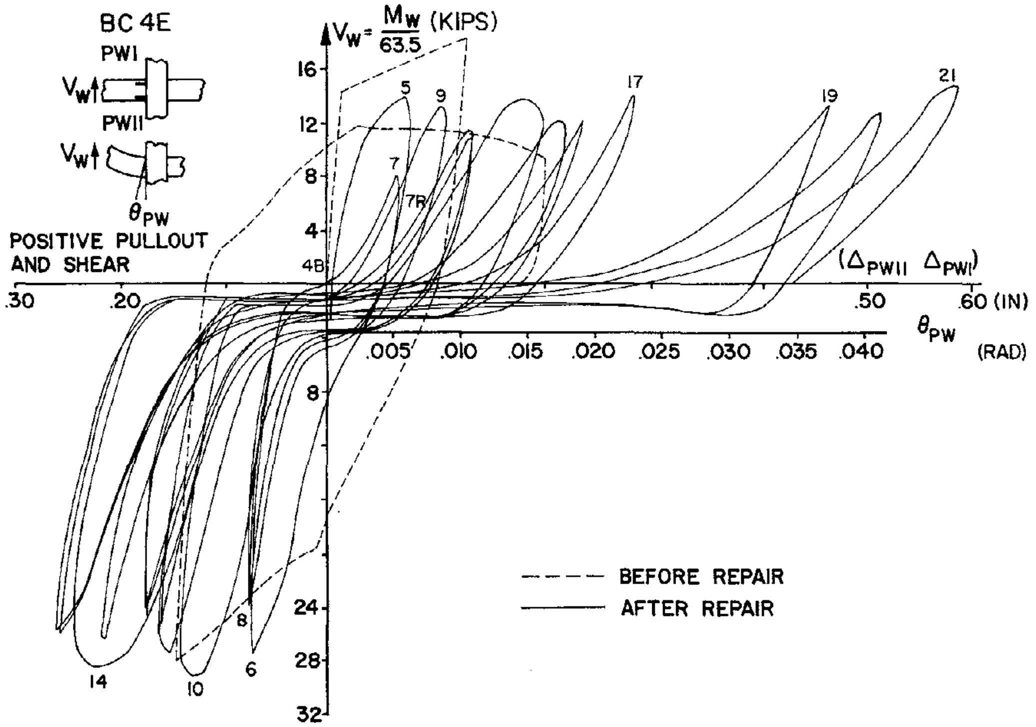

Fig. 5.10 Push-in and Pull-out Rotations at West Column Face Before and After Epoxy Repair

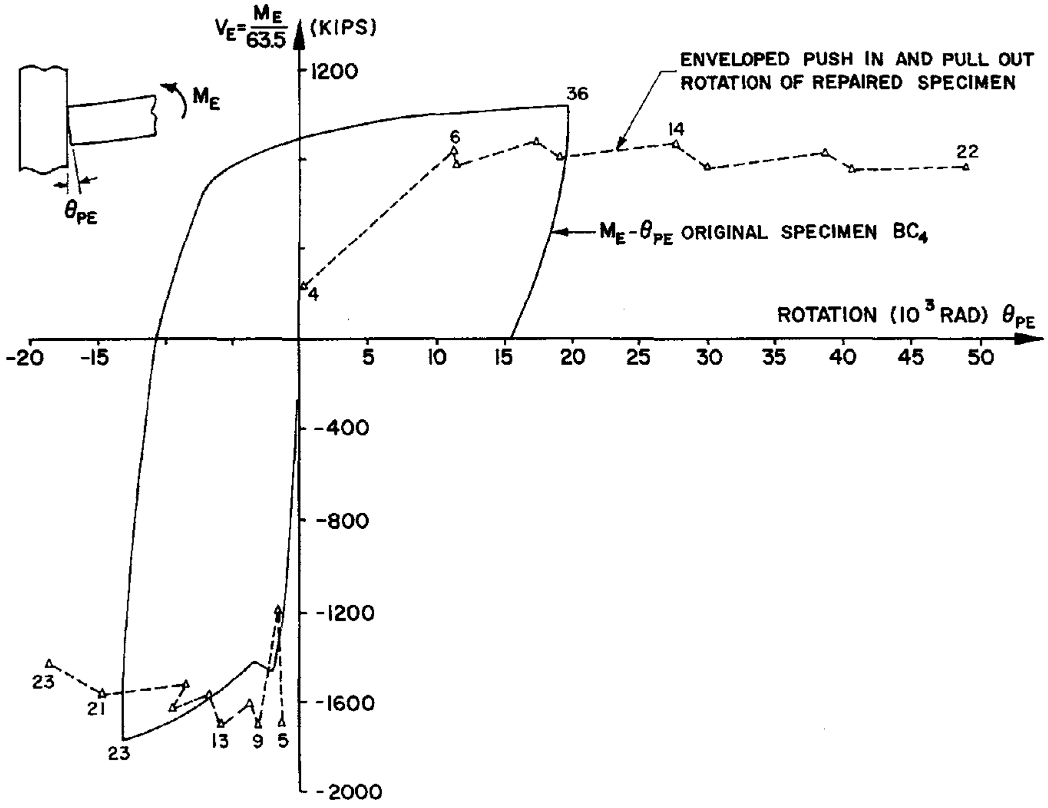

Fig. 5.11 Push-in and Pull-out Rotations at East Column Face Before and After Epoxy Repair

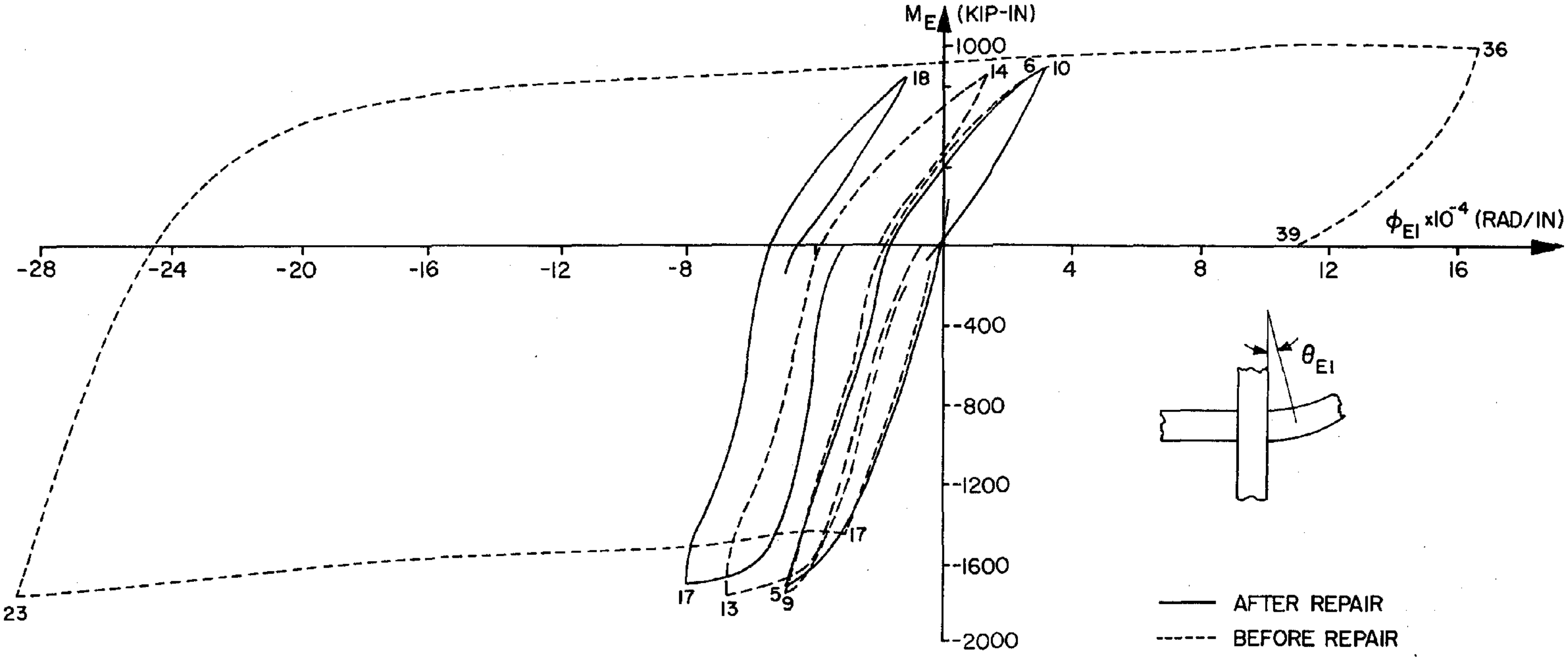

Fig. 5.12 $M_{E1} - \phi_{E1}$ Diagram Before and After Epoxy Repair

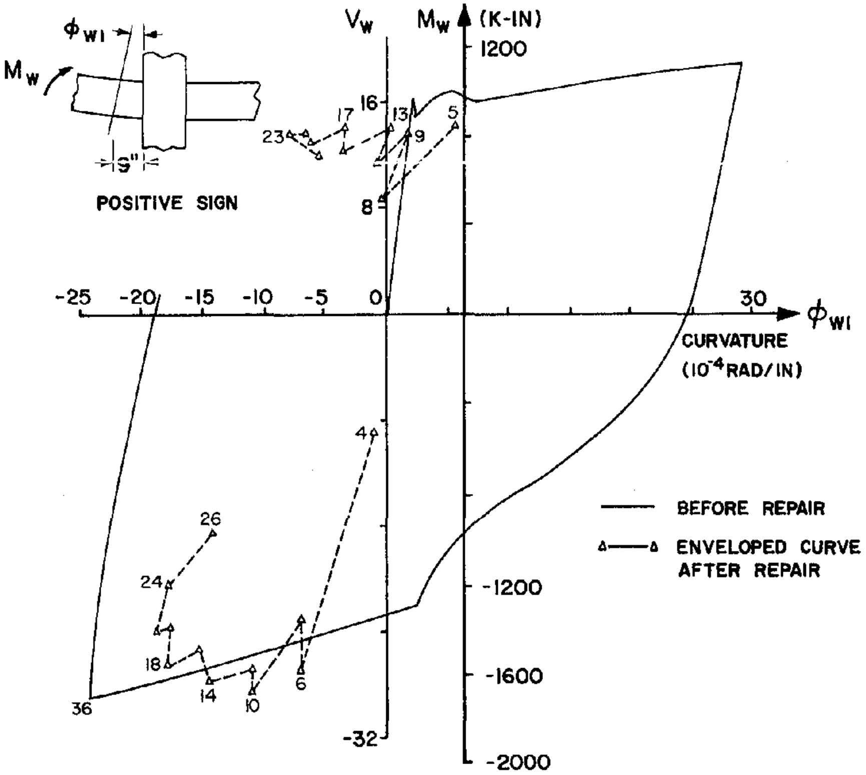

Fig. 5.13 $M_{W1}-\phi_{W1}$ Diagram Before and After Epoxy Repair

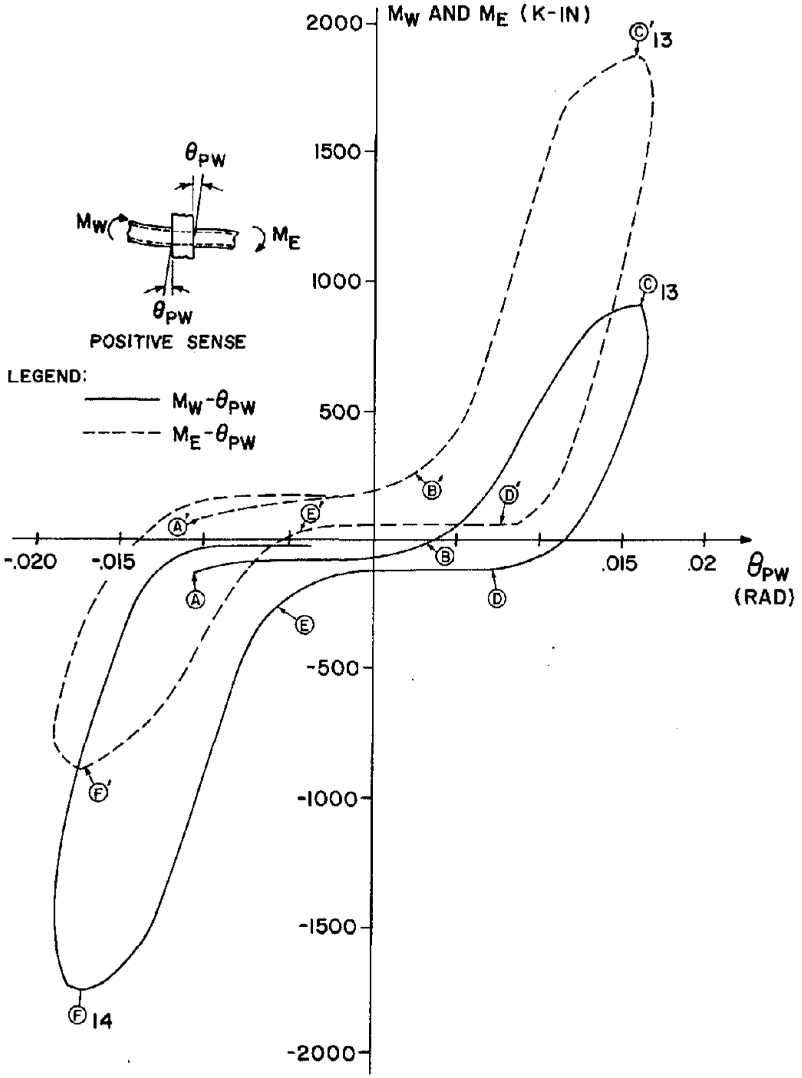

Fig. 5.14 Typical $M_W-\theta_{PW}$ and $M_E-\theta_{PW}$ Loop, Specimen BC4E

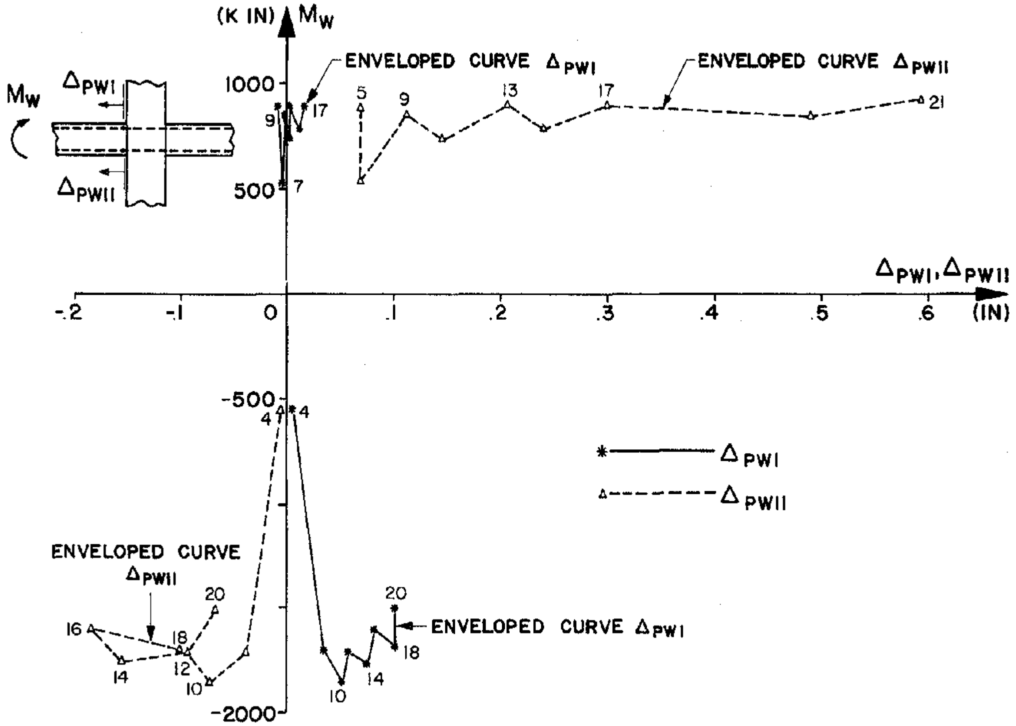

Fig. 5.15 Slippage of Top and Bottom Steel Bar at West Column Face, Specimen BC4E

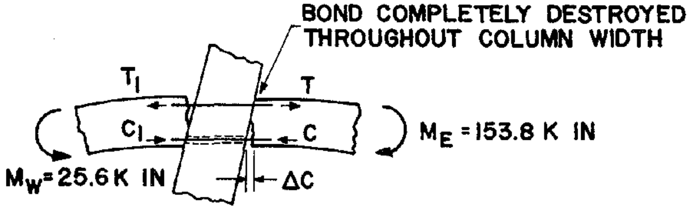

(a) DEFORMED SHAPE IN THE RANGE A TO B

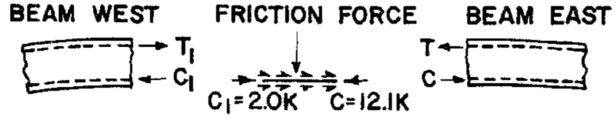

(b) FREE-BODY DIAGRAM FOR ABOVE

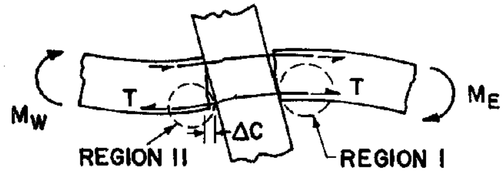

(c) DEFORMED SHAPE IN THE RANGE B TO C

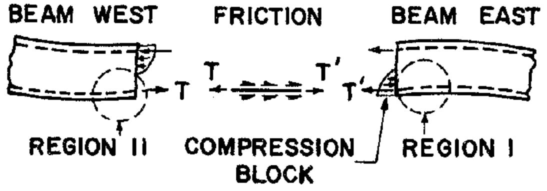

(d) FREE-BODY DIAGRAM FOR ABOVE

Fig. 5.16 Illustrations of the Repaired Connection Behavior During Second Phase (Large Displacements)

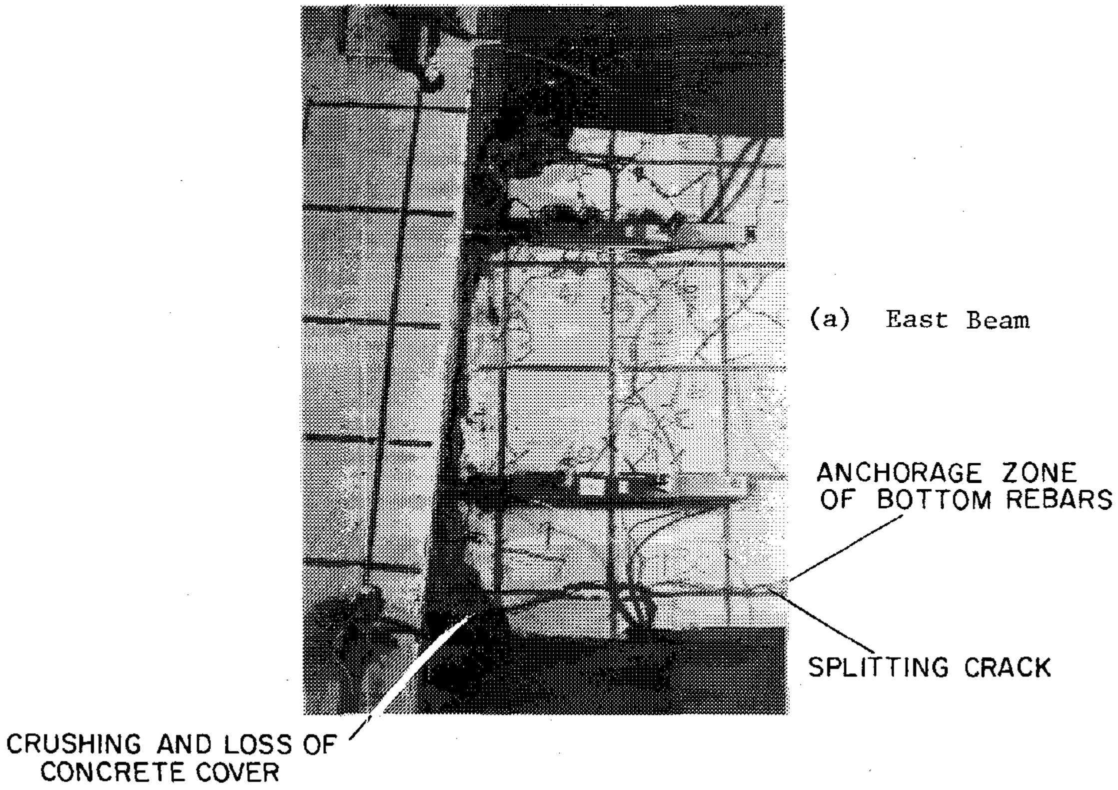

(a) East Beam

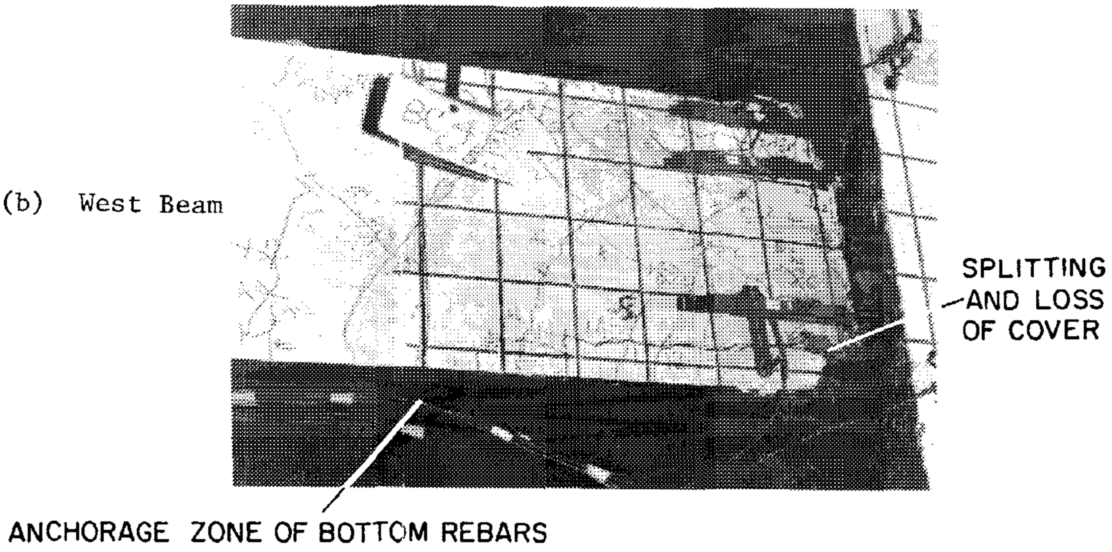

(b) West Beam

Fig. 5.17 Close-up of Splitting Crack Locations, Specimen BC4E

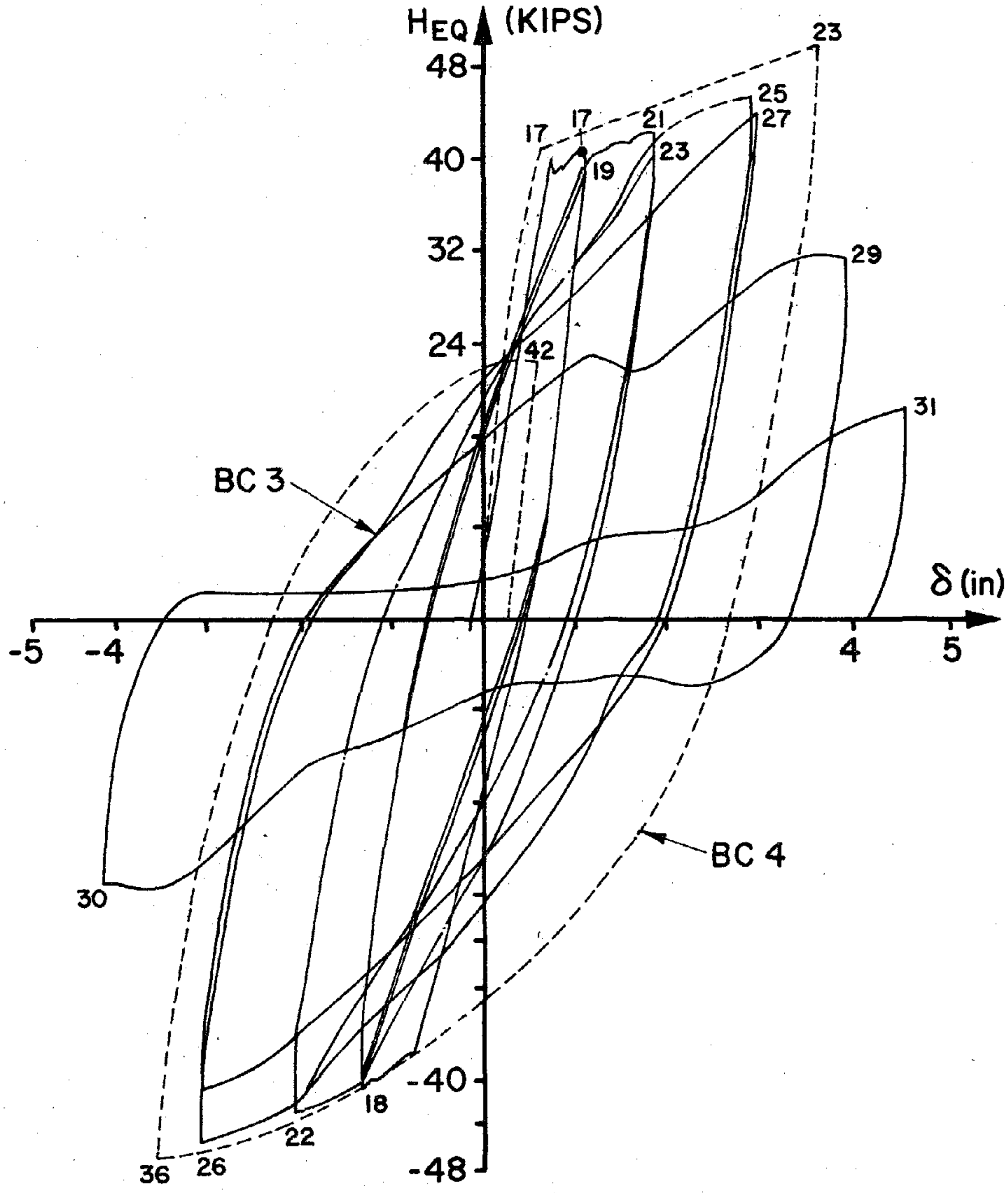

Fig. 6.1 $H_{EQ} - \delta$ Diagram for Specimens BC3 and BC4

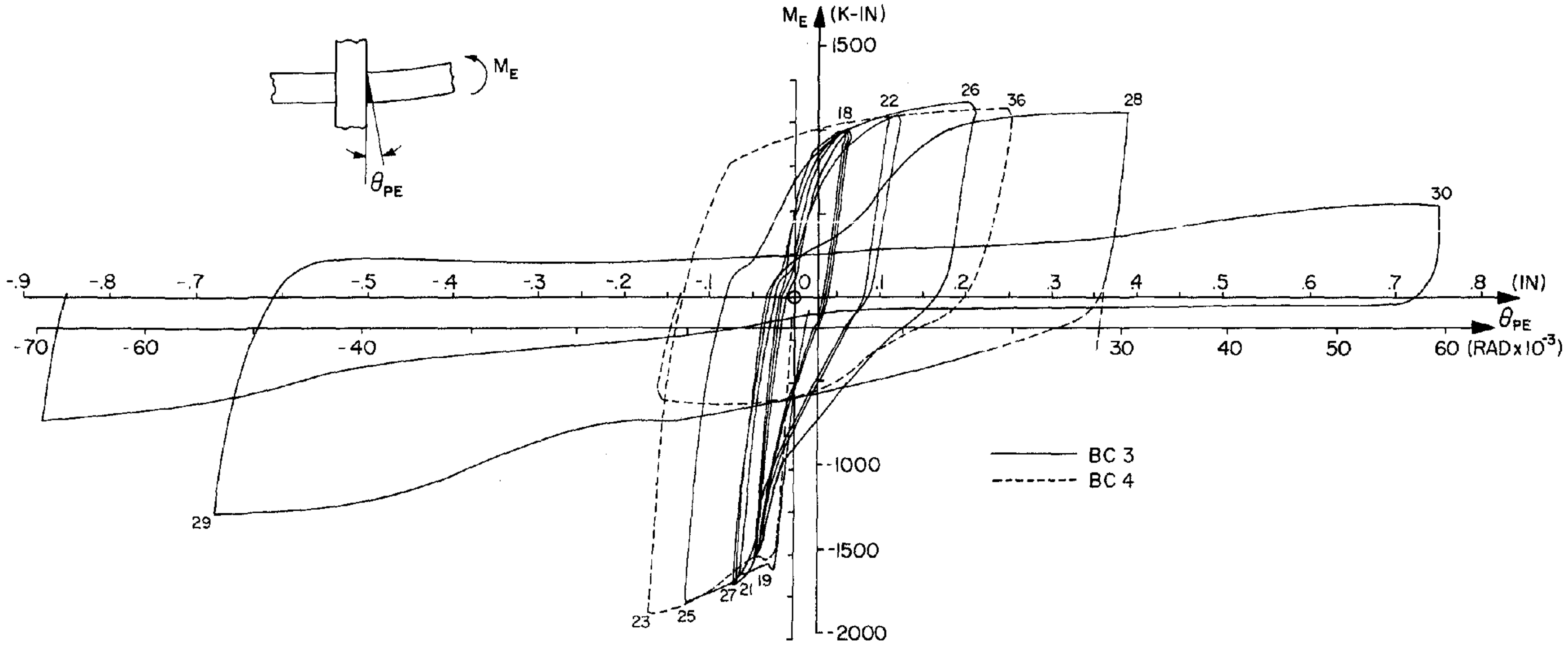

Fig. 6.2 $M_E - \theta_{PE}$ Diagram for Specimens BC3 and BC4

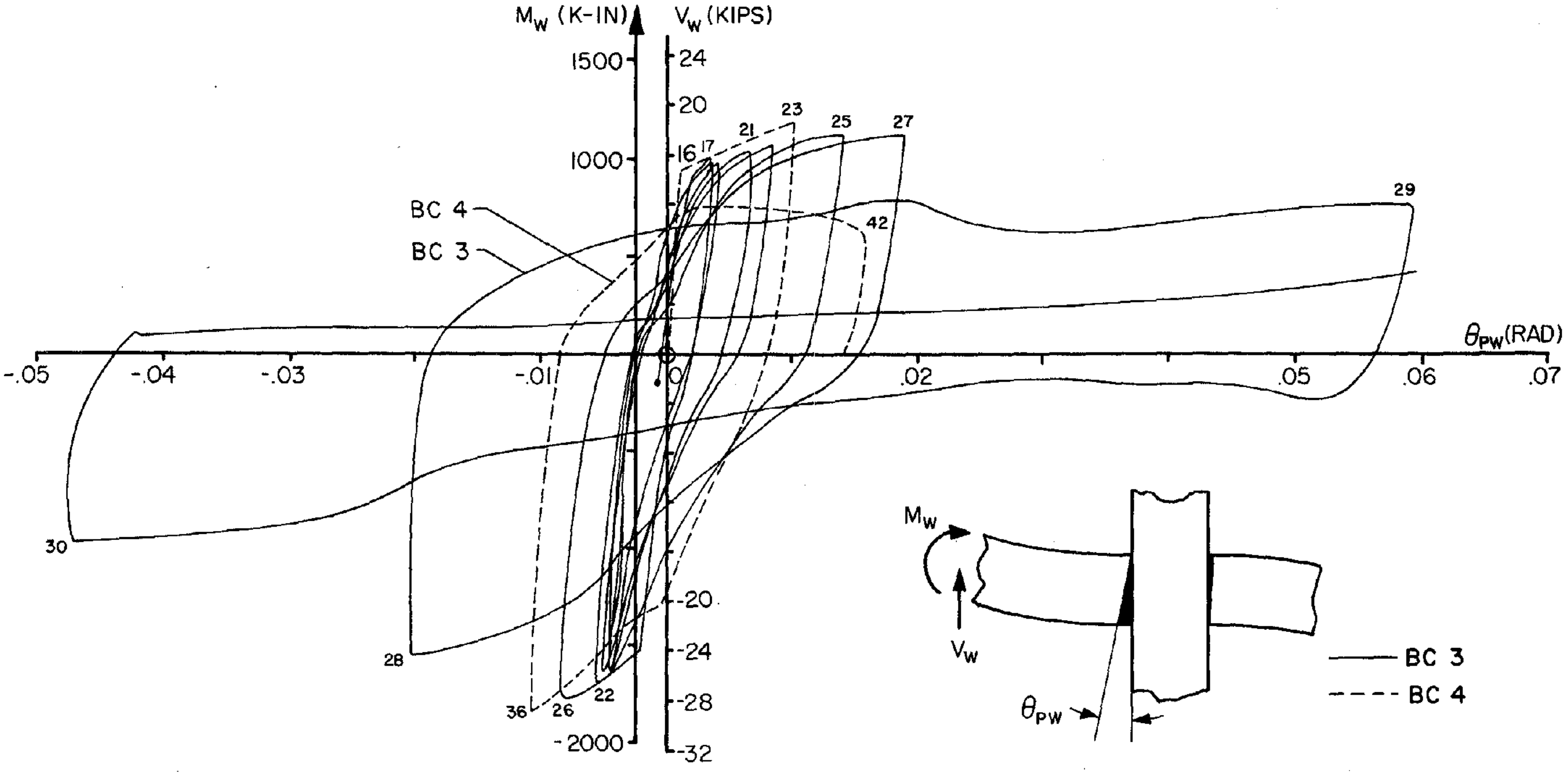

Fig. 6.3 $M_W - \theta_{PW}$ Diagram for Specimens BC3 and BC4

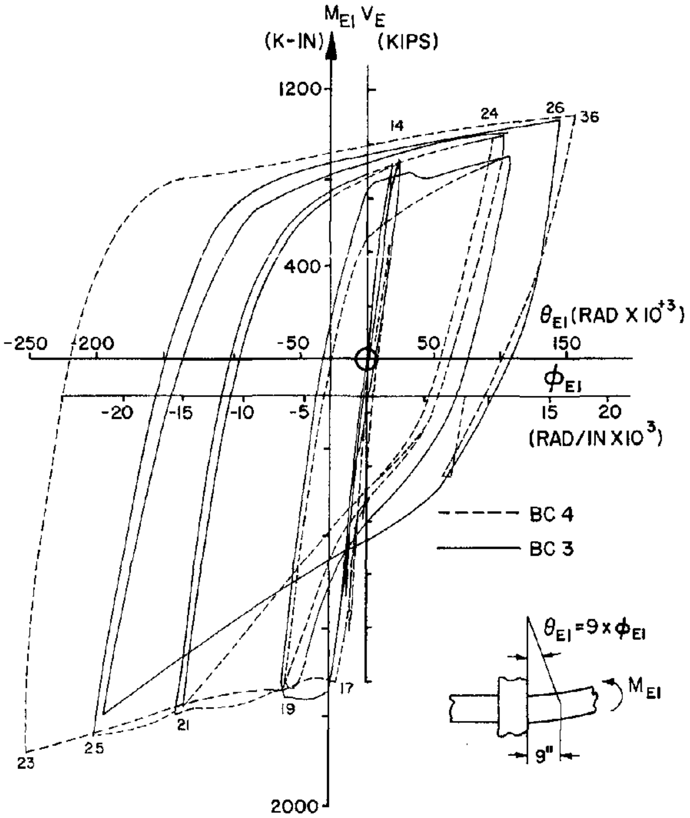

Fig. 6.4 M_{E1}-ϕ_{E1} Diagram for Specimens BC3 and BC4

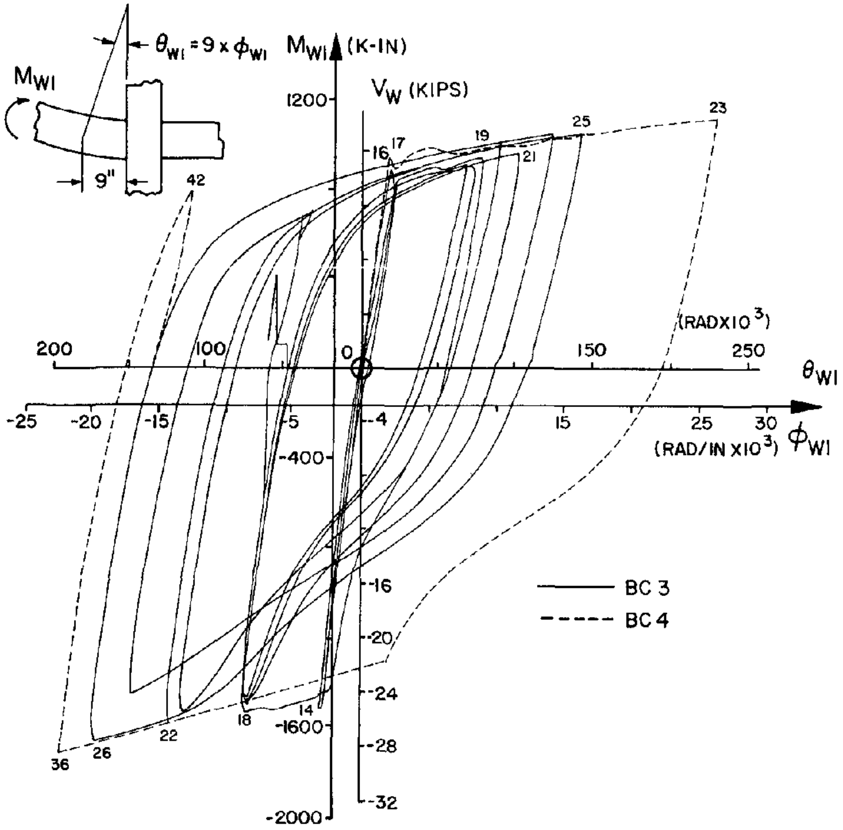

Fig. 6.5 M_{W1}-ϕ_{W1} Diagram for Specimens BC3 and BC4

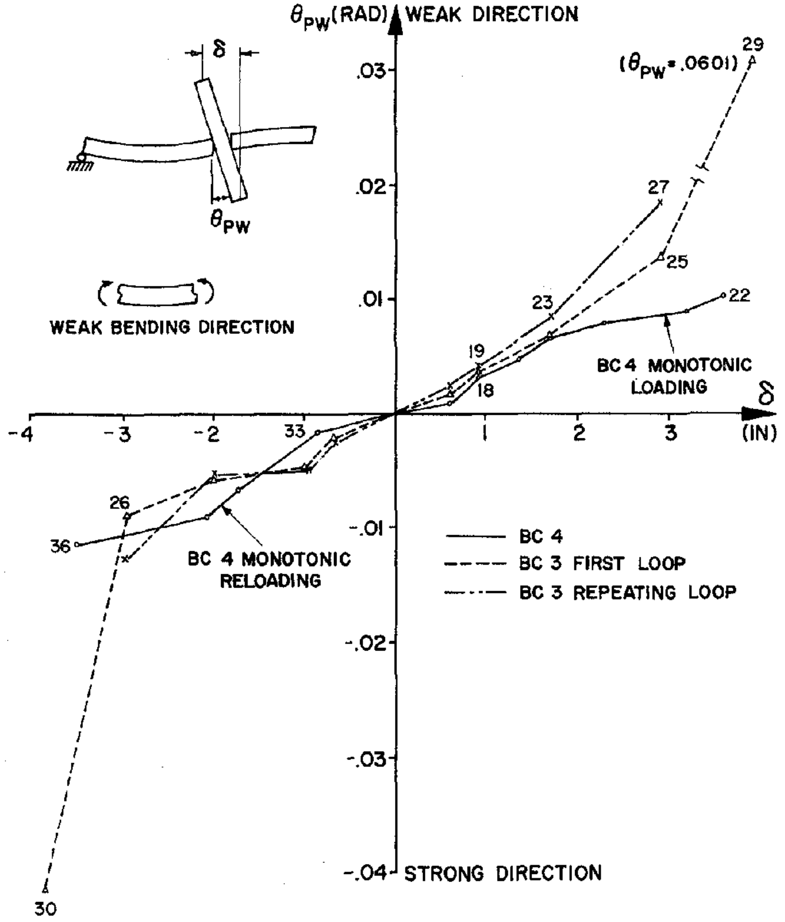

Fig. 6.6 Horizontal Displacement vs. Fixed End Rotation of the West Beam

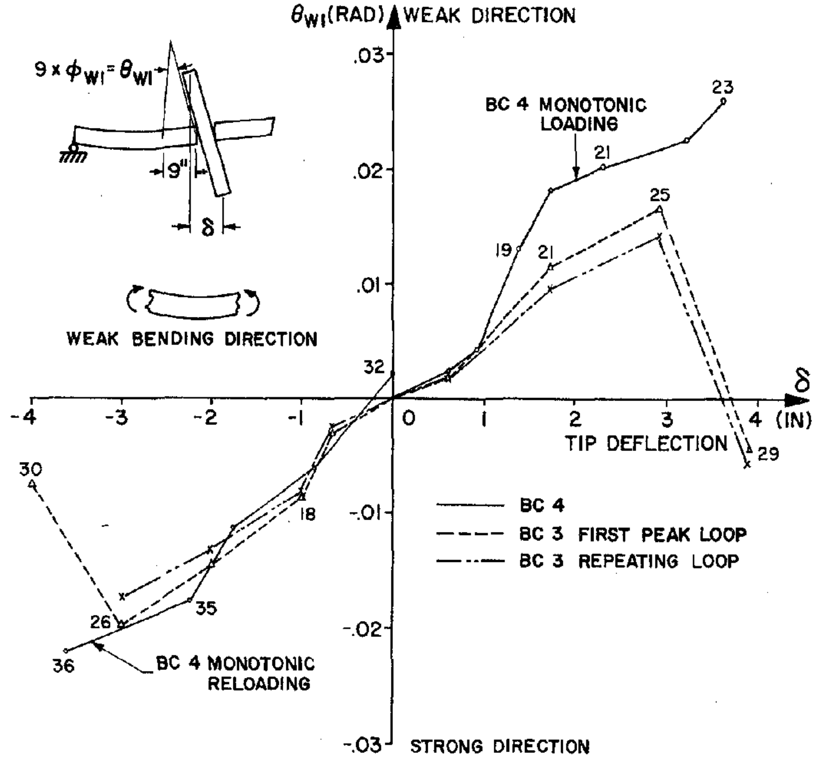

Fig. 6.7 Horizontal Deflection vs. Rotation in BW1

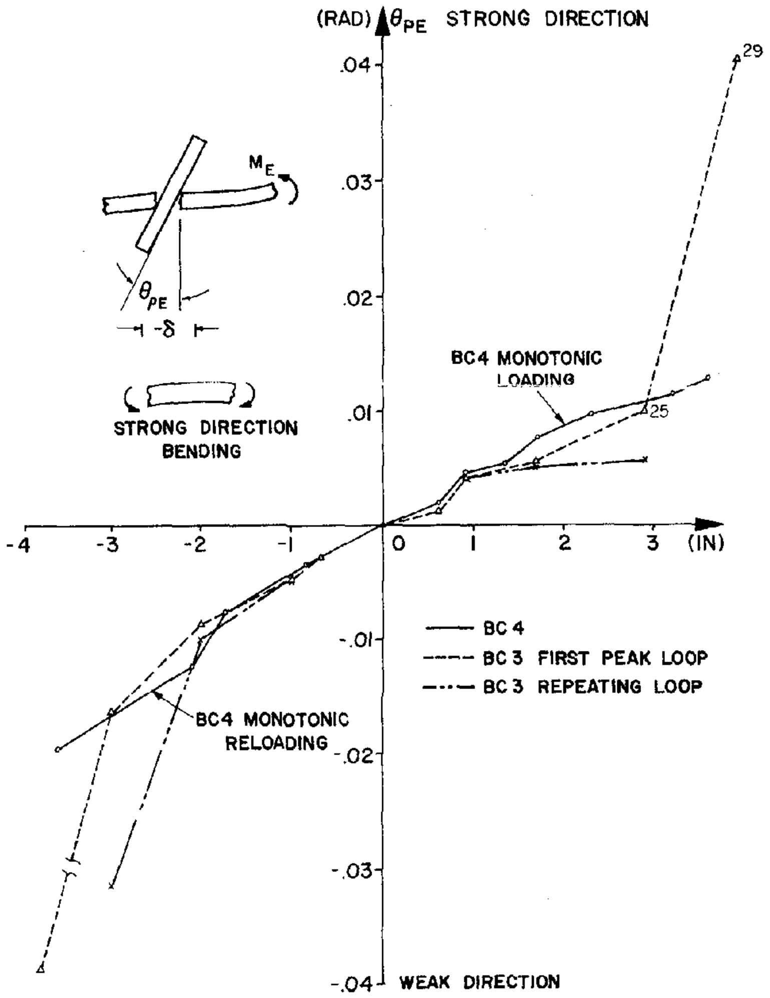

Fig. 6.8 Deflection vs. Fixed End Rotation of the East Beam

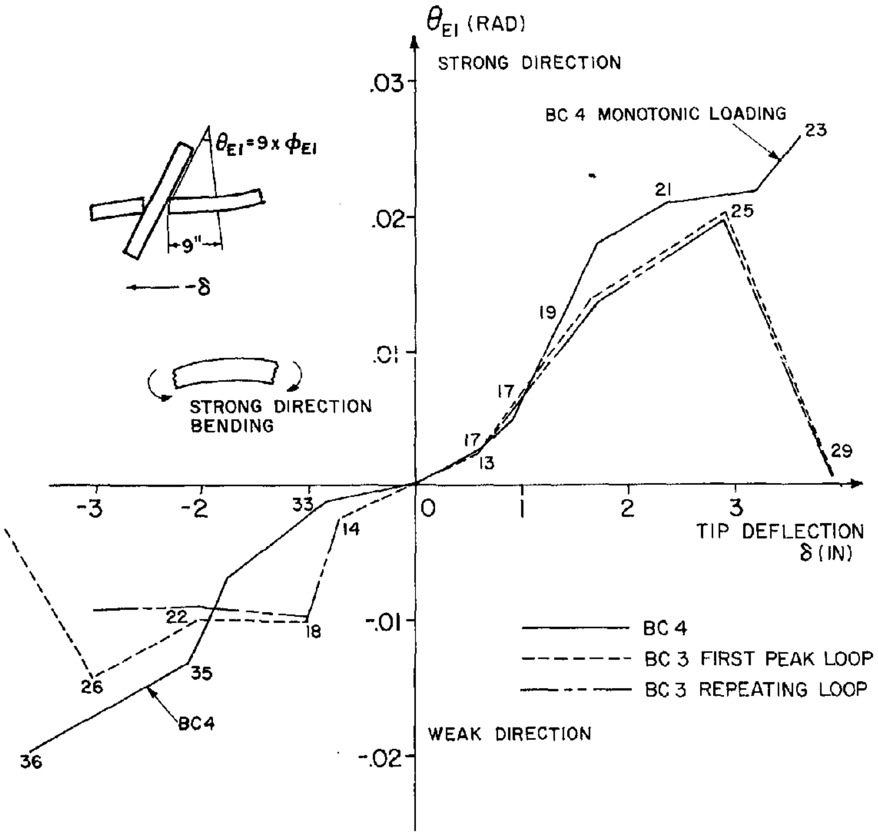

Fig. 6.9 Horizontal Deflection vs. Rotation in BE1

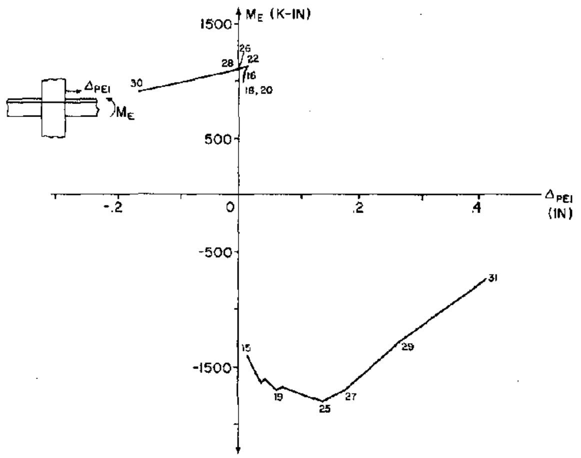

Fig. 6.10 Slippage, Δ_{PE1}, of the Top Rebars, Specimen BC3

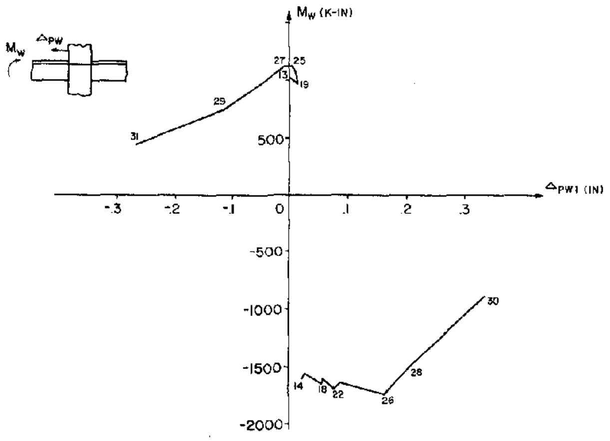

Fig. 6.11 Slippage, Δ_{PW1}, of the Top Rebars, Specimen BC3

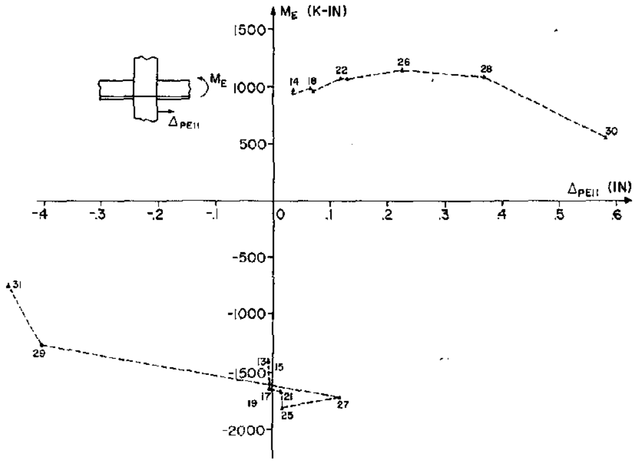

Fig. 6.12 Slippage, Δ_{PE11}, of the Bottom Rebars, Specimen BC3

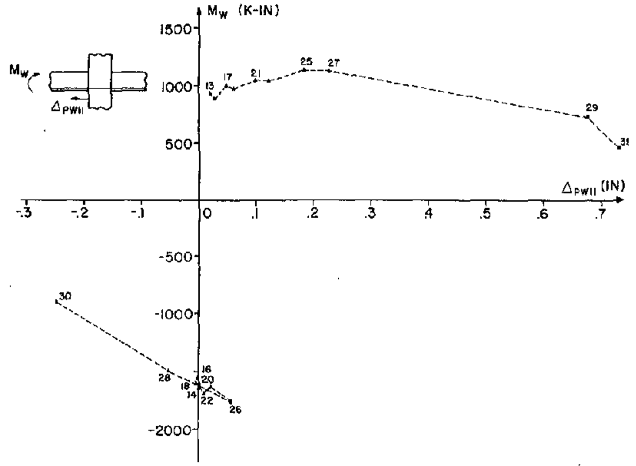

Fig. 6.13 Slippage, Δ_{PW11}, of the Bottom Rebars, Specimen BC3

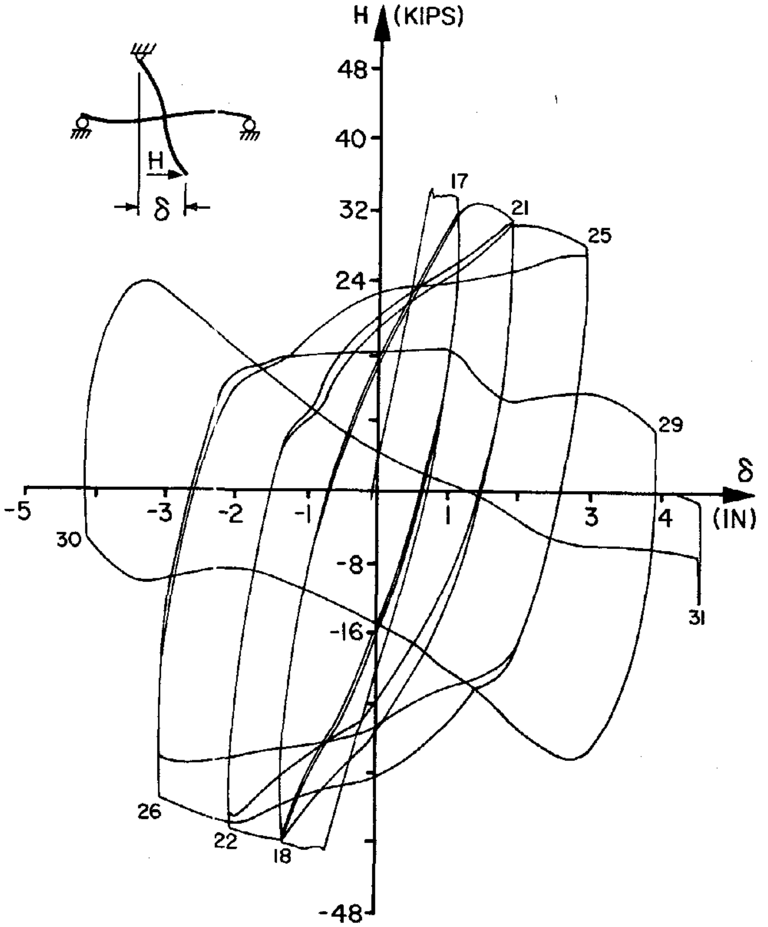

Fig. 6.14 H - δ Diagram for Specimen BC3

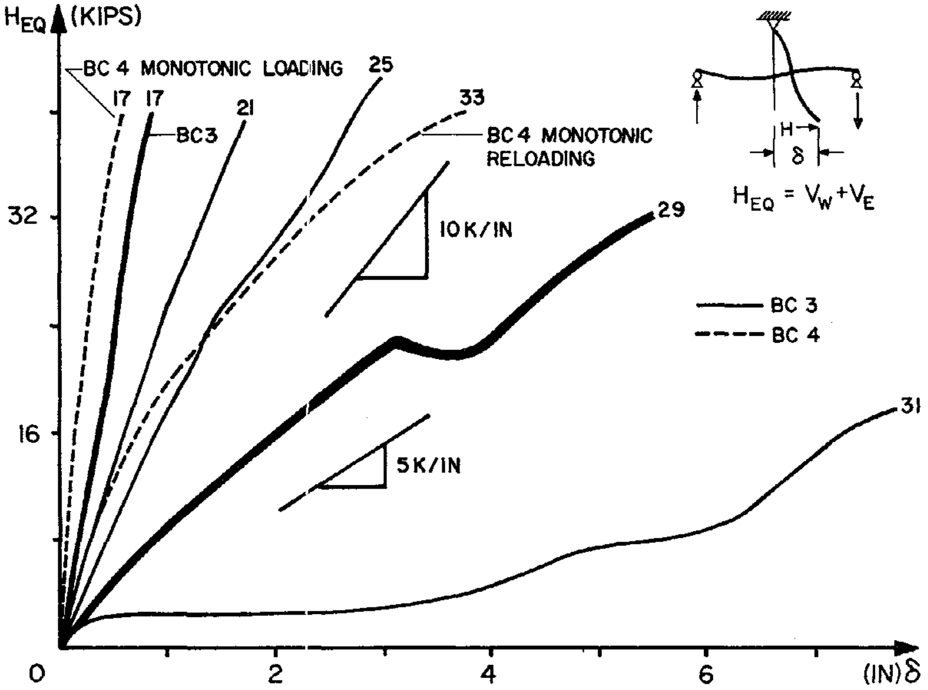

Fig. 6.15 Deterioration of Total Stiffness at Different Load Cycles

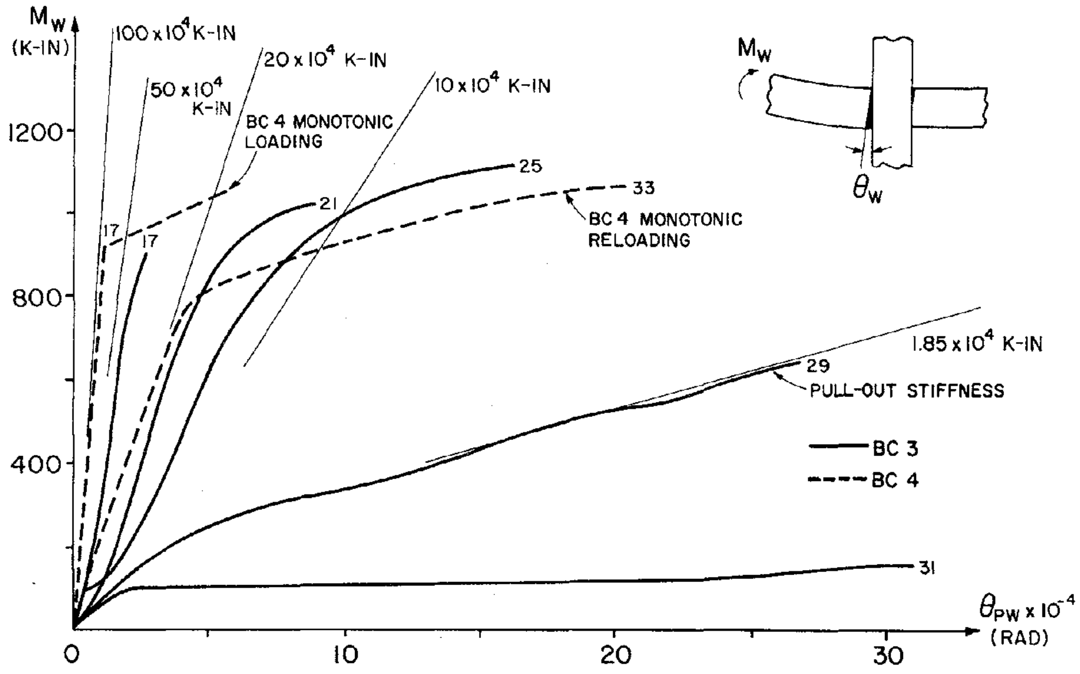

Fig. 6.16 Deterioration of Pull-out Stiffness at Different Load Cycles, West Side

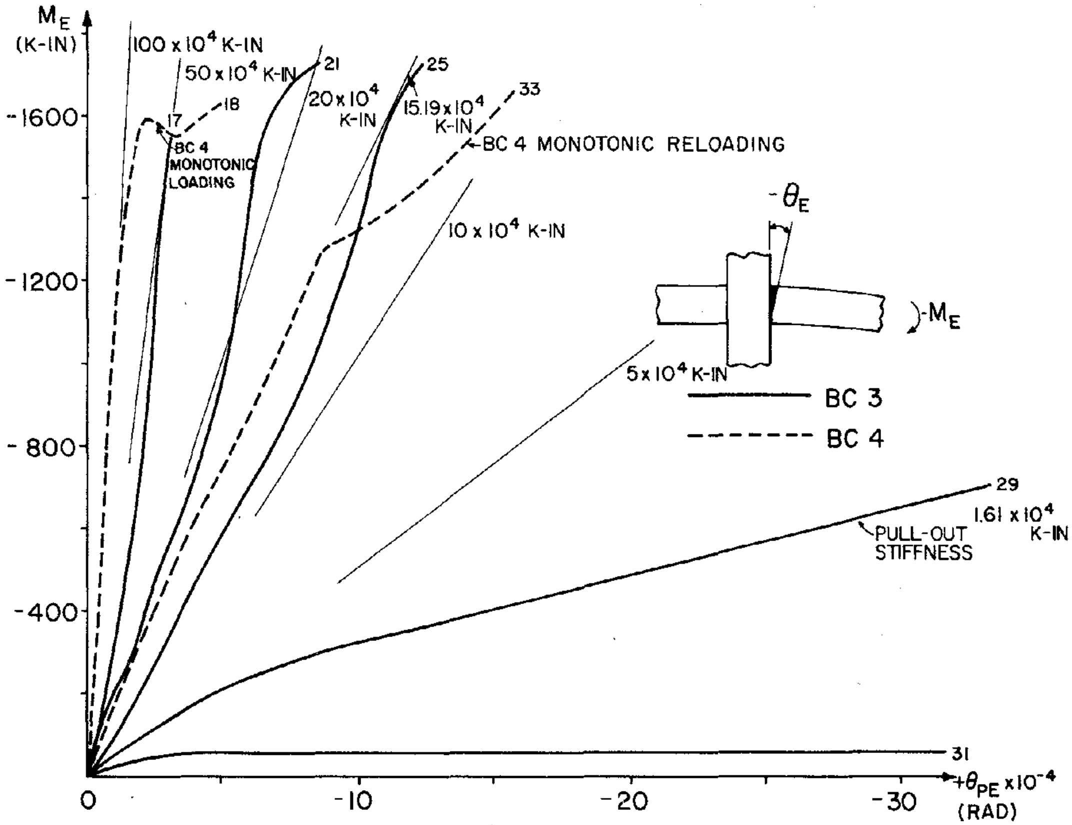

Fig. 6.17 Deterioration of Pull-out Stiffness at Different Load Cycles, East Side

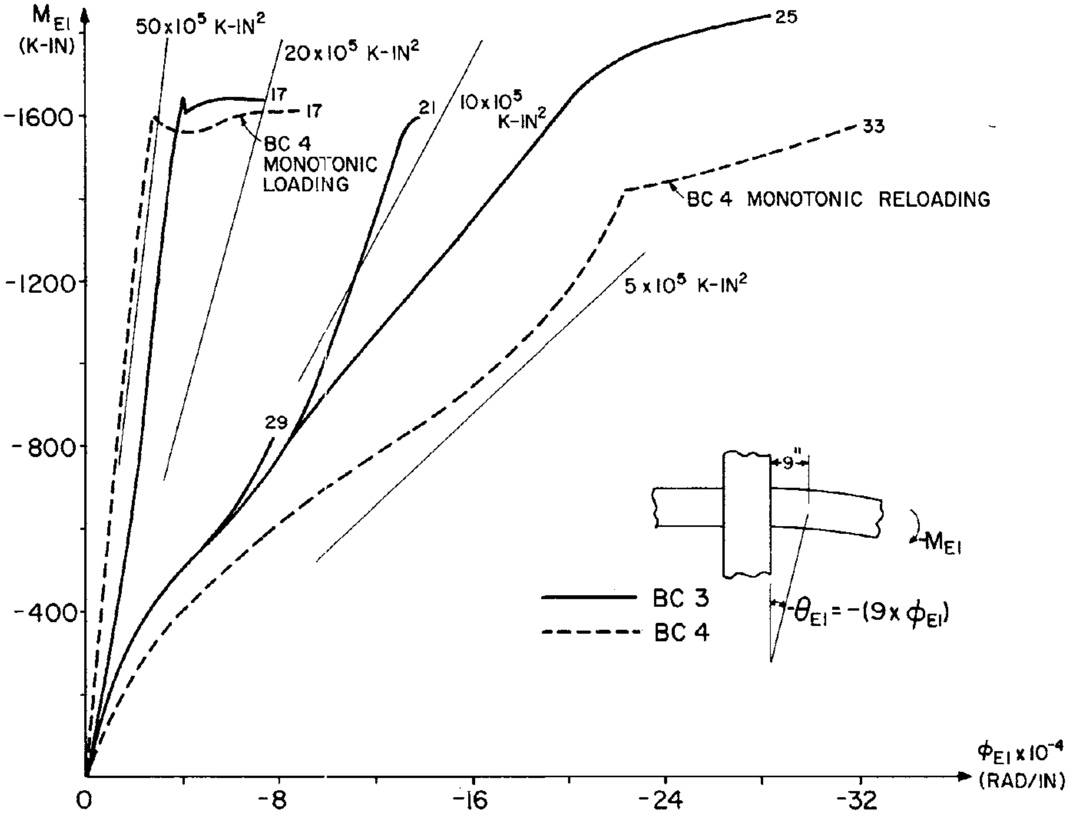

Fig. 6.18 Deterioration of Beam Stiffness at Different Load Cycles, East Side

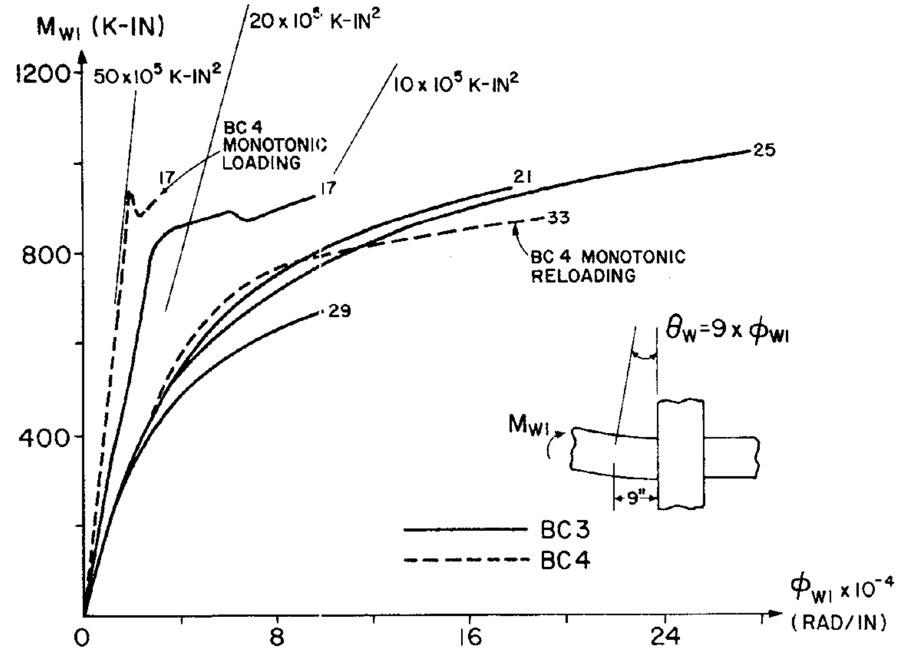

Fig. 6.19 Deterioration of Beam Stiffness at Different Load Cycles, West Side

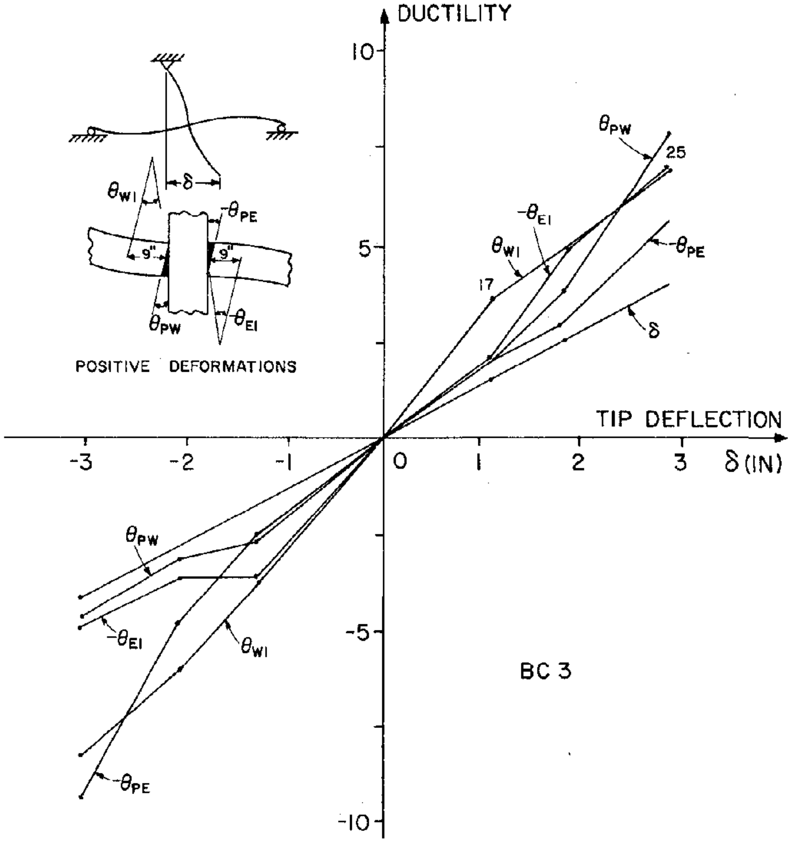

Fig. 6.20 Ductilities for Specimen BC3

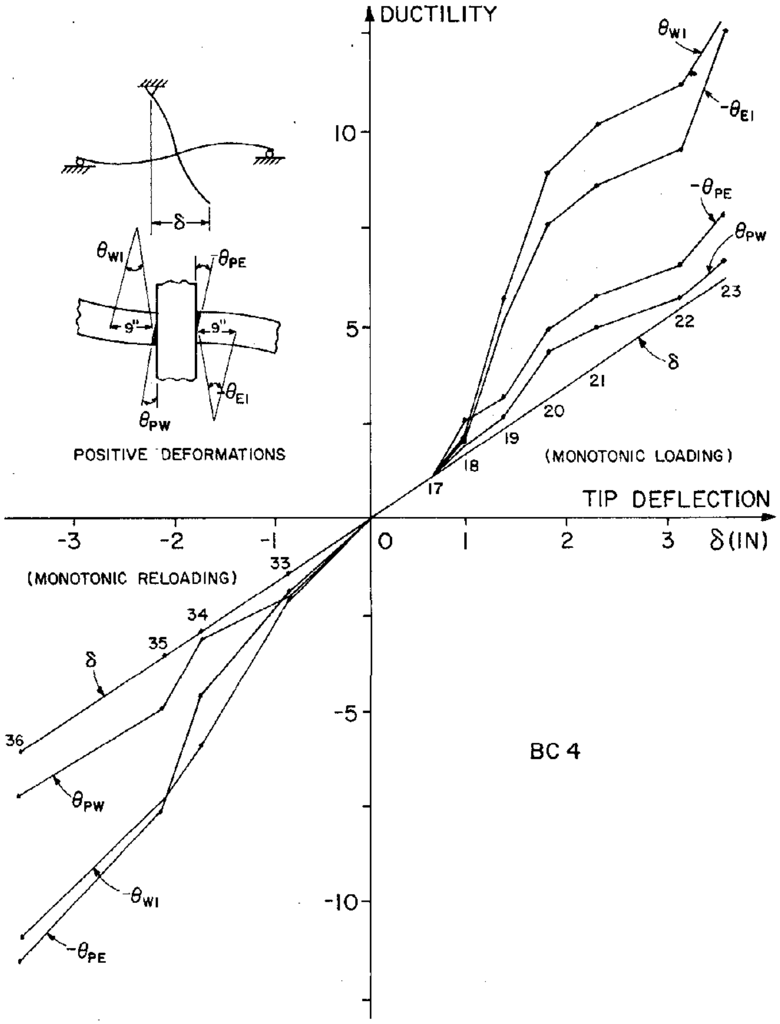

Fig. 6.21 Ductilities for Specimen BC4

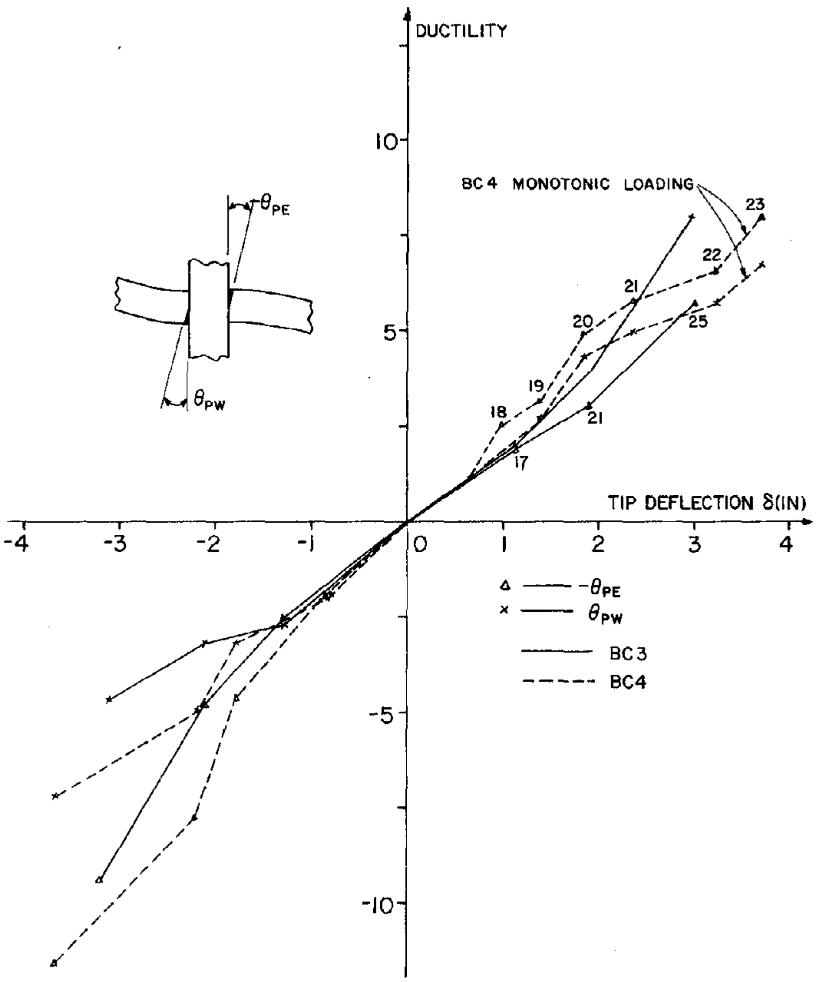

Fig. 6.22 Pull-out Ductilities for Different Loading Histories

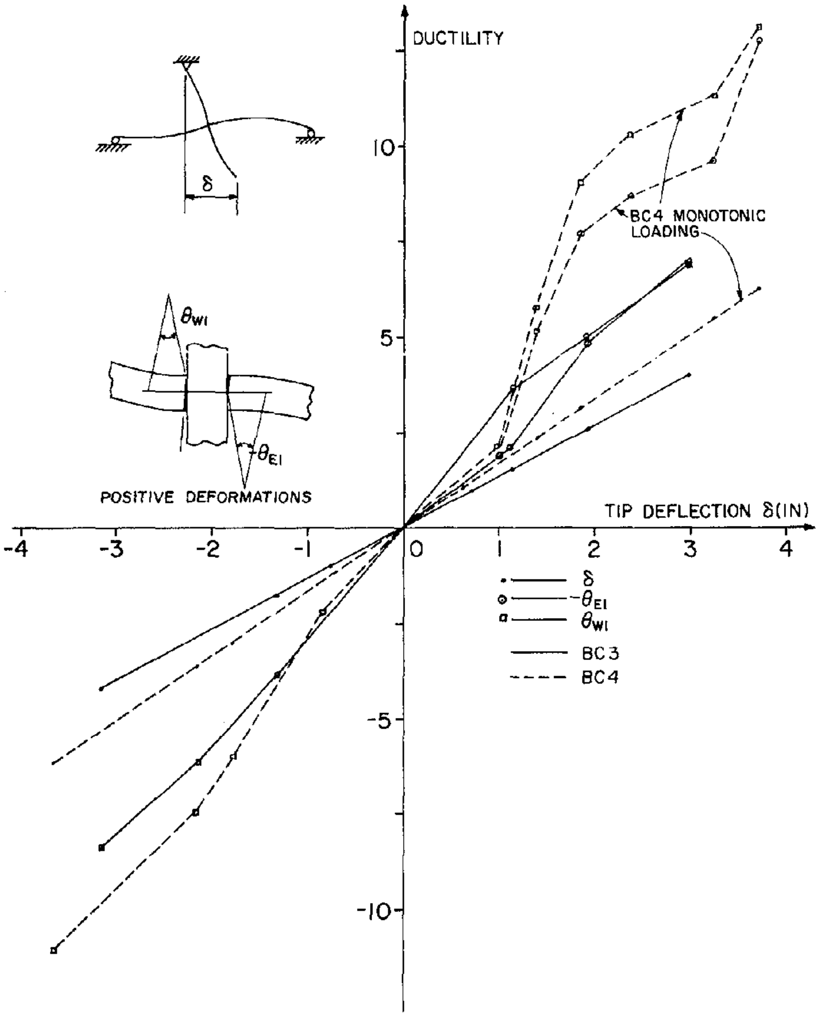

Fig. 6.23 Curvature and Tip Deflection Ductilities for Different Loading Histories

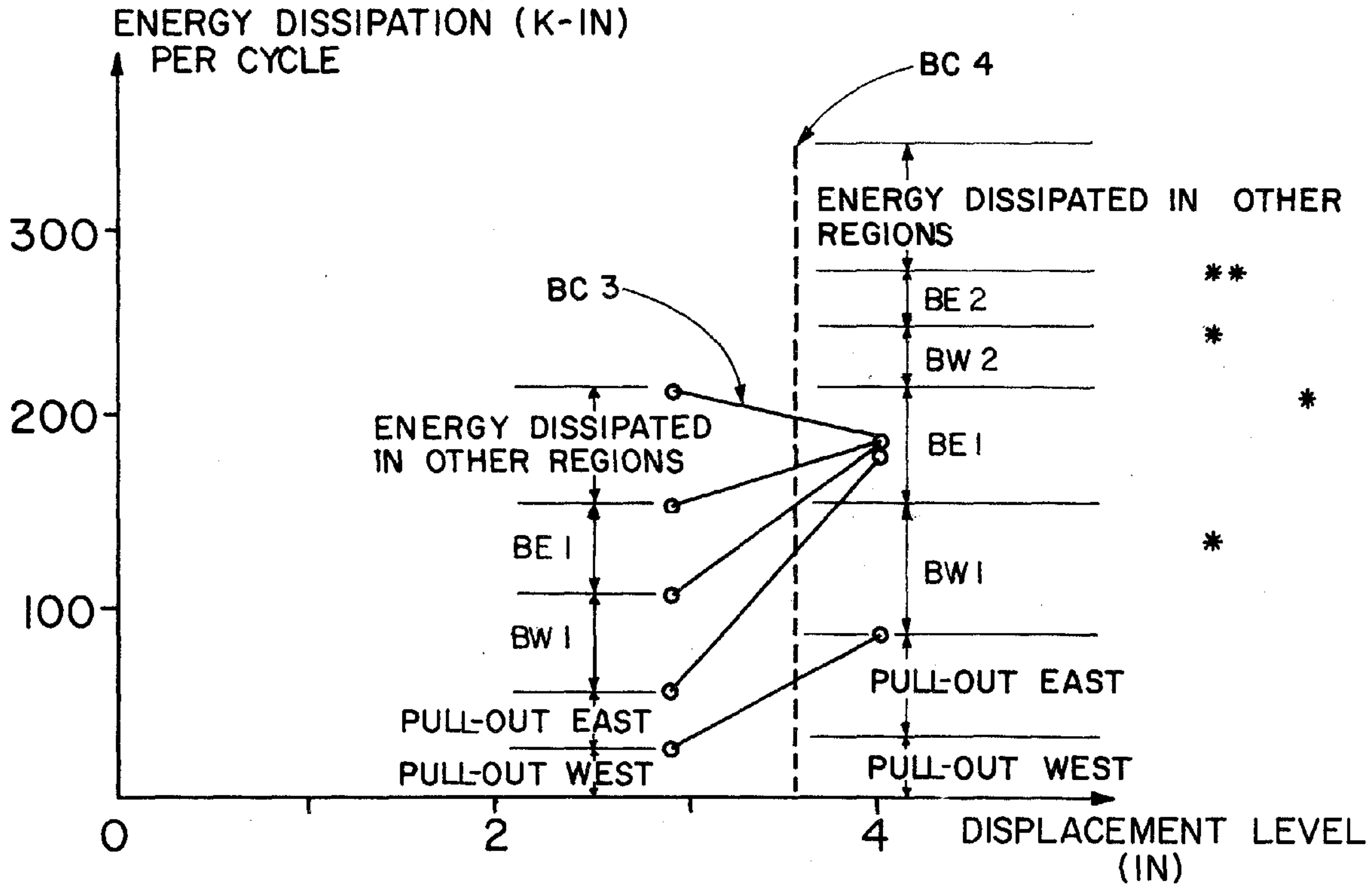

Fig. 6.24 Components of Energy Dissipation per Cycle for Specimens BC3 and BC4

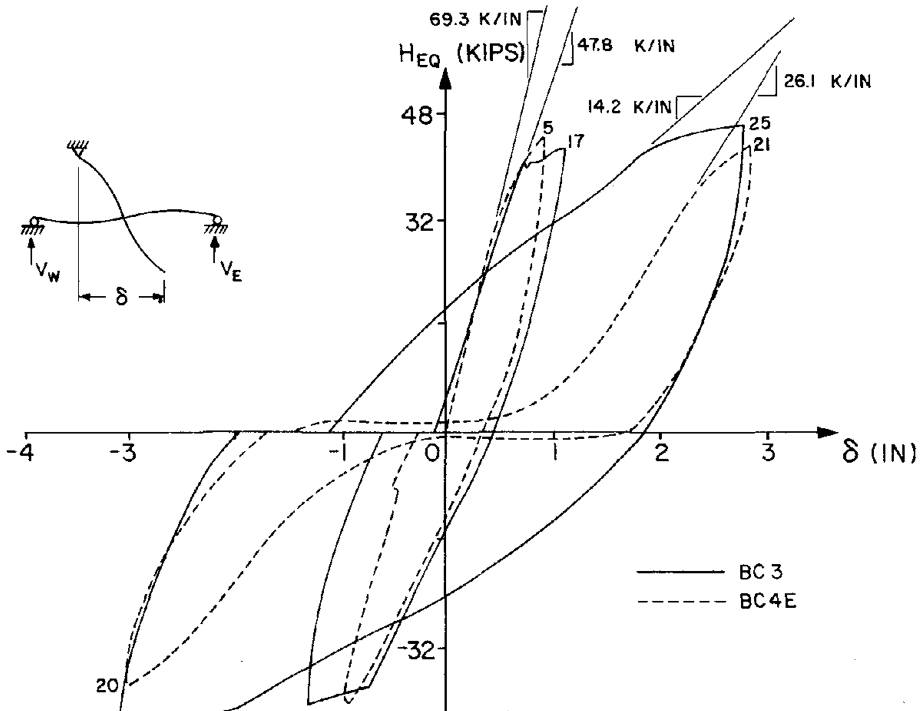

(a) AT DISPLACEMENT LEVELS OF 1 IN. AND 2.9 IN.

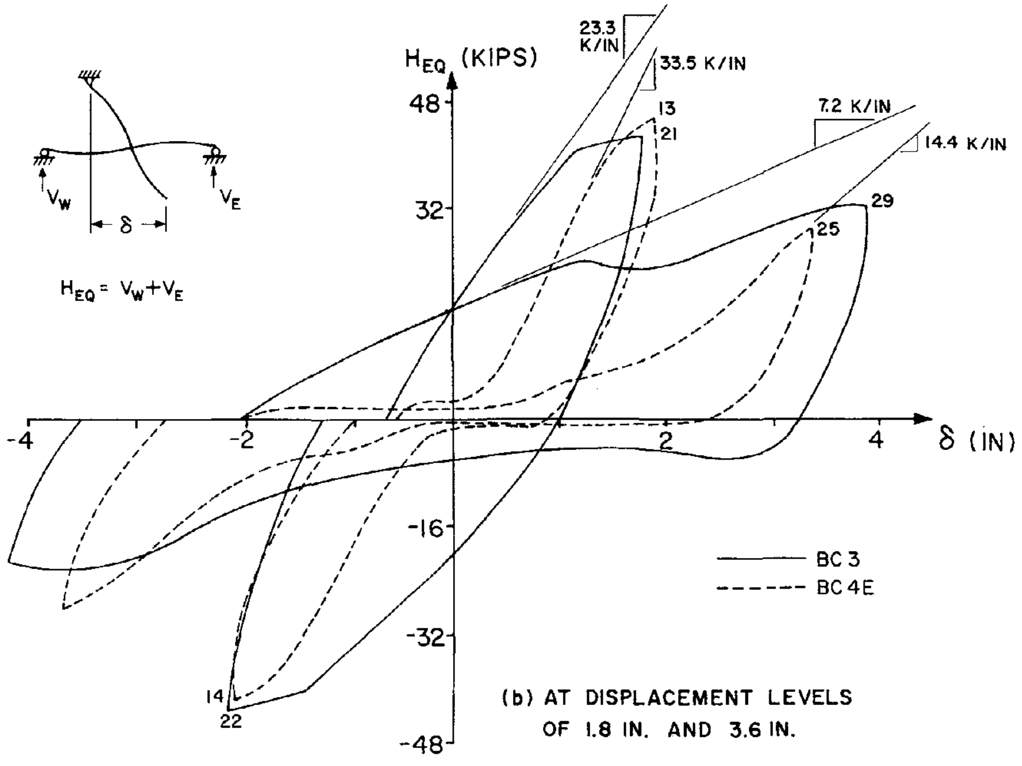

(b) AT DISPLACEMENT LEVELS OF 1.8 IN. AND 3.6 IN.

Fig. 7.1 Comparison of H_{EQ}-δ for Specimens BC3 and BC4E

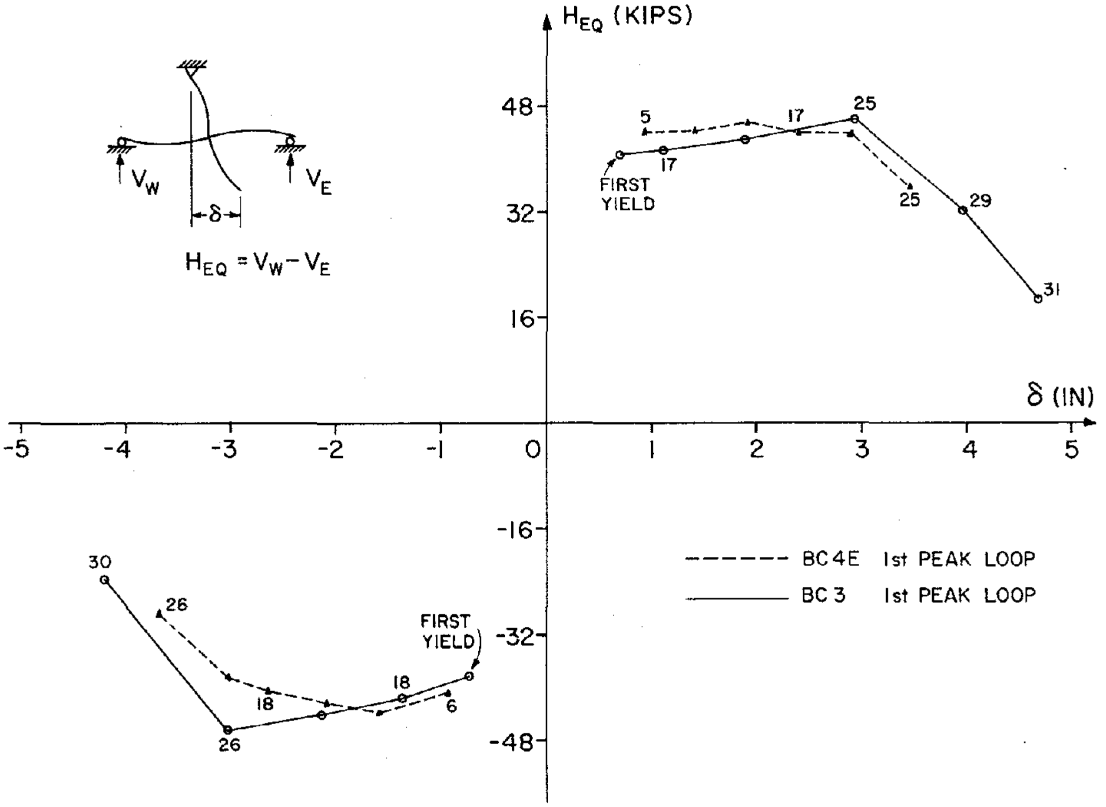

Fig. 7.2 Strength Envelope for First Loading to New Peak Displacement

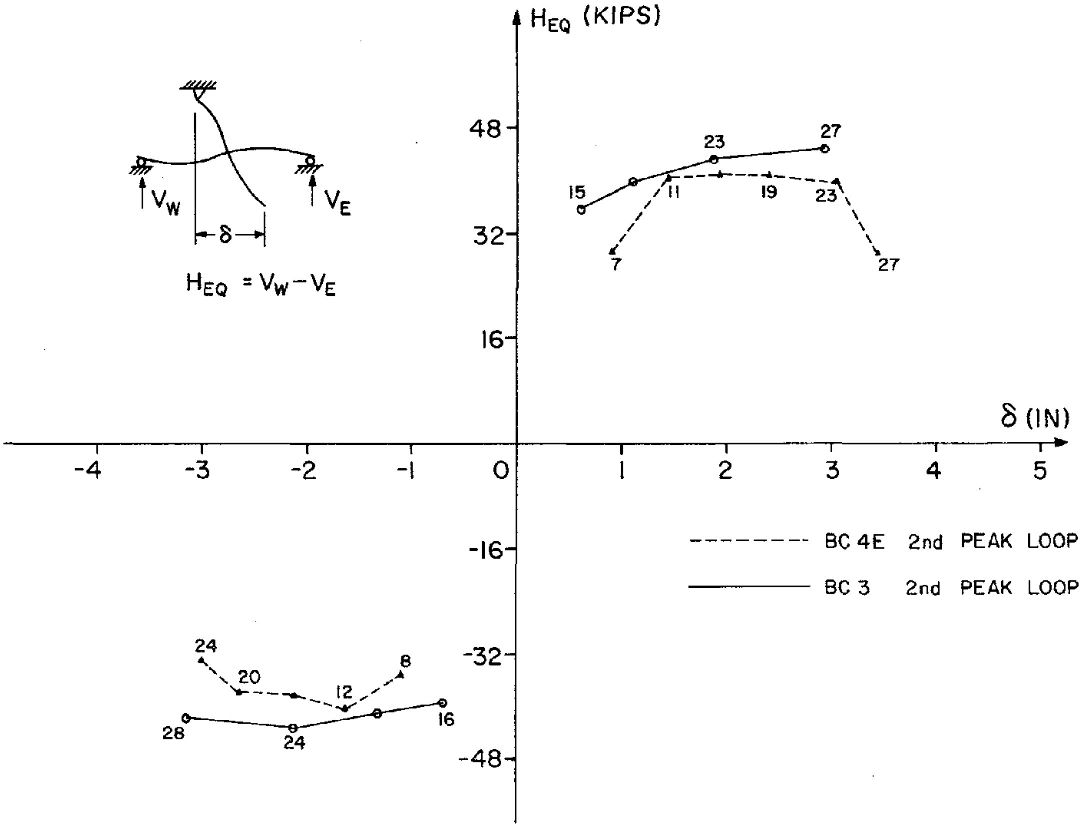

Fig. 7.3 Strength Envelope of Second Loop at Peak Displacement

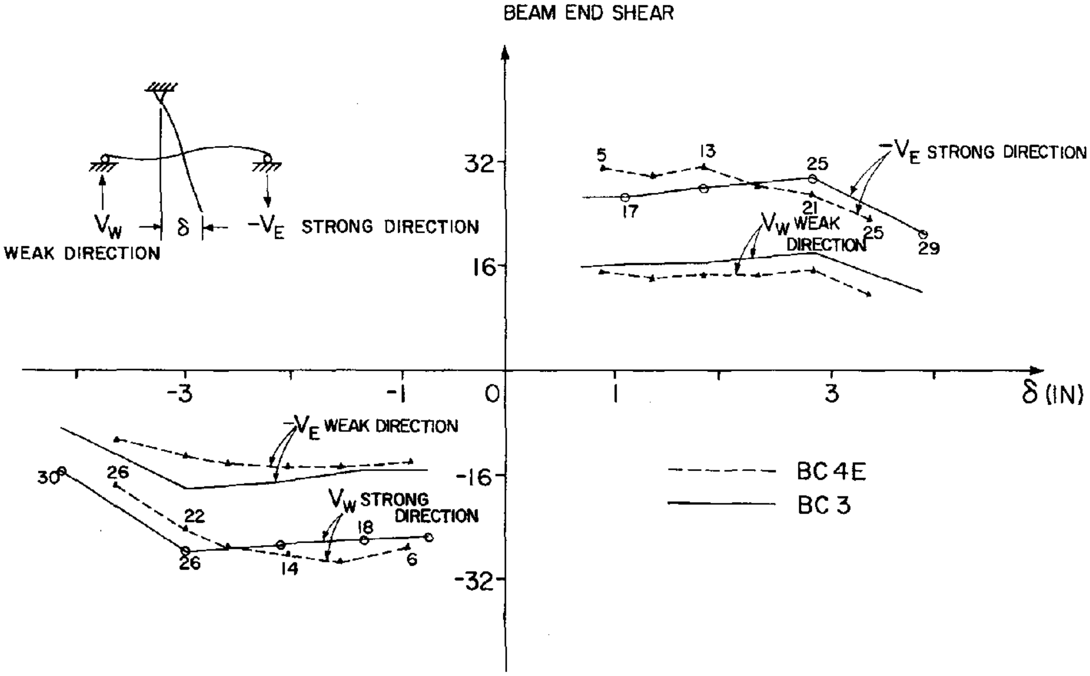

Fig. 7.4 Shear Envelope for BC3 and BC4E

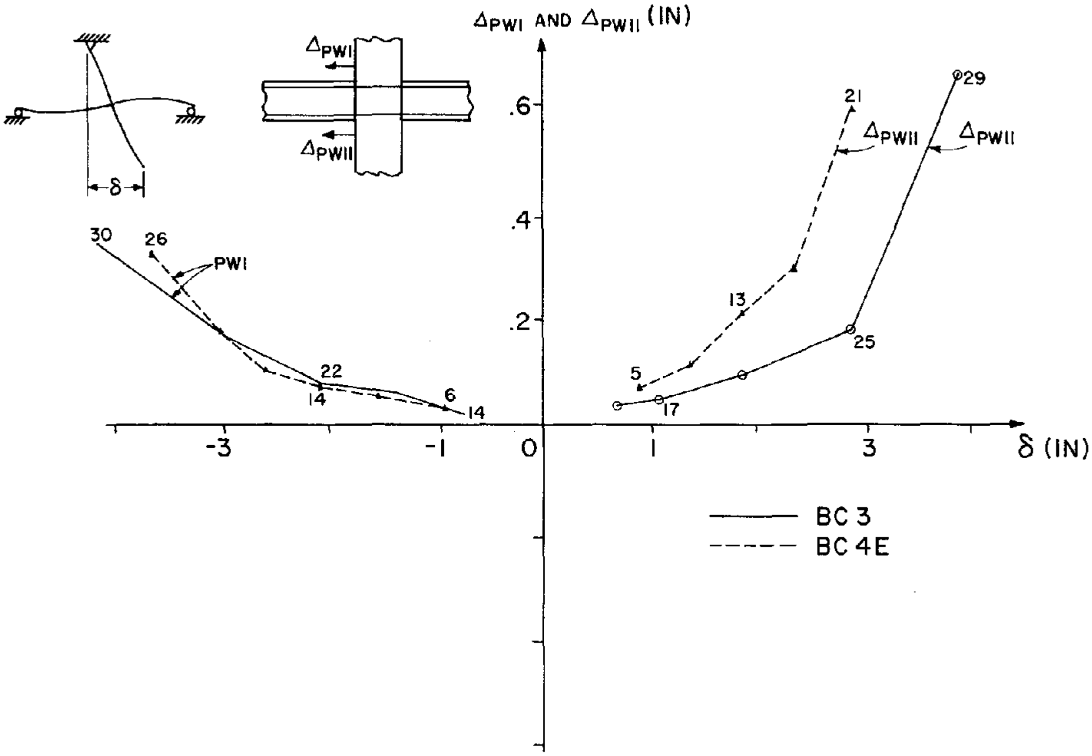

Fig. 7.5 Slip Envelope at Different Displacement Levels

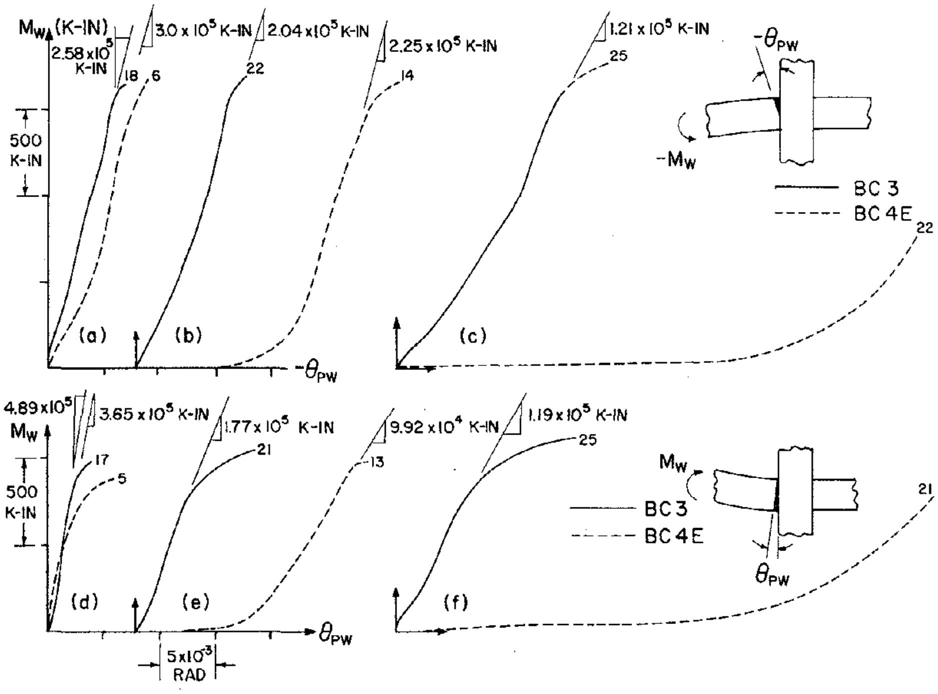

Fig. 7.6 Comparison of Pull-out Stiffness for Specimens BC3 and BC4E

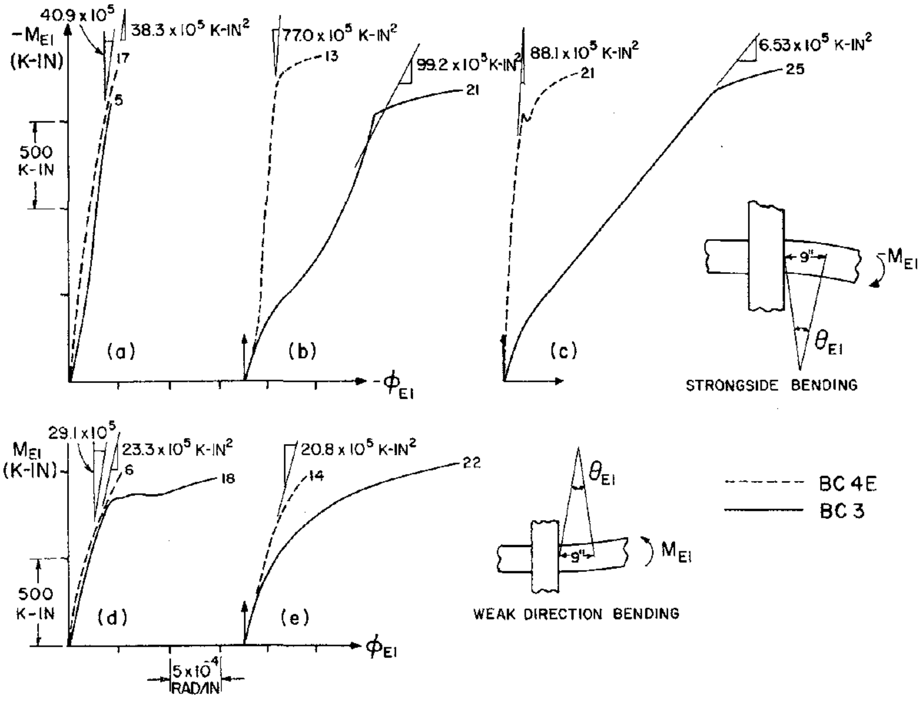

Fig. 7.7 Comparison of Bending Stiffness for Specimens BC3 and BC4E

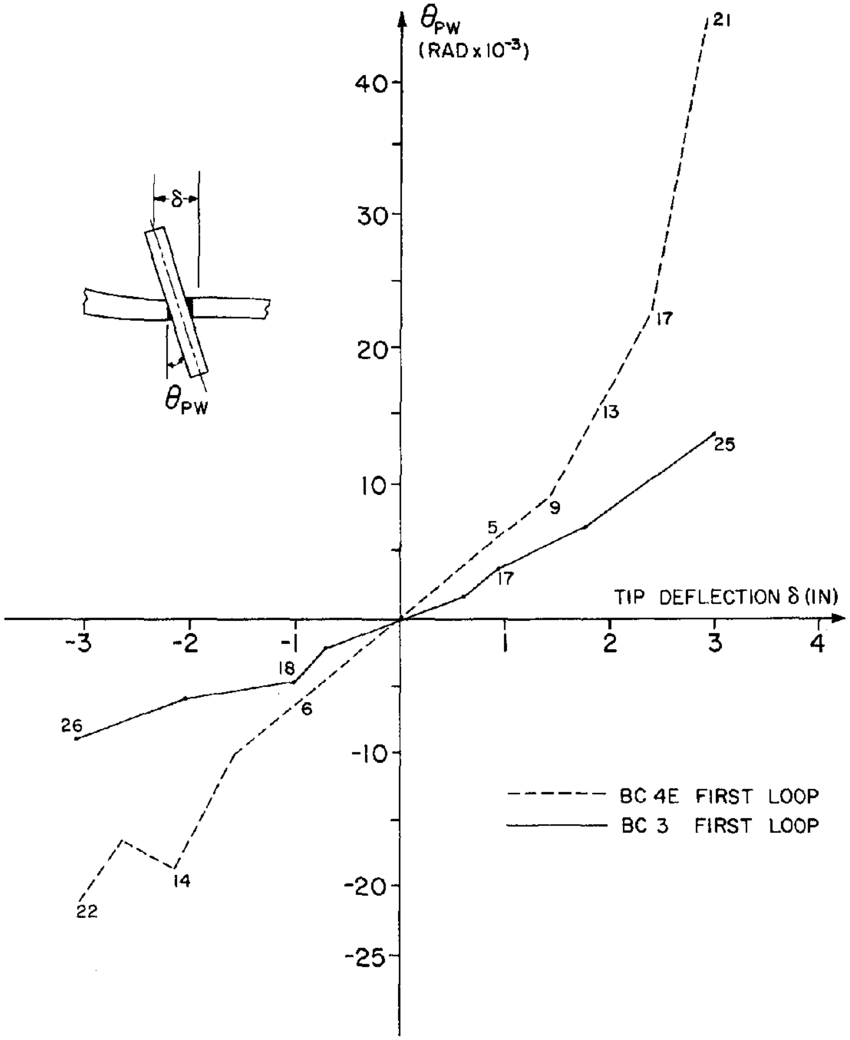

Fig. 7.8 Envelope of Pull-out Rotation vs. Horizontal Deflection

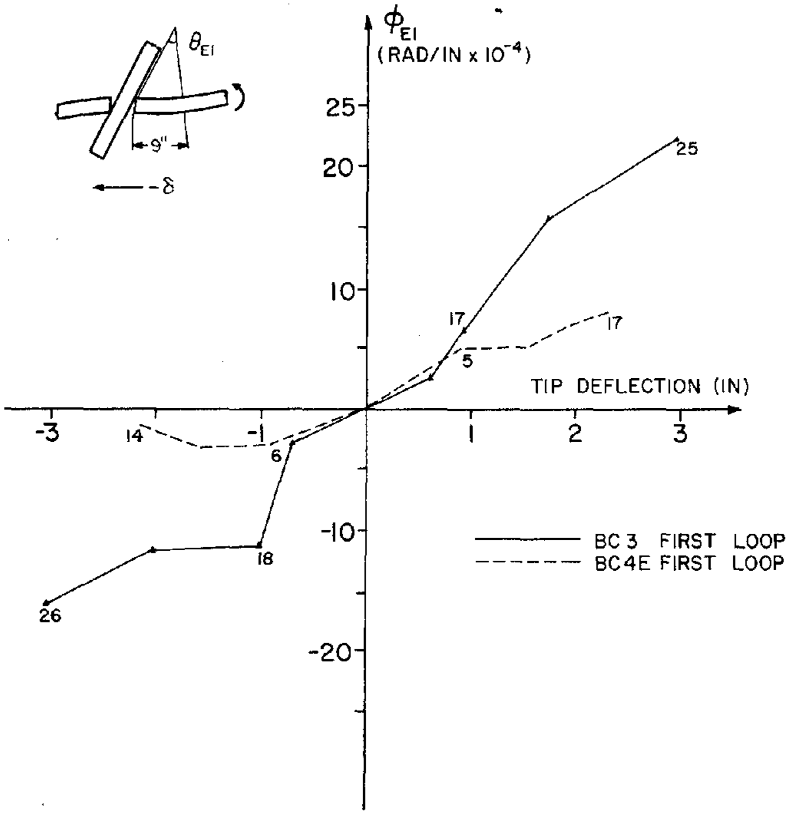

Fig. 7.9 Envelope of Beam Rotation vs. Horizontal Deflection

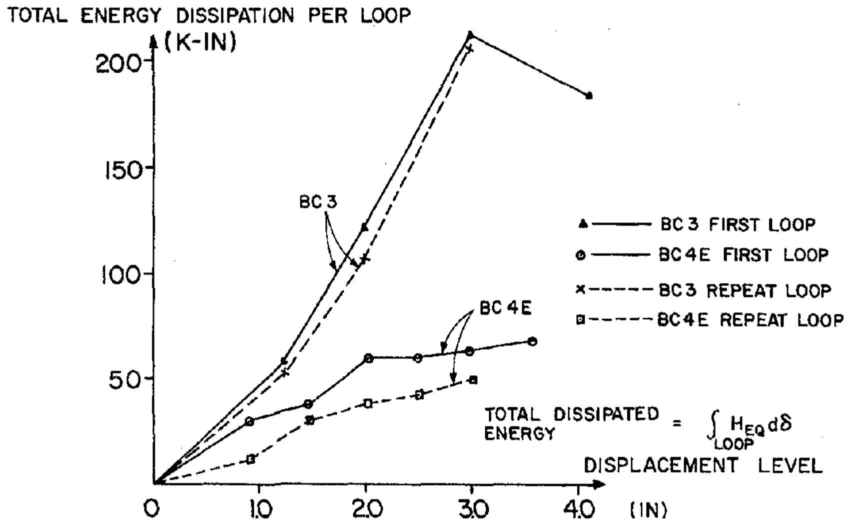

Fig. 7.10 Total Energy Dissipation vs. Displacement Level

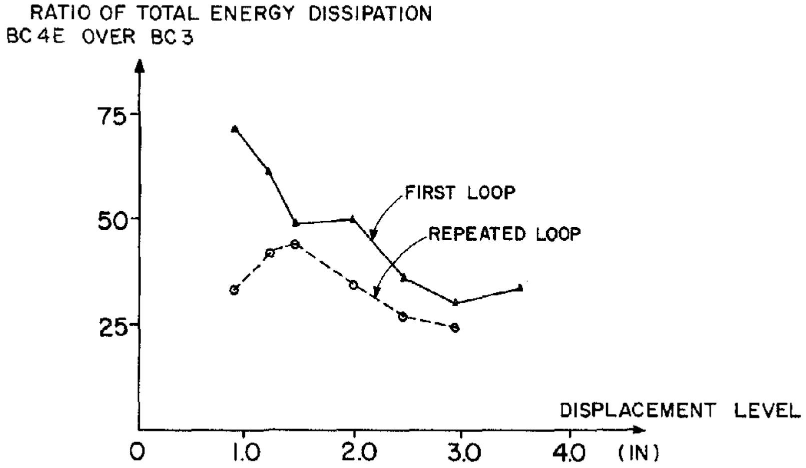

Fig. 7.11 Comparison of Energy Dissipation Between Specimens BC4E and BC3

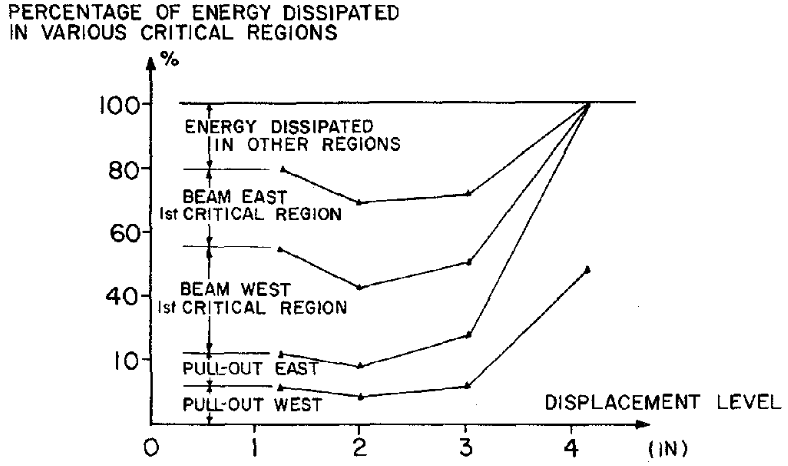

Fig. 7.12 Percentage of Energy Dissipated in Critical Regions of BC3 (First Cycle)

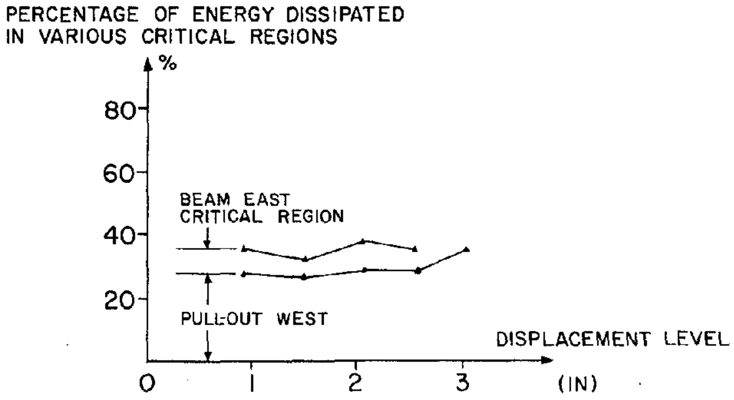

Fig. 7.13 Percentage of Energy Dissipated in Critical Regions of BC4E (First Cycle)

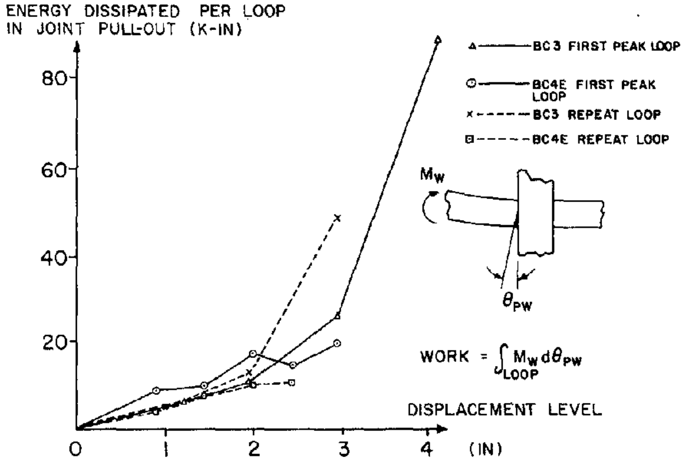

Fig. 7.14 Energy Dissipated in the Joint at Different Displacement Levels in Specimens BC3 and BC4E

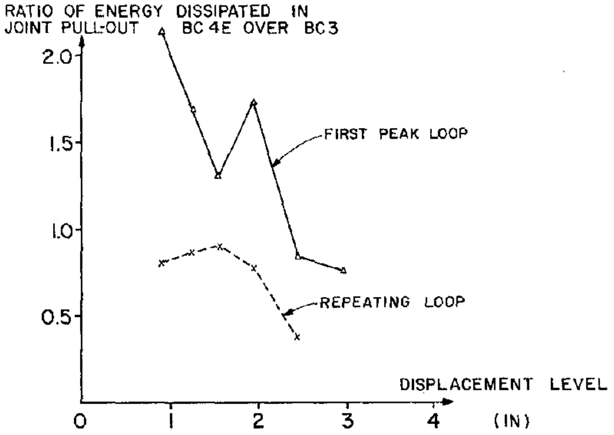

Fig. 7.15 Comparison of Energy Dissipated in the Joint by BC3 and BC4E

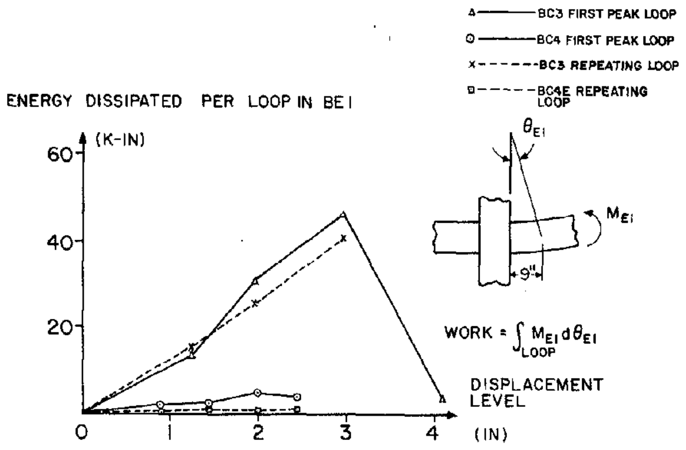

Fig. 7.16 Energy Dissipated per Loop in BE1

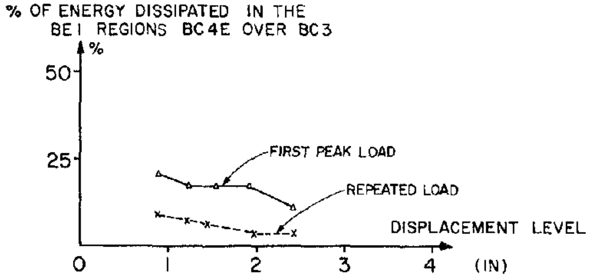

Fig. 7.17 Percentage of Energy Dissipated in the BE1 Regions of BC3 and BC4E

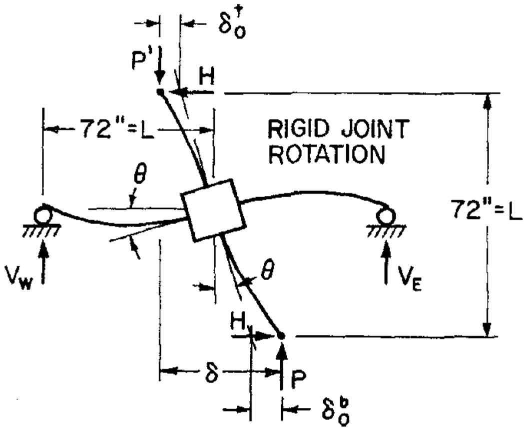

Fig. 8.1 Deformed Configuration of the Beam-Column Subassemblage with Rigid Joint

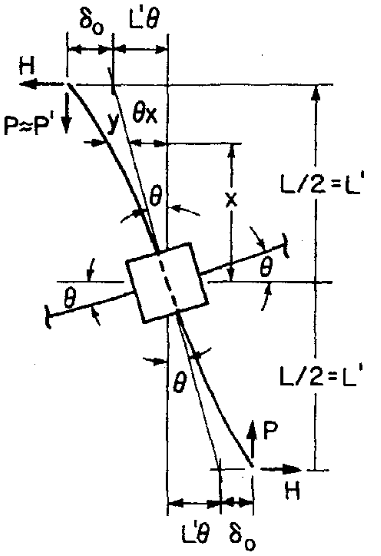

Fig. 8.2 Deflection Due to Column Deformation and Fixed End Rotation

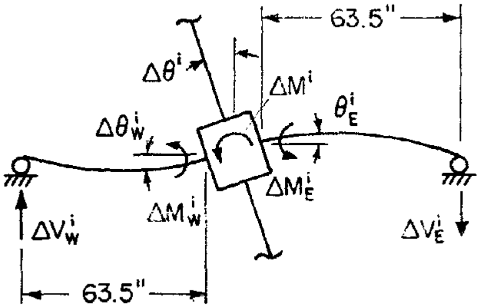

Fig. 8.3 Deformed Shape of the Beams

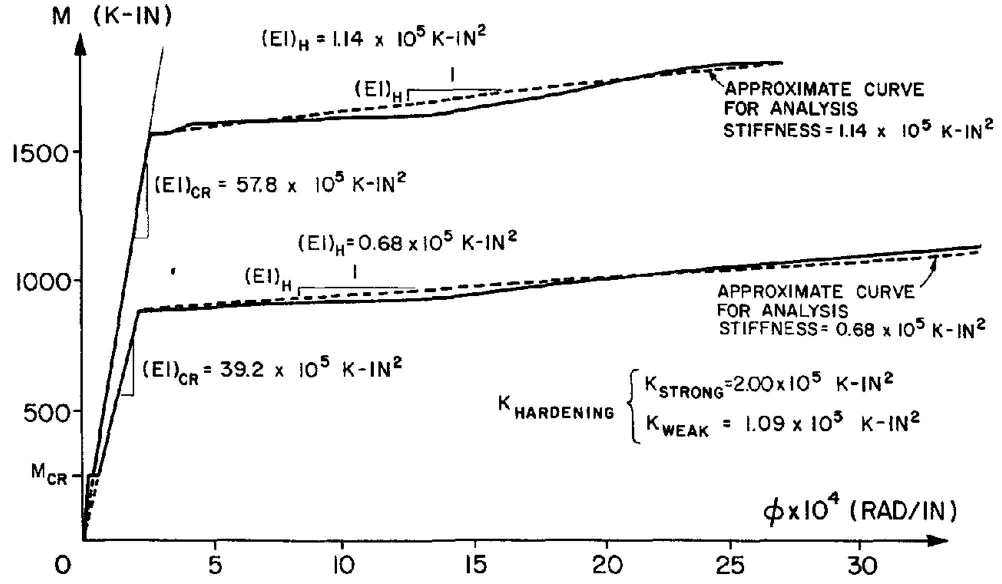

Fig. 8.4 Theoretical and Approximate Bilinear M-ϕ Diagrams

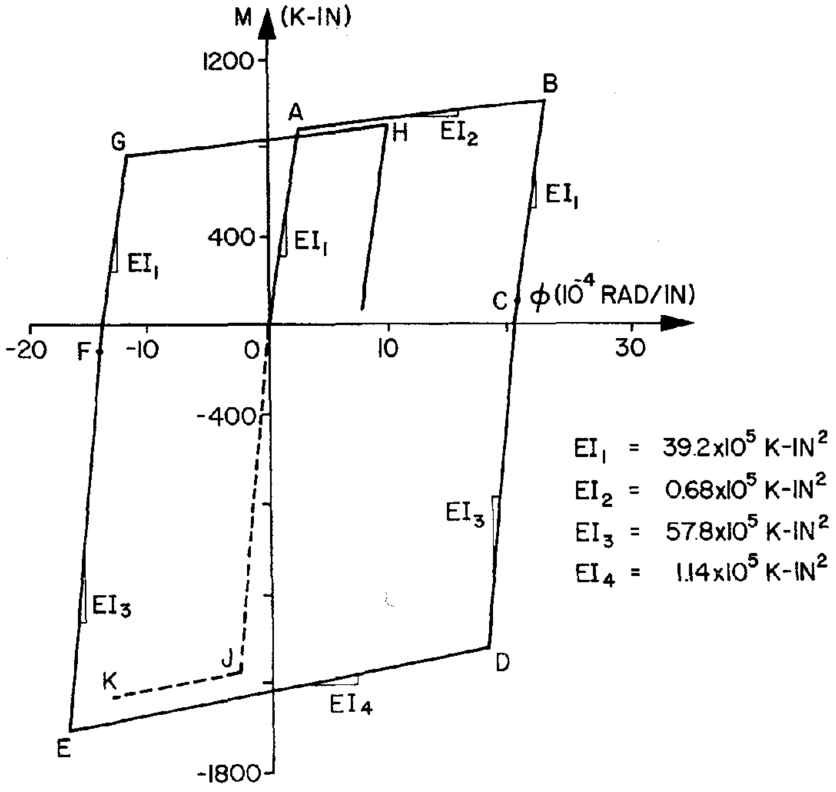

Fig. 8.5 Idealized Calculated Moment Curvature Diagram for BC4 Beams

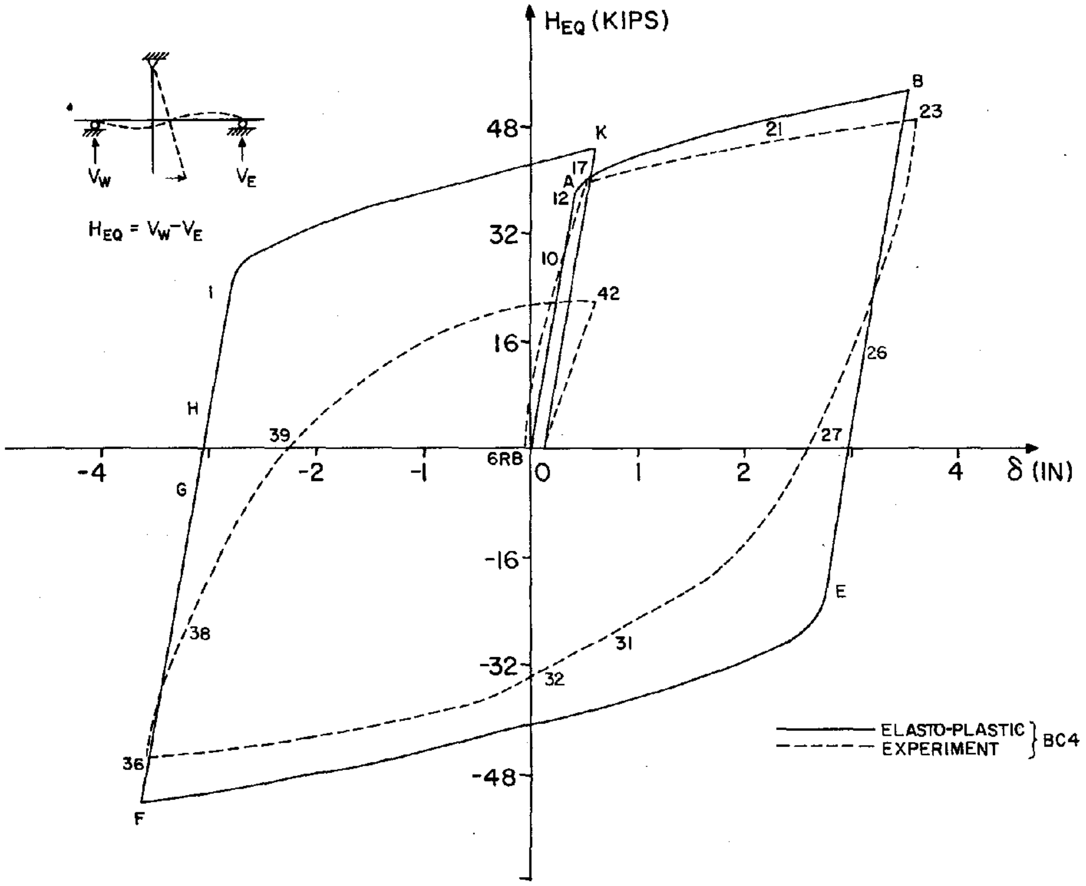

Fig. 8.6 Comparison Between Experimental and Predicted H_{EQ}-δ Diagrams for BC4 Using Elasto-Plastic Model

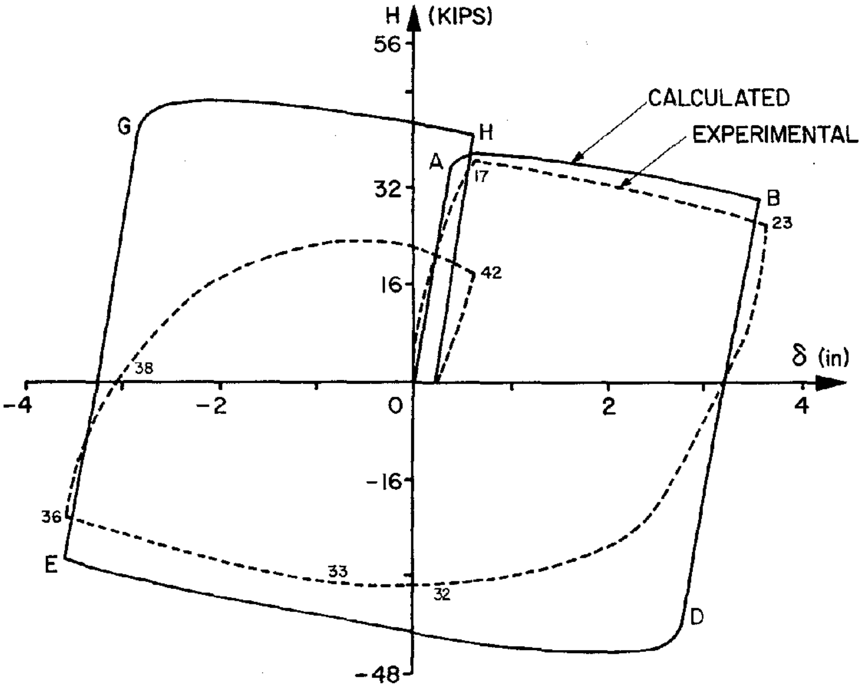

Fig. 8.7 Comparison Between Experimental and Predicted H_{EQ}-δ Diagrams for BC4 Using Elasto-Plastic Model

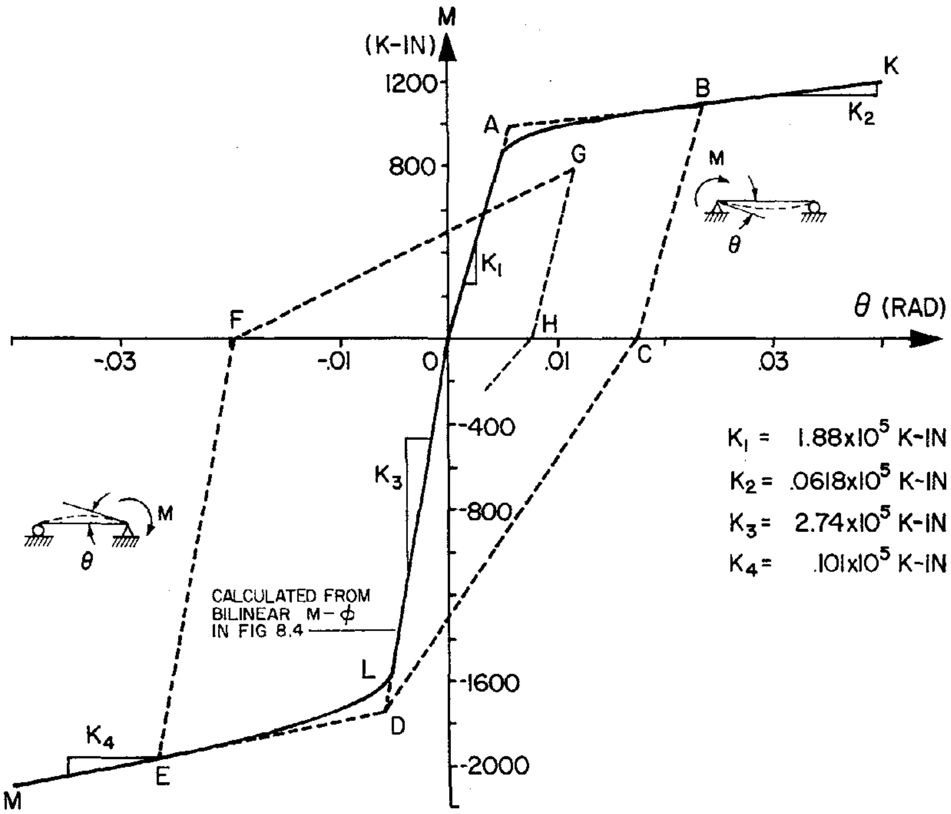

Fig. 8.8 Calculated M-θ Diagram for BC4 Beams Due to an End Moment M. Dashed Lines Illustrate Degrading Model

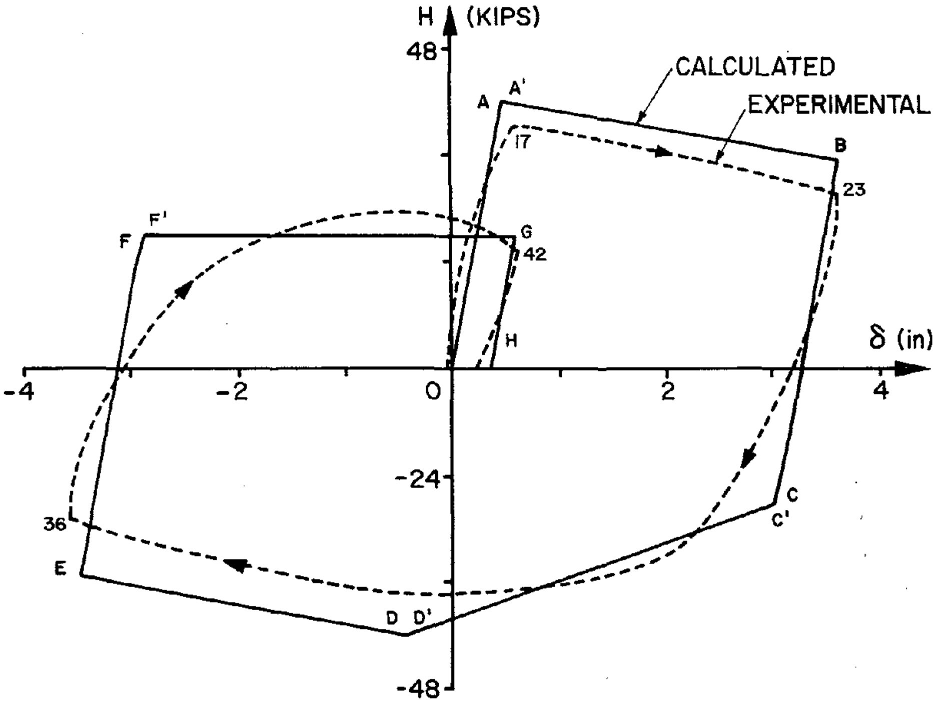

Fig. 8.9 Comparison Between Experimental and Calculated H-δ Diagrams for BC4 Using Degrading Model

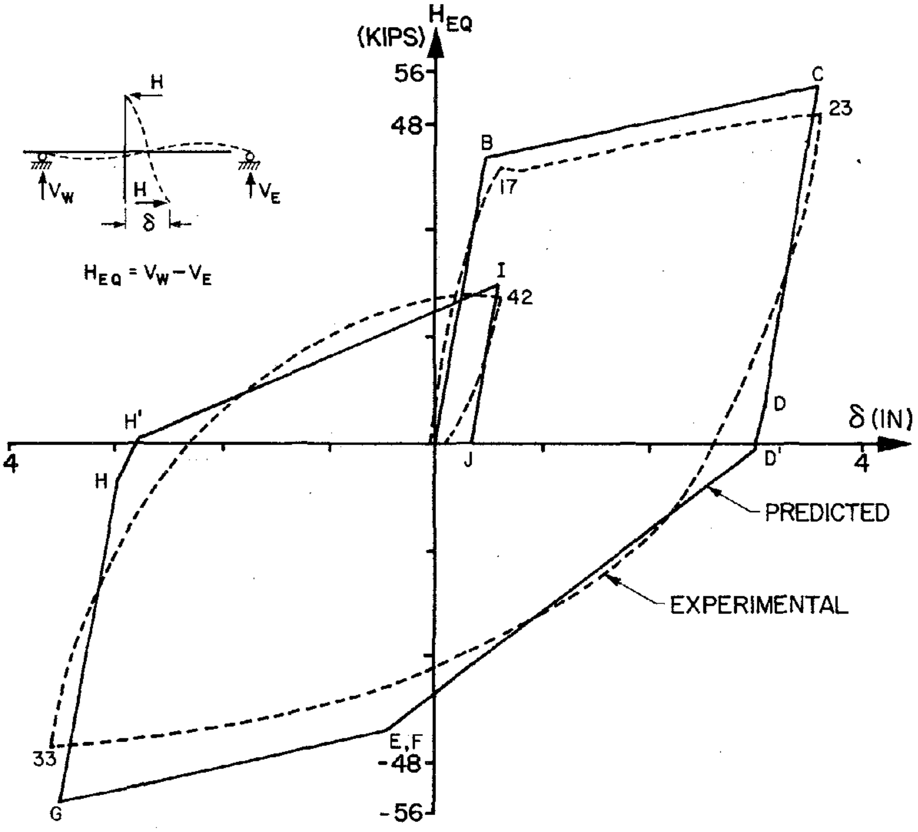

Fig. 8.10 Comparison Between Experimental and Calculated H_{EQ}-δ Diagrams for BC4 Using Degrading Model

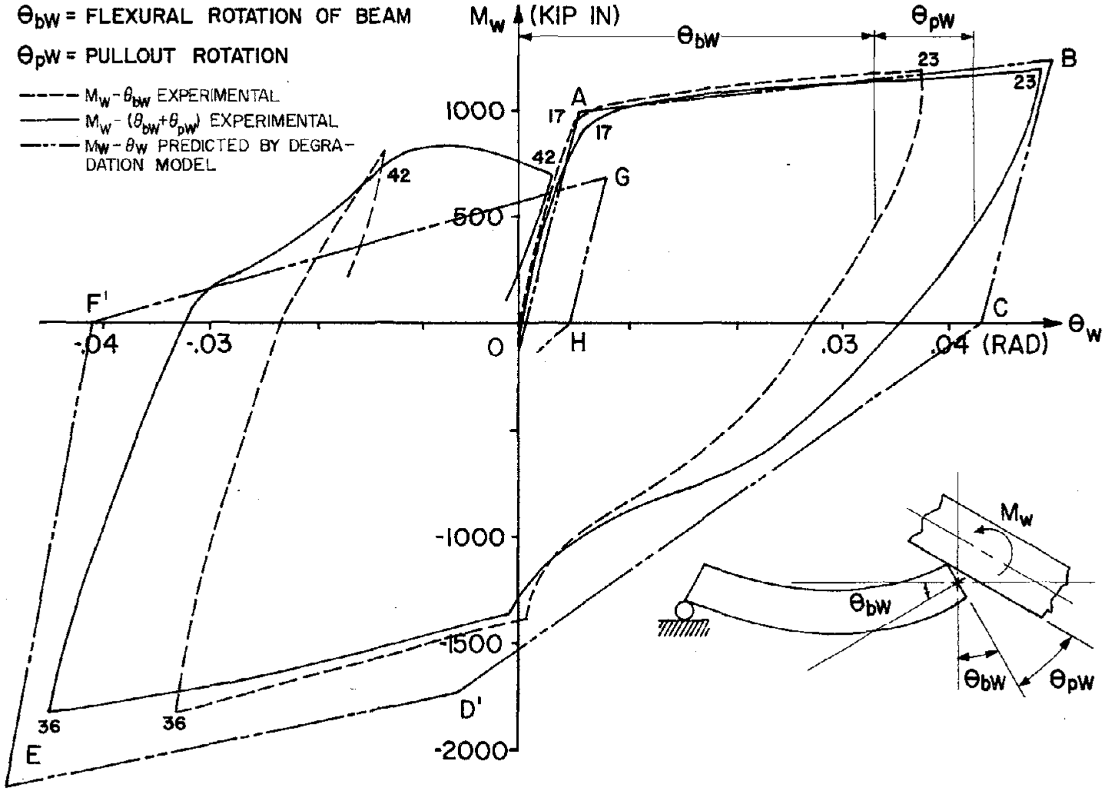

Fig. 8.11 Comparison of Experimental and Calculated West Beam End Rotations for BC4

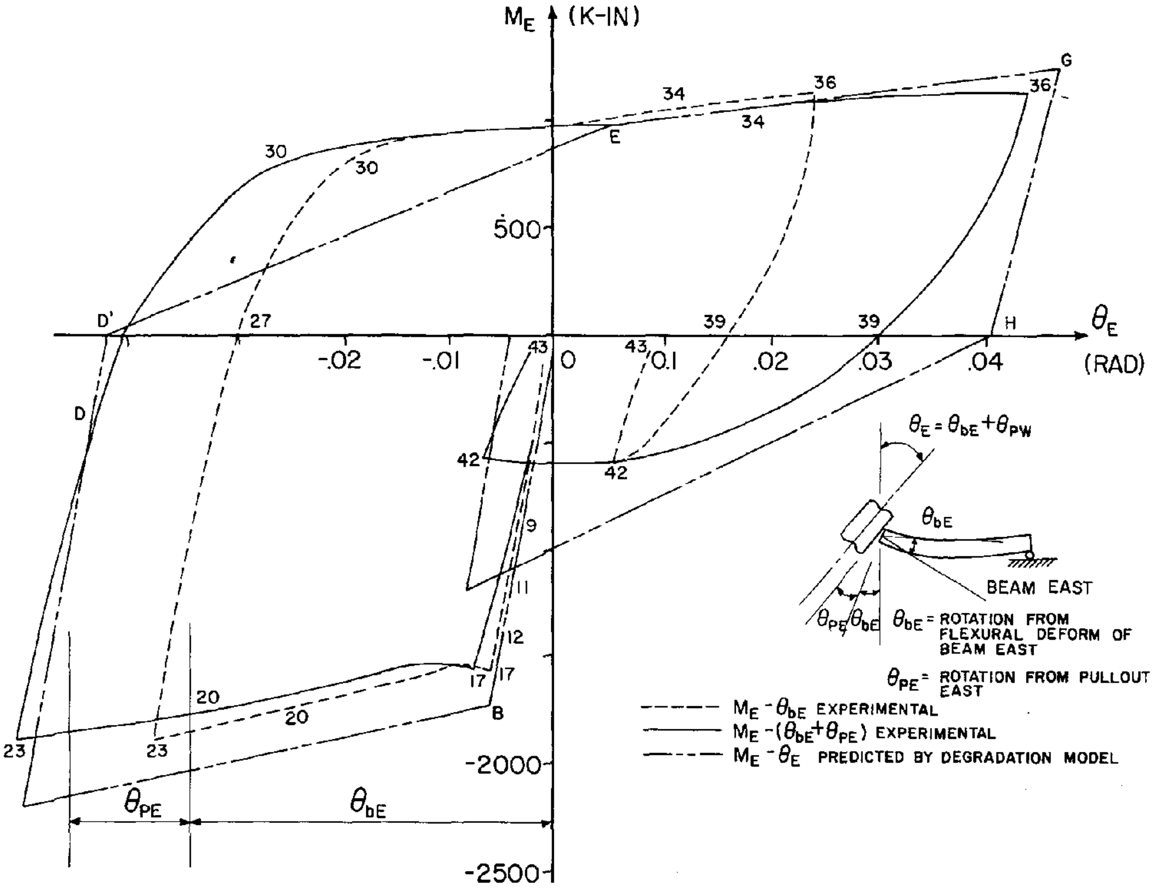

Fig. 8.12 Comparison of Experimental and Calculated East Beam End Rotations for BC4

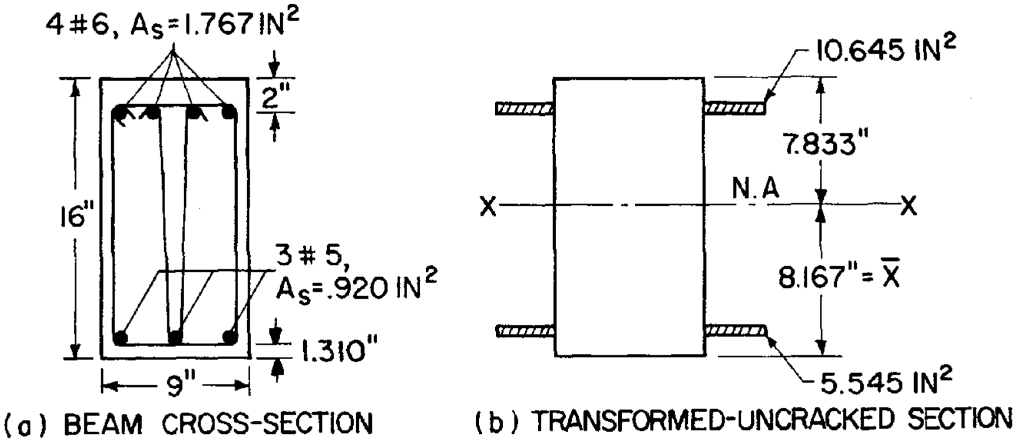

Fig. A.1 Beam Section

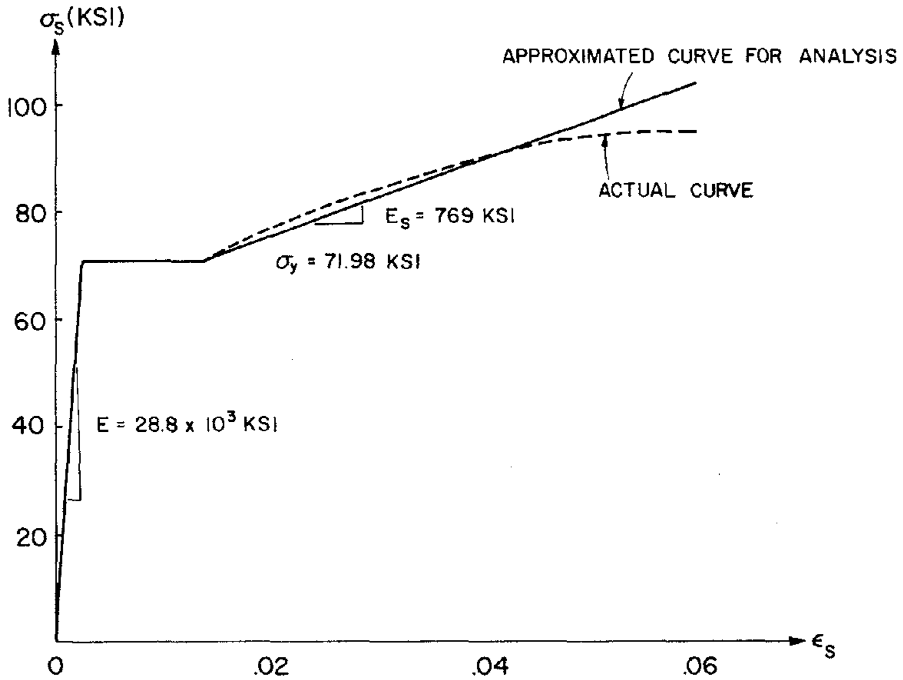

Fig. A.2 Actual and Approximate $\sigma_s - \varepsilon_s$ Curve

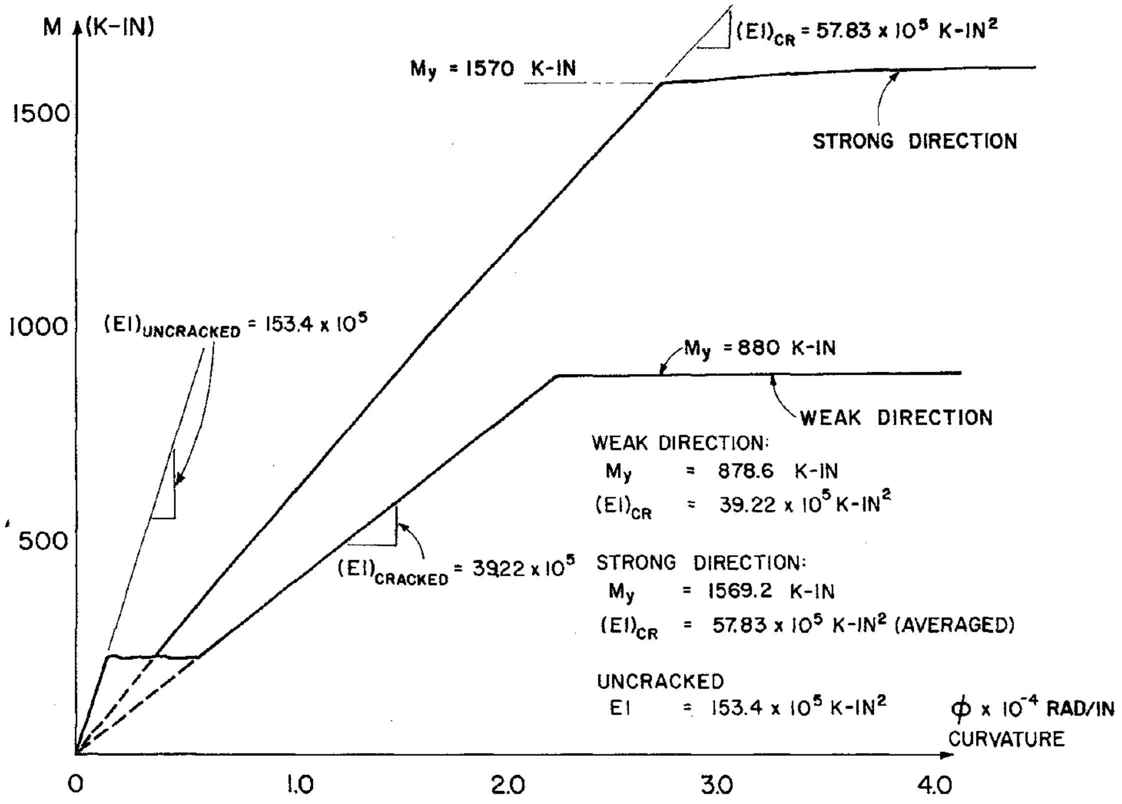

Fig. A.3 Calculated M-ϕ Diagram (Elastic and First Yield Range)

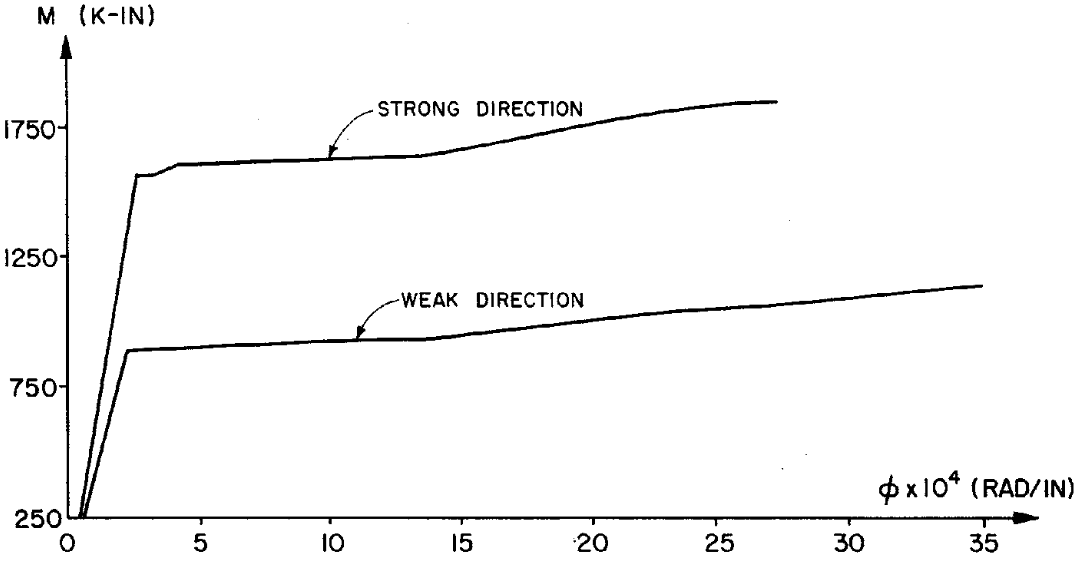

Fig. A.4 Calculated M-ϕ Diagram (Yield and Strain Hardening Range)

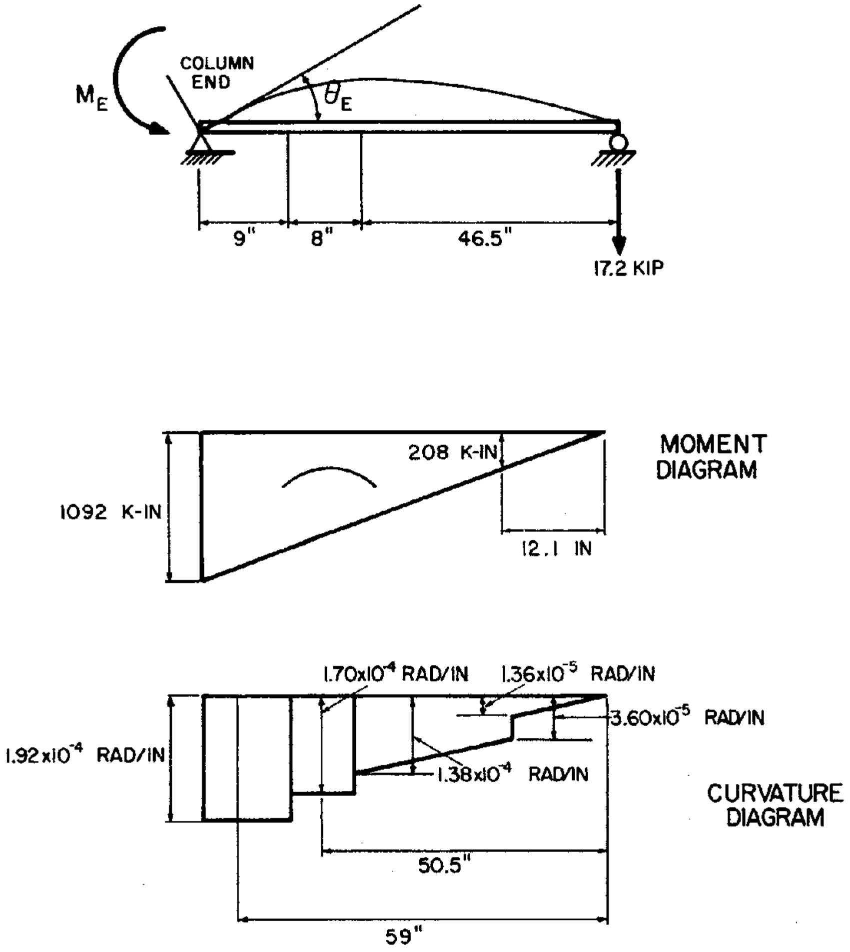

Fig. B.1 Deflected Beam, Moment, and Curvature Diagrams

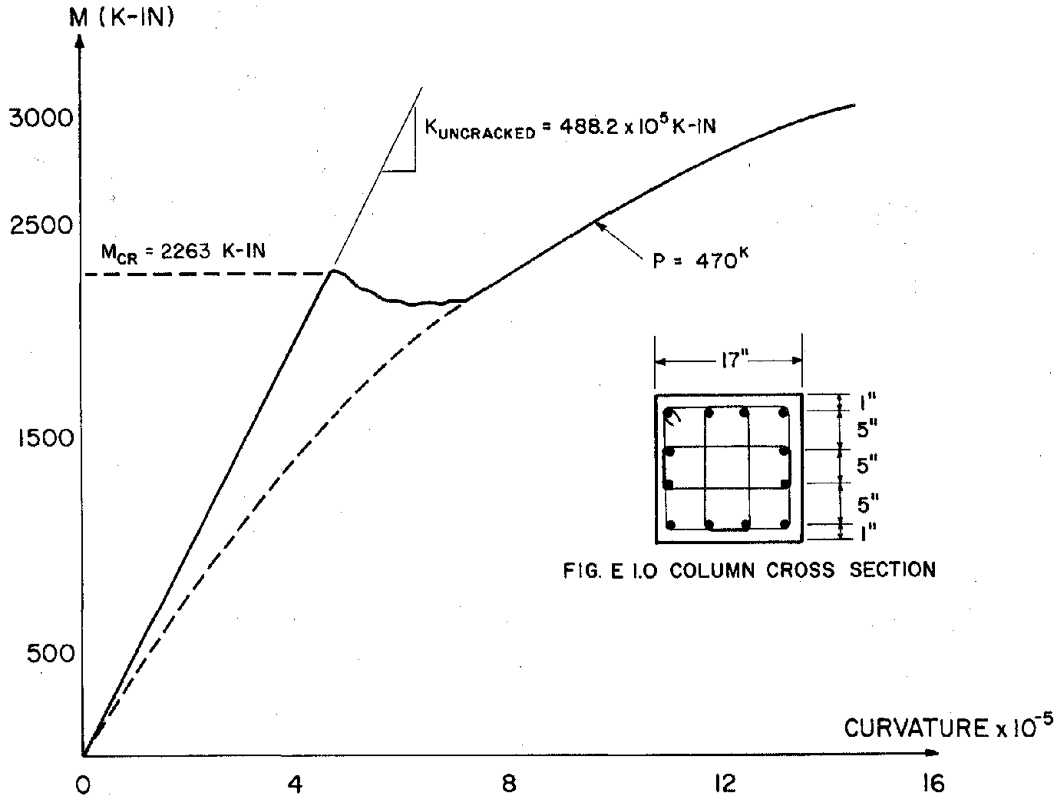

Fig. D.1 M-ϕ Diagram for Column with 470 kip Axial Load

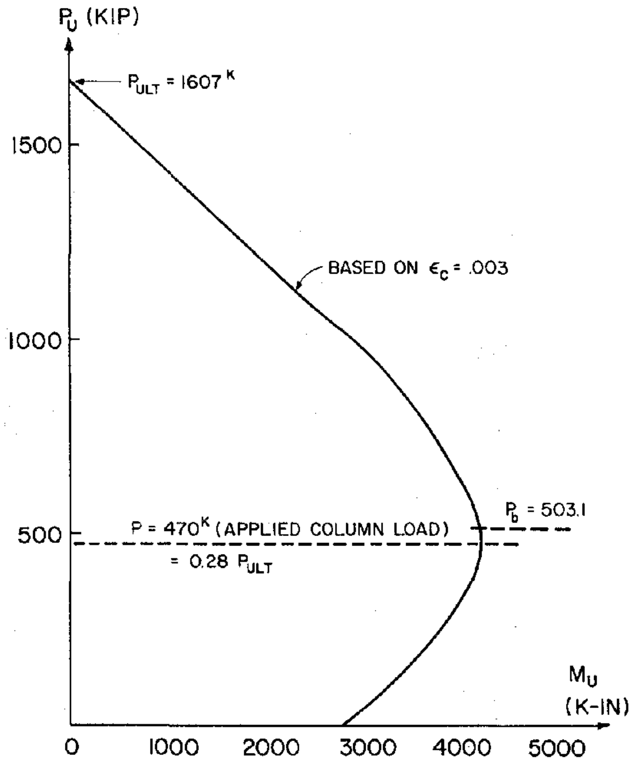

Fig. D.2 Column Interaction Curve

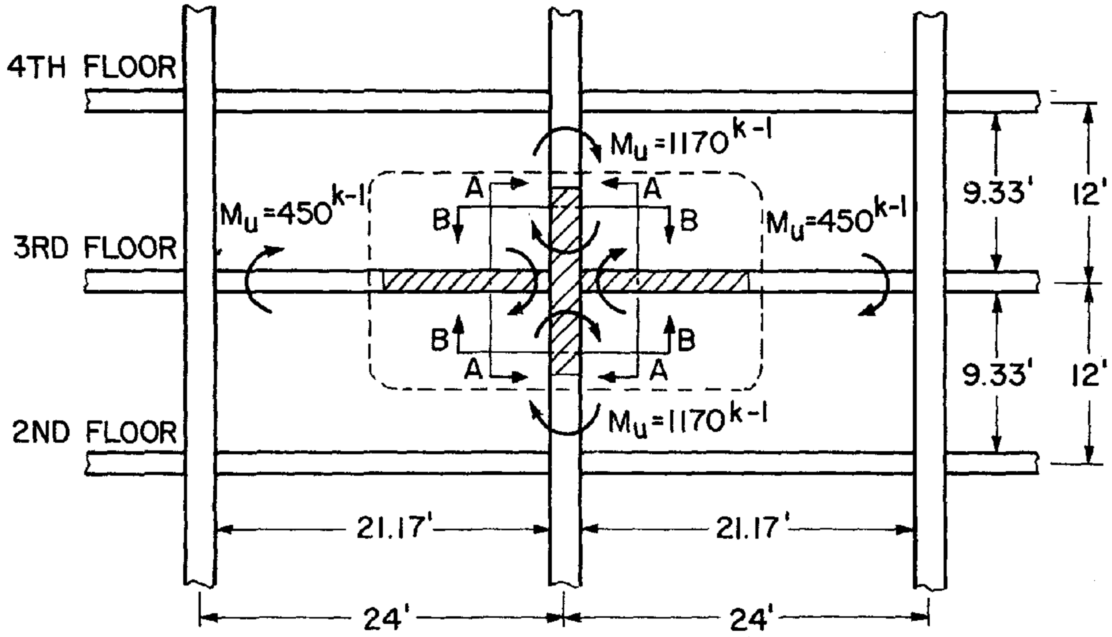

(a) Prototype Frame and Design Moments

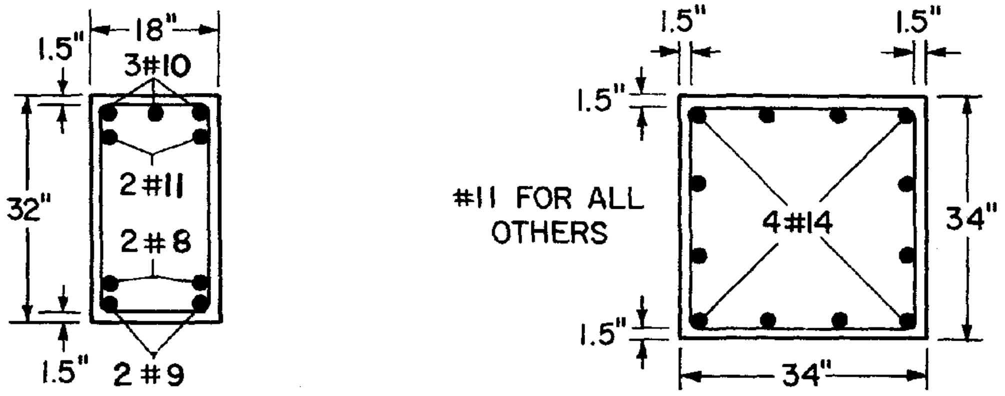

(b) Prototype Beam Section (A-A)

(c) Prototype Column Section (B-B)

Fig. E.1 Detail of Prototype Frame

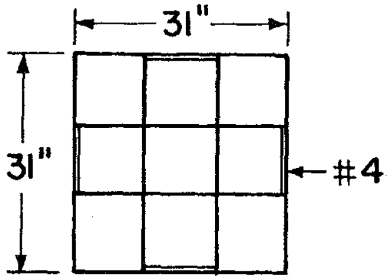

Fig. E.2 Stirrups in Prototype Column

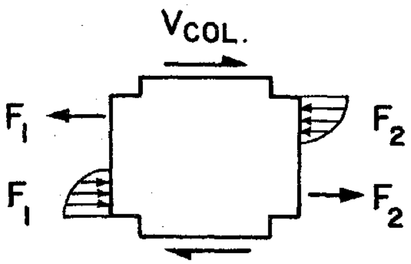

Fig. E.3 Joint Free-Body Diagram

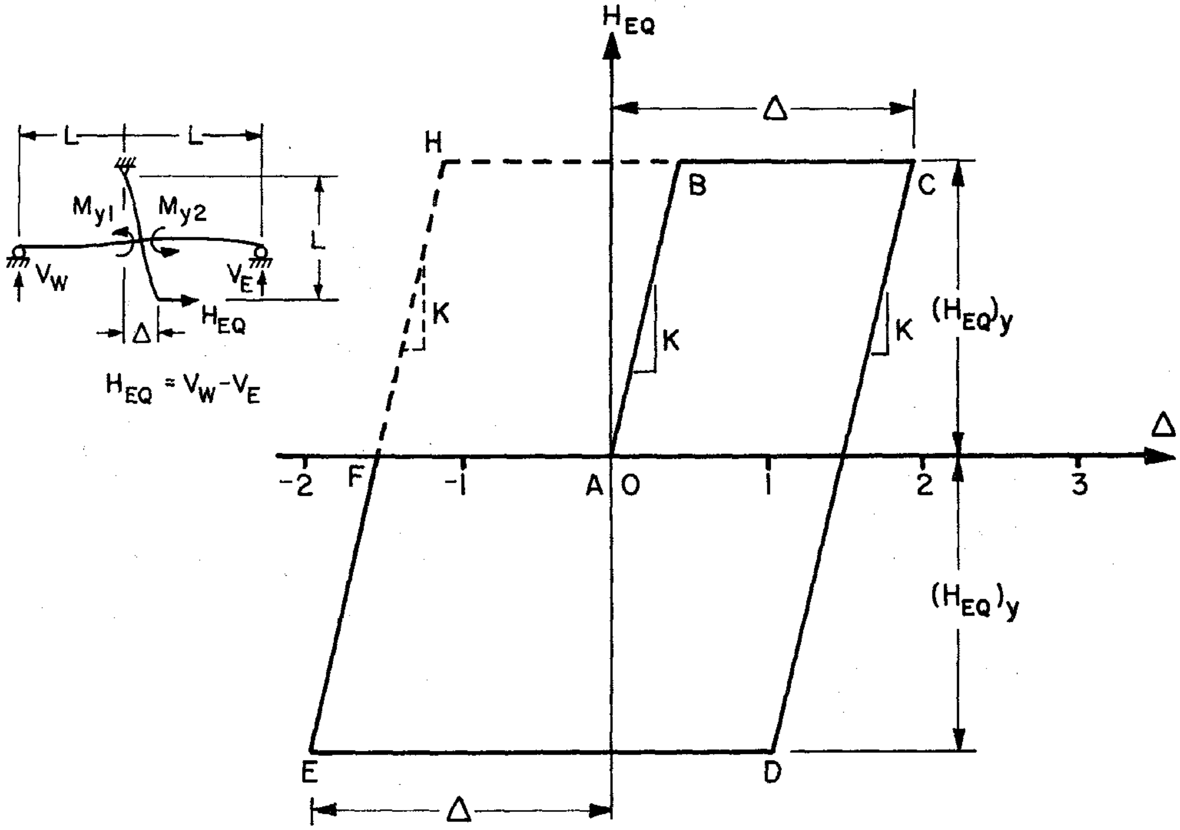

Fig. F.1 $H_{EQ} - \Delta$ Calculated Using Elasto-Plastic Model

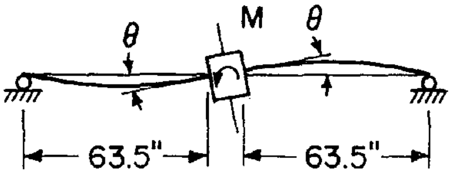

Fig. F.2 Joint Rotation Due to Flexibility of Beams

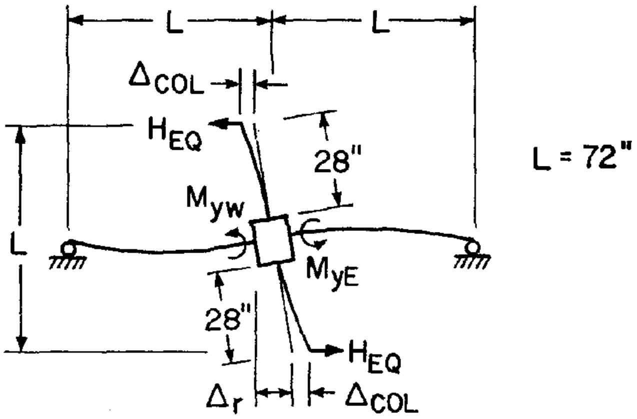

Fig. F.3 Subassemblage Deformation

APPENDIX A

This appendix contains calculations of the flexural bending properties of the beams in subassemblage BC4. This includes:

1) Uncracked section stiffnesses
2) Cracking moments
3) Moment curvature diagrams.

For brevity, the flexural bending properties of sections which have four #6 bars in tension will be called "strong direction" properties. Those with three #5 bars in tension will be called "weak direction" properties (see Fig. A.1a and A.1b).

A.1 Uncracked Section Stiffness

The modulus of elasticity of the concrete at 18 days, E_c, from Fig. 2.4 is

$$E_c = 4.10 \times 10^6 \text{ psi}$$

The modulus of elasticity of the steel reinforcement, E_s, is taken from Fig. A.2.

$$E_s = 28.8 \times 10^3 \text{ ksi}$$

$$\therefore \quad n = \frac{E_s}{E_c} = \frac{28.8 \times 10^3}{4.10 \times 10^3} = 7.02$$

The transformed-section concrete area = 16×9 + 10.6 + 5.5

= 160 in^2 (see Fig. A1)

$$\bar{x} = \frac{5.5\times1.31 + 10.6\times14 + 144\times8}{160} = 8.17 \text{ in.}$$

$$I_x = 5.5(8.17-1.31)^2 + 10.6(5.83)^2 + 9\times16^3/12 + 9\times16\times0.17^2 = 3700 \text{ in.}^4$$

The uncracked section stiffness, $(EI)_{uncr}$, $= M/\phi = I_x E_c$

$$= 3700 \times 4.10 \times 10^3$$

$$(EI)_{uncr} = 152 \times 10^5 \text{ k-in.}^2$$

A.2 Cracking Moments, M_{cr}

A.2.1 Weak-Direction Cracking Moment

The maximum tensile strength of the concrete as determined from splitting tensile tests is 450 psi (see Table 3-II).

$$M_{crw} = \frac{\sigma I_x}{c} = \frac{0.45 \times 3700}{8.17}$$

$$= 204 \text{ k-in.}$$

A.2.2 Strong Direction Cracking Moment

$$M_{crs} = \frac{0.450 \times 3700}{7.83} = 213 \text{ k-in.}$$

Since the two cracking moments are nearly equal, the value of M_{cr} in all further calculations is taken as the average of the M_{crw} and M_{crs}.

$$\therefore M_{cr} = 208 \text{ k-in.}$$

A.3 Moment-Curvature Diagrams for the Beam Sections

To model moment-curvature diagrams for the BC4 beams some assumptions concerning the behavior of reinforced concrete under flexural loads were made. Two assumptions: that plane sections remain plane under bending; and that the tensile strength of the concrete is zero, are generally accepted approximations. Other assumptions made are that the characteristic concrete stress-strain curve, including the prolonged descending branch, is that of the 18-day curve shown in Fig. 2.4, and the characteristic steel stress-strain curve is the tri-linear approximation shown in Fig. A.2.

Figure A.3 illustrates the M-ϕ relation in the elastic range while Fig. A.4 shows the yielding as well as post yield range for weak and strong directions of bending.

Table A.1 gives some of the numerical values of the important flexural bending properties for the beam section.

APPENDIX B

Calculations for modifying the elastic range BC4 member stiffness by including the flexibility of the joints.

Calculations are the same for both the east beam and pull-out east as for the west beam and pull-out west. Only the flexural stiffness of the beam and rotation of the joint are considered since the influence of shear deformation in the beam is small and can be neglected. Except for regions up to 17 in. from the column faces (the critical regions whose stiffnesses are listed in Table 4.1) the stiffnesses of the rest of the beam as described in Appendix A are:

cracking moment = 208 k-in.
cracked section stiffness of the weak side = 39.2×10^5 k-in^2
cracked section stiffness of the strong side = 57.8×10^5 k-in^2
uncracked section stiffness = 152×10^5 k-in^2

The bending moment diagram shown in Fig. B.1 is constructed by using the average beam end reaction between LP 9 - LP 12, $V_E = 17.2$ kip. From the curvature stiffnesses mentioned above, the curvature variation along the beam is established, and the fixed-end rotation is determined by integrating the curvature over the length of the beam.

Rotation including pull-out

$$\theta_{\varepsilon} = \frac{1090}{5.83 \times 10^{5}} + 1.92 \times 10^{-4} \times 9 \times \frac{59}{63.5} + 1.70 \times 10^{-4} \times 8 \times \frac{50.5}{63.5}$$

$$+ \frac{(1.38 \times 10^{-4} - 3.60 \times 10^{-5})(34.4)(12.1 + \frac{2}{3}\ (34.4))}{2\ (63.5)} +$$

$$+ \frac{3.60 \times 10^{-5}(34.4)(12.1 + \frac{1}{2}\ (34.4))}{63.5} + \frac{1.36 \times 10^{-5}(12.1)^{2}(\frac{2}{3})}{2\ (63.5)}$$

$$= 1.87 \times 10^{-3} + 1.61 \times 10^{-3} + 1.08 \times 10^{-3} + 9.68 \times 10^{-4}$$

$$+ 5.71 \times 10^{-4} + 1.05 \times 10^{-5}$$

$$= 6.11 \times 10^{-3} \text{ rad}$$

$$K_E = \frac{1090}{6.11 \times 10^{-3}} = 1.78 \times 10^{5} \text{ k-in.}$$

Rotation excluding pull-out

$$\theta_E = 1.61 \times 10^{-3} + 1.08 \times 10^{-3} + 9.68 \times 10^{-4} + 5.71 \times 10^{-4} + 1.05 \times 10^{-5}$$

$$= 4.24 \times 10^{-3}$$

$$K_E = \frac{1090}{4.24 \quad 10^{-3}} = 2.57 \times 10^{5} \text{ k-in.}$$

$$\text{and} \quad \therefore \quad \frac{K_E \text{ including pull-out}}{K_E \text{ excluding pull-out}} = 0.69 \ .$$

APPENDIX C

WORKING LOAD BENDING MOMENT AND DIAGONAL TENSION CRACKING LOAD FOR BC4 BEAMS

C.1 Allowable Bending Moment

The allowable working stresses are: (see UBC 2610-2611)

$$\text{for concrete in compression:} \quad f_c = 0.45\, f'_c$$

$$\text{for deformed rebars } (f_y = 60 \text{ ksi}): \quad f_s = 0.40\, f_y$$

Weak direction: The allowable steel stress governs, hence

$$M_a = f_s A_s jd + C'_s \left(\frac{kd}{3} - d'\right)$$

where $j = 1 - \frac{k}{3}$, C'_s = force in compression steel

and $k = \left[n^2(\rho' + \rho)^2 + 2n\left(\rho + \frac{\rho' d'}{d}\right)\right]^{\frac{1}{2}} - n(\rho + \rho')$

$$M_{AW} = 293 \text{ k-in.}$$

Strong direction: Similar to the weak direction, the steel stress governs and the moment at working stress level is

$$M_{AS} = 534 \text{ k-in.}$$

C.2 Diagonal Tension Cracking Load

The beams are assumed to exhibit diagonal tension cracks when the nominal shear stress v_c reaches the value

$$v_c = 1.9\sqrt{f'_c} + 2500\, \rho \frac{V_u d}{M_u} \qquad \text{(ACI-1971, EQN. 11-4)}$$

Based on this value for v_c the predicted shears at cracking are

weak direction: $V_c = 17.7$ k

strong direction: $V_c = 17.4$ k

APPENDIX D

PROPERTIES OF THE COLUMN

D.1 Axial Load Causing Yielding in the Column, P_y

$$P_{max} = (A_g - A_s)f'_c + A_s f_y$$

The column section shown in Fig. D.1 has a $P = 1510$ k

$$\therefore \frac{P}{P_y} = \frac{470}{1510} = 0.31$$

D.2 Uncracked Section Stiffness and Cracking Moment

Following the same procedures used in A.1 and recognizing the effects of the axial load $P = 470$ kip leads

$$M_{cr} = 2260 \text{ k-in.,} \quad \text{and}$$

an uncracked section stiffness

$$K_{uncr} = 48.8 \times 10^6 \text{ k-in}^2$$

D.3 Moment Curvature Diagram

Following the computational procedures outlined in A.3 and recognizing the effects of 470 k axial load, the M-ϕ diagram constructed is shown in Fig. D.1.

D.4 Column Interaction Curve

Figure D.2 shows the column interaction curve.

APPENDIX E

DESIGN OF THE SUBASSEMBLAGES

The prototype subassemblages are models of a third story beam-column joint of a 20-story R/C ductile moment resisting frame, shown in Fig. 2.1. The ultimate subassemblage design moments and its beam and column reinforcement are taken from Ref. [11] and are shown in Figs. E.1a to E.1c. Calculations of the ultimate moment capacities in this appendix are based on the design material properties of $f'_c = 4000$ psi and $f_y = 60$ ksi.

E.1 Beam Section

The amount of longitudinal reinforcement in the prototype near the column faces consists of

Bottom Reinforcement 2#8 + 2#9 for $A_s = 3.58\ \text{in}^2$,

and Top Reinforcement 2#11 + 3#10 for $A_s = 1.93\ \text{in}^2$.

For a half scale model, the required bottom reinforcement

$$A_s = \frac{3.58}{4} = 0.90\ \text{in}^2 \quad (\text{provided } 3\#5 \quad A_s = 0.92)$$

and the required top reinforcement

$$A_s = \frac{6.93}{4} = 1.73\ \text{in}^2 \quad (\text{provided } 4\#5 \quad A_s = 1.77).$$

The ratio of provided bottom reinforcement to top is $\frac{0.92}{1.77} = 0.52$.

The beam sections of the prototype and the model are shown in Fig. E.1b and Fig. A.1a, respectively.

E.2 Design Beam Shear Capacity (Prototype)

From Ref. [11], the simple span shear force at the column face is due to:

Concrete dead load + Girder dead load = 23.9 k

Reduced live load = 7.8 k

V_{D+L} = 31.7 k

$$V_u = \frac{M_u^A + M_u^B}{L} + 1.4\ V_{D+L}$$

where M_u^A and M_u^B are the ultimate moment capacities of the beams, for bending in the strong and weak directions, see Fig. E.1a, and L equals the span length.

From Ref. [11], we have

$$M_u^A = 750 \text{ k-ft}, \quad M_u^B = 450 \text{ k-ft}$$

Therefore

$$V_u = \frac{1200}{21.17} + 1.4(31.7) = 101 \text{ k}$$

$$v_u = \frac{V_u}{bd} = \frac{101 \times 1000}{18 \times 28} = 200 \text{ psi} .$$

while $$v_c = 2\phi\sqrt{f'_c} = 2 \times 0.85 \times \sqrt{4000} = 108 \text{ psi},$$

$$d \approx 28''$$

and $$V_c = v_c\ bd = \frac{108 \times 18 \times 28}{10^3} = 54.4 \text{ k}$$

$$V'_u = V_u - V_c = 101 - 54.4 = 46.6 \text{ k}$$

The maximum allowable stirrup spacing, s, according to the UBC and ACI codes, is determined as follows. Since $v_c < 6\sqrt{f'_c}$, a maximum spacing of d/2 is tried (UBC 2617-g).

$$\frac{d}{2} = 14 \text{ in.}$$

However,

$$\text{(UBC 2617-d)} \quad s = \frac{\phi f_y d}{V'_u} Av{,}\text{min} = \frac{0.85 \times 60 \times 28 \times .40}{46.6} = 12.3 \text{ in.} \,,$$

$$\text{(UBC 2617-g)} \quad Av{,}\text{min} = .0015\ bs$$

or

$$s = \frac{0.4}{.0015 \times 18} = 14.8 \text{ in.}$$

$$\text{(ACI EQ. 11-1)} \quad Av{,}\text{min} = \frac{50\ bs}{f_y} = \frac{50 \times 18 \times 14.8}{60 \times 10^3} = 0.22 \text{ in}^2 < 0.4 \text{ in}^2 .$$

However, for seismic loading the maximum spacing of stirrup ties should be less than:

$$\text{(UBC 2630-c)} \quad s = \frac{d}{4} \,; \quad s = \frac{28}{4} = 7 \text{ in.} < 12 \text{ in.}$$

$$s = 16\ db = 8 \text{ in.} > 7 \text{ in.}$$

$$\text{(ACI A.5.9)} \quad \frac{Avd}{s} = 0.15 \begin{cases} A'_s \\ \\ A_s \end{cases} \text{or} \quad s = \frac{.40 \times 28}{.15 \times 6.93} = 10.8 \text{ in.} < \frac{d}{4}$$

Use 7 in. spacing between stirrups with the first stirrup at 2 in. from the column face. Eight stirrups are provided at each end of the beams to cover a region larger than 2d (UBC 2630-c).

E.3 Beam Shear Reinforcement (Model)

For the half scale model, 8#2 closed tie stirrups were placed $\frac{7}{2}$ in. = 3.5 in. apart with the first stirrup at 1 in. from the column face. In addition, #2 hair pin stirrups tie the reinforcing bars not tied by the closed stirrups. (See Fig. 2.3b.) This additional transverse reinforcement is placed in an attempt to prevent the development of local buckling in rebars observed in previous cantilever tests, Ref. [11].

E.4 Column Size and Column Reinforcement

The 34 in. × 34 in. prototype column section with 4#14 + 8#11 bars ($A_s = 21.5\ \text{in}^2$) as longitudinal reinforcement is used in the second and third stories of the building, see Fig. E.1c. For the half scale model, a 17 in. 17 in. column section with 12#6 bars ($A_s = 5.28\ \text{in}^2$) is used, as shown in Fig. 2.3.

E.5 Column Shear Reinforcement (Prototype)

Since the ultimate strength of the column section is larger than that of the beam section (strong column-weak girder design),

$$M_u^T = M_u^B > \frac{1}{2} M_b$$

where M_u^T and M_u^B are the moment capacities of the columns above and below the third floor and M_b is the sum of the moment capacities of the two beams framing into the column. (See Fig. E.1a.)

$$V_u = \frac{M_u^B + \frac{1}{2} M_b}{h} = \frac{1170 + 600}{9.33} = 190\ \text{k}$$

$$\frac{P_d}{A_g f'_c} = \frac{2740}{(34)^2\ 4} = 0.59 > .12$$

where P_d is the maximum design axial load in the column.

$$\therefore\ \text{(UBC 2617-b)}\quad v_c = \phi\left(1.9\sqrt{f'_c} + 2500\,\frac{\rho_w Vd}{M'}\right)$$

but

$$M' = M - N\left(\frac{4t-d}{8}\right)$$

does not apply because by inspection M' is negative.

$$\text{(ACI 11-6)}\quad v_c = 2\phi\sqrt{f'_c}\,(1 + .0005N_u/A_g)\ .$$

Using N in place of N_u as the minimum axial load in the column, N is estimated as $N \approx N_u/1.4 = \frac{2740}{1.4} = 1960k$. Then

$$v_c = 2\phi\sqrt{f'_c}\left(1 + \frac{.0005 \times 1960 \times 10^3}{(34)^2}\right) = 3.7\phi\ \sqrt{f'_c}$$

But the maximum allowable stress is

$$\text{(ACI 11-7, UBC 2617-b)} \qquad v_{cmax} = 3.5\phi\ \sqrt{f'_c(1 + .002\ N/A_g)}$$

$$= 7.3\phi\ \sqrt{f'_c} > 3.7\phi\ \sqrt{f'_c}\ .$$

Therefore $v_c = 3.7\phi\ \sqrt{f'_c} = 3.7 \times .85\ \sqrt{4000} = 199$ psi .

For $b = 34$ in., $d = 31$ in.

$$V_c = \frac{199 \times 34 \times 31}{10^3} = 210^k > V_u$$

Thus the minimum spacing requirement of the stirrups governs and $s = 15.5$ in.

E.6 Design of the Transverse Reinforcement for Confinement Requirements

$$\text{(UBC 2630-4)} \qquad A''_{sh} = 0.45\ ah''\ \frac{f'_c}{f_y h''}\left(\frac{A_g}{A_c} - 1\right)$$

$$= 0.45\ ah''\ \frac{f'_c}{f_y h''}\left(\left(\frac{34}{31}\right)^2 - 1\right)$$

$$= .091\ ah''\ \frac{f'_c}{f_y h''} < 0.12\ ah''\ \frac{f'_c}{f_y h''}$$

$$\therefore A''_{sh} = 0.12\ ah''\ \frac{f'_c}{f_y h''}$$

The prototype uses #4 bars for the column stirrups as shown in Fig. E.2, where we have $h = 31$ in. and $A''_{sh} = 4 \times 0.2 = 0.8$ in^2.

$$a = \frac{0.8 \times 60}{0.12 \times 31 \times 4} = 3.2 \text{ in.} < 15.5 \text{ in.} \quad \text{(for shear)}$$

The model uses #2 rebar with $\frac{3.2}{2} = 1.6$ in. (see Fig. 2.3c).

E.7 Column Joint Reinforcement

When plastic hinges form in the girders, we have

$$V_{col} = \frac{\frac{1}{2} M_b{}^T + \frac{1}{2} M_b{}^B}{\ell_c}$$

$$= \frac{600 + 600}{9.33} = 129 \text{ k}$$

The maximum shear in the joint, see Fig. E.3, is

$$V_j = F_1 + F_2 - V_{col}$$

$$= 6.93 \times 60 + 3.58 \times 60 - 129 = 502 \text{ k}$$

From section E.5, $V_c = 210$ k

$$A_v f_s \frac{d}{s} = V_u - V_s$$

$$s = \frac{f_s d A_v}{v_u - v_c} = \frac{60 \times 31}{502 - 210} A_v = 6.37 A_v$$

Using the stirrups as shown in Fig. E.2 as joint shear reinforcement, then

$$S = 6.37 \times .8 = 5.10 \text{ in.}$$

And the number of stirrups needed is $\frac{26}{5.10} = 5.10$ or 6, where 26 in. is the distance between the top and bottom longitudinal reinforcement in the girder. The prototype uses six stirrups at $\frac{26}{6} = 4.33$ in. apart. The model uses #2 stirrups spaced at $\frac{4.33}{2} = 2.2$ in. spacing.

APPENDIX F

SUBASSEMBLAGE HYSTERETIC LOOPS CALCULATED USING AN ELASTO-PLASTIC MODEL

Calculation of idealized hysteretic loops provides the means by which the subassemblage energy dissipation can be approximated analytically. This calculated energy dissipation serves as a basis for comparison with the actual energy dissipation measured in tests BC4 and BC4E.

The elasto-plastic loop shown in Fig. F.1 is a function of two parameters: the elastic stiffness, k, and the yielding load, $(H_{EQ})_Y$. The subassemblage yielding load is assumed to develop under an $(H_{EQ})_Y$ such that both theoretical beam yielding capacities are reached (see Table A.1). From Fig. F.3 it can be seen that

$$(H_{EQ})_Y = \frac{M_{YW} + M_{YE}}{63.5} = \frac{880 + 1570}{63.5} = 38.6 \text{ k}$$

where M_{YW} = the yield moment in the weak direction

and M_{YE} = the yield moment in the strong direction.

To determine the elastic stiffness of a subassemblage, the following assumptions are made:

1) The effects of joint slippage, shear deformation in the beams, and shear deformation in the connection are negligible.

2) The beam sections are cracked.

Having made the assumptions above the rotational stiffness offered by the beams, as shown in Fig. F.2, is

$$\frac{M}{\theta} = \frac{3(EI)_E}{63.5} + \frac{3(EI)_W}{63.5} \tag{F.1}$$

where $(EI)_E$ and $(EI)_W$ represent the theoretical cracked sectional stiffnesses of the east and west beams taken from Table A.1. From Fig. F.3, it can be seen that

$$M = 72\ H_{EQ}, \quad \Delta_r = \theta \times 72 \tag{F.2}$$

Substituting M, and θ and the section stiffnesses into Eq. F.1 leads to

$$72\ \frac{H_{EQ}}{\Delta_r/72} = \frac{3 \times 39.2 \times 10^5}{63.5} + \frac{3 \times 57.8 \times 10^5}{63.5} = 4.58 \times 10^5$$

$$\Delta_r = \frac{(72)^2}{4.585 \times 10^5} H_{EQ} = 1.13 \times 10^{-2}\ H_{EQ} \tag{F.2}$$

The deflection contributed by the column flexural deformation is

$$\Delta_{col} = \frac{H_{EQ}(28)^3}{3(EI)_{col}} = \frac{H_{EQ}(28)^3}{3 \times 488 \times 10^5}$$

$$= 1.50 \times 10^{-4}\ H_{EQ} \tag{F.3}$$

where $(EI)_{col}$ = flexural sectional stiffness of the column (see Fig. E.1b). The total deflection Δ can be expressed as a function of Δ_{col} and Δ_r, as

$$\Delta = 2\ \Delta_{col} + \Delta_r$$

$$= 1.16 \times 10^{-2}\ H_{EQ}$$

Therefore $$\frac{H_{EQ}}{\Delta} = k = 86.2 \text{ k/in.}$$

At a given displacement level Δ (see Fig. F.1), the energy dissipation is represented by the area enclosed either by the loop OBCDEF, for a subassemblage loaded to first yielding, or by the loop FHCDEF for any cycles after the first yield cycle. For loop OBCDEF, the energy dissipated is

$$u = 3\left(\Delta - \frac{(H_{EQ})_Y}{k}\right)(H_{EQ})_Y$$
$$= 115.74(\Delta - .448) \text{ k-in.} \qquad (F.4)$$

While for loop FHCDEF,

$$u = 4\left(\Delta - \frac{(H_{EQ})_Y}{k}\right)(H_{EQ})_Y$$
$$= 154.32(\Delta - .448) \text{ k-in.} \qquad (F.5)$$

EARTHQUAKE ENGINEERING RESEARCH CENTER REPORTS

NOTE: Numbers in parenthesis are Accession Numbers assigned by the National Technical Information Service; these are followed by a price code. Copies of the reports may be ordered from the National Technical Information Service, 5285 Port Royal Road, Springfield, Virginia, 22161. Accession Numbers should be quoted on orders for reports (PB --- ---) and remittance must accompany each order. Reports without this information were not available at time of printing. Upon request, EERC will mail inquirers this information when it becomes available.

EERC 67-1 "Feasibility Study Large-Scale Earthquake Simulator Facility," by J. Penzien, J.G. Bouwkamp, R.W. Clough and D. Rea - 1967 (PB 187 905)A07

EERC 68-1 Unassigned

EERC 68-2 "Inelastic Behavior of Beam-to-Column Subassemblages Under Repeated Loading," by V.V. Bertero - 1968 (PB 184 888)A05

EERC 68-3 "A Graphical Method for Solving the Wave Reflection-Refraction Problem," by H.D. McNiven and Y. Mengi - 1968 (PB 187 943)A03

EERC 68-4 "Dynamic Properties of McKinley School Buildings," by D. Rea, J.G. Bouwkamp and R.W. Clough - 1968 (PB 187 902)A07

EERC 68-5 "Characteristics of Rock Motions During Earthquakes," by H.B. Seed, I.M. Idriss and F.W. Kiefer - 1968 (PB 188 338)A03

EERC 69-1 "Earthquake Engineering Research at Berkeley," - 1969 (PB 187 906)A11

EERC 69-2 "Nonlinear Seismic Response of Earth Structures," by M. Dibaj and J. Penzien - 1969 (PB 187 904)A08

EERC 69-3 "Probabilistic Study of the Behavior of Structures During Earthquakes," by R. Ruiz and J. Penzien - 1969 (PB 187 886)A06

EERC 69-4 "Numerical Solution of Boundary Value Problems in Structural Mechanics by Reduction to an Initial Value Formulation," by N. Distefano and J. Schujman - 1969 (PB 187 942)A02

EERC 69-5 "Dynamic Programming and the Solution of the Biharmonic Equation," by N. Distefano - 1969 (PB 187 941)A03

EERC 69-6 "Stochastic Analysis of Offshore Tower Structures," by A.K. Malhotra and J. Penzien - 1969 (PB 187 903)A09

EERC 69-7 "Rock Motion Accelerograms for High Magnitude Earthquakes," by H.B. Seed and I.M. Idriss - 1969 (PB 187 940)A02

EERC 69-8 "Structural Dynamics Testing Facilities at the University of California, Berkeley," by R.M. Stephen. J.G. Bouwkamp, R.W. Clough and J. Penzien - 1969 (PB 189 111)A04

EERC 69-9 "Seismic Response of Soil Deposits Underlain by Sloping Rock Boundaries," by H. Dezfulian and H.B. Seed 1969 (PB 189 114)A03

EERC 69-10 "Dynamic Stress Analysis of Axisymmetric Structures Under Arbitrary Loading," by S. Ghosh and E.L. Wilson 1969 (PB 189 026)A10

EERC 69-11 "Seismic Behavior of Multistory Frames Designed by Different Philosophies," by J.C. Anderson and V. V. Bertero - 1969 (PB 190 662)A10

EERC 69-12 "Stiffness Degradation of Reinforcing Concrete Members Subjected to Cyclic Flexural Moments," by V.V. Bertero, B. Bresler and H. Ming Liao - 1969 (PB 202 942)A07

EERC 69-13 "Response of Non-Uniform Soil Deposits to Travelling Seismic Waves," by H. Dezfulian and H.B. Seed - 1969 (PB 191 023)A03

EERC 69-14 "Damping Capacity of a Model Steel Structure," by D. Rea, R.W. Clough and J.G. Bouwkamp - 1969 (PB 190 663)A06

EERC 69-15 "Influence of Local Soil Conditions on Building Damage Potential during Earthquakes," by H.B. Seed and I.M. Idriss - 1969 (PB 191 036)A03

EERC 69-16 "The Behavior of Sands Under Seismic Loading Conditions," by M.L. Silver and H.B. Seed - 1969 (AD 714 982)A07

EERC 70-1 "Earthquake Response of Gravity Dams," by A.K. Chopra - 1970 (AD 709 640)A03

EERC 70-2 "Relationships between Soil Conditions and Building Damage in the Caracas Earthquake of July 29, 1967," by H.B. Seed, I.M. Idriss and H. Dezfulian - 1970 (PB 195 762)A05

EERC 70-3 "Cyclic Loading of Full Size Steel Connections," by E.P. Popov and R.M. Stephen - 1970 (PB 213 545)A04

EERC 70-4 "Seismic Analysis of the Charaima Building, Caraballeda, Venezuela," by Subcommittee of the SEAONC Research Committee: V.V. Bertero, P.F. Fratessa, S.A. Mahin, J.H. Sexton, A.C. Scordelis, E.L. Wilson, L.A. Wyllie, H.B. Seed and J. Penzien, Chairman - 1970 (PB 201 455)A06

EERC 70-5 "A Computer Program for Earthquake Analysis of Dams," by A.K. Chopra and P. Chakrabarti - 1970 (AD 723 994)A05

EERC 70-6 "The Propagation of Love Waves Across Non-Horizontally Layered Structures," by J. Lysmer and L.A. Drake 1970 (PB 197 896)A03

EERC 70-7 "Influence of Base Rock Characteristics on Ground Response," by J. Lysmer, H.B. Seed and P.B. Schnabel 1970 (PB 197 897)A03

EERC 70-8 "Applicability of Laboratory Test Procedures for Measuring Soil Liquefaction Characteristics under Cyclic Loading," by H.B. Seed and W.H. Peacock - 1970 (PB 198 016)A03

EERC 70-9 "A Simplified Procedure for Evaluating Soil Liquefaction Potential," by H.B. Seed and I.M. Idriss - 1970 (PB 198 009)A03

EERC 70-10 "Soil Moduli and Damping Factors for Dynamic Response Analysis," by H.B. Seed and I.M. Idriss - 1970 (PB 197 869)A03

EERC 71-1 "Koyna Earthquake of December 11, 1967 and the Performance of Koyna Dam," by A.K. Chopra and P. Chakrabarti 1971 (AD 731 496)A06

EERC 71-2 "Preliminary In-Situ Measurements of Anelastic Absorption in Soils Using a Prototype Earthquake Simulator," by R.D. Borcherdt and P.W. Rodgers - 1971 (PB 201 454)A03

EERC 71-3 "Static and Dynamic Analysis of Inelastic Frame Structures," by F.L. Porter and G.H. Powell - 1971 (PB 210 135)A06

EERC 71-4 "Research Needs in Limit Design of Reinforced Concrete Structures," by V.V. Bertero - 1971 (PB 202 943)A04

EERC 71-5 "Dynamic Behavior of a High-Rise Diagonally Braced Steel Building," by D. Rea, A.A. Shah and J.G. Bouwkamp 1971 (PB 203 584)A06

EERC 71-6 "Dynamic Stress Analysis of Porous Elastic Solids Saturated with Compressible Fluids," by J. Ghaboussi and E. L. Wilson - 1971 (PB 211 396)A06

EERC 71-7 "Inelastic Behavior of Steel Beam-to-Column Subassemblages," by H. Krawinkler, V.V. Bertero and E.P. Popov 1971 (PB 211 335)A14

EERC 71-8 "Modification of Seismograph Records for Effects of Local Soil Conditions," by P. Schnabel, H.B. Seed and J. Lysmer - 1971 (PB 214 450)A03

EERC 72-1 "Static and Earthquake Analysis of Three Dimensional Frame and Shear Wall Buildings," by E.L. Wilson and H.H. Dovey - 1972 (PB 212 904)A05

EERC 72-2 "Accelerations in Rock for Earthquakes in the Western United States," by P.B. Schnabel and H.B. Seed - 1972 (PB 213 100)A03

EERC 72-3 "Elastic-Plastic Earthquake Response of Soil-Building Systems," by T. Minami - 1972 (PB 214 868)A08

EERC 72-4 "Stochastic Inelastic Response of Offshore Towers to Strong Motion Earthquakes," by M.K. Kaul - 1972 (PB 215 713)A05

EERC 72-5 "Cyclic Behavior of Three Reinforced Concrete Flexural Members with High Shear," by E.P. Popov, V.V. Bertero and H. Krawinkler - 1972 (PB 214 555)A05

EERC 72-6 "Earthquake Response of Gravity Dams Including Reservoir Interaction Effects," by P. Chakrabarti and A.K. Chopra - 1972 (AD 762 330)A08

EERC 72-7 "Dynamic Properties of Pine Flat Dam," by D. Rea, C.Y. Liaw and A.K. Chopra - 1972 (AD 763 928)A05

EERC 72-8 "Three Dimensional Analysis of Building Systems," by E.L. Wilson and H.H. Dovey - 1972 (PB 222 438)A06

EERC 72-9 "Rate of Loading Effects on Uncracked and Repaired Reinforced Concrete Members," by S. Mahin, V.V. Bertero, D. Rea and M. Atalay - 1972 (PB 224 520)A08

EERC 72-10 "Computer Program for Static and Dynamic Analysis of Linear Structural Systems," by E.L. Wilson, K.-J. Bathe, J.E. Peterson and H.H.Dovey - 1972 (PB 220 437)A04

EERC 72-11 "Literature Survey - Seismic Effects on Highway Bridges," by T. Iwasaki, J. Penzien and R.W. Clough - 1972 (PB 215 613)A19

EERC 72-12 "SHAKE-A Computer Program for Earthquake Response Analysis of Horizontally Layered Sites," by P.B. Schnabel and J. Lysmer - 1972 (PB 220 207)A06

EERC 73-1 "Optimal Seismic Design of Multistory Frames," by V.V. Bertero and H. Kamil - 1973

EERC 73-2 "Analysis of the Slides in the San Fernando Dams During the Earthquake of February 9, 1971," by H.B. Seed, K.L. Lee, I.M. Idriss and F. Makdisi - 1973 (PB 223 402)A14

EERC 73-3 "Computer Aided Ultimate Load Design of Unbraced Multistory Steel Frames," by M.B. El-Hafez and G.H. Powell 1973 (PB 248 315)A09

EERC 73-4 "Experimental Investigation into the Seismic Behavior of Critical Regions of Reinforced Concrete Components as Influenced by Moment and Shear," by M. Celebi and J. Penzien - 1973 (PB 215 884)A09

EERC 73-5 "Hysteretic Behavior of Epoxy-Repaired Reinforced Concrete Beams," by M. Celebi and J. Penzien - 1973 (PB 239 568)A03

EERC 73-6 "General Purpose Computer Program for Inelastic Dynamic Response of Plane Structures," by A. Kanaan and G.H. Powell - 1973 (PB 221 260)A08

EERC 73-7 "A Computer Program for Earthquake Analysis of Gravity Dams Including Reservoir Interaction," by P. Chakrabarti and A.K. Chopra - 1973 (AD 766 271)A04

EERC 73-8 "Behavior of Reinforced Concrete Deep Beam-Column Subassemblages Under Cyclic Loads," by O. Küstü and J.G. Bouwkamp - 1973 (PB 246 117)A12

EERC 73-9 "Earthquake Analysis of Structure-Foundation Systems," by A.K. Vaish and A.K. Chopra - 1973 (AD 766 272)A07

EERC 73-10 "Deconvolution of Seismic Response for Linear Systems," by R.B. Reimer - 1973 (PB 227 179)A08

EERC 73-11 "SAP IV: A Structural Analysis Program for Static and Dynamic Response of Linear Systems," by K.-J. Bathe, E.L. Wilson and F.E. Peterson - 1973 (PB 221 967)A09

EERC 73-12 "Analytical Investigations of the Seismic Response of Long, Multiple Span Highway Bridges," by W.S. Tseng and J. Penzien - 1973 (PB 227 816)A10

EERC 73-13 "Earthquake Analysis of Multi-Story Buildings Including Foundation Interaction," by A.K. Chopra and J.A. Gutierrez - 1973 (PB 222 970)A03

EERC 73-14 "ADAP: A Computer Program for Static and Dynamic Analysis of Arch Dams," by R.W. Clough, J.M. Raphael and S. Mojtahedi - 1973 (PB 223 763)A09

EERC 73-15 "Cyclic Plastic Analysis of Structural Steel Joints," by R.B. Pinkney and R.W. Clough - 1973 (PB 226 843)A08

EERC 73-16 "QUAD-4: A Computer Program for Evaluating the Seismic Response of Soil Structures by Variable Damping Finite Element Procedures," by I.M. Idriss, J. Lysmer, R. Hwang and H.B. Seed - 1973 (PB 229 424)A05

EERC 73-17 "Dynamic Behavior of a Multi-Story Pyramid Shaped Building," by R.M. Stephen, J.P. Hollings and J.G. Bouwkamp - 1973 (PB 240 718)A06

EERC 73-18 "Effect of Different Types of Reinforcing on Seismic Behavior of Short Concrete Columns," by V.V. Bertero, J. Hollings, O. Küstü, R.M. Stephen and J.G. Bouwkamp - 1973

EERC 73-19 "Olive View Medical Center Materials Studies, Phase I," by B. Bresler and V.V. Bertero - 1973 (PB 235 986)A06

EERC 73-20 "Linear and Nonlinear Seismic Analysis Computer Programs for Long Multiple-Span Highway Bridges," by W.S. Tseng and J. Penzien - 1973

EERC 73-21 "Constitutive Models for Cyclic Plastic Deformation of Engineering Materials," by J.M. Kelly and P.P. Gillis 1973 (PB 226 024)A03

EERC 73-22 "DRAIN - 2D User's Guide," by G.H. Powell - 1973 (PB 227 016)A05

EERC 73-23 "Earthquake Engineering at Berkeley - 1973," (PB 226 033)A11

EERC 73-24 Unassigned

EERC 73-25 "Earthquake Response of Axisymmetric Tower Structures Surrounded by Water," by C.Y. Liaw and A.K. Chopra 1973 (AD 773 052)A09

EERC 73-26 "Investigation of the Failures of the Olive View Stairtowers During the San Fernando Earthquake and Their Implications on Seismic Design," by V.V. Bertero and R.G. Collins - 1973 (PB 235 106)A13

EERC 73-27 "Further Studies on Seismic Behavior of Steel Beam-Column Subassemblages," by V.V. Bertero, H. Krawinkler and E.P. Popov - 1973 (PB 234 172)A06

EERC 74-1 "Seismic Risk Analysis," by C.S. Oliveira - 1974 (PB 235 920)A06

EERC 74-2 "Settlement and Liquefaction of Sands Under Multi-Directional Shaking," by R. Pyke, C.K. Chan and H.B. Seed 1974

EERC 74-3 "Optimum Design of Earthquake Resistant Shear Buildings," by D. Ray, K.S. Pister and A.K. Chopra - 1974 (PB 231 172)A06

EERC 74-4 "LUSH - A Computer Program for Complex Response Analysis of Soil-Structure Systems," by J. Lysmer, T. Udaka, H.B. Seed and R. Hwang - 1974 (PB 236 796)A05

EERC 74-5 "Sensitivity Analysis for Hysteretic Dynamic Systems: Applications to Earthquake Engineering," by D. Ray 1974 (PB 233 213)A06

EERC 74-6 "Soil Structure Interaction Analyses for Evaluating Seismic Response," by H.B. Seed, J. Lysmer and R. Hwang 1974 (PB 236 519)A04

EERC 74-7 Unassigned

EERC 74-8 "Shaking Table Tests of a Steel Frame - A Progress Report," by R.W. Clough and D. Tang - 1974 (PB 240 869)A03

EERC 74-9 "Hysteretic Behavior of Reinforced Concrete Flexural Members with Special Web Reinforcement," by V.V. Bertero, E.P. Popov and T.Y. Wang - 1974 (PB 236 797)A07

EERC 74-10 "Applications of Reliability-Based, Global Cost Optimization to Design of Earthquake Resistant Structures," by E. Vitiello and K.S. Pister - 1974 (PB 237 231)A06

EERC 74-11 "Liquefaction of Gravelly Soils Under Cyclic Loading Conditions," by R.T. Wong, H.B. Seed and C.K. Chan 1974 (PB 242 042)A03

EERC 74-12 "Site-Dependent Spectra for Earthquake-Resistant Design," by H.B. Seed, C. Ugas and J. Lysmer - 1974 (PB 240 953)A03

EERC 74-13 "Earthquake Simulator Study of a Reinforced Concrete Frame," by P. Hidalgo and R.W. Clough - 1974 (PB 241 944)A13

EERC 74-14 "Nonlinear Earthquake Response of Concrete Gravity Dams," by N. Pal - 1974 (AD/A 006 583)A06

EERC 74-15 "Modeling and Identification in Nonlinear Structural Dynamics - I. One Degree of Freedom Models," by N. Distefano and A. Rath - 1974 (PB 241 548)A06

EERC 75-1 "Determination of Seismic Design Criteria for the Dumbarton Bridge Replacement Structure, Vol. I: Description, Theory and Analytical Modeling of Bridge and Parameters," by F. Baron and S.-H. Pang - 1975 (PB 259 407)A15

EERC 75-2 "Determination of Seismic Design Criteria for the Dumbarton Bridge Replacement Structure, Vol. II: Numerical Studies and Establishment of Seismic Design Criteria," by F. Baron and S.-H. Pang - 1975 (PB 259 408)A11 (For set of EERC 75-1 and 75-2 (PB 259 406))

EERC 75-3 "Seismic Risk Analysis for a Site and a Metropolitan Area," by C.S. Oliveira - 1975 (PB 248 134)A09

EERC 75-4 "Analytical Investigations of Seismic Response of Short, Single or Multiple-Span Highway Bridges," by M.-C. Chen and J. Penzien - 1975 (PB 241 454)A09

EERC 75-5 "An Evaluation of Some Methods for Predicting Seismic Behavior of Reinforced Concrete Buildings," by S.A. Mahin and V.V. Bertero - 1975 (PB 246 306)A16

EERC 75-6 "Earthquake Simulator Study of a Steel Frame Structure, Vol. I: Experimental Results," by R.W. Clough and D.T. Tang - 1975 (PB 243 981)A13

EERC 75-7 "Dynamic Properties of San Bernardino Intake Tower," by D. Rea, C.-Y. Liaw and A.K. Chopra - 1975 (AD/A008 406) A05

EERC 75-8 "Seismic Studies of the Articulation for the Dumbarton Bridge Replacement Structure, Vol. I: Description, Theory and Analytical Modeling of Bridge Components," by F. Baron and R.E. Hamati - 1975 (PB 251 539)A07

EERC 75-9 "Seismic Studies of the Articulation for the Dumbarton Bridge Replacement Structure, Vol. 2: Numerical Studies of Steel and Concrete Girder Alternates," by F. Baron and R.E. Hamati - 1975 (PB 251 540)A10

EERC 75-10 "Static and Dynamic Analysis of Nonlinear Structures," by D.P. Mondkar and G.H. Powell - 1975 (PB 242 434)A08

EERC 75-11 "Hysteretic Behavior of Steel Columns," by E.P. Popov, V.V. Bertero and S. Chandramouli - 1975 (PB 252 365)A11

EERC 75-12 "Earthquake Engineering Research Center Library Printed Catalog," - 1975 (PB 243 711)A26

EERC 75-13 "Three Dimensional Analysis of Building Systems (Extended Version)," by E.L. Wilson, J.P. Hollings and H.H. Dovey - 1975 (PB 243 989)A07

EERC 75-14 "Determination of Soil Liquefaction Characteristics by Large-Scale Laboratory Tests," by P. De Alba, C.K. Chan and H.B. Seed - 1975 (NUREG 0027)A08

EERC 75-15 "A Literature Survey - Compressive, Tensile, Bond and Shear Strength of Masonry," by R.L. Mayes and R.W. Clough - 1975 (PB 246 292)A10

EERC 75-16 "Hysteretic Behavior of Ductile Moment Resisting Reinforced Concrete Frame Components," by V.V. Bertero and E.P. Popov - 1975 (PB 246 388)A05

EERC 75-17 "Relationships Between Maximum Acceleration, Maximum Velocity, Distance from Source, Local Site Conditions for Moderately Strong Earthquakes," by H.B. Seed, R. Murarka, J. Lysmer and I.M. Idriss - 1975 (PB 248 172)A03

EERC 75-18 "The Effects of Method of Sample Preparation on the Cyclic Stress-Strain Behavior of Sands," by J. Mulilis, C.K. Chan and H.B. Seed - 1975 (Summarized in EERC 75-28)

EERC 75-19 "The Seismic Behavior of Critical Regions of Reinforced Concrete Components as Influenced by Moment, Shear and Axial Force," by M.B. Atalay and J. Penzien - 1975 (PB 258 842)A11

EERC 75-20 "Dynamic Properties of an Eleven Story Masonry Building," by R.M. Stephen, J.P. Hollings, J.G. Bouwkamp and D. Jurukovski - 1975 (PB 246 945)A04

EERC 75-21 "State-of-the-Art in Seismic Strength of Masonry - An Evaluation and Review," by R.L. Mayes and R.W. Clough 1975 (PB 249 040)A07

EERC 75-22 "Frequency Dependent Stiffness Matrices for Viscoelastic Half-Plane Foundations," by A.K. Chopra, P. Chakrabarti and G. Dasgupta - 1975 (PB 248 121)A07

EERC 75-23 "Hysteretic Behavior of Reinforced Concrete Framed Walls," by T.Y. Wong, V.V. Bertero and E.P. Popov - 1975

EERC 75-24 "Testing Facility for Subassemblages of Frame-Wall Structural Systems," by V.V. Bertero, E.P. Popov and T. Endo - 1975

EERC 75-25 "Influence of Seismic History on the Liquefaction Characteristics of Sands," by H.B. Seed, K. Mori and C.K. Chan - 1975 (Summarized in EERC 75-28)

EERC 75-26 "The Generation and Dissipation of Pore Water Pressures during Soil Liquefaction," by H.B. Seed, P.P. Martin and J. Lysmer - 1975 (PB 252 648)A03

EERC 75-27 "Identification of Research Needs for Improving Aseismic Design of Building Structures," by V.V. Bertero 1975 (PB 248 136)A05

EERC 75-28 "Evaluation of Soil Liquefaction Potential during Earthquakes," by H.B. Seed, I. Arango and C.K. Chan - 1975 (NUREG 0026)A13

EERC 75-29 "Representation of Irregular Stress Time Histories by Equivalent Uniform Stress Series in Liquefaction Analyses," by H.B. Seed, I.M. Idriss, F. Makdisi and N. Banerjee - 1975 (PB 252 635)A03

EERC 75-30 "FLUSH - A Computer Program for Approximate 3-D Analysis of Soil-Structure Interaction Problems," by J. Lysmer, T. Udaka, C.-F. Tsai and H.B. Seed - 1975 (PB 259 332)A07

EERC 75-31 "ALUSH - A Computer Program for Seismic Response Analysis of Axisymmetric Soil-Structure Systems," by E. Berger, J. Lysmer and H.B. Seed - 1975

EERC 75-32 "TRIP and TRAVEL - Computer Programs for Soil-Structure Interaction Analysis with Horizontally Travelling Waves," by T. Udaka, J. Lysmer and H.B. Seed - 1975

EERC 75-33 "Predicting the Performance of Structures in Regions of High Seismicity," by J. Penzien - 1975 (PB 248 130)A03

EERC 75-34 "Efficient Finite Element Analysis of Seismic Structure - Soil - Direction," by J. Lysmer, H.B. Seed, T. Udaka, R.N. Hwang and C.-F. Tsai - 1975 (PB 253 570)A03

EERC 75-35 "The Dynamic Behavior of a First Story Girder of a Three-Story Steel Frame Subjected to Earthquake Loading," by R.W. Clough and L.-Y. Li - 1975 (PB 248 841)A05

EERC 75-36 "Earthquake Simulator Study of a Steel Frame Structure, Volume II - Analytical Results," by D.T. Tang - 1975 (PB 252 926)A10

EERC 75-37 "ANSR-I General Purpose Computer Program for Analysis of Non-Linear Structural Response," by D.P. Mondkar and G.H. Powell - 1975 (PB 252 386)A08

EERC 75-38 "Nonlinear Response Spectra for Probabilistic Seismic Design and Damage Assessment of Reinforced Concrete Structures," by M. Murakami and J. Penzien - 1975 (PB 259 530)A05

EERC 75-39 "Study of a Method of Feasible Directions for Optimal Elastic Design of Frame Structures Subjected to Earthquake Loading," by N.D. Walker and K.S. Pister - 1975 (PB 257 781)A06

EERC 75-40 "An Alternative Representation of the Elastic-Viscoelastic Analogy," by G. Dasgupta and J.L. Sackman - 1975 (PB 252 173)A03

EERC 75-41 "Effect of Multi-Directional Shaking on Liquefaction of Sands," by H.B. Seed, R. Pyke and G.R. Martin - 1975 (PB 258 781)A03

EERC 76-1 "Strength and Ductility Evaluation of Existing Low-Rise Reinforced Concrete Buildings - Screening Method," by T. Okada and B. Bresler - 1976 (PB 257 906)A11

EERC 76-2 "Experimental and Analytical Studies on the Hysteretic Behavior of Reinforced Concrete Rectangular and T-Beams," by S.-Y.M. Ma, E.P. Popov and V.V. Bertero - 1976 (PB 260 843)A12

EERC 76-3 "Dynamic Behavior of a Multistory Triangular-Shaped Building," by J. Petrovski, R.M. Stephen, E. Gartenbaum and J.G. Bouwkamp - 1976 (PB 273 279)A07

EERC 76-4 "Earthquake Induced Deformations of Earth Dams," by N. Serff, H.B. Seed, F.I. Makdisi & C.-Y. Chang - 1976 (PB 292 065)A08

EERC 76-5 "Analysis and Design of Tube-Type Tall Building Structures," by H. de Clercq and G.H. Powell - 1976 (PB 252 220) A10

EERC 76-6 "Time and Frequency Domain Analysis of Three-Dimensional Ground Motions, San Fernando Earthquake," by T. Kubo and J. Penzien (PB 260 556)A11

EERC 76-7 "Expected Performance of Uniform Building Code Design Masonry Structures," by R.L. Mayes, Y. Omote, S.W. Chen and R.W. Clough - 1976 (PB 270 098)A05

EERC 76-8 "Cyclic Shear Tests of Masonry Piers, Volume 1 - Test Results," by R.L. Mayes, Y. Omote, R.W. Clough - 1976 (PB 264 424)A06

EERC 76-9 "A Substructure Method for Earthquake Analysis of Structure - Soil Interaction," by J.A. Gutierrez and A.K. Chopra - 1976 (PB 257 783)A08

EERC 76-10 "Stabilization of Potentially Liquefiable Sand Deposits using Gravel Drain Systems," by H.B. Seed and J.R. Booker - 1976 (PB 258 820)A04

EERC 76-11 "Influence of Design and Analysis Assumptions on Computed Inelastic Response of Moderately Tall Frames," by G.H. Powell and D.G. Row - 1976 (PB 271 409)A06

EERC 76-12 "Sensitivity Analysis for Hysteretic Dynamic Systems: Theory and Applications," by D. Ray, K.S. Pister and E. Polak - 1976 (PB 262 859)A04

EERC 76-13 "Coupled Lateral Torsional Response of Buildings to Ground Shaking," by C.L. Kan and A.K. Chopra - 1976 (PB 257 907)A09

EERC 76-14 "Seismic Analyses of the Banco de America," by V.V. Bertero, S.A. Mahin and J.A. Hollings - 1976

EERC 76-15 "Reinforced Concrete Frame 2: Seismic Testing and Analytical Correlation," by R.W. Clough and J. Gidwani - 1976 (PB 261 323)A08

EERC 76-16 "Cyclic Shear Tests of Masonry Piers, Volume 2 - Analysis of Test Results," by R.L. Mayes, Y. Omote and R.W. Clough - 1976

EERC 76-17 "Structural Steel Bracing Systems: Behavior Under Cyclic Loading," by E.P. Popov, K. Takanashi and C.W. Roeder - 1976 (PB 260 715)A05

EERC 76-18 "Experimental Model Studies on Seismic Response of High Curved Overcrossings," by D. Williams and W.G. Godden - 1976 (PB 269 548)A08

EERC 76-19 "Effects of Non-Uniform Seismic Disturbances on the Dumbarton Bridge Replacement Structure," by F. Baron and R.E. Hamati - 1976 (PB 282 981)A16

EERC 76-20 "Investigation of the Inelastic Characteristics of a Single Story Steel Structure Using System Identification and Shaking Table Experiments," by V.C. Matzen and H.D. McNiven - 1976 (PB 258 453)A07

EERC 76-21 "Capacity of Columns with Splice Imperfections," by E.P. Popov, R.M. Stephen and R. Philbrick - 1976 (PB 260 378)A04

EERC 76-22 "Response of the Olive View Hospital Main Building during the San Fernando Earthquake," by S. A. Mahin, V.V. Bertero, A.K. Chopra and R. Collins - 1976 (PB 271 425)A14

EERC 76-23 "A Study on the Major Factors Influencing the Strength of Masonry Prisms," by N.M. Mostaghel, R.L. Mayes, R. W. Clough and S.W. Chen - 1976 (Not published)

EERC 76-24 "GADFLEA - A Computer Program for the Analysis of Pore Pressure Generation and Dissipation during Cyclic or Earthquake Loading," by J.R. Booker, M.S. Rahman and H.B. Seed - 1976 (PB 263 947)A04

EERC 76-25 "Seismic Safety Evaluation of a R/C School Building," by B. Bresler and J. Axley - 1976

EERC 76-26 "Correlative Investigations on Theoretical and Experimental Dynamic Behavior of a Model Bridge Structure," by K. Kawashima and J. Penzien - 1976 (PB 263 388)A11

EERC 76-27 "Earthquake Response of Coupled Shear Wall Buildings," by T. Srichatrapimuk - 1976 (PB 265 157)A07

EERC 76-28 "Tensile Capacity of Partial Penetration Welds," by E.P. Popov and R.M. Stephen - 1976 (PB 262 899)A03

EERC 76-29 "Analysis and Design of Numerical Integration Methods in Structural Dynamics," by H.M. Hilber - 1976 (PB 264 410)A06

EERC 76-30 "Contribution of a Floor System to the Dynamic Characteristics of Reinforced Concrete Buildings," by L.E. Malik and V.V. Bertero - 1976 (PB 272 247)A13

EERC 76-31 "The Effects of Seismic Disturbances on the Golden Gate Bridge," by F. Baron, M. Arikan and R.E. Hamati - 1976 (PB 272 279)A09

EERC 76-32 "Infilled Frames in Earthquake Resistant Construction," by R.E. Klingner and V.V. Bertero - 1976 (PB 265 892)A13

UCB/EERC-77/01	"PLUSH - A Computer Program for Probabilistic Finite Element Analysis of Seismic Soil-Structure Interaction," by M.P. Romo Organista, J. Lysmer and H.B. Seed - 1977
UCB/EERC-77/02	"Soil-Structure Interaction Effects at the Humboldt Bay Power Plant in the Ferndale Earthquake of June 7, 1975," by J.E. Valera, H.B. Seed, C.F. Tsai and J. Lysmer - 1977 (PB 265 795)A04
UCB/EERC-77/03	"Influence of Sample Disturbance on Sand Response to Cyclic Loading," by K. Mori, H.B. Seed and C.K. Chan - 1977 (PB 267 352)A04
UCB/EERC-77/04	"Seismological Studies of Strong Motion Records," by J. Shoja-Taheri - 1977 (PB 269 655)A10
UCB/EERC-77/05	"Testing Facility for Coupled-Shear Walls," by L. Li-Hyung, V.V. Bertero and E.P. Popov - 1977
UCB/EERC-77/06	"Developing Methodologies for Evaluating the Earthquake Safety of Existing Buildings," by No. 1 - B. Bresler; No. 2 - B. Bresler, T. Okada and D. Zisling; No. 3 - T. Okada and B. Bresler; No. 4 - V.V. Bertero and B. Bresler - 1977 (PB 267 354)A08
UCB/EERC-77/07	"A Literature Survey - Transverse Strength of Masonry Walls," by Y. Omote, R.L. Mayes, S.W. Chen and R.W. Clough - 1977 (PB 277 933)A07
UCB/EERC-77/08	"DRAIN-TABS: A Computer Program for Inelastic Earthquake Response of Three Dimensional Buildings," by R. Guendelman-Israel and G.H. Powell - 1977 (PB 270 693)A07
UCB/EERC-77/09	"SUBWALL: A Special Purpose Finite Element Computer Program for Practical Elastic Analysis and Design of Structural Walls with Substructure Option," by D.Q. Le, H. Peterson and E.P. Popov - 1977 (PB 270 567)A05
UCB/EERC-77/10	"Experimental Evaluation of Seismic Design Methods for Broad Cylindrical Tanks," by D.P. Clough (PB 272 280)A13
UCB/EERC-77/11	"Earthquake Engineering Research at Berkeley - 1976," - 1977 (PB 273 507)A09
UCB/EERC-77/12	"Automated Design of Earthquake Resistant Multistory Steel Building Frames," by N.D. Walker, Jr. - 1977 (PB 276 526)A09
UCB/EERC-77/13	"Concrete Confined by Rectangular Hoops Subjected to Axial Loads," by J. Vallenas, V.V. Bertero and E.P. Popov - 1977 (PB 275 165)A06
UCB/EERC-77/14	"Seismic Strain Induced in the Ground During Earthquakes," by Y. Sugimura - 1977 (PB 284 201)A04
UCB/EERC-77/15	"Bond Deterioration under Generalized Loading," by V.V. Bertero, E.P. Popov and S. Viwathanatepa - 1977
UCB/EERC-77/16	"Computer Aided Optimum Design of Ductile Reinforced Concrete Moment Resisting Frames," by S.W. Zagajeski and V.V. Bertero - 1977 (PB 280 137)A07
UCB/EERC-77/17	"Earthquake Simulation Testing of a Stepping Frame with Energy-Absorbing Devices," by J.M. Kelly and D.F. Tsztoo - 1977 (PB 273 506)A04
UCB/EERC-77/18	"Inelastic Behavior of Eccentrically Braced Steel Frames under Cyclic Loadings," by C.W. Roeder and E.P. Popov - 1977 (PB 275 526)A15
UCB/EERC-77/19	"A Simplified Procedure for Estimating Earthquake-Induced Deformations in Dams and Embankments," by F.I. Makdisi and H.B. Seed - 1977 (PB 276 820)A04
UCB/EERC-77/20	"The Performance of Earth Dams during Earthquakes," by H.B. Seed, F.I. Makdisi and P. de Alba - 1977 (PB 276 821)A04
UCB/EERC-77/21	"Dynamic Plastic Analysis Using Stress Resultant Finite Element Formulation," by P. Lukkunapvasit and J.M. Kelly - 1977 (PB 275 453)A04
UCB/EERC-77/22	"Preliminary Experimental Study of Seismic Uplift of a Steel Frame," by R.W. Clough and A.A. Huckelbridge 1977 (PB 278 769)A08
UCB/EERC-77/23	"Earthquake Simulator Tests of a Nine-Story Steel Frame with Columns Allowed to Uplift," by A.A. Huckelbridge - 1977 (PB 277 944)A09
UCB/EERC-77/24	"Nonlinear Soil-Structure Interaction of Skew Highway Bridges," by M.-C. Chen and J. Penzien - 1977 (PB 276 176)A07
UCB/EERC-77/25	"Seismic Analysis of an Offshore Structure Supported on Pile Foundations," by D.D.-N. Liou and J. Penzien 1977 (PB 283 180)A06
UCB/EERC-77/26	"Dynamic Stiffness Matrices for Homogeneous Viscoelastic Half-Planes," by G. Dasgupta and A.K. Chopra - 1977 (PB 279 654)A06
UCB/EERC-77/27	"A Practical Soft Story Earthquake Isolation System," by J.M. Kelly, J.M. Eidinger and C.J. Derham - 1977 (PB 276 814)A07
UCB/EERC-77/28	"Seismic Safety of Existing Buildings and Incentives for Hazard Mitigation in San Francisco: An Exploratory Study," by A.J. Meltsner - 1977 (PB 281 970)A05
UCB/EERC-77/29	"Dynamic Analysis of Electrohydraulic Shaking Tables," by D. Rea, S. Abedi-Hayati and Y. Takahashi 1977 (PB 282 569)A04
UCB/EERC-77/30	"An Approach for Improving Seismic - Resistant Behavior of Reinforced Concrete Interior Joints," by B. Galunic, V.V. Bertero and E.P. Popov - 1977 (PB 290 870)A06

UCB/EERC-78/01	"The Development of Energy-Absorbing Devices for Aseismic Base Isolation Systems," by J.M. Kelly and D.F. Tsztoo - 1978 (PB 284 978)A04
UCB/EERC-78/02	"Effect of Tensile Prestrain on the Cyclic Response of Structural Steel Connections, by J.G. Bouwkamp and A. Mukhopadhyay - 1978
UCB/EERC-78/03	"Experimental Results of an Earthquake Isolation System using Natural Rubber Bearings," by J.M. Eidinger and J.M. Kelly - 1978 (PB 281 686)A04
UCB/EERC-78/04	"Seismic Behavior of Tall Liquid Storage Tanks," by A. Niwa - 1978 (PB 284 017)A14
UCB/EERC-78/05	"Hysteretic Behavior of Reinforced Concrete Columns Subjected to High Axial and Cyclic Shear Forces," by S.W. Zagajeski, V.V. Bertero and J.G. Bouwkamp - 1978 (PB 283 858)A13
UCB/EERC-78/06	"Inelastic Beam-Column Elements for the ANSR-I Program," by A. Riahi, D.G. Row and G.H. Powell - 1978
UCB/EERC-78/07	"Studies of Structural Response to Earthquake Ground Motion," by O.A. Lopez and A.K. Chopra - 1978 (PB 282 790)A05
UCB/EERC-78/08	"A Laboratory Study of the Fluid-Structure Interaction of Submerged Tanks and Caissons in Earthquakes," by R.C. Byrd - 1978 (PB 284 957)A08
UCB/EERC-78/09	"Model for Evaluating Damageability of Structures," by I. Sakamoto and B. Bresler - 1978
UCB/EERC-78/10	"Seismic Performance of Nonstructural and Secondary Structural Elements," by I. Sakamoto - 1978
UCB/EERC-78/11	"Mathematical Modelling of Hysteresis Loops for Reinforced Concrete Columns," by S. Nakata, T. Sproul and J. Penzien - 1978
UCB/EERC-78/12	"Damageability in Existing Buildings," by T. Blejwas and B. Bresler - 1978
UCB/EERC-78/13	"Dynamic Behavior of a Pedestal Base Multistory Building," by R.M. Stephen, E.L. Wilson, J.G. Bouwkamp and M. Button - 1978 (PB 286 650)A08
UCB/EERC-78/14	"Seismic Response of Bridges - Case Studies," by R.A. Imbsen, V. Nutt and J. Penzien - 1978 (PB 286 503)A10
UCB/EERC-78/15	"A Substructure Technique for Nonlinear Static and Dynamic Analysis," by D.G. Row and G.H. Powell - 1978 (PB 288 077)A10
UCB/EERC-78/16	"Seismic Risk Studies for San Francisco and for the Greater San Francisco Bay Area," by C.S. Oliveira - 1978
UCB/EERC-78/17	"Strength of Timber Roof Connections Subjected to Cyclic Loads," by P. Gülkan, R.L. Mayes and R.W. Clough - 1978
UCB/EERC-78/18	"Response of K-Braced Steel Frame Models to Lateral Loads," by J.G. Bouwkamp, R.M. Stephen and E.P. Popov - 1978
UCB/EERC-78/19	"Rational Design Methods for Light Equipment in Structures Subjected to Ground Motion," by J.L. Sackman and J.M. Kelly - 1978 (PB 292 357)A04
UCB/EERC-78/20	"Testing of a Wind Restraint for Aseismic Base Isolation," by J.M. Kelly and D.E. Chitty - 1978 (PB 292 833)A03
UCB/EERC-78/21	"APOLLO - A Computer Program for the Analysis of Pore Pressure Generation and Dissipation in Horizontal Sand Layers During Cyclic or Earthquake Loading," by P.P. Martin and H.B. Seed - 1978 (PB 292 835)A04
UCB/EERC-78/22	"Optimal Design of an Earthquake Isolation System," by M.A. Bhatti, K.S. Pister and E. Polak - 1978 (PB 294 735)A06
UCB/EERC-78/23	"MASH - A Computer Program for the Non-Linear Analysis of Vertically Propagating Shear Waves in Horizontally Layered Deposits," by P.P. Martin and H.B. Seed - 1978 (PB 293 101)A05
UCB/EERC-78/24	"Investigation of the Elastic Characteristics of a Three Story Steel Frame Using System Identification," by I. Kaya and H.D. McNiven - 1978
UCB/EERC-78/25	"Investigation of the Nonlinear Characteristics of a Three-Story Steel Frame Using System Identification," by I. Kaya and H.D. McNiven - 1978
UCB/EERC-78/26	"Studies of Strong Ground Motion in Taiwan," by Y.M. Hsiung, B.A. Bolt and J. Penzien - 1978
UCB/EERC-78/27	"Cyclic Loading Tests of Masonry Single Piers: Volume 1 - Height to Width Ratio of 2," by P.A. Hidalgo, R.L. Mayes, H.D. McNiven and R.W. Clough - 1978
UCB/EERC-78/28	"Cyclic Loading Tests of Masonry Single Piers: Volume 2 - Height to Width Ratio of 1," by S.-W.J. Chen, P.A. Hidalgo, R.L. Mayes, R.W. Clough and H.D. McNiven - 1978
UCB/EERC-78/29	"Analytical Procedures in Soil Dynamics," by J. Lysmer - 1978

UCB/EERC-79/01	"Hysteretic Behavior of Lightweight Reinforced Concrete Bean-Column Subassemblages," by B. Forzani, E.P. Popov, and V.V. Bertero - 1979
UCB/EERC-79/02	"The Development of a Mathematical Model to Predict the Flexural Response of Reinforced Concrete Beams to Cyclic Loads, Using System Identification," by J.F. Stanton and H.D. McNiven - 1979
UCB/EERC-79/03	"Linear and Nonlinear Earthquake Response of Simple Torsionally Coupled Systems," by C.L. Kan and A.K. Chopra - 1979
UCB/EERC-79/04	"A Mathematical Model of Masonry for Predicting Its Linear Seismic Response Characteristics," by Y. Mengi and H.D. McNiven - 1979
UCB/EERC-79/05	"Mechanical Behavior of Light Weight Concrete Confined with Different Types of Lateral Reinforcement," by M.A. Manrique and V.V. Bertero - 1979
UCB/EERC-79/06	"Static Tilt Tests of a Tall Cylindrical Liquid Storage Tank," by R.W. Clough and A. Niwa - 1979
UCB/EERC-79/07	"The Design of Steel Energy Absorbing Restrainers and Their Incorporation Into Nuclear Power Plants for Enhanced Safety: Volume 1 - Summary Report," by P.N. Spencer, V.F. Zackay, and E.R. Parker - 1979
UCB/EERC-79/08	"The Design of Steel Energy Absorbing Restrainers and Their Incorporation Into Nuclear Power Plants for Enhanced Safety: Volume 2 - The Development of Analyses for Reactor System Piping," "*Simple Systems*" by M.C. Lee, J. Penzien, A.K. Chopra, and K. Suzuki "*Complex Systems*" by G.H. Powell, E.L. Wilson R.W. Clough and D.G. Row - 1979
UCB/EERC-79/09	"The Design of Steel Energy Absorbing Restrainers and Their Incorporation Into Nuclear Power Plants for Enhanced Safety: Volume 3 - Evaluation of Commerical Steels," by W.S. Owen, R.M.N. Pelloux, R.O. Ritchie, M. Faral, T. Ohhashi, J. Toplosky, S.J. Hartman, V.F. Zackay, and E.R. Parker - 1979
UCB/EERC-79/10	"The Design of Steel Energy Absorbing Restrainers and Their Incorporation Into Nuclear Power Plants for Enhanced Safety: Volume 4 - A Review of Energy-Absorbing Devices," by J.M. Kelly and M.S. Skinner - 1979
UCB/EERC-79/11	"Conservatism In Summation Rules for Closely Spaced Modes," by J.M. Kelly and J.L. Sackman - 1979

UCB/EERC-79/12	"Cyclic Loading Tests of Masonry Single Piers Volume 3 - Height to Width Ratio of 0.5," by P.A. Hidalgo, R.L. Mayes, H.D. McNiven and R.W. Clough - 1979
UCB/EERC-79/13	"Cyclic Behavior of Dense Coarse-Grain Materials in Relation to the Seismic Stability of Dams," by N.G. Banerjee, H.B. Seed and C.K. Chan - 1979
UCB/EERC-79/14	"Seismic Behavior of R/C Interior Beam-Column Subassemblages," by S. Viwathanatepa, E. Popov and V.V. Bertero - 1979